3-24-2019

Texture Evolution of Non-Oriented Electrical Steels during Thermomechanical Processing

Mehdi Mehdi
University of Windsor

Texture Evolution of Non-Oriented Electrical Steels during Thermomechanical Processing

by

Mehdi Mehdi

A Dissertation
Submitted to the Faculty of Graduate Studies
through the Department of Mechanical, Automotive & Materials Engineering
in Partial Fulfillment of the Requirements for
the Degree of Doctor of Philosophy at the
University of Windsor

Windsor, Ontario, Canada

Texture Evolution of Non-Oriented Electrical Steels during Thermomechanical Processing

by

Mehdi Mehdi

APPROVED BY:

_____

K. Verbeken, External Examiner
Ghent University

_____

N. Kar
Department of Electrical Engineering

_____

R. Riahi
Department of Mechanical, Automotive & Materials Engineering

_____

V. Stoilov
Department of Mechanical, Automotive & Materials Engineering

_____

Y. He, Co-Advisor
Department of Mechanical, Automotive & Materials Engineering

_____

A. Edrisy, Co-Advisor
Department of Mechanical, Automotive & Materials Engineering

February 4, 2019

DECLARATION OF CO-AUTHORSHIP/PREVIOUS PUBLICATIONS

1. Co-Authorship Declaration

I hereby declare that this dissertation incorporates research results obtained by the author under the co-supervision of Dr. Afsaneh Edrisy and Dr. Youliang He. I would also like to declare that Dr. Erik J. Hilinski (formerly US Steel and now Tempel Steel, USA) played a vital role in providing the materials used in Chapters 3-7 as well as contributing to the scientific discussion of the obtained results and revising the final manuscripts. I certify that, with the above qualification, this dissertation, and the research to which it refers, is the product of my own work. Dr. Leo Kestens (Ghent University, Belgium) has also significantly contributed to the scientific discussion that led to completion of the manuscripts of which Chapters 3 and 4 are based on.

2. Declaration of Previous Publications

This dissertation includes five original papers that have been published/submitted or to be submitted in peer-reviewed journals as follows:

Chapter 3: M. Mehdi, Y. He, E. J. Hilinski, L. A. Kestens, A. Edrisy, The Formation of the Cube ({100}<001>) Texture in Non-oriented Electrical Steels (to be submitted).

Chapter 4: M. Mehdi, Y. He, E. J. Hilinski, L. A. Kestens, A. Edrisy, The Origins of the Goss Orientation in a 2.8 wt% Si Non-oriented Electrical Steel, Journal of Steel Research International (submitted).

Chapter 5: M. Mehdi, Y. He, E. J. Hilinski, A. Edrisy, Texture Evolution of a 2.8% Si Non-oriented Electrical Steel and the Elimination of the <111>//ND Texture, Journal of Metallurgical and Materials Transactions A (submitted).

Chapter 6: Mehdi, Mehdi, Youliang He, Erik J. Hilinski, and Afsaneh Edrisy, Effect of Skin Pass Rolling Reduction Rate on the Texture Evolution of a Non-oriented Electrical Steel after Inclined Cold Rolling. Journal of Magnetism and Magnetic Materials, 429 (2017): 148-160. (published)

Chapter 7: Mehdi, Mehdi, Youliang He, Erik J. Hilinski, and Afsaneh Edrisy, Non-oriented Electrical Steel with Core Losses Comparable to Grain-oriented Electrical Steel, Journal of Magnetism and Magnetic Materials (submitted).

I certify that I have obtained a written permission from the copyright owner(s) to include the above published/to be published material(s) in my dissertation. I certify that the above material describes work completed during my registration as graduate student at the University of Windsor. I declare that, to the best of my knowledge, my dissertation does not infringe upon anyone's copyright nor violate any proprietary rights and that any ideas, techniques, quotations, or any other material from the work of other people included in my dissertation, published or otherwise, are fully acknowledged in accordance with the standard referencing practices. Furthermore, to the extent that I have included copyrighted material that surpasses the bounds of fair dealing within the meaning of the Canada Copyright Act, I certify that I have obtained a written permission from the copyright owner(s) to include such material(s) in my dissertation. I declare that this is a true copy of my dissertation, including any final revisions, as approved by my dissertation committee and the Graduate Studies office, and that this dissertation has not been submitted for a higher degree to any other University or Institution.

ABSTRACT

The aim of this research is to improve the magnetic properties of non-oriented electrical steels (NOES) for magnetic cores used in electric motors. This was done by controlling the grain size and the final texture of the electrical steel sheets, such that the magnetically favourable θ-fibre (<100>//ND) components are promoted, while the magnetically unfavourable γ-fibre (<111>//ND) components are suppressed. The origins of the magnetically favourable cube and Goss textures were investigated through all thermomechanical processing stages using electron backscatter diffraction (EBSD) techniques. Three types of Goss regions were found after cold rolling. The first two types were embedded inside deformed {111}<112> grains, while the third type was located at grain boundaries. Similarly, the cube texture was also retained at grain boundaries, as well as inside the shear bands of deformed rotated Goss {110}<110> grains. Partial recrystallization led to the preferential nucleation of the Goss and cube nuclei.

The effect of annealing time and grain growth on the texture evolution of NOES was investigated. It was found that by simply changing the *annealing time*, the texture showed significantly different features, i.e. depending on the annealing time, the Goss ({011}<100>), the θ-fibre (<001>//normal direction, ND) or the γ-fibre (<111>//ND) may dominate the texture. The formation of the various textures during annealing at different times was discussed against the oriented growth theory based on a statistic analysis of the grain boundary misorientation and grain size.

In order to improve the final texture in non-oriented electrical steel, an unconventional cold rolling scheme was employed, in which the cold rolling was carried out at an angle (i.e. 30°, 45°, 60°, and 90°) to the hot rolling direction (HRD). It was found that cold rolling at an angle of 60° resulted in substantially improving the crystallographic texture of NOES. Furthermore, the effect

of skin pass rolling at various reduction rates from 5–20% on the texture evolution was investigated.

Finally, the effect of annealing temperature on the microstructure and texture of 3.2% Si steel was studied. It was found that having coarse grains after hot band annealing combined with high temperature annealing can result in significantly weakened γ-fibre components, and promoting the θ-fibre texture. The magnetic properties were measured using Epstein frame test and magnetic Barkhausen noise analysis (MBN). It was found that the DC core losses and MBN_{rms} decreased with increasing grain size, due to the decrease in pinning sites. On the other hand, AC measurements revealed that the optimized texture and grain size was achieved after annealing at 850°C for 60 minutes, with AC core losses comparable to those obtained from commercially available grain-oriented electrical steel (GOES) with the same Si content and sheet thickness.

DEDICATION

I would like to dedicate this work primarily to the Prophet Muhammad and his Holy purified household (Ahlul-bayt) peace be upon them. They certainly are the lanterns of darkness and the treasures of knowledge. They are my shelter, my guide and the light that has always given my life meaning. Everything I am, and everything I will ever be, I owe to them.

I would like to dedicate this work to my mother Rajaa Hassan, my father Alaa Mehdi, my siblings, Raed Mehdi, Hiba Mehdi, Mariam Mehdi and Hossein Mehdi as well as my nephew and nieces Mohammed Hadi, Zahraa, Zainab and Narjis (Anoos). You are the closest people to my heart and I would not be here today if it was not for your endless love and support.

To Imam Al-Mahdi and his holy mother, Narjis.

ACKNOWLEDGEMENTS

First and foremost, I would like to sincerely acknowledge and thank my wonderful supervisors, Dr. Afsaneh Edrisy and Dr. Youliang He for their continuous support and motivation throughout my journey. They have taught me most of what I know about materials engineering and showed me the way great science research can be conducted. To them, I am forever in debt.

I would also like to thank Dr. Erik Hilinski and Dr. Leo Kestens for their enormous help with my research. I have benefited a lot from our discussions and your feedback and critical comments were always mind opening and inspiring for me.

I am also grateful to Dr. Mark Kozdras for his continuous support, Maciej Podlesny for his help in the Magnetic Barkhausen measurements, Michael Attard and Raul Santos for their help on hot rolling, cold rolling and annealing, and to Renata Zavadil, Catherine Bibby, Pei Liu and Dr. Jian Li for their assistance on EBSD characterization and sample preparation.

I am also very grateful for all the help that Dr. Kora Farokhzadeh has provided me with, ever since joining the department. I have always found her extremely helpful and very patient in dealing with her colleagues. I am also grateful to Dr. Mehdi Sanjari for the many productive discussions concerning electrical steels.

Finally, I am also very thankful to my respected committee members, Dr. Reza Riahi, Dr. Vesselin Stoilov, Dr. Narayan Kar and Dr. Kim Verbeken, for taking the time to review my work and adding considerable value to my research.

TABLE OF CONTENTS

LIST OF TABLES

LIST OF FIGURES

Chapter 2

Chapter 3

Chapter 5

LIST OF ABBREVIATIONS/SYMBOLS

AC	**Alternating current**
ASTM	**American Society for Testing and Materials**
BCC	**Body centered cubic**
CRD	**Cold rolling direction**
CSL	**Coincident site lattice**
DC	**Direct current**
EBSD	**Electron backscatter diffraction**
EV	**Electric vehicles**
FCC	**Face Centered Cubic**
GND	**Geometrically necessary dislocations**
GOES	**Grain oriented electrical steel**
GOS	**Grain orientation spread**
HRD	**Hot rolling direction**
IPF	**Inverse pole figure**
IQ	**Image quality**
KAM	**Kennel average misorientation**
K-S	**Kudjomov-Sachs**
MBN	**Magnetic Barkhausen noise**
ND	**Normal direction**
NOES	**Non-oriented electrical steel**
N-W	**Nishiyama–Wassermann**

ODF	**Orientation distribution function**
OIM	**Orientation imaging microscopy**
RD	**Rolling direction**
RMS	**Root mean square**
RF	**Rodrigues-Frank space**
SEM	**Scanning electron microscopy**
TD	**Transverse direction**
XRD	**X-ray Diffraction**

NOMENCLATURE

H	Magnetizing field (A/m)
B	Flux density (T)
μ	Permeability (H/m)
μ_0	Permeability of free space (H/m)
χ	Magnetic susceptibility
J	Magnetic polarization (T)
I	Current (A)
Φ_B	Magnetic flux (Wb)
$\mathcal{E}$	Electromotive force, EMF (V)
W_t	Total energy core loss (J/m^3)
W_h,	Hysteresis energy loss (J/m^3)
W_{cl}	Classical eddy current energy loss (J/m^3)
W_{exc}	Excess energy loss (J/m^3)
P_t	Total power loss (W/Kg)
P_h	Hysteresis power loss (W/Kg)
P_e	Excess power loss (W/Kg)
K_1	Magnetocrystalline anisotropy constant (J/m^3)
μ_B	Bohr magneton
ρ	Electrical resistivity ($\Omega \cdot m$)
d	Grain size (μm)
σ_y	Yield strength (MPa)
ϕ_1	First Euler angle (°)
Φ	Second Euler angle (°)
ϕ_2	Third Euler angle (°)
M	Taylor factor

A_θ	Texture factor (°)
α	<110>//RD fibre
γ	<111>//ND fibre
θ	<100>//ND fibre
B_s	Saturation flux (T)
μ_r	Relative permeability
f	Magnetizing frequency (Hz)
$\vec{M}$	Magnetization vector (A/m)
E	Magnetocrystalline energy $(\mathrm{J/m^3})$
$f(g)$	Orientation distribution function
V_f	Volume fraction
R	Rodrigues vector
σ	Stress (MPa)
ε	Strain

Chapter 1 Introduction

Non-oriented electrical steel (NOES) is an indispensable soft magnetic material for applications in rotating machines, generators, electric vehicles, actuators, alternators, etc. Although a specific crystallographic orientation, like the Goss ({011}<100>) in grain-oriented electrical steel, is not designated to be produced in the material, the crystal axes of the final steel sheets are actually desired to be aligned to the magnetization directions of the magnetic core, in order to reduce core loss and increase permeability. Thus, crystallographic textures that can enhance the magnetic properties of the lamination are highly demanded. Although it has long been recognized that optimizing the crystallographic texture of non-oriented electrical steel can improve the efficiency of the electric motors, limited improvement of the magnetic quality of the steel has been achieved through texture optimization. This is because the final texture of the steel sheet is affected by all the thermomechanical processing steps used to produce the thin sheets, and the metallurgical mechanisms that govern the evolution of texture during thermomechanical processing have not been completely understood.

The objective of this research is to improve the magnetic properties of non-oriented electrical steels through the optimization of crystallographic texture. Focus was placed on the final annealing process to understand the formation mechanisms of specific textures and how to control them. In addition to changing the operational parameters during conventional rolling and annealing processes, a special rolling scheme, i.e. inclined rolling, has been used to investigate the formation mechanisms of the cube texture – a texture of particular interest for non-oriented electrical steels. Electron backscatter diffraction (EBSD) techniques were employed as the main characterization tool to investigate the texture as well as grain boundary characteristics, the latter being particularly

important for the understanding of nucleation and grain growth. The magnetic properties of the produced steel sheets were measured by standard Epstein frame method and compared to commercially available electrical steel grade. Local magnetic response of the electrical steel was also investigated by magnetic Barkhausen noise (MBN) analysis. A texture factor was utilized to evaluate the anisotropy of the steel sheets in various directions. Non-oriented electrical steels with silicon concentrations varying from 0.9 to 3.2 wt% were studied. All the steel processing was carried out using pilot-scale facilities under controlled conditions, the results obtained may be directly utilized in industrial mass production after validation tests.

The findings of this dissertation were presented in scientific journal publication formats in Chapters 3 to 7, and a summary of the contributions to knowledge was given at the end of the dissertation (Chapter 8). A literature review was presented in Chapter 2 to introduce background information about this research. The following summarizes the structure of the dissertation and briefly introduces the content of each Chapter.

Chapter 2: A literature review that introduces the material to be studied and the history of related research in this field. It also includes discussion on the different types of core losses in non-oriented electrical steels and their relations to the material's chemistry, dimension, microstructure and texture, which provides background information and motivation for the current research.

Chapter 3: The formation mechanisms of the cube ({001}<001>) texture during annealing of high silicon (2.8-3.2 wt%) non-oriented electrical steels were investigated under conventional rolling and inclined rolling conditions. Two origins of the cube orientations were identified, either at the grain boundaries of deformed cube grains or at the shear bands of deformed {110}<110> (rotated

Goss) grains. The formation of the cube volumes within the deformed matrix was attributed to the partial retention of the original cube grain during plane-strain compression (cube at grain boundaries), or to the geometric softening of the rotated Goss through the formation of shear bands (cube at shear bands). The formation of recrystallized cube grains after annealing was due to the nucleation of the small low-stored-energy cube volumes in the deformed matrix after cold rolling. These mechanisms provide potential technical routes to producing the cube texture in non-oriented electrical steels.

Chapter 4: The origins of the Goss grains in a cold-rolled non-oriented electrical steel (2.8 wt% Si) were investigated using electron backscatter diffraction (EBSD) techniques. Three locations of the Goss grains were observed in the deformed matrix, i.e. those within the shear bands of two symmetrically equivalent {111}<112> grains, those embedded in the microbands of one of the {111}<112> grains, and those at the grain boundaries between the {111}<112> and {113}<361> grains. The formation mechanisms of these three types of Goss grains during plane-strain deformation were explained using the transition band model and the rigid inclusion model by considering their specific crystallographic orientation relationships with respect to the surrounding deformed matrix. The formation of the clusters of Goss grains in the recrystallized steel was explained by an oriented growth theory due to the Goss nuclei formed at the {111}<112> and {113}<361> grain boundaries having special ~35°<110> misorientations with respect to their neighbours and having high mobility.

Chapter 5: A 2.8 wt% Si non-oriented electrical steel was thermomechanically processed using conventional hot rolling, hot band annealing, cold rolling and final annealing routes. The evolution

of texture during these processes was investigated. The final annealing was conducted at 750°C for various times (10 to 120 minutes), and it was found that by simply changing the annealing time, the texture showed significantly different features, i.e. depending on the annealing time, the Goss ({011}<100>), the θ-fibre (<001>//normal direction, ND) or the γ-fibre (<111>//ND) may dominate the texture. Annealing for 60 or 90 minutes can essentially eliminate the magnetically unfavourable <111>//ND texture while promoting the desired <001>//ND texture. On the other hand, annealing at the same temperature for 30 or 120 minutes, the <111>//ND texture is strengthened and the favorable <001>//ND texture is weakened. The formation of the typical textures observed in each process was examined with respect to known mechanisms existing in the literature. The formation of the various textures during annealing at different times was discussed against the oriented growth theory based on a statistic analysis of the grain boundary misorientation and grain size. It is seen that during annealing at different times, the grain boundary character (e.g. mobility) and the grain size may determine the growth of certain orientations, which give rises to the different textures after annealing for different times.

Chapter 6: In order to promote the magnetically favourable <001>//ND texture (θ-fibre) and minimize the unfavourable <111>//ND fibre (γ-fibre) in non-oriented electrical steel, an unconventional cold rolling scheme was employed in this study, in which the cold rolling was carried out at an angle (i.e. 30°, 45°, 60°, and 90°) to the hot rolling direction (HRD). After annealing, two steel sheets (i.e. those after cold rolling at 60° and 45° to the HRD) were found to have considerably different textures from other sheets, i.e. showing the strongest and the weakest θ-fibre textures, respectively. These two sheets were then subjected to skin pass rolling to various reduction rates from 5% to 20% to investigate the effect of rolling reduction on the evolution of

texture. It was found that during skin pass rolling, the cube texture ({001}<100>) was gradually weakened and the rotated cube orientation ({001}<110>) was strengthened. With the increase of the reduction rate, the {112}<110> orientation on the α-fibre became a major component. Upon final annealing, the cube texture was slightly restored, but the volume fraction was considerably lower than that before skin pass rolling.

Chapter 7: A 3.2% Si non-oriented electrical steel (NOES) was processed using conventional rolling routes. The hot-rolled plate was annealed at 860°C for 24 hours and cold rolled to a thickness of 0.35 mm. The cold-rolled sheets were subjected to final annealing at various temperatures ranging from 750 °C to 1150 °C. The evolution of texture during all the thermomechanical processing stages was investigated by electron backscatter diffraction techniques (EBSD). It was found that the annealing temperature had a profound effect on the texture. At higher temperatures and shorter holding times, the desired <100>//ND texture was promoted while the detrimental <111>//ND texture was weakened. The magnetic properties of the steel sheets were measured by Epstein frame method, and it was found that the AC core loss of the NOES annealed at 850°C for 60 minutes was comparable to grain-oriented electrical steel (GOES) with the same silicon content, even in the rolling direction.

Chapter 8: A summary of the achievements and contributions to knowledge.

Chapter 2 Literature Review

2.1 Magnetic materials

Magnetic materials can be classified into three major groups (Fig. 2.1): 1) hard magnetic materials, 2) soft magnetic materials, and 3) magnetic recording materials. Hard magnetic materials are a class of materials that are hard to magnetize and demagnetize. These materials have high coercivity and hysteresis, and can be used to make permanent magnets. Soft magnetic materials are materials that are easy to magnetize and demagnetize, and have substantially lower coercivity and hysteresis. Soft magnetic materials are also distinguished from other magnetic materials by their high permeability and low energy loss [1-5]. Their coercivity is of the order of ~40 A/m (close to the earth's magnetic field strength) [5]. Magnetic recording materials are a subclass of hard magnetic materials and are sometimes referred to as "semi-hard magnets".

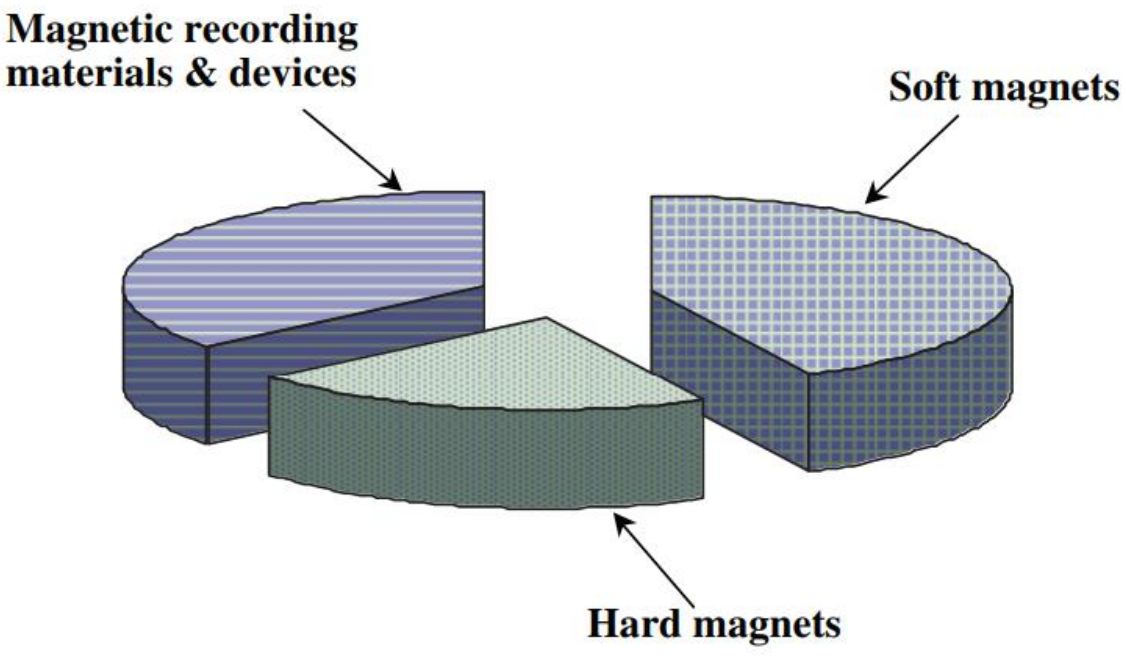

Fig. 2.1. The types of magnetic materials and their market shares [5].

Soft magnetic materials have been widely used for more than 100 years for the generation, conversion, and distribution of electricity. They have been employed in heavy-duty flux multipliers as the core material for transformers, motors and generators. Additionally, they have also been used as light-duty flux multipliers for small transformers and inductors. The approximate market value of soft magnetic steels was €20 billion in 2015, with an approximate annual growth rate of 5% [5].

Soft magnetic materials can be further divided into several subclasses such as: Fe-Si steels, amorphous soft magnets, soft ferrites, nickel-iron (Permalloy), cobalt-iron, etc. (Fig. 2.2). Fe-Si alloys are the most widely used soft magnetic materials in the market today. They are referred to as *electrical steels* or *silicon steels*, and are subdivided into *non-oriented electrical steel* (NOES) and *grain-oriented electrical steel* (GOES) [1-5]. GOES became the material of choice for transformers after the development of the Goss process in the 1930s [5, 6]. This steel exhibits remarkable magnetic properties (high permeability, high flux saturation and low core loss) in the rolling direction (RD), but is highly anisotropic and expensive to process, which is not ideal for rotating machine applications. On the other hand, non-oriented electrical steels are much more suitable for rotating machines (motors and generators) due to their much more isotropic magnetic properties. NOES is the focus of this thesis, and the final applications include conventional electric motors, generators as well as traction motors in hybrid and electric vehicles [5-8].

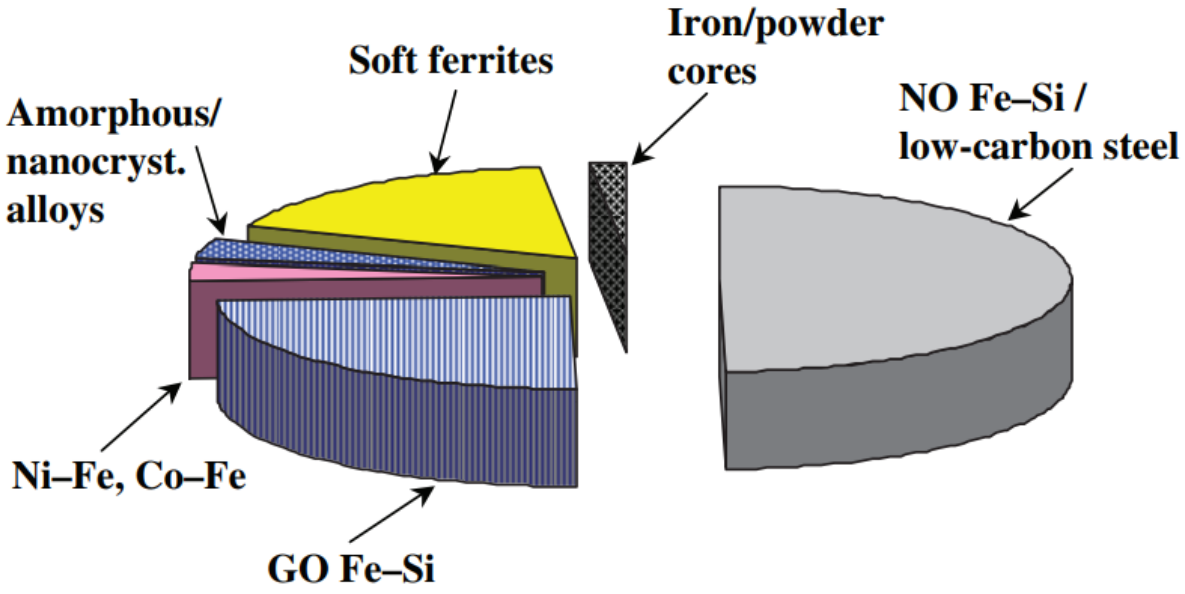

Fig. 2.2. The subclasses of soft magnetic materials and their market shares [5].

2.1.1 Non-oriented electrical steel (NOES)

Non-oriented electrical steels come in a variety of grades and their specifications are defined in several standards, including ASTM A677 [9], IEC 60404-8-4, IEC 60404-8-6, and IEC 60404-8-8 [5]. The material designation is given based on the steel sheet's thickness as well as the alternating current (AC) power loss (in W/kg) at a frequency of 50 Hz and a peak induction of 1.5 T. For example, a non-oriented electrical steel sheet with a designation of M250-35A has a sheet thickness of 0.35 mm and a power loss of 2.50 W/kg at a frequency of 50 Hz and a peak induction of 1.5 T. The American standards and designations [9] are slightly different. The core loss according to the ASTM A677 is measured at 1.5 T and a frequency of 60 Hz, and the loss is reported in W/lb. The same non-oriented steel mentioned earlier would have the designation of 36F145, which means a thickness of 0.36 mm and a power loss of 1.45 W/lb at 60 Hz and a peak induction of 1.5 T [5-9].

Non-oriented electrical steels can either be fully processed (higher grades) or semi-processed (lower grades with Si < 2 wt %). The fully processed NOES are usually hot rolled to a thickness of ~2.5 mm, and then cold rolled to an intermediate gauge. This is followed by an intermediate anneal and a second cold rolling process to obtain the required thickness. The two-stage cold rolling procedure and the intermediate anneal are the main defining features of the fully processed NOES [5-8, 10]. The steel sheets are then subject to decarburization annealing and grain growth annealing to obtain the required grain size. An insulating coating is finally applied to the steel sheets before punching and core assembly. The fully processed NOES generally does not undergo stress-relief heat treatment after punching. On the other hand, semi-processed NOES is processed through single-stage cold rolling followed by annealing and skin pass rolling (temper rolling) with a reduction between 4% and 12% [10]. The steel sheets are coated by the steel producer, but the punching and the final stress relief annealing are left to the customer. The final stress-relief annealing is vital in achieving the required grain size and the desired final magnetic properties [5-8, 10]. The typical thermomechanical procedures for fully processed and semi-processed NOES are summarized in Fig. 2.3 and 2.4, respectively.

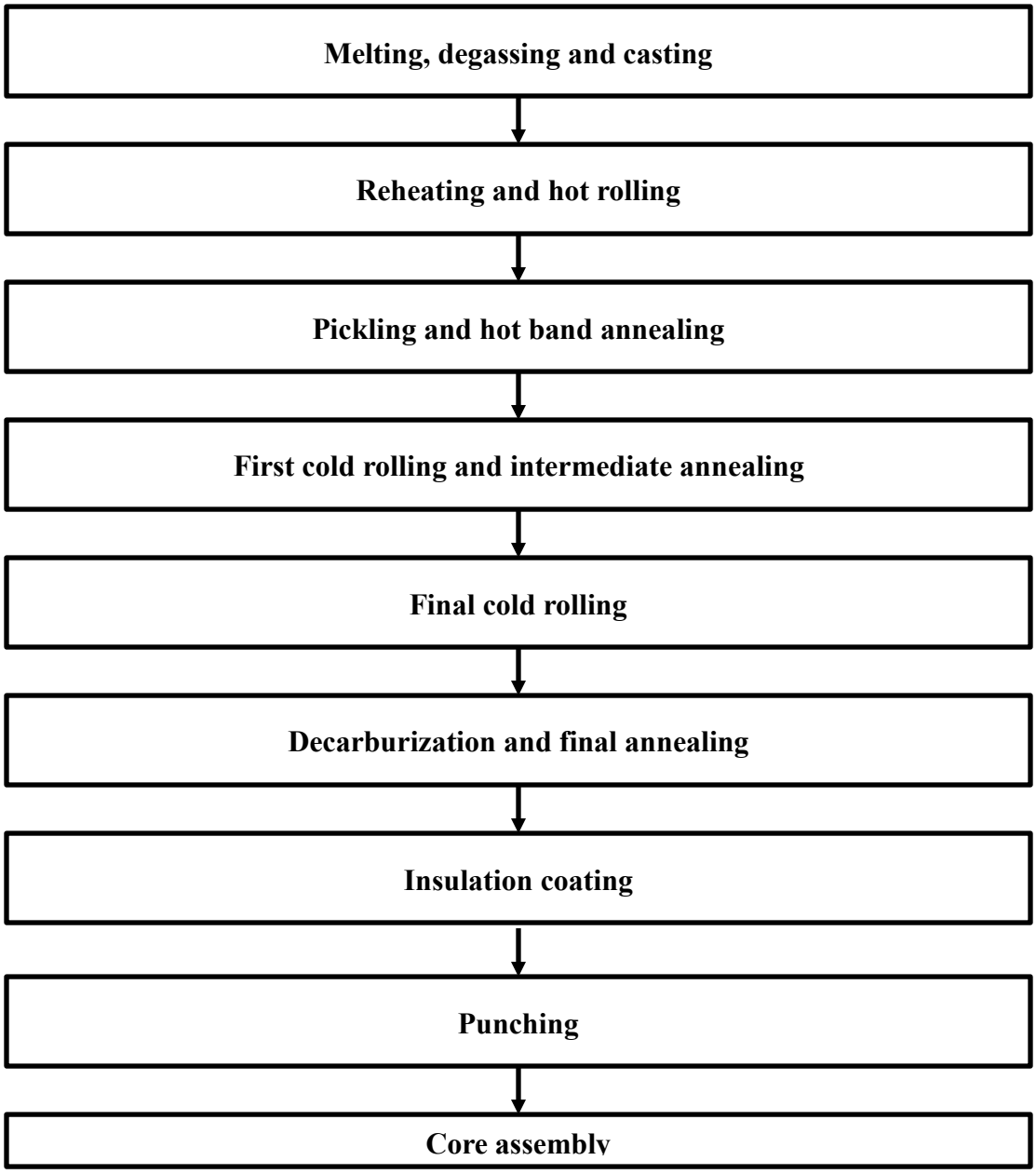

Fig. 2.3. Common processing steps for fully processed non-oriented electrical steels.

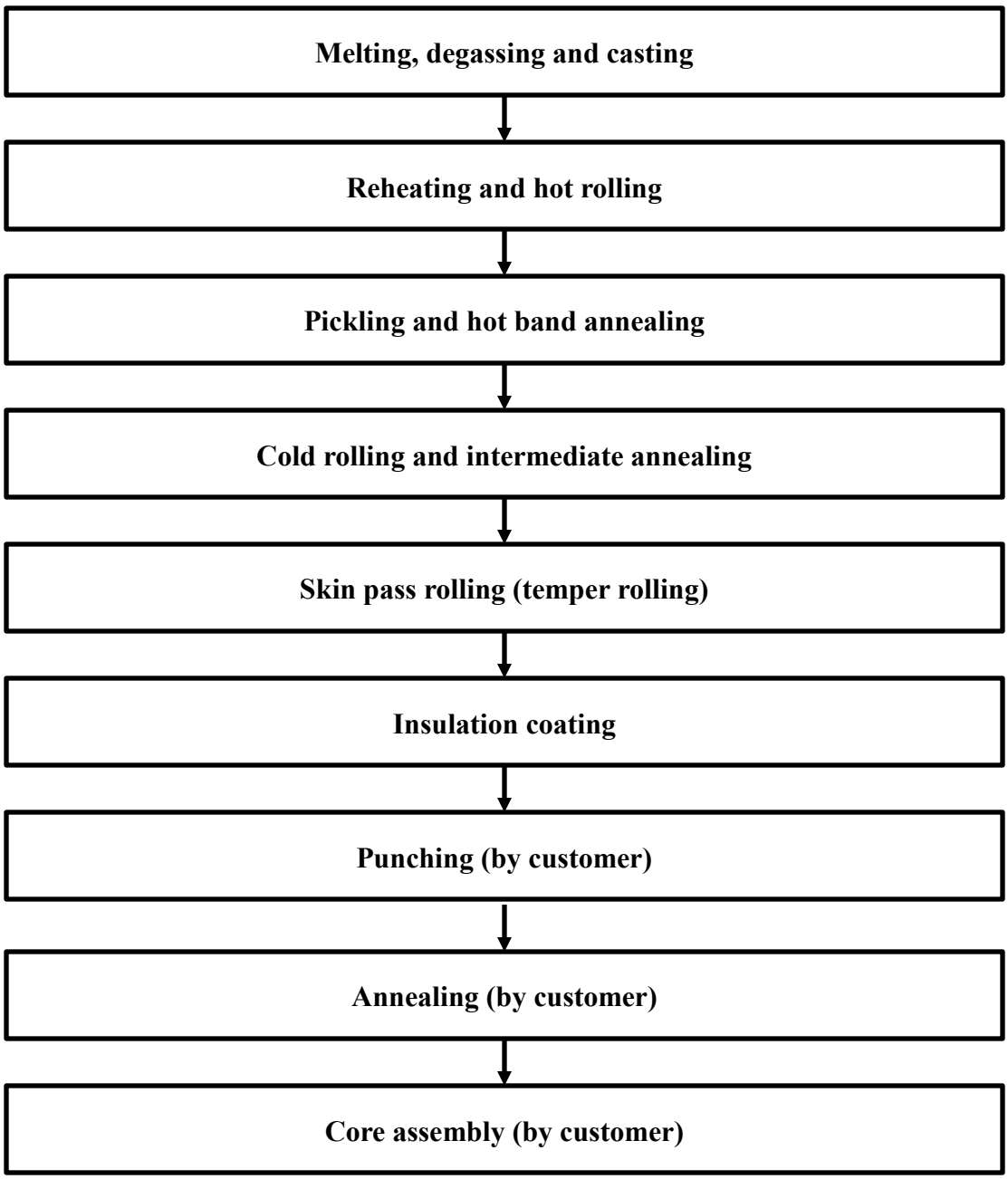

Fig. 2.4. Typical processing steps for semi-processed non-oriented electrical steels.

The major alloying element in non-oriented electrical steel is silicon, with a concentration varying between 0 and ~3.5 wt %. Silicon has a substantial effect on the electrical, magnetic and mechanical properties of the electrical steel, which is discussed separately in the following

sections. Other minor alloying elements include: aluminum (0.2-0.8 wt%), manganese (0.1-0.3 wt %), and sometimes antimony. The top commercial grades of NOES has ~4.0 wt % (Al + Si) if it is processed conventionally. The addition of Si, Al and Mn increases the material's electrical resistivity and thus reduces the eddy current loss. On the other hand, aluminum prevents magnetic aging through N precipitation, and lowers the primary recrystallization temperature. Manganese is used to capture the residual sulfur impurities from thermomechanical processing through the formation of MnS precipitates. The magnetic and mechanical properties of NOES are also strongly affected by impurities, thus the steel is required to maintain very low levels of C, O, N and S [5-8].

Despite what the name might suggest, the magnetic properties of *non-oriented* electrical steels are actually NOT *isotropic*. The magnetic properties of NOES vary by 10-20% along different directions due to the magnetocrystalline anisotropy of bcc iron and the final crystallographic texture of the steel sheet. They are preferred for high efficiency applications that involve high power rotating machines. The semi-processed sheets have a typical thickness between 0.50 mm and 0.65 mm, while the fully processed grades range from 0.10 mm to 0.65 mm. The reduction in sheet thickness is necessary for high efficiency applications, since it leads to a decrease in eddy current loss. The decrease of eddy current loss may be limited by the Si concentration (usually up to 3.5%), since Si addition lowers the ductility of the material, and the final sheet thickness that can be achieved by cold rolling is limited. Thus, the competing effects of the chemical composition, texture, microstructure as well as mechanical properties on the final magnetic properties require an optimized process to obtain the desired magnetic properties for a given application [1-3, 5-7, 10].

2.2 Fundamentals of magnetism and magnetic properties

The magnetic flux density, or sometimes referred to as magnetic induction **B**, is measured in Tesla (T), and is related to the magnetic field strength **H** (measured in Am^{-1}), through the permeability μ ($H\ m^{-1}$), of the material. The relationship between the magnetic induction and the magnetic excitation is expressed as [1-4]:

$$\boldsymbol{B} = \mu\, \boldsymbol{H} \tag{2.1}$$

It should be noted that both **H** and **B** are vectors, and in free space (vacuum or air) they have the same direction. The permeability in free space is a constant, μ_o = 1.257×10^{-6} Hm^{-1}, thus $\boldsymbol{B} = \mu_0\, \boldsymbol{H}$.

If there is a ferromagnetic material in the free space, the application of a magnetic field **H** results in the creation of a magnetization **M** in the ferromagnetic material by the realignment of the magnetic domains, i.e. a magnetic polarization (with an intensity of **J**) is created:

$$\boldsymbol{J} = \mu_o \boldsymbol{M} \tag{2.2}$$

Thus the overall magnetic flux density is calculated as:

$$\boldsymbol{B} = \mu_o \boldsymbol{H} + \boldsymbol{J} = \mu_o(\boldsymbol{H} + \boldsymbol{M}) \tag{2.3}$$

Magnetic susceptibility, χ, is another constant that measures the extent to which a material can be magnetized by an external magnetic field, i.e.

$$\chi = \frac{M}{\boldsymbol{H}} \tag{2.4}$$

Thus

$$\boldsymbol{B} = \mu_o(\boldsymbol{H} + \boldsymbol{M}) = \mu_o(1 + \chi)\boldsymbol{H} = \mu_o \mu_r \boldsymbol{H} \tag{2.5}$$

where $\mu_r = 1 + \chi$ is the relative permeability of the material, thus

$$\mu = \mu_o\,(1 + \chi) = \mu_o \mu_r \tag{2.6}$$

Both relative permeability and susceptibility are material properties, based on which a material can be classified into diamagnetic, paramagnetic, ferromagnetic, ferrimagnetic, or antiferromagnetic, etc. [1-4]. Table 2.1 shows the relative susceptibility of various materials and their classifications.

Table 2.1. The susceptibility or relative permeability values of some diamagnetic, paramagnetic, ferromagnetic and ferrimagnetic materials [11-12].

Kind of magnetism and examples	Susceptibility, χ
(I) Diamagnetism	
Copper	-1.0×10^{-5}
Zinc	-1.4×10^{-5}
Gold	-3.6×10^{-5}
Mercury	-3.2×10^{-5}
Water	-0.9×10^{-5}
Hydrogen (n.t.p.)**	-0.2×10^{-8}
(II) Paramagnetism	
Lithium	$+4.4\times10^{-5}$
Sodium	$+0.62\times10^{-5}$
Aluminum	$+2.2\times10^{-5}$
Vanadium	$+38\times10^{-5}$
Palladium	$+79\times10^{-5}$
Neodymium	$+34\times10^{-5}$
Air† (n.t.p.)	$+36\times10^{-8}$
	Approximate highest value of relative permeability, $\mu'(=1+\chi)$
(III) Ferromagnetism	
Iron crystals	1.4×10^{6}
Cobalt crystals	$\approx10^{3}$
Nickel crystals	$\approx10^{6}$
3.5% Si–Fe (transformer sheets)	7×10^{4}
(single crystals)	3.8×10^{6}
(IV) Ferrimagnetism	
Fe_3O_4	100
Ferrites	5000

2.3 Core losses

Core loss is also known as iron loss, which is the energy loss caused by the alternating magnetization of the magnetic core usually made of iron (electrical steel). The total iron loss at every cycle of magnetization for a given frequency *f* can be written as [1-5, 14]:

$$W(f) = W_h + W_{cl}(f) + W_{exc}(f) \tag{2.7}$$

where W_h is the static (DC) hysteresis core loss which is independent of frequency *f*, $W_{cl}(f)$ is the classical eddy current loss, and $W_{exc}(f)$ is the excess loss. The area of the hysteresis loop represents the energy loss during the magnetization and demagnetization process [5, 14].

2.3.1 Hysteresis loss

Before magnetization, the electrical steel is magnetically neutral, i.e. there is no magnetic field in the material. This is due to the fact that the magnetic domains are randomly oriented in the material, and their overall magnetic effects cancel each other. This is referred to as the demagnetized state in which the current (**I**) is **I**=**H**=**0**. As the material is magnetized through an external magnetic field (**H**), the domains that have their magnetic axis aligned with the external magnetic field direction grow at the expense of those that are misaligned along the magnetization direction.

Fig. 2.5 shows a typical hysteresis loop (B-H curve) corresponding to the magnetization and demagnetization processes. The initial magnetization follows the OABC route until the material reaches saturation (point C), where a maximum magnetic flux density B_m is reached [13]. If now the magnetizing force is reduced to zero (**I = 0**), the material will not return to the initial neutral state, i.e. a residual flux density B_r will remain in the material, which is called remnant (point D). This means that in order to completely demagnetize the material, a magnetizing force

in the opposite direction has to be applied. The magnitude of **H** required to remove the residual flux density is referred to as coercivity (or coercive force), H_c (point E). Furthermore, when the magnetization force is applied in the opposite direction, the material becomes magnetized with an opposite polarity until saturation is reached again (point F). The closed loop CDEFGC is called a hysteresis loop and the enclosed area is proportional to the energy loss. The equation for the hysteresis loss can thus be written as [13]:

$$W_h = \oint HdB \tag{2.8}$$

which can be estimated using the following empirical formula [13]:

$$W_h = K_h(B_m)^x \tag{2.9}$$

where K_h and x are material dependent parameters.

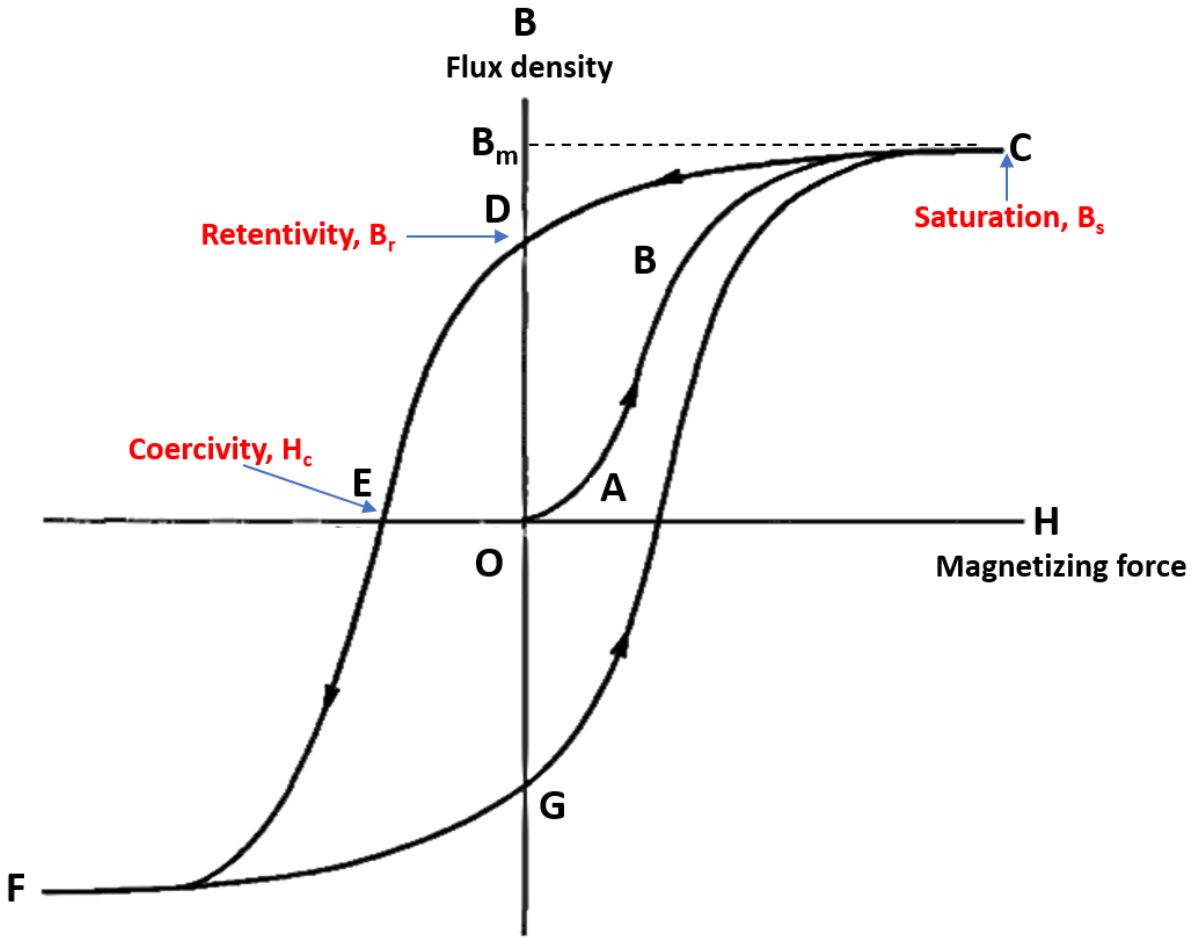

Fig. 2.5. Hysteresis loop showing the relationship between magnetizing field **H** and the flux density **B** [13]

2.3.2 The eddy current loss

Non-oriented electrical steels are often used under alternating current (AC) conditions, meaning that the magnetic properties have to be quantified under time-varying magnetic flux density (often in sinusoidal format). Therefore, using Faraday's law the magnetic flux can be written as [1-4]:

$$\Phi_B = \iint_{\Sigma(t)} B(r,t) \cdot dA \tag{2.10}$$

where Φ_B is magnetic flux, dA is an element of a moving surface $\Sigma(t)$, and B(r, t) is the magnetic flux density. Faraday's law of induction indicates that with any change in the magnetic flux over time an electromotive force, EMF, will be induced in the coil. The EMF ($\mathcal{E}$) can be written as [1-4]:

$$\mathcal{E} = -\frac{d\Phi_B}{dt} \tag{2.11}$$

This EMF results in circulating current known as eddy current that flows inside the material, which in turn results in eddy current loss. This energy loss can thus be calculated from the Maxwell-Faraday equation by assuming a very thin, infinite sheet with a constant permeability as well as a time-varying alternating flux. The eddy current loss can be written as [5, 14]:

$$W_{cl}(f) = \frac{\pi^2}{k}\sigma d^2 B_m^2 f = \frac{\pi^2}{k\rho} d^2 B_m^2 f \quad (J/m^3) \tag{2.12}$$

where d is the sheet thickness, σ is the electrical conductivity, ρ is electrical resistivity, B_m is the peak flux density, f is frequency, and k is a constant depending on the magnetization waveform, which is often taken to be 6 if the wave has a sinusoidal form for an infinitely wide sheet.

2.3.3 The excess loss

The excess loss is also known as the anomalous loss. The exact origin of the excess loss remains a subject of debate in the literature. It is generally accepted that the excess loss arises from motion of large domains. Since the excess loss arises from the motion, creation and annihilation of magnetic domains, some researchers have suggested that W_h and W_{exc} might be caused by the same phenomena. The excess loss is usually determined by subtracting the total loss from the

hysteresis loss and the classical eddy current loss, as shown in Eq. 2.7. Or, it may be estimated using the following equation [5, 14]:

$$W_{exc}(f) = k_{exc}\sqrt{\sigma f}B_m^{3/2} \quad (J/m^3) \tag{2.13}$$

where k_{exc} is a material fitting parameter related to the domain structure and the structural properties of the material. Apparently, the excess loss is related to the electrical conductivity, frequency and the saturation flux density, etc.

The variation of the overall power loss with magnetizing frequency is shown in Fig. 2.6. The total loss consists of a quasi-static term (area of the hysteresis loop at DC, and frequency independent), a classical eddy current loss term ($\propto f$), and an excess loss term ($\propto \sqrt{f}$) [5, 14].

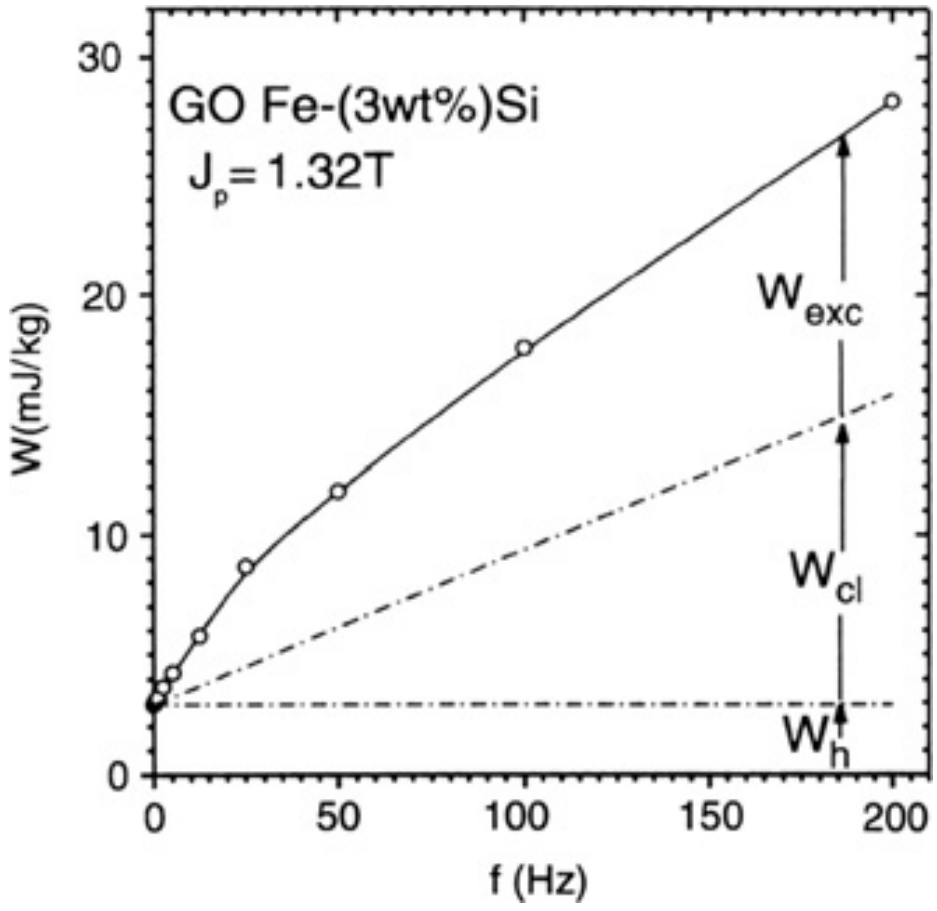

Fig. 2.6. The variations of W_h, W_{cl} and W_{exc} with respect to the frequency for GOES at B=1.32 T [14].

Using the loss terms for all the three losses, a combined total energy loss per cycle can be written as:

$$W_t = P/f = K_h(B_m)^x + \frac{\pi^2}{k\rho} d^2 B_m^2 f + k_{exc}\sqrt{\sigma f} B_m^{3/2} \quad (2.14)$$

which can be converted to power loss in the following way:

$$P_t = K_h(B_m)^x f + \frac{\pi^2}{k\rho} d^2 B_m^2 f^2 + k_{exc}\sqrt{\sigma} B_m^{3/2} f^{3/2} \quad (2.15)$$

2.4 The effect of grain size

The power loss in non-oriented electrical steel is highly dependent on grain size. The total power loss decreases with the increase of grain size up to an optimum value (around 150 μm) as shown in Fig. 2.7 [6]; after that, the total loss slightly increases with the grain size. This is because the hysteresis loss, the eddy current loss and the excess loss have opposite relations with respect to grain size: the hysteresis loss decreases with grain size, while the eddy current and excess losses increase with grain size. In fact, Bertotti et al. was able to fit the relation between the hysteresis loss and grain size to a similar pattern as the well-known Hall-Petch relation (Fig. 2.8) [5, 15]. On the other hand, the excess loss was found to increase with grain size ($W_{exc} \propto \sqrt{d}$) as shown in Fig. 2.9a. The competing effects of eddy current/excess and hysteresis losses lead to an optimized grain size, which is highly dependent on the chemical composition of the material and the processing history.

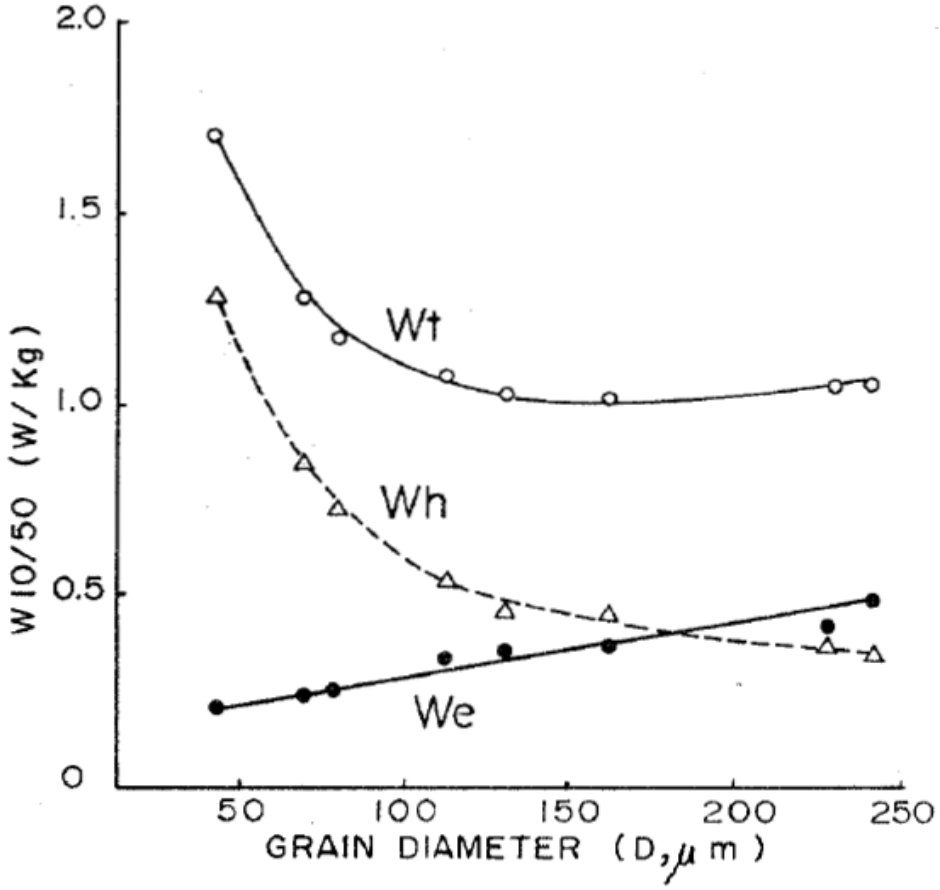

Fig. 2.7. Variations of the total power loss, W_t, hysteresis loss, W_h, and eddy current losses, W_e, with respect to grain diameter [6].

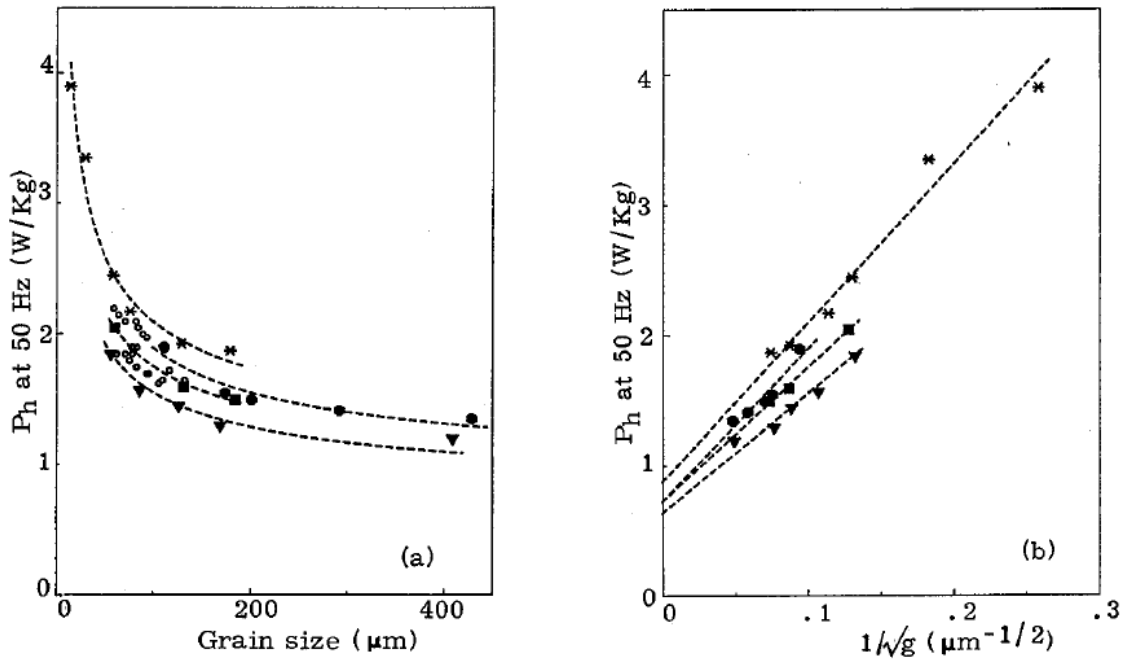

Fig. 2.8. (a) Variation of hysteresis loss, P_h, with grain size (g), and (b) hysteresis loss plotted against $1/\sqrt{g}$ [15].

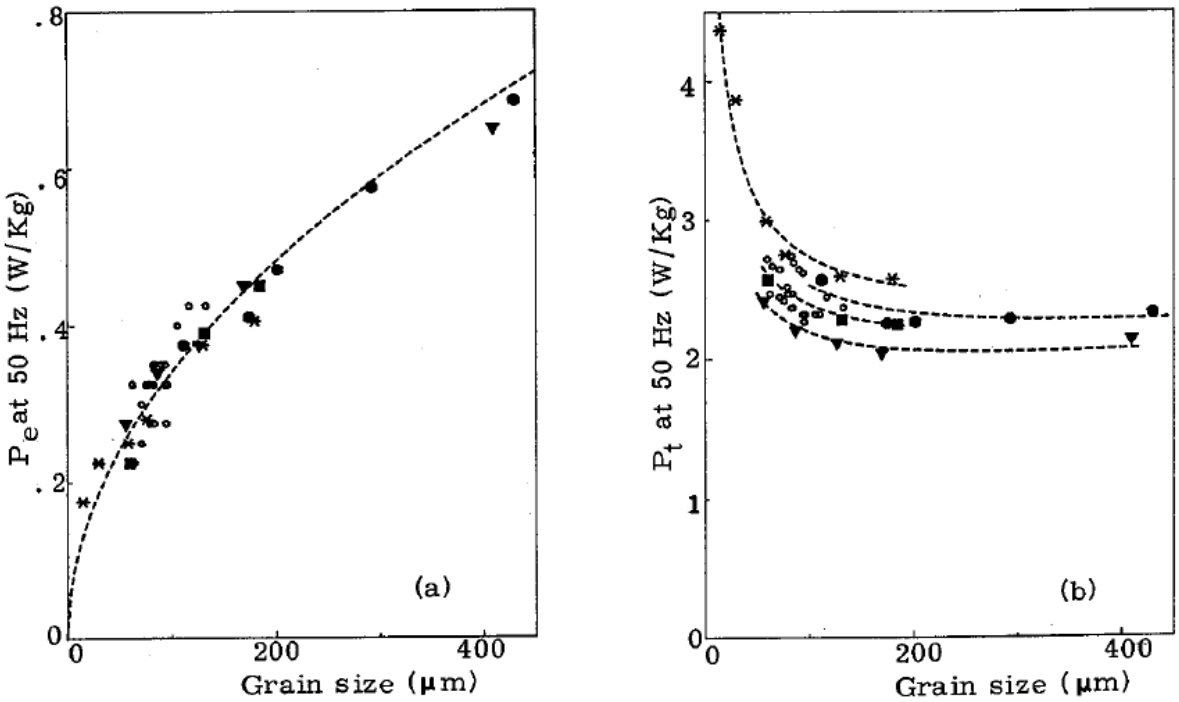

Fig. 2.9. The relationship between power loss and grain size (g): (a) excess power loss (P_e) vs. grain size ($P_e \propto \sqrt{g}$), and (b) the total power losses P_t vs. grain size [15]**.**

Since power losses are also highly dependent on frequency, it is important to understand the effect of frequency on power losses. As mentioned before, hysteresis loss is considered as quasi-static, thus it is independent of frequency. On the other hand, both eddy current and excess losses increase with increasing frequency as shown in Eqs. 2.12 and 2.13. This means that at low frequencies, hysteresis loss becomes the dominant term, and a larger grain size is favoured in reducing the total loss. By contrast, at high frequencies, eddy current and excess losses start to dominate, thus for high frequency applications, a smaller grain size would lead to less total loss (Fig. 2.10). Thus, the optimal grain size for low core loss may be dependent on the application.

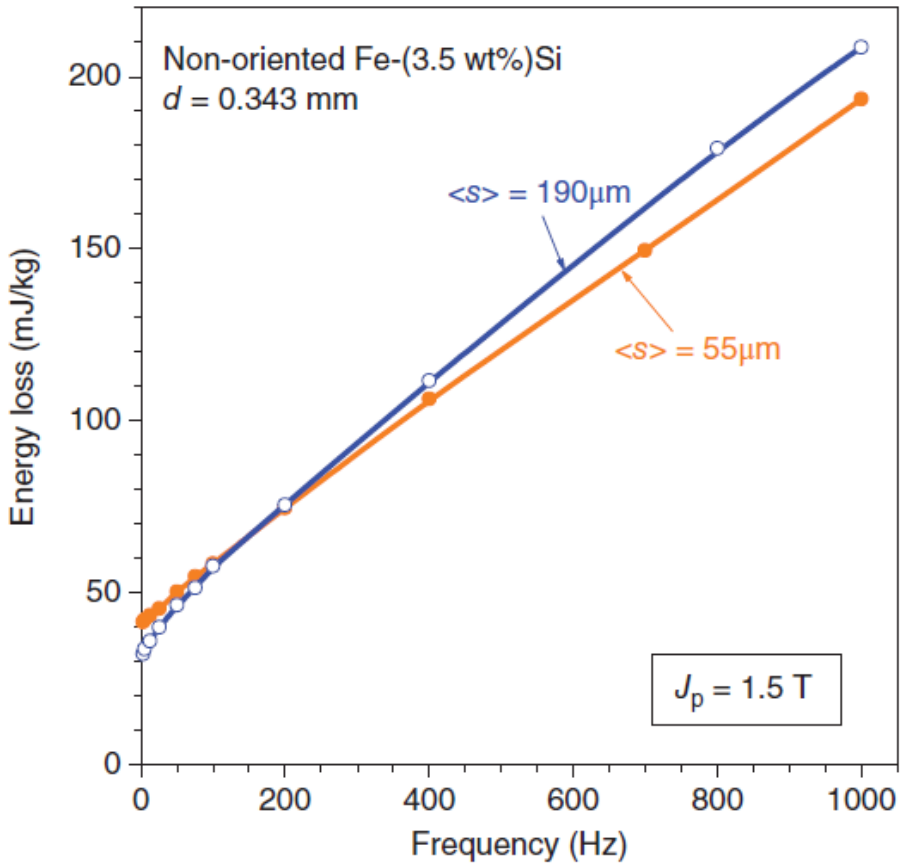

Fig. 2.10. The variation of the total energy loss with respect to frequency for a 3.5 wt. % Si non-oriented electrical steel with two grain sizes 55 μm and 190 μm [5].

2.5 The effect of impurities

The presence of impurities such as C, O, N and S in non-oriented electrical steels significantly affects the magnetic properties. An increase in impurities leads to an increase in coercivity and thus increasing the area of the hysteresis loop, which in turn results in an increase in power loss. This is because the formation of precipitates of these elements with other elements leads to the pinning of domain walls and thus hindering their growth and motion when an external magnetization force is applied. This pinning effect results in an increase in the frictional force between the domains and the precipitates, giving rise to an increase in hysteresis loss. In addition, precipitates can also indirectly affect the magnetic properties of non-oriented electrical steel by retarding the grain growth, which may restrict the final grain size. For example, the sulfur content in non-oriented electrical steel should be controlled below 10 ppm (0.0010%) in order to achieve the optimized grain size discussed in the previous section. Fig. 2.11 shows the effect of sulfur content on the grain size of non-oriented electrical steel that has been annealed at similar conditions. The two most important precipitates that are produced in electrical steel are AlN and MnS [5, 6, 10].

In addition to precipitates, other defects or structural elements may also pin the motion of magnetic domain walls, e.g. vacancies, inclusions, dislocations, grain boundaries [5], etc. Thus, a clean material and stress relief annealing can significantly decrease the core loss. A microstructure with large grain size may also decrease the hysteresis loss because of the reduced grain boundaries. Usually, heat treatment of electrical steels has to be conducted in protected environments in order to prevent oxidation and diffusion of other impurities, which could significantly impact the magnetic properties. Finally, some researchers [5] have reported that the formation of inclusions

and precipitates in electrical steels favours the development of magnetically detrimental textures (γ-fibre). This in return results in the increase of iron loss in the material [5].

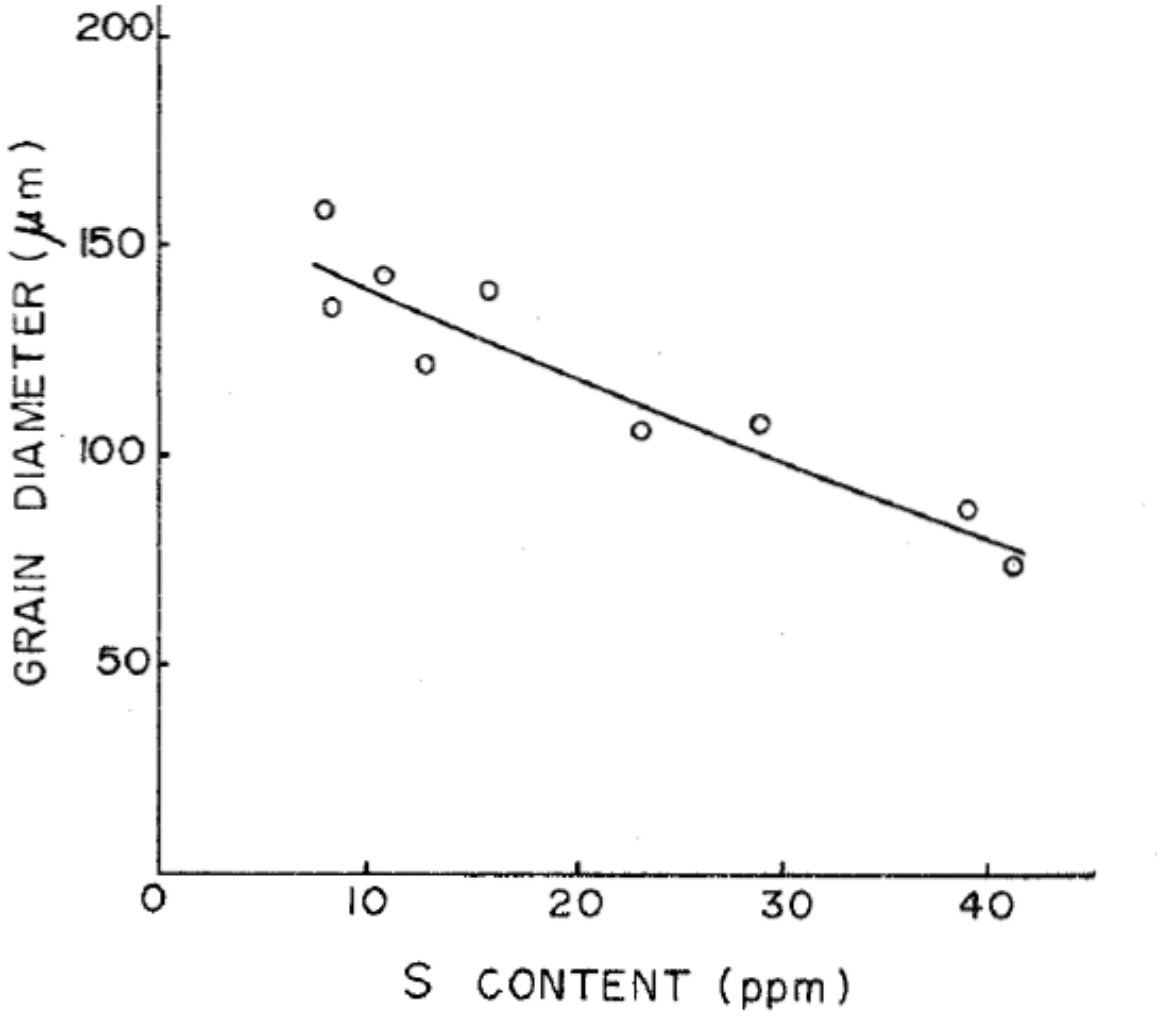

Fig. 2.11. The relationship between the grain size and the sulfur content in a 3% Si steel [6].

2.6 The effects of sheet thickness and residual stress

2.6.1 Sheet thickness

The thickness of the final steel sheets for the magnetic core used in either electric motors or transformers has a significant effect on the eddy current loss. Equation 2.12 shows that the eddy current loss is inversely proportional to the thickness of the sheet [14]. Therefore, reducing the thickness of the electrical steel sheet can significantly decrease the core loss. Table 2.2 shows the dependence of core loss in fully processed NOES on the sheet thickness. It can be seen that the reduction in core loss for medium frequency applications (400 Hz) can be ~13% when the sheet thickness is reduced from 0.27 mm to 0.10 mm. At high frequencies (2.5 kHz), the reduction of core loss can reach 55% [5]. However, with the increase of the silicon content in the steel, producing thin steel sheets by cold rolling becomes increasingly difficult. This would require additional processing stages such as, two stage cold rolling and intermediate annealing, which would increase the cost of the steel. If the silicon content is increased to ~4.0% or more, it is essentially not possible to cold roll the steel.

Table 2.2. The effect of sheet thickness on the core loss of fully processed NOES at 400 Hz and 2.5 kHz [5].

Grade	Sheet thickness (mm)	Maximum specific loss at 1.0 T (W/kg)	
		$f = 400$ Hz	$f = 2.5$ kHz
NO27	0.27	15.0	300
NO20	0.20	15.0	215
NO18	0.178	14.3	179
NO12	0.127	13.5	152
NO10	0.10	13.0	135

2.6.2 Residual stress

The magnetic properties of electrical steels are significantly affected by the stresses introduced during the manufacturing process. Since all the electrical steels are normally subject to annealing to obtain a recrystallized microstructure, the stresses induced during steel sheet manufacturing are usually released. However, when punching laminates from the steel sheet, or when applying coating onto the sheet surfaces, mechanical stress or thermal stress may be induced. If the final core is not annealed again to release these stresses, the magnetic properties will be deteriorated. The heavy dislocations induced at the cutting edges of the steel sheet act as pinning sites to the motion of magnetic domains and hence increase the coercivity and the hysteresis loss. The residual stresses arising from the plastic deformation near the cutting edges may also result in microstructural changes [16]. It has been shown [16] that the punching process can result in an increase of power loss by ~10-40%. The magnetically deteriorated region can extend a few millimetres from the cut edges. In addition, the cutting process may also decrease the magnetic induction up to ~20-70% [17-19]. Thus, stress-relief annealing is an indispensable step for non-oriented electrical steel lamination after punching [16-19].

2.7 The effect of Si content

Silicon is added to non-oriented electrical steel to increase the electrical resistivity of the steel so that the eddy current loss can be reduced. Silicon atoms form substitutional solid solution in steel due to the comparable atomic radius to iron (silicon ~0.132 nm and iron ~0.126 nm) [20]. Silicon is a well-known ferrite phase (α-bcc) stabilizer [21]. Consequently, the austenitic phase (γ) is suppressed at higher silicon contents, and the steel remains in the ferritic phase (α) during all the thermomechanical processing stages [21, 22]. The addition of silicon to iron reduces the ductility of the steel, making cold deformation of the steel more difficult. On the other hand, to

reduce eddy current loss, the thickness of the steel sheet is required to be minimum. Thus, to balance between the electrical resistivity and the achievable sheet thickness, the silicon content is usually limited to ~3.2 wt.% [22]. Electrical steels with 6.5 wt% silicon have also been commercially produced, but unconventional technologies such as chemical vapour deposition [23] had to be used. The processing of high silicon steels using strip casting and warm rolling is still in research stage, and there is no commercial production of these steels [24].

The addition of silicon changes both the electrical resistivity and the magnetocrystalline anisotropy constant, as shown in Fig. 2.12 [6, 22, 25]. Pure iron has a resistivity of 9.71×10^{-8} Ω·m at room temperature, while silicon has a resistivity of 0.1-60 Ω·m [22]. When 3 wt% of silicon is added to iron, the material's resistivity increases by four times [22, 26]. The effect of resistivity and the material's thickness on the eddy current loss is shown in Equation 2.12. It is worth noting that eddy current loss is proportional to the square of frequency, while the hysteresis loss is linearly proportional to frequency. Therefore, at high frequencies, eddy current loss will dominate the losses, thus reducing the sheet thickness and increasing the resistivity become extremely important for high frequency applications [22].

The introduction of silicon atoms into the iron lattice results in significant changes to the magnetic properties of electrical steel [27]. An iron atom has a magnetic dipole moment of 2.2 Bohr magnetons (μ_B), while the silicon atom's magnetic dipole moment is zero [22]. This means that the silicon atoms cannot hold on to magnetization, resulting in an overall decrease in retentivity. The addition of silicon also leads to the decrease of magnetic permeability at high magnetic inductions, due to the decrease in the maximum magnetic flux density, which decreases the core loss by decreasing the area of the hysteresis loop (B-H curve). Some researchers have reported a drop of 6% in core loss when the silicon content increases by 1% [22]. Thus, the addition

of silicon facilitates the magnetization and demagnetization of the electrical steel, which is vital for soft magnetic materials that are used in rotating machines.

Magnetostriction is another property to be considered, which is defined as the change of the shape and dimensions of a ferromagnetic material during the process of magnetization [22, 26]. The magnetization process results in domain wall motion as well as atomic moment rotation, which leads to a change of atomic bonding and subsequently a change in the physical dimensions of the material (magnetostriction). Magnetostriction causes energy loss in the form of heat (due to friction) and sound when the material is magnetized and demagnetized continuously. The addition of silicon significantly decreases magnetostriction as have been shown by several researchers [7, 22].

In summary, the addition of silicon reduces the eddy current loss, which is important at high frequencies. It also reduces the hysteresis loss by decreasing the maximum magnetic flux density (Fig. 2.13) [5, 7]. Therefore, for high-torque applications where high magnetic induction and magnetic flux density are much more important than the resistivity, a balanced silicon content is required to maintain high magnetic flux density while minimizing the energy loss. In addition, copper loss (the energy loss due to heat generation in the copper winding) becomes a concern at high silicon contents due to the decrease in magnetic permeability, since a large current is needed to magnetize and demagnetize the electrical steel [22]. In addition, the addition of silicon makes the steel harder and more brittle (Fig. 2.13), thus it is harder to process the NOES if the Si levels are high.

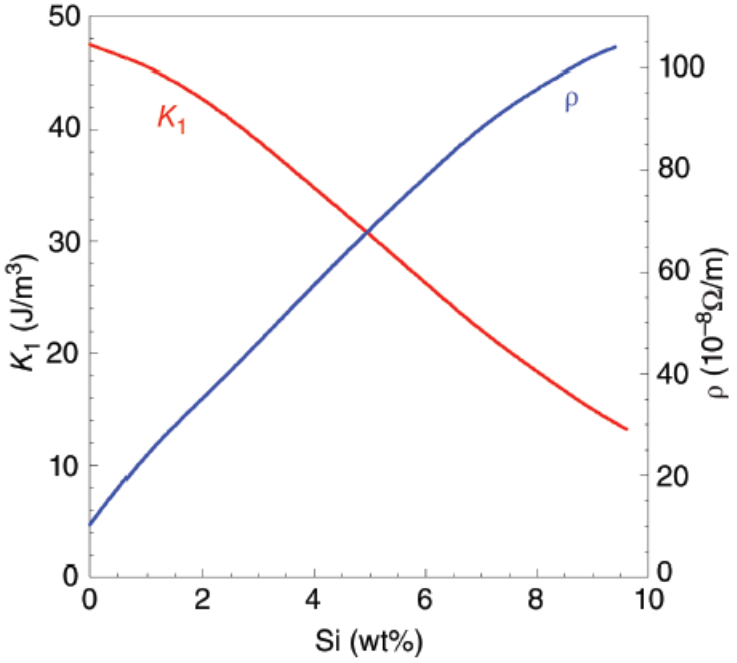

Fig. 2.12. The effect of silicon content on the electrical resistivity (ρ) and the magnetocrystalline anisotropy constant (K_1) of electrical steels [5].

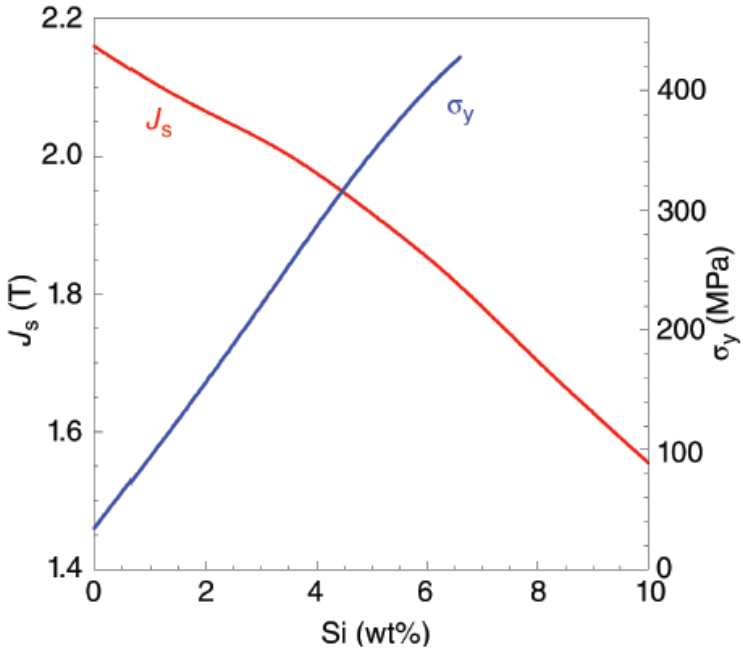

Fig. 2.13. The effect of silicon content on maximum magnetic flux induction (J_s) and yield strength (σ_y) [5].

2.8 Magnetocrystalline anisotropy

Due to the body-centred-cubic (bcc) crystal structure, the ferrite (bcc iron) of the electrical steel possesses magnetocrystalline anisotropy. This means that the magnetic properties are directionally dependent and the magnetization process is not the same in all directions. Fig. 2.14 shows the magnetization curves of bcc single crystal. It can be seen that the <100> crystal direction is the easy magnetization axis, and the <111> is the hard magnetization axis, with <110> in between. In other words, if magnetized in the <100> direction, saturation can be reached by a smaller external magnetization field, while higher excitation field is required to saturate in the <110> and <111> axes [1].

When an external magnetic field is applied along the easy magnetization direction (<100>), the steel could be saturated by the growth of the magnetic domains that are aligned with the external field. On the other hand, when the external magnetic field is applied along the medium (<110>) or hard (<111>) magnetization axes, the growth of magnetic domains is not enough to result in magnetic saturation. In this case, magnetic domain rotation becomes a necessity, which is more energy intensive and requires a substantially higher external magnetic field to magnetize the steel [1].

The magnetocrystalline energy (E), which is defined as the work required to deflect the magnetic moment in a single crystal from easy to hard magnetization direction [1], can be calculated using the cosines (α_1, α_2 and α_3) of the angles (a, b, c) between the magnetization vector (M_s) and the crystal axes as:

$$E = K_0 + K_1 (\alpha_1^2\alpha_2^2 + \alpha_2^2\alpha_3^2 + \alpha_3^2\alpha_1^2) + K_2 (\alpha_1^2\alpha_2^2\alpha_3^2) + \cdots \quad (2.16)$$

where K_0, K_1 and K_2 are material constants that represent the isotropy, first-order and second-order anisotropy, respectively. The magnetocrystalline anisotropy of bcc iron at various directions is

summarized in Table 2.3. It is worth noting that the addition of Si decreases the K_1 constant and thus decreasing magnetocrystalline anisotropy as shown in Fig. 2.12 [1].

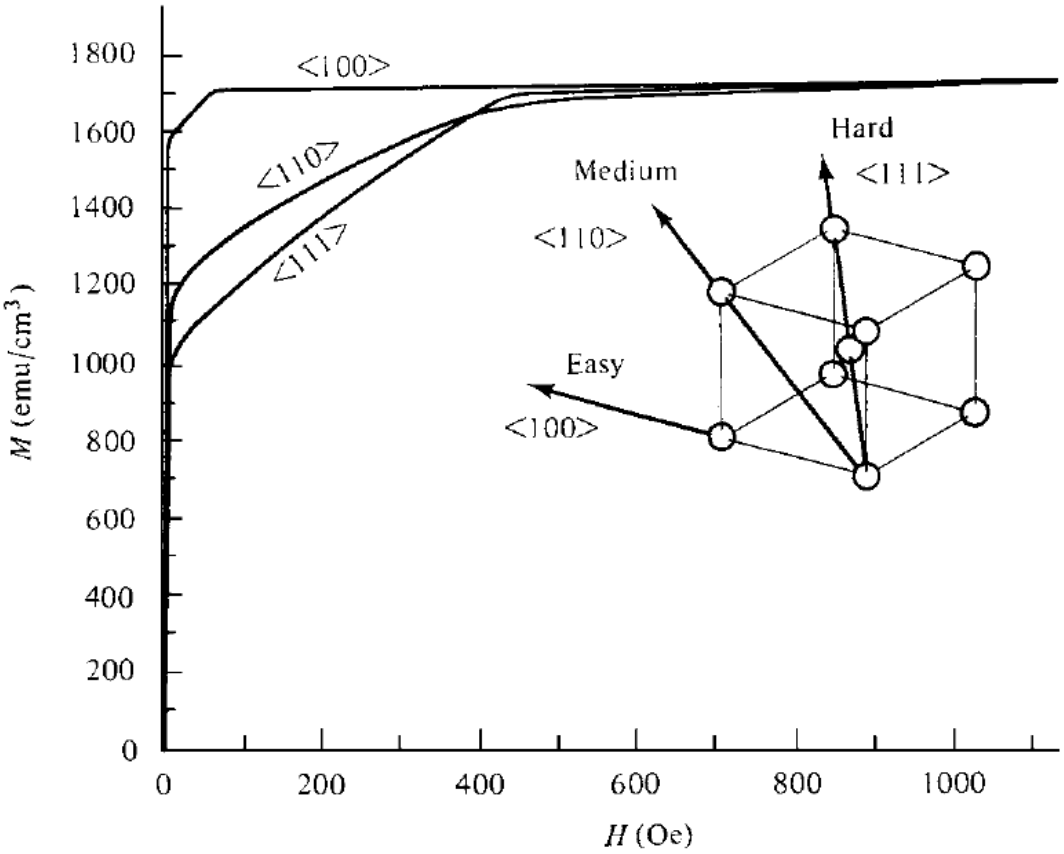

Fig. 2.14. The magnetization curve of single crystal iron (bcc) [1].

Table 2.3. The magnetocrystalline anisotropy energy for bcc single crystal [1].

[u v w]	a	b	c	α_1	α_2	α_3	E
[100]	0	90°	90°	1	0	0	K_0
[110]	45°	45°	90°	$1/\sqrt{2}$	$1/\sqrt{2}$	0	$K_0 + K_1/4$
[111]	54.7°	54.7°	54.7°	$1/\sqrt{3}$	$1/\sqrt{3}$	$1/\sqrt{3}$	$K_0 + K_1/3 + K_2/27$

2.9 Effect of crystallographic texture on magnetic properties

2.9.1 Crystallographic texture and its representation

Crystallographic texture is the distribution of the crystal orientations in a polycrystalline material. The texture is normally formulated as the distribution functions (density functions) of the crystal orientations with respect to the sample coordinate system, e.g. the rolling, transverse and normal directions (RD, TD, ND) of a rolled plate or sheet. In most polycrystalline materials the grain orientations are not randomly distributed, and they tend to develop a preferred orientation distribution during the fabrication process. The development of a texture in the material makes the material behave anisotropically, e.g. the strength, ductility, magnetic permeability, toughness, electrical conductivity, thermal expansion, etc., show different values in different directions. In many cases the changes in these values may be large, and could be in the order of 20-50% [28, 29].

The orientation of a crystal is defined as the rotation required to bring the sample coordinate system (e.g. the RD-TD-ND) into coincidence with the crystal coordinate system (e.g. the [100], [010] and [001] axes) [28, 29]. Depending on how the rotation is parametrized, there are a number of ways to mathematically describe the orientation. The most commonly used parameters are the three Euler angles (φ_1, Φ, φ_2) that describe the rotation by three consecutive rotations about the Z, X and the new Z axes (the Bunge notation) [28]. Most of the texture characterization systems, e.g. x-ray diffraction (XRD), electron backscatter diffraction (EBSD), etc., use Euler angles as the fundamental parameters for texture analysis. From the Euler angles, a number of other parameterizations, e.g. angle-axis pair, quaternion, Rodrigues-Frank vector, Miller indices (or ideal orientation), etc., can be derived and the orientations can be represented using several

different methods. The most commonly used representation methods include pole figure, orientation distribution function (ODF), Rodrigues-Frank space and inverse pole figure.

One of the most common representations of orientations is pole figure [28, 29], which is the stereographic projection of a set of crystallographic planes (plane normal) in the crystal to the sample coordinate system. Due to crystal symmetry, usually a number of symmetrically equivalent poles of the same set of planes will be present in a pole figure [30, 31]. Most of the XRD techniques measure the pole figures of a few sets of planes, and obtain the orientation distribution functions through a pole figure inversion process from the pole densities [1, 28].

Another common representation method is the orientation distribution function in Euler space, which can be displayed in a three dimensional space, or more often, in consecutive two-dimensional sections with one fixed Euler angle (e.g. φ_2 = constant). The crystallographic texture of polycrystalline materials is normally represented in Euler space using orientation distribution function, $f(g)$, which is defined as

$$\frac{\mathrm{d}V}{V} = f(g)dg \tag{2.17}$$

where $\frac{\mathrm{d}V}{V}$ is the volume fraction of an arbitrary orientation g with an orientation spread of dg within the sample. The orientation distribution function (ODF) is usually calculated using a series of generalized spherical harmonics:

$$f(\varphi_1, \Phi, \varphi_2) = \sum_{l=0}^{\infty} \sum_{m=-l}^{+l} \sum_{n=-l}^{+l} C_l^{m\,n} e^{-im\varphi_2} P_l^{m\,n}(\phi) e^{-in\varphi_1} \tag{2.18}$$

where $(\varphi_1, \Phi, \varphi_2)$ are the three Euler angles, $P_l^{m\,n}(\phi)$ are generalizations of the associated Legendre functions, $C_l^{m\,n}$ are the series coefficient [28].

The textures measured in this study are mostly represented in Euler space using orientation distribution functions. Although the Euler angles are defined in the ranges $0 \leq \varphi_1, \varphi_2 \leq 2\pi$ and $0 \leq \Phi \leq \pi$, the textures of cubic materials in orthorhombic sample symmetry (rolled plate or sheet) can be represented in a fundamental region defined in $0° \leq (\varphi_1, \Phi, \varphi_2) \leq \pi/2$. For rolled cubic materials, most of the dominant texture components can be represented at the φ_2=45° section of the Euler space [32, 33]. The common texture fibres and components appearing in the electrical steels in this study are shown in Fig. 2.15 [32-34].

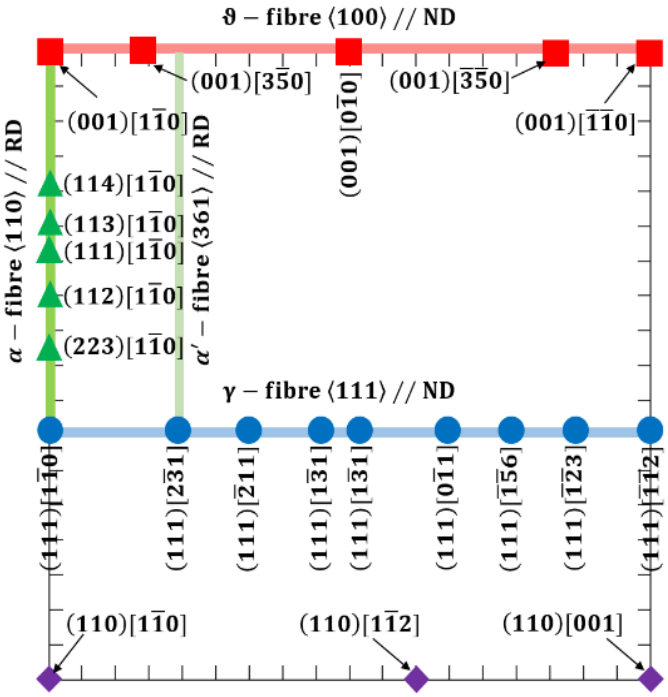

Fig. 2.15 The texture key showing the major texture components and fibres on the φ_2=45° section of the ODFs (Bunge notation) for bcc materials.

The major fibre components of bcc and fcc metals are summarized in Table 2.4 and their positions in the three-dimensional Euler space are shown in Fig. 2.16. The list of the major texture components in bcc along with their corresponding Euler angles and Miller indices are also

summarized in Table 2.4. The names of these texture and fibre components will be frequently used throughout this dissertation.

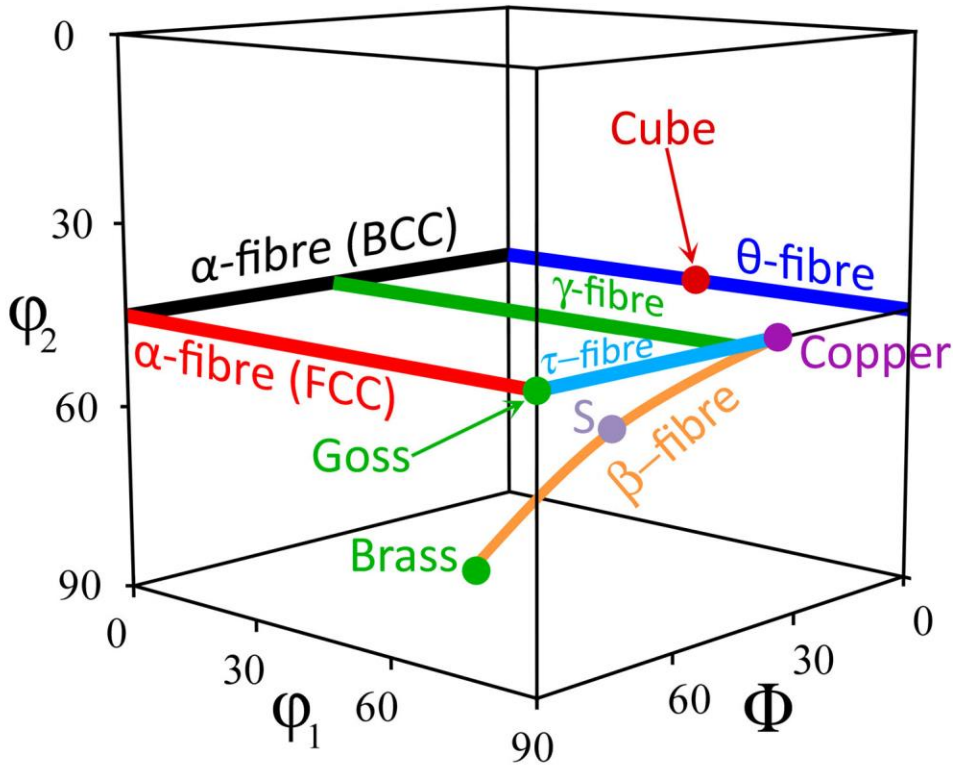

Fig. 2.16. The position of the major fibres and texture components in FCC and BCC materials in Euler space [34].

Table 2.4. The major texture fibres in BCC and FCC materials along with their designations [30].

Fibre nomenclature	Crystal structure	Fibre axis
α	FCC	<110>//RD
γ	FCC	<111>//ND
τ	FCC	<110>//TD
β	FCC	-
α	BCC	<110>//RD
θ	BCC	<001>//ND
γ	BCC	<111>//RD

Table 2.5. The major texture components in BCC and FCC alloys along with their common names, as well as their corresponding Euler angles and Miller indices [35].

Texture component	Miller indices	φ_1	Φ	φ_2
Cube	{001}<100>	45°	0°	45°
Rotated cube	{001}<110>	0°	0°	45°
Goss	{110}<100>	90°	90°	45°
Copper	{112}<111>	90°	35°	45°
Brass	{110}<112>	55°	90°	45°
Rotated Goss	{110}<110>	0°	90°	45°
Dillamore	{4 4 11}<11 11 8>	90°	27.2°	45°

The volume fraction of a given orientation (or fibre) within a specific tolerance or range can be calculated as [28, 30]:

$$V_f\ (\varphi_1,\ \Phi,\ \varphi_2) = \int_{\varphi_1-\Delta\varphi_1}^{\varphi_1+\Delta\varphi_1}\int_{\Phi-\Delta\Phi}^{\Phi+\Delta\Phi}\int_{\varphi_2-\Delta\varphi_2}^{\varphi_2+\Delta\varphi_2} f\ (\varphi_1,\ \Phi,\ \varphi_2)\sin\Phi\ d\varphi_1 d\Phi d\varphi_2 \qquad (2.28)$$

which may be used to quantitatively compare the texture in a material.

In rolled plate or sheet a common and convenient method of describing texture is the use of the Miller indices, i.e. {hkl}<uvw>, which implies that the crystal {hkl} plane is parallel to the sheet/plate plane, while the <uvw> crystal direction is parallel to the rolling direction. A well-known example is the Goss texture, which is described as {011}<100>, meaning that the crystal {011} plane is parallel to the sheet plane, while the crystal <100> direction is in the rolling direction.

Occasionally, it is more convenient to use a rotation (ω) around a specific crystal direction **d** (d_1, d_2, d_3) to represent the orientation (angle-axis representation), instead of using the three Euler angles around the three crystal axes. Since this method specifically defines the rotation angle and the rotation axis, it is very useful for the description of grain boundary misorientation between adjacent grains. A common use of this method is the description of the coincident site lattice (CSL), e.g. Σ3 representing 60°<111>, Σ5 representing 36.9°<100>, Σ9 representing 38.9°<110>, etc. From the angle-axis representation, it is able to derive the quaternion representation (**q**) [36] and the Rodrigues-Frank space [36-38] representation (**R**), i.e.

$$\boldsymbol{q} = \left(q_0, q_1, q_2, q_{3,}\right) = \left(cos\frac{\omega}{2}, d_1 sin\frac{\omega}{2}, d_2 sin\frac{\omega}{2}, d_3 sin\frac{\omega}{2}\right) \qquad (2.19)$$

$$\boldsymbol{R} = \left(\ R_1, R_2, R_{3,}\right) = \ tan\frac{\omega}{2}(\ d_1, d_2, d_3) \qquad (2.20)$$

Quaternion is usually used to calculate the orientations, but it is rarely directly used to represent orientation since it needs a 4-dimenisonal space to display. The Rodrigues-Frank space

may be used to represent orientations and misorientations, but it is necessary to define the fundamental zone before it can be used. The fundamental zone of the Rodrigues-Frank space of cubic crystals is shown in Fig. 2.17, which is conveniently used in the representation of grain boundary misorientation during recrystallization or phase transformation [37].

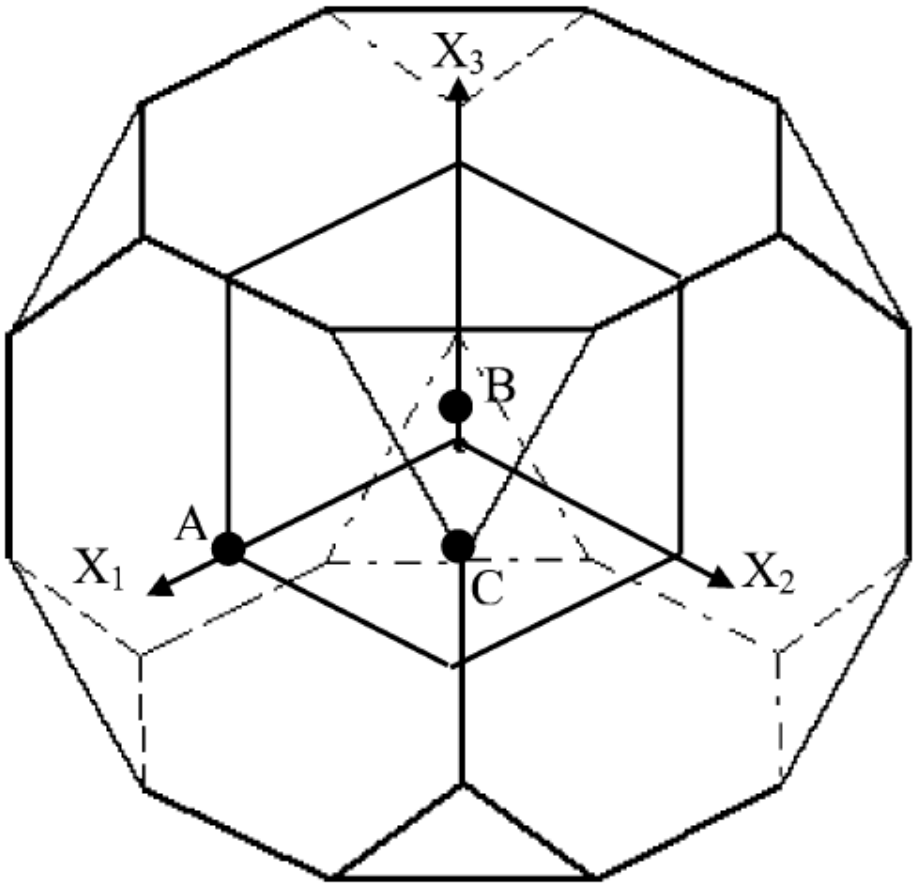

Fig. 2.17. The fundamental zone of the Rodrigues-Frank space for cubic symmetry. Three typical angle axis pairs plotted are: A: 45° <110>, B: 60° <111> and C: 62.8° <1 1 $(\sqrt{2}-1)$ > [37].

In some cases, it is more convenient to represent the sample coordinate system in the crystal coordinate system in stereographic projection. This forms the inverse pole figure representation. For example, if only one sample direction is relevant, e.g. in drawing or extrusion, the major axis

can be represented in the stereographic projection of the crystal axes. An important use of the inverse pole figure representation is the color key for the EBSD orientation map, as shown in Fig. 2.18. Each color in the triangular inverse pole figure represents the alignment of a certain sample axis (e.g. ND) to a specific crystal axis (e.g. [100]).

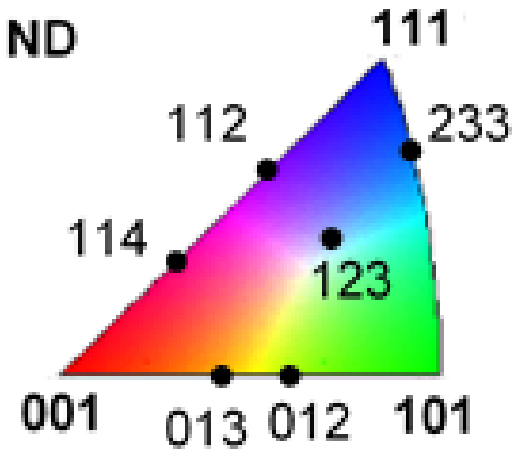

Fig. 2.18. The colour key for EBSD orientation maps using an inverse pole figure representation.

2.10 Texture evolution during thermomechanical processing of electrical steel

The microstructure and texture of metals change significantly during thermomechanical processing. It is very rare for metals to be randomly oriented during thermomechanical processing, and thus they develop preferred crystal orientations. The microstructure and texture of electrical steel are highly dependent on chemical composition, deformation and annealing parameters as well as the presence of impurities and inter-metallics. Casting develops columnar grains that have preferred crystal orientations during the solidification process. Hot rolling allows the steel to form stable deformation textures as well as initiating dynamic and static recrystallization. High temperature annealing or deformation also gives rise to transformation texture due to phase transformation between fcc and bcc in low Si steel. Cold rolling introduces a large amount of

plastic deformation in the material and thus results in lattice rotations, elongation of grains, grain fragmentation as well as the development of discontinuities in the form of kinks, microbands and shear bands [33]. Final annealing results in recovery, nucleation and grain growth that give rise to recrystallization textures and stress free grains. This section will summarize the effect of thermomechanical processing on the texture and microstructure evolution of non-oriented electrical steels.

2.10.1 Hot rolling textures

Electrical steels exhibit a significant heterogeneity throughout the thickness after hot rolling. In terms of microstructure, the surface is made of equiaxed grains that have been either dynamically or statically recrystallized (or both). On the other hand, the central layer has elongated grains which are not recrystallized. In terms of texture, the central region is usually composed of a strong α-fibre (<110>//RD) as well as a strong γ-fibre (<111>/ND) [33, 40-45]. The texture of the central region is very similar to that predicted under plane-strain deformation. The surface region is dominated by shear textures with strong intensities at Goss ({011}<100>), copper ({112}<111>) and brass ({110}<112>). The high shear strain at the surface layer is due to the frictional force between the material and the rolls [33].

Since Si is considered as a ferrite (α) stabilizer, only when the amount of Si in the steel is low (<~2.0%) would there be the γ (fcc) → α (bcc) phase transformation. For low Si electrical steels, the texture and microstructure after hot rolling are very similar to those of low carbon steel (IF steel). The transformation textures have been widely studied [46-47]. For low Si electrical steels that are hot rolled in the full austenitic phase, the subsequent cooling to the ferritic phase gives rise to a relatively random texture as well as small recrystallized grains. On the other hand,

electrical steels with high Si content undergo dynamic recovery during hot rolling, which prevents the occurrence of recrystallization and thus the deformation textures (shear and rolling) are present in the final hot-rolled material [33, 34, 40-43].

Therefore, electrical steels with low alloying content, i.e. (Si +2Al) < 2 wt%, can be hot rolled under more conditions because of the phase transformation, i.e., 1) austenitic rolling, 2) two-phase rolling, 3) mixed rolling, and 4) ferritic rolling, as shown in Fig. 2.19 [48]. Some researchers have reported that the two-phase rolling and mixed rolling are preferable for increasing the intensity of the magnetically favourable cube texture {100}<001> for low and medium Si steels. Adopting these hot rolling schemes would allow the production of highly permeable electrical steels without hot band annealing. On the other hand, for electrical steels with high silicon content, i.e. (Si +2Al) > 2 wt%, hot band annealing is recommended prior to cold rolling [48].

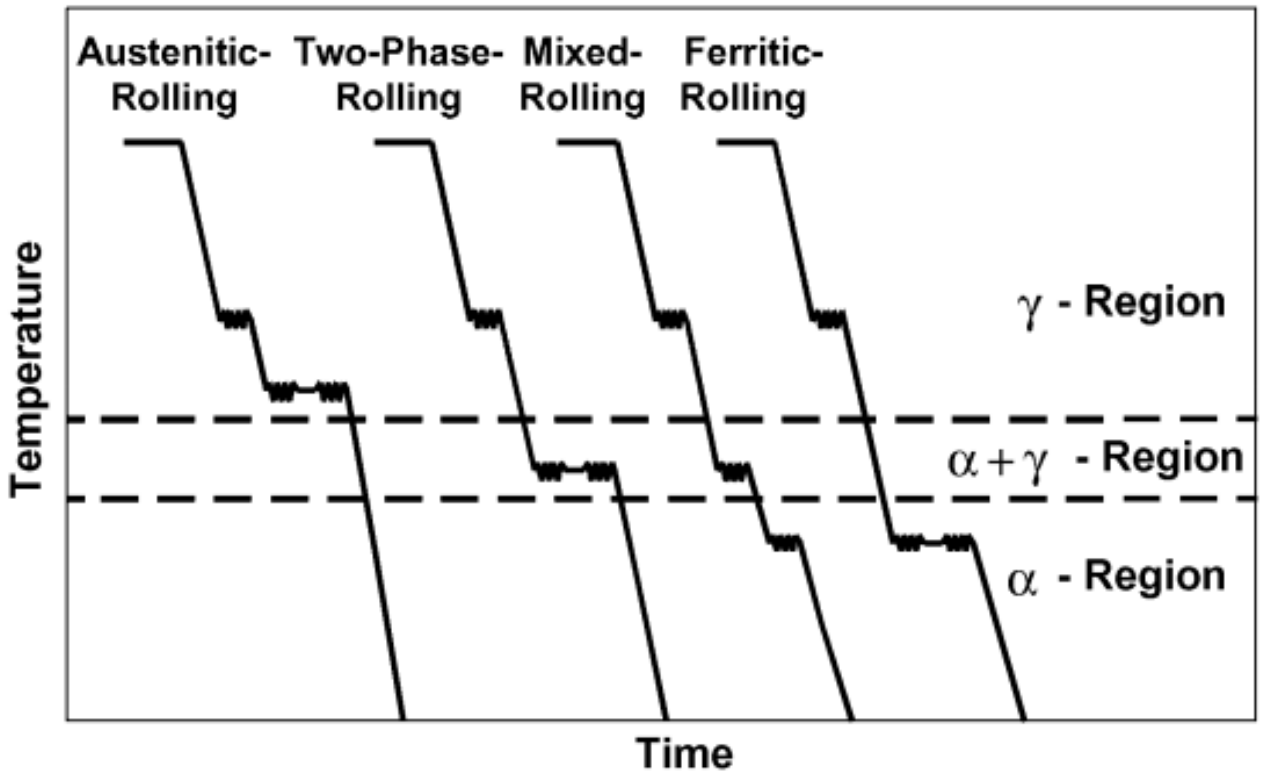

Fig. 2.19. Hot rolling schemes for electrical steel that undergoes phase transformations [48].

Lee et al. [29] reported that electrical steels with large and coarse grain sizes after hot band annealing can slow down the recrystallization process after cold rolling, and retard the development of the <111>//ND texture while promoting the <001>//ND texture. As a result, it can decrease the anisotropy of the material and consequently improve the magnetic properties. Similar results were obtained by several other researchers using electrical steels with different Si contents [49-51]. de Dafe et al. [51] attributed this to the intensity increase in shear bands, which favoured the nucleation of magnetically favourable crystal orientations.

Hölscher et al. [52] found that the major shear and rolling texture components in bcc metals are related to each other by a rotation of 90° about the transverse direction (TD). This was due to

the symmetry of the slip systems according to the Sachs model which results in at least one glide system with a Schmid factor of zero. Thus by a rotation of 90° about TD, the rolling stress state results in the maximum resolved shear stress to be along the shear direction [52].

2.10.2 Cold rolling textures

In metals, plastic deformation occurs by slip, twinning, or both, depending on the type of metal, deformation temperature and the stacking fault energy. The slip systems in bcc metals are mainly {110}<111>, {112}<111> and {123}<111>. Thus, the slip direction for bcc metals is always <111>, and the slip plane varies depending on the deformation temperature and the type of metal [33, 34, 40-43]. During plastic deformation, the crystal lattice rotates, which results in the change of crystallographic orientation. Even if the crystals in the material are initially randomly oriented, the limited number of slip systems give rise to well-defined final crystal orientations, and thus the material becomes strongly textured after deformation [33, 43]. The cold rolling textures of all bcc metals are very similar to each other and are not significantly affected by the temperature of deformation or the addition of solutes. Typical texture of bcc metal after rolling is featured by a continuous α-fibre <110>//RD stretching from the rotated cube component {001}<110> to the {111}<110> component as well as a continuous γ-fibre <111>//ND ranging from {111}<110> to {111}<112> (refer to Fig. 2.15) [33, 34,40-43].

It should be noted that, there usually exists a texture gradient throughout the thickness of the rolled sheet, which is inherited from the hot rolling microstructure and texture. Near the surface, the Goss {110}<001> orientation changes to rotated cube {001}<110>, while in the subsurface regions, the Goss rotates into the {111}<112> along the γ-fibre (<111>//ND). These crystal orientations are strengthened with the increase in cold rolling reduction as shown in Fig.

2.20. On the other hand, the {001}<110> and {112}<110> on the α-fibre and the {111}<110> on the γ-fibre become the dominant textures in the central region of the rolled sheet. High cold rolling reductions result in the strengthening of the {001}<011> and {112}<011> components as shown in Fig. 2.21 [33, 40-42].

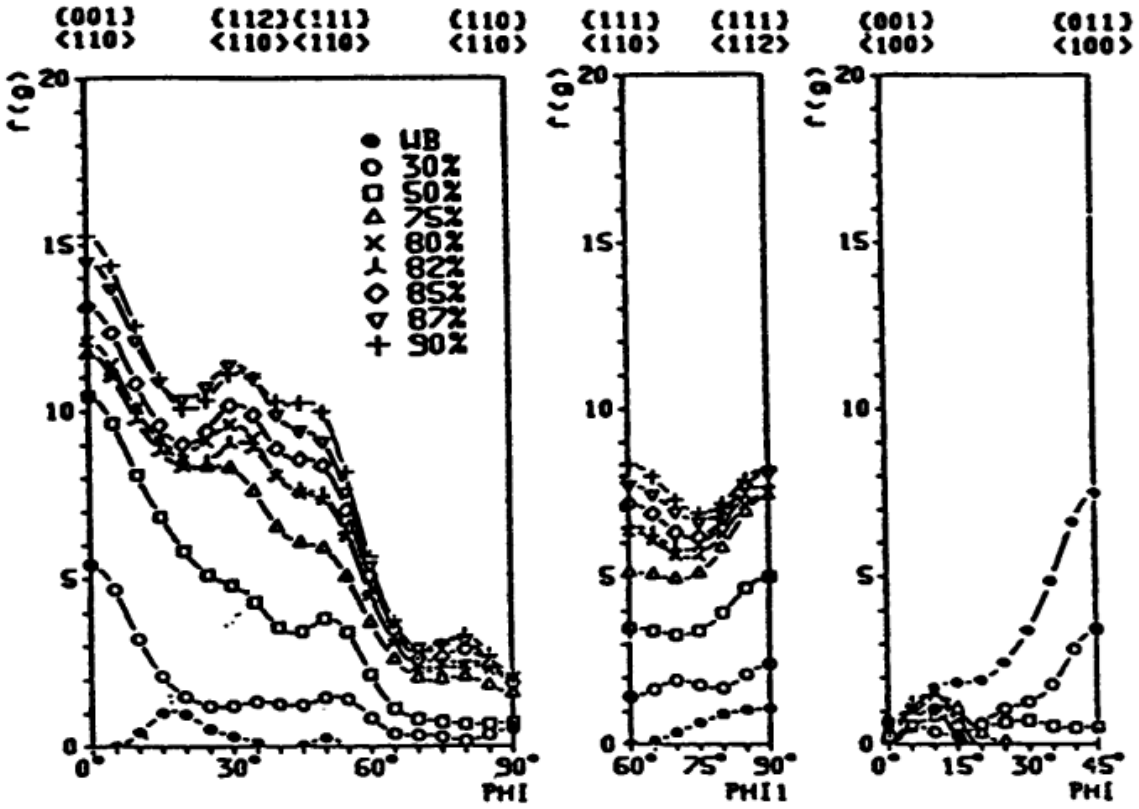

Fig. 2.20. The evolution of cold rolling textures for Fe-Si with respect to the percentage of reduction in the near surface region [42].

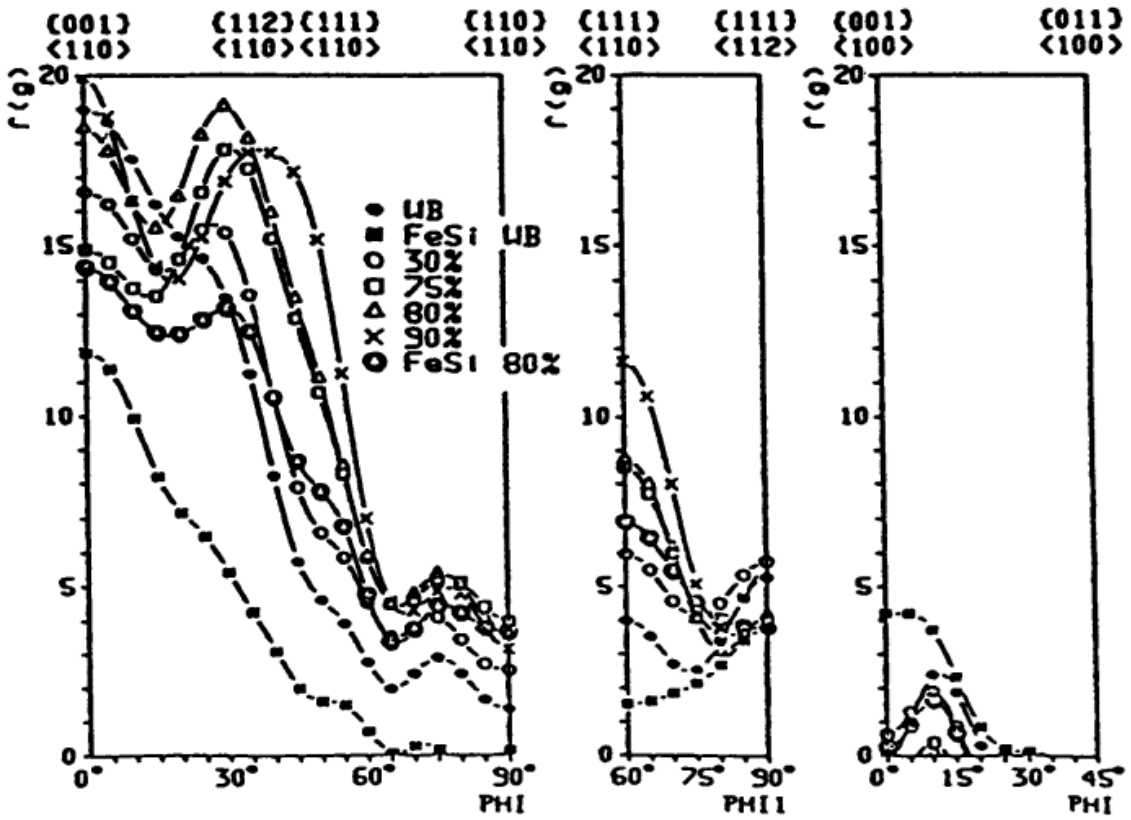

Fig. 2.21. The evolution of cold rolling textures for Fe-Si with respect to the percentage of reduction in the central region [42].

One of the distinct features of deformation in metals is the formation of deformation bands, which are regions that usually have a constant orientation different from the rest of its surroundings [10]. Kink bands are usually parallel lines to each other and involves double orientation change. On the other hand, strain inhomogeneity results in the formation of shear bands, which are inclined at approximately 17°~35° to the rolling direction (RD). Shear bands are a result of rolling instability and are affected by chemical composition, texture and the microstructural constraints of the metal. Many researchers have reported that coarse grains that are developed after hot band annealing favour the formation of shear bands in steels, and are known to be preferential sites for the nucleation of new grains during recrystallization [33, 53, 54].

2.10.3 Annealing textures

During cold rolling, the steel undergoes a significant amount of plastic deformation, which leads to the elongation of grains and the introduction of defects (e.g. dislocations) in the material. This causes an increase in the amount of stored energy inside the grains, and generates large residual stresses. It was discussed earlier that dislocations and residual stresses are detrimental to the magnetic properties in electrical steel by acting as pinning sites to the motion of magnetic domain walls. It is therefore necessary to remove the residual stress from the material through annealing treatment [10, 33].

Annealing involves heating up the material to a relatively high temperature (above recrystallization temperature), holding the material at a certain temperature for a period of time and cooling it to room temperature. From a metallurgical point of view, this treatment contains three stages: (1) recovery, (2) recrystallization, and (3) grain growth. The annealing process results in the nucleation of new grains that grow and consume the deformed matrix. The driving force for this process is the reduction of the stored energy in the material. The microstructure after annealing is significantly different from the original deformed grains, as the elongated grains are replaced with smaller equiaxed grains [33].

Two frequently cited theories regarding the formation of the recrystallization texture are *oriented nucleation* and *oriented growth* theories. Oriented nucleation theory assumes that the nuclei formed during the early stages of annealing have a preferred crystal orientation relative to the surrounding deformed matrix, and these will determine the final texture of the material. On the other hand, oriented growth theory assumes that the nuclei are randomly oriented and that the recrystallization textures are determined by the preferential growth of certain orientations [33].

The oriented nucleation theory assumes that the nuclei must have an orientation that are close to or the same as the orientation of a region in the deformed matrix from which it originated.

One of the first evidences for this theory is the Dillamore and Katoh paper (1974), which calculated and explained the origin of the <411> fibre texture during the compression of polycrystalline iron [33, 55]. Doherty (1978) later confirmed the existence of the <411> nuclei in the transition band [33, 56].

By contrast, oriented growth theory assumes that specific orientation relationships have a higher mobility and more rapid migration speed than others. The most important examples of these relationships were given by Lücke and his coworkers as the 40°<111> relationship in fcc metals as well as the 30°<110> relationship in bcc metals [33, 57, 58].

It is now assumed that none of these theories is capable of explaining the recrystallization textures exclusively and thus a more moderate and a less polarizing approach is appropriate. It is generally accepted now that oriented nucleation does occur in metals, such as Goss nucleation in the {111}<112> shear bands, which has been observed using electron backscatter diffraction (EBSD) [10, 59]. In fact, there is no evidence that random nucleation ever occurs in metals. Furthermore, there is a lot of evidence that the mobility of the grain boundaries is dependent on crystal orientation (under certain circumstances) [33].

When it comes to bcc steel, the recrystallization textures are very closely related to those developed after cold rolling. The two main fibres after annealing are the α-fibre and the γ-fibre, which are also observed in the deformed state. For the α-fibre, recrystallization results in the elimination of texture components between {001}<110> and {112}<110>, which are two of the prominent components in the rolled-state as shown in Fig. 2.22a. On the other hand, the maximum intensity along the α-fibre is localized at the {111}<110>. The γ-fibre that is formed after recrystallization of bcc steel is almost continuous. The maximum intensity is switched from {111}<110> in the rolled state to {111}<112> after annealing, as shown in Fig. 2.22b. The overall

intensity of the γ-fibre components increases after recrystallization as compared to those developed after cold rolling.

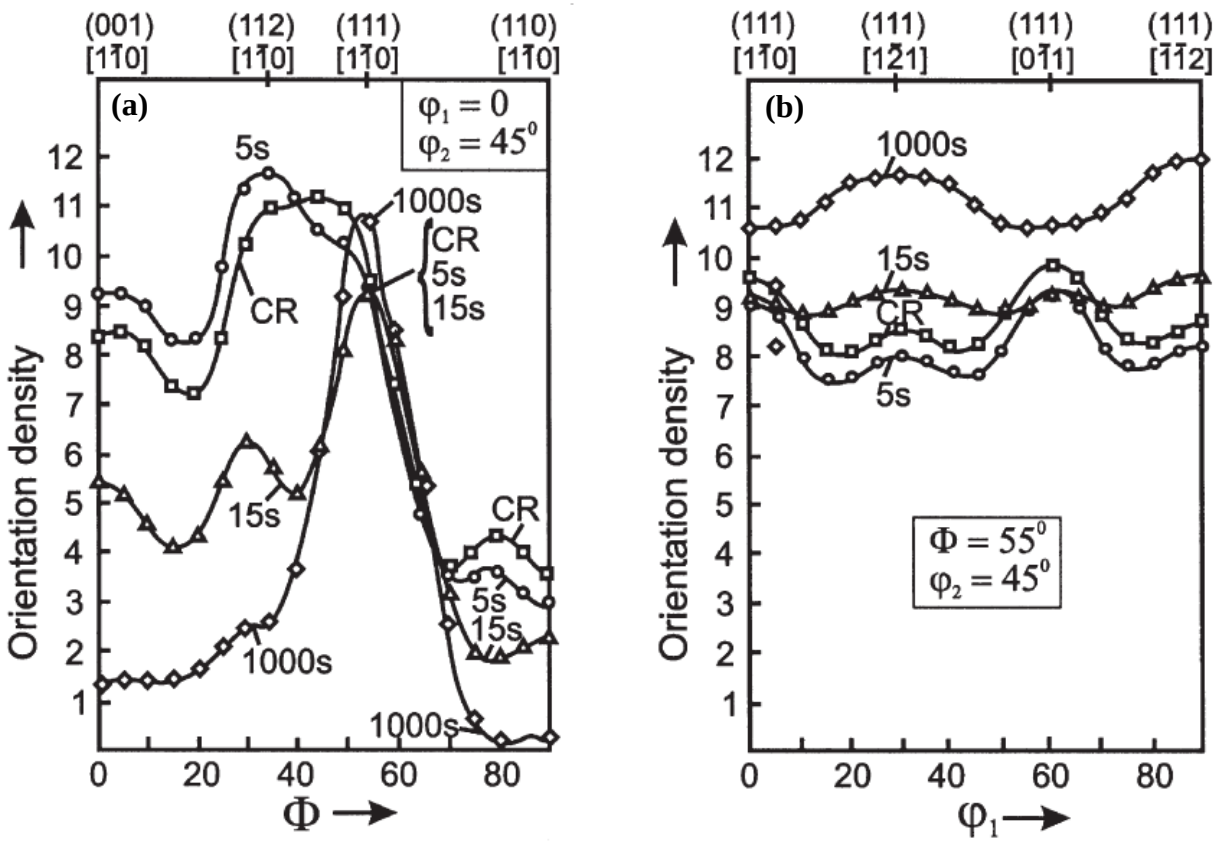

Fig. 2.22. Orientation distribution density of cold rolled steel at different stages of recrystallization: (a) The α-fibre (<110>//RD), and (b) the γ-fibre (<111>//ND) [33, 60].

There are some differences associated with the addition of silicon that distinguish the electrical steel texture from those of low carbon steel or IF steel. On the α-fibre, the rotated cube {001}<110> and {112}<110> are slightly stronger in intensity in electrical steels, while the {111}<110> is slightly weaker as shown in Fig. 2.23 in electrical steels. Furthermore, intermediate rolling reduction favours the formation of the magnetically favourable Goss {110}<001> orientation (maximum at 80% reduction). The Goss orientation is believed to form in the shear

bands of the {111}<112> deformed grains, and nucleates preferentially at the early stages of annealing due to the high stored energy in the shear bands and the high angle grain boundary with respect to the deformed matrix. It is also well known that recrystallization starts in the deformed γ-fibre grains due to their high stored energy. The newly formed nuclei have very similar orientations to the deformed grains, and thus the γ-fibre dominated the final texture of the material. The increase in intensity of the {111}<112> component and the decrease in the {112}<110> were explained using oriented growth theory, since these two components have highly mobile 35°<110> relationship with respect to the deformed matrix [41, 42]. This relationship allows the {111}<112> grains to nucleate during early stage recrystallization and consume the dominant deformation texture {112}<110> in the surrounding matrix [42]. The same orientation relationship was used to explain the growth of the Goss {110}<001> grains in the deformed {111}<112> grains [42].

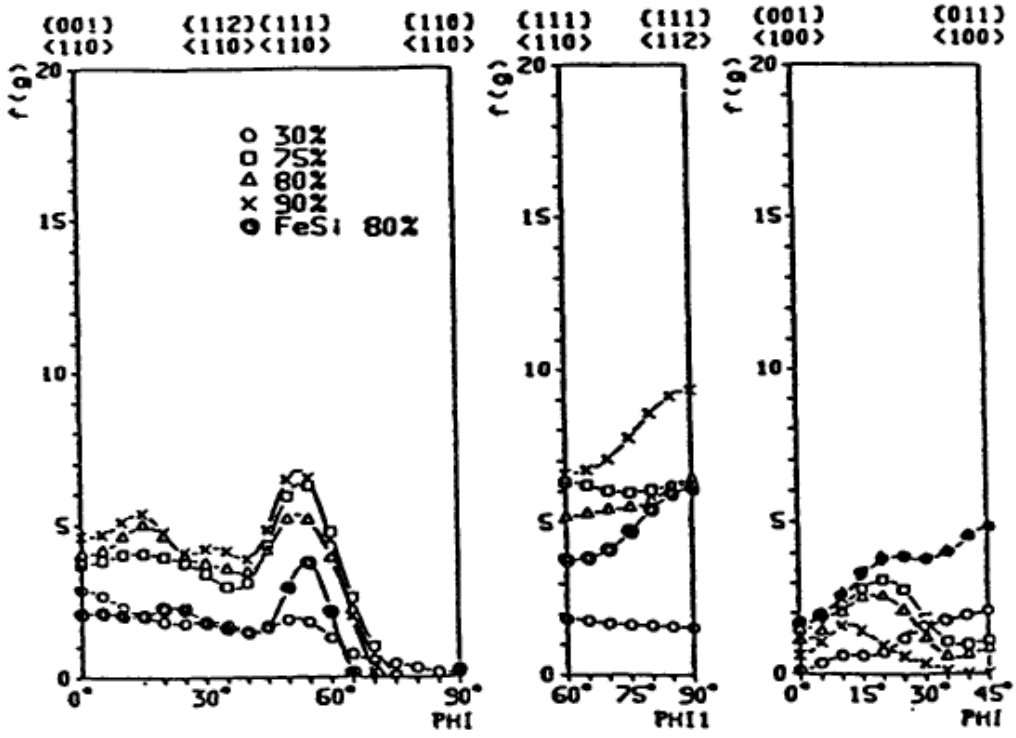

Fig. 2.23. Orientation distribution density of cold-rolled Si steel fully annealed after cold rolling at different reductions [42].

A summary of the texture evolution during thermomechanical processing is shown in Fig. 2.24 [61]. It can be seen that the hot rolling, cold rolling and annealing textures are very similar to each other. The most important fibre textures are α (<110>//RD) and γ (<111>//ND). Several operational parameters have been widely studied in the literature such as reduction percentage, hot rolling temperature, chemical composition, heating rate, solute concentration, role of precipitates as well as annealing time and temperature, but no major change of the final texture of the steel has been achieved.

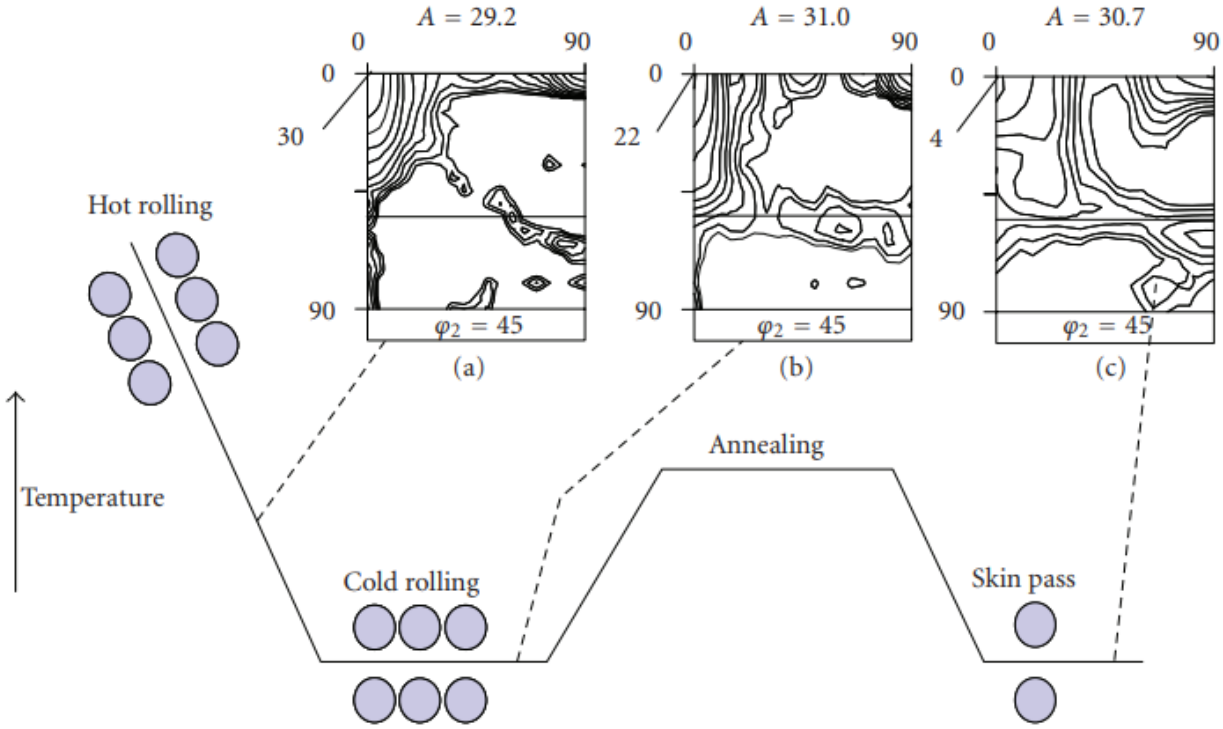

Fig. 2.24. The texture evolution of non-oriented electrical steel during thermomechanical processing [61].

2.11 Methods of improving the texture of non-oriented electrical steel

2.11.1 Cross rolling

It is well known that the final annealing texture is highly dependent on the textures developed during the cold rolling process. Therefore, in order to change the final annealing texture in non-oriented electrical steels, the cold rolling textures must be altered. This is not readily achievable considering the fact that the magnetically detrimental textures in electrical steels (α-fibre and γ-fibre) are the stable orientation after cold rolling. One successful method was the so-called *cross rolling*, in which the hot-rolled plate was rotated 90° about the normal direction (ND) during cold rolling so that the hot rolling direction (RD) becomes the transverse direction (TD) during cold rolling (Fig. 2.25). This rotation does not have a substantial effect on the γ-fibre, but it rotates the α-fibre from <110>//RD to <110>//TD [61].

Cross-rolling results in a very strong rotated cube texture {001}<110>, and eliminates the γ-fibre texture after cold rolling. Primary recrystallization results in the development of a slightly randomized texture with a maximum around {112}<110> on the α-fibre. However, after skin pass rolling (4-8%) a semi-continuous θ-fibre is developed with a very high intensity. This fibre texture is the optimum texture for non-oriented electrical steel [61].

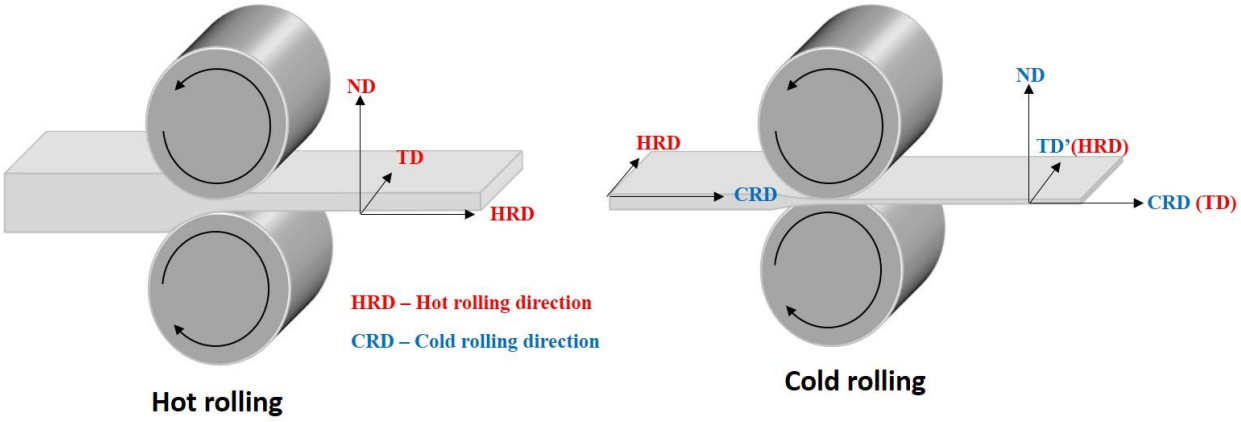

Fig. 2.25. A schematic representation of the cross-rolling process.

2.11.2 Inclined rolling

He et al. [62, 63] developed a similar cold rolling process in which the hot rolling direction is rotated about the normal direction (ND), but at an angle less than 90° (*inclined rolling*) so that the initial texture is also altered, but not the same as the cross rolling (by 90°), as shown in Fig. 2.26. Subsequent cold rolling and annealing led to the formation of magnetically favourable textures, especially at inclination angles of 45° and 60°, and a reduction in the magnetic core losses.

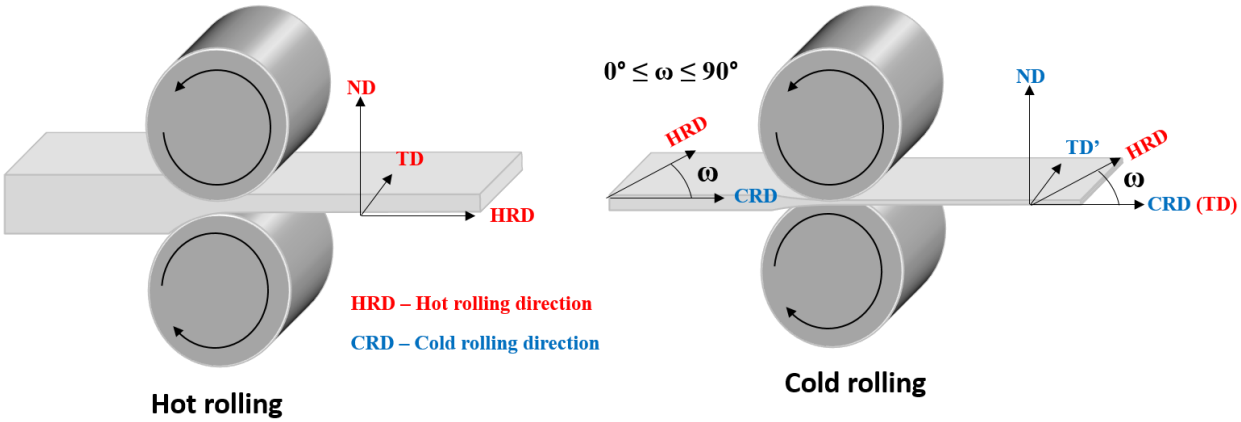

Fig. 2.26. A schematic representation of the inclined rolling process.

2.11.3 Skew rolling

Another unconventional rolling scheme that is used to alter the cold rolling texture is called *skew rolling* (Fig. 2.27). In this scheme, instead of rotating the sample about the normal direction (ND) so that the hot rolling direction is not the same as the cold rolling direction (like cross rolling and inclined rolling), the sample is fed into the rolls at an angle varying between 0° and 45°. This results in three-dimensional deformation of the steel sheet due to the frictional force decomposed into two components, one acting along the rolling direction (RD) and the other acting along the transverse direction (TD). Therefore, the cold rolling can no longer be treated as plane-strain deformation. Significantly different textures were obtained for some of the rolling configurations especially for low Si non-oriented steel, with a final texture after annealing being very close to the ideal cube {100}<001> orientation [64-65].

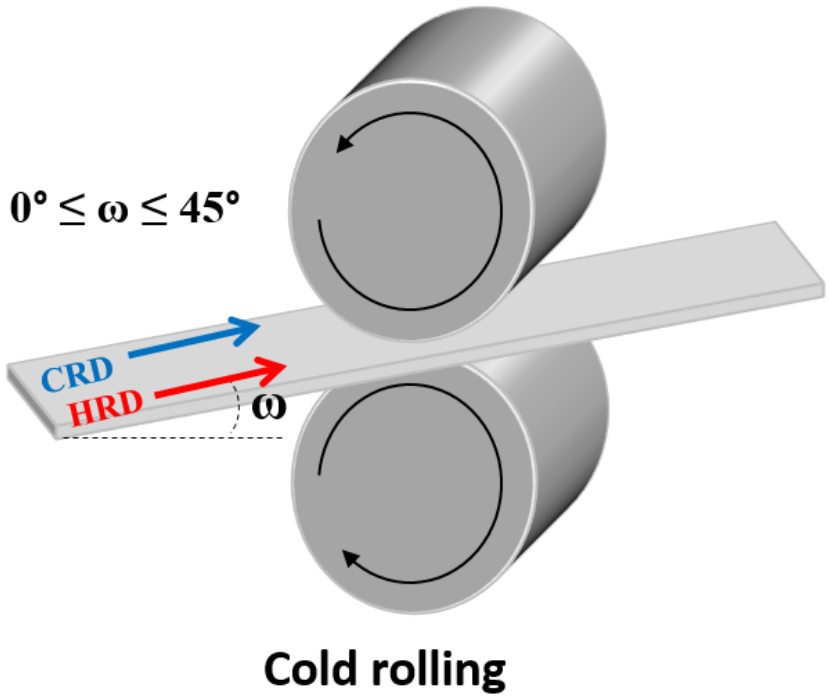

Fig. 2.27. Schematic illustration of the skew rolling process.

2.11.4 Surface textures

Yoshinaga et al. [61, 66] were able to produce a relatively strong {100}<110> texture on the surface of a cold-rolled steel by subjecting the material to a short time annealing at high temperature (full austenite phase) and taking the advantage of the relationships between the austenite and ferrite phases. In order to allow the magnetically favourable textures formed on the surface to grow into the bulk of the rolled sheet, Tomida [67] proposed a two-stage annealing process. In the first treatment, the surface textures were formed when Mn (austenite phase stabilizer) was diffused out of the surface layers, to promote the $\gamma \rightarrow \alpha$ transformation. The second treatment allowed the surface ferrites to consume the austenite bulk, resulting in columnar microstructure with large grain size [61, 67].

2.11.5 Strip casting and warm rolling

Another attempt to improve the magnetic properties and alter the crystallographic texture of non-oriented electrical steel was the use of strip casting. In this procedure, a twin-roll strip caster is used to produce electrical steel sheets with a thickness of ~2 mm. The as-cast sheets can then be mildly hot rolled and subsequently cold rolled (or warm rolled if the Si is greater than 4.5%) down to a final thickness of 0.5-0.35 mm. The as-cast sheet developed columnar grains with a pronounced texture concentrated at the <100>//ND (θ-fibre). On the other hand, the texture developed after cold rolling and annealing revealed a weak <111>//ND fibre and a stronger <100>//ND fibre, with a maximum intensity at the {001}<510>. This resulted in a decrease in core loss and an increase in magnetic induction [68-71].

References

1. Cullity, B. D., & Graham, C. D. (2011). Introduction to magnetic materials. John Wiley & Sons.

2. Jiles, D. (2015). Introduction to magnetism and magnetic materials. CRC press.

3. Coey, J. M. (2010). Magnetism and magnetic materials. Cambridge University Press.

4. Chen, C. W. (2013). Magnetism and metallurgy of soft magnetic materials. Courier Corporation.

5. Fiorillo, F., Bertotti, G., Appino, C., and Pasquale, M.: Soft magnetic materials. In Wiley Encyclopedia of Electrical and Electronics Engineering, Peterca, M., ed. (Wiley, Hoboken, New Jersey, 2016)

6. Matsumura, K., & Fukuda, B. (1984). Recent developments of non-oriented electrical steel sheets. IEEE Transactions on Magnetics, 20(5), 1533-1538.

7. Oda, Y., Kohno, M., & Honda, A. (2008). Recent development of non-oriented electrical steel sheet for automobile electrical devices. Journal of Magnetism and Magnetic Materials, 320(20), 2430-2435.

8. Petrovic, D. S. (2010). Non-oriented electrical steel sheets. Materiali in tehnologije, 44(6), 317-325.

9. ASTM A677-07, Standard Specification for Nonoriented Electrical Steel Fully Processed Types, ASTM International, West Conshohocken, PA, 2007

10. Park, J. T. (2002). Development of annealing texture in nonoriented electrical steels (Doctoral dissertation, McGill University Libraries).

11. Brailsford, F. (1966). Physical principles of magnetism. London.

12. Bates, L. F 1963 Modern Magnetism.

13. Chikazumi, S., & Graham, C. D. (2009). Physics of Ferromagnetism 2e (Vol. 94). Oxford University Press on Demand.

14. Moses, A. J. (2012). Energy efficient electrical steels: Magnetic performance prediction and optimization. Scripta Materialia, 67(6), 560-565.

15. Bertotti, G., Di Schino, G., Milone, A. F., & Fiorillo, F. (1985). On the effect of grain size on magnetic losses of 3% non-oriented SiFe. Le Journal de Physique Colloques, 46(C6), C6-385.

16. Saleem, A., Goldbaum, D., Brodusch, N., Gauvin, R., & Chromik, R. R. (2018). Microstructure and mechanical property connections for a punched non-oriented electrical steel lamination. Materials Science and Engineering: A, 725, 456-465.

17. Harstick, H. M. S., Ritter, M., Plath, A., & Riehemann, W. (2014). EBSD investigations on cutting edges of non-oriented electrical steel. Metallography, Microstructure, and Analysis, 3(4), 244-251.

17. Saleem, A., Alatawneh, N., Chromik, R. R., & Lowther, D. A. (2016). Effect of shear cutting on microstructure and magnetic properties of non-oriented electrical steel. IEEE Transactions on Magnetics, 52(5), 1-4.

18. Rygal, R., Moses, A. J., Derebasi, N., Schneider, J., & Schoppa, A. (2000). Influence of cutting stress on magnetic field and flux density distribution in non-oriented electrical steels. Journal of magnetism and Magnetic Materials, 215, 687-689.

19. Saleem, A., Goldbaum, D., Brodusch, N., Gauvin, R., & Chromik, R. R. (2018). Microstructure and mechanical property connections for a punched non-oriented electrical steel lamination. Materials Science and Engineering: A, 725, 456-465.

20. Gonzalez F, Houbaert Y. A review of ordering phenomena in iron-silicon alloys. Rev Met. 2013;49(3):178–199

21. Kubaschewski O. Iron-binary phase diagrams. Berlin: Springer Science & Business Media; 2013.

22. Hawezy, D. (2017). The influence of silicon content on physical properties of non-oriented silicon steel. Materials Science and Technology, 33(14), 1560-1569.

23. Yao, Y. C., Sha, Y. H., Liu, J. L., Zhang, F., & Zuo, L. (2014). Texture and magnetic properties of rolled Fe-6.5 wt.% Si thin sheets. Journal of Electronic Materials, 43(1), 121-125.

24. Liu, H. T., Liu, Z. Y., Sun, Y., Gao, F., & Wang, G. D. (2013). Development of λ-fiber recrystallization texture and magnetic property in Fe–6.5 wt% Si thin sheet produced by strip casting and warm rolling method. Materials Letters, 91, 150-153.

25. Lyudkovsky, G., Rastogi, P. K., & Bala, M. (1986). Nonoriented electrical steels. JOM, 38(1), 18-26.Konadu SN. Non-destructive testing and surface evaluation of electrical steels. Cardif: Cardiff University; 2006.

26. Golding EW, Widdis FC. Electrical measurements and measuring instruments. London: I. Pitman; 1963.

27. Slater, J. C. (1964). Atomic radii in crystals. The Journal of Chemical Physics, 41(10), 3199-3204.

28. Bunge, H. J. (2013). Texture analysis in materials science: mathematical methods. Elsevier.

29. Randle, V., & Engler, O. (2014). Introduction to texture analysis: macrotexture, microtexture and orientation mapping. CRC press.

30. Suwas, S., & Ray, R. K. (2014). Representation of Texture. In Crystallographic Texture of Materials (pp. 11-38). Springer, London.

31. Cullity, B. D., & Stock, S. R. (2014). Elements of X-ray Diffraction. Pearson Education.

32. Kestens, L., & Jacobs, S. (2008). Texture control during the manufacturing of nonoriented electrical steels. Texture, Stress, and Microstructure, 2008.

33. Humphreys, F. J., & Hatherly, M. (2012). Recrystallization and related annealing phenomena. Elsevier.

34. Kestens, L. A. I., & Pirgazi, H. (2016). Texture formation in metal alloys with cubic crystal structures.

35. Li, Y., Chen, L., Tang, J., Zhao, G., & Zhang, C. (2018). Effects of asymmetric feeder on microstructure and mechanical properties of high strength Al-Zn-Mg alloy by hot extrusion. Journal of Alloys and Compounds, 749, 293-304.

36. He, Y. (2005). Grain-scale characterization of FCC/BCC correspondence relations and variant selection.

37. He, Y., Godet, S., & Jonas, J. J. (2005). Representation of misorientations in Rodrigues–Frank space: application to the Bain, Kurdjumov–Sachs, Nishiyama–Wassermann and Pitsch orientation relationships in the Gibeon meteorite. Acta materialia, 53(4), 1179-1190.

38. Frank, C. (1988). Orientation mapping: 1987 mrs fall meeting von hippel award lecture. MRS Bulletin, 13(3), 24-31.

39. O. Rodrigues:*J. des Mathématiques Pures et Appliquées*, 1840, vol. 5, pp. 380–440.

40. Raabe, D. (2003). Overview on basic types of hot rolling textures of steels. steel research international, 74(5), 327-337.

41. Raabe, D., & Lücke, K. (1994). Rolling and annealing textures of bcc metals. In Materials Science Forum (Vol. 157, pp. 597-610). Trans Tech Publications.

42. Hölscher, M., Raabe, D., & Lücke, K. (1991). Rolling and recrystallization textures of bcc steels. steel research, 62(12), 567-575.

43. Hu, H. (1974). Texture of metals. Texture, Stress, and Microstructure, 1(4), 233-258.

44. Ray, R. K., Jonas, J. J., & Hook, R. E. (1994). Cold rolling and annealing textures in low carbon and extra low carbon steels. International materials reviews, 39(4), 129-172.

45. Park, Y. B., Lee, D. N., & Gottstein, G. (1998). The evolution of recrystallization textures in body centred cubic metals. Acta materialia, 46(10), 3371-3379.

46. Sandoval, L., Urbassek, H. M., & Entel, P. (2009). The Bain versus Nishiyama–Wassermann path in the martensitic transformation of Fe. New Journal of Physics, 11(10), 103027.

47. Ray, R. K., & Jonas, J. J. (1990). Transformation textures in steels. International Materials Reviews, 35(1), 1-36.

48. Fischer, O., & Schneider, J. (2003). Influence of deformation process on the improvement of non-oriented electrical steel. Journal of Magnetism and Magnetic Materials, 254, 302-306.

49. Lee, K. M., Huh, M. Y., Lee, H. J., Park, J. T., Kim, J. S., Shin, E. J., & Engler, O. (2015). Effect of hot band grain size on development of textures and magnetic properties in 2.0% Si non-oriented electrical steel sheet. Journal of Magnetism and Magnetic Materials, 396, 53-64.

50. Yashiki, H., & Okamoto, A. (1987). Effect of hot-band grain size on magnetic properties of non-oriented electrical steels. IEEE transactions on magnetics, 23(5), 3086-3088.

51. De Dafe, S. S. F., da Costa Paolinelli, S., & Cota, A. B. (2011). Influence of thermomechanical processing on shear bands formation and magnetic properties of a 3% Si non-oriented electrical steel. Journal of Magnetism and Magnetic Materials, 323(24), 3234-3238.

52. Hölscher, M., Raabe, D., & Lücke, K. (1994). Relationship between rolling textures and shear textures in fcc and bcc metals. Acta metallurgica et materialia, 42(3), 879-886.

53. Barrett, C. S. (1939). Structure of iron after compression. Trans. Aime, 135, 296.

54. Haratani, T., Hutchinson, W. B., Dillamore, I. L., & Bate, P. (1984). Contribution of shear banding to origin of Goss texture in silicon iron. Metal Science, 18(2), 57-66.

55. Dillamore, I. L., & Katoh, H. (1974). The mechanisms of recrystallization in cubic metals with particular reference to their orientation-dependence. Metal Science, 8(1), 73-83.

56. Doherty, R. D. (1978). Recrystallization of metallic materials. Ed. By Frank Haessner. Dr. Riederer Verlag GmbH, Stuttgart.

57. Ibe, G. E. R. H. A. R. D., & Lücke, K. (1966). Growth selection during recrystallization of single crystals. Recrystallization, Grain Growth and Textures, 434.

58. Lücke, K. (1984). The formation of recrystallization textures in metals and alloys. In Proceedings of 7th International Conference on Textures of Materials (ICOTOM 7) (pp. 195-210).

59. Park, J. T., & Szpunar, J. A. (2003). Evolution of recrystallization texture in nonoriented electrical steels. Acta Materialia, 51(11), 3037-3051.

60. Emren, F., Von Schlippenbach, U., & Lücke, K. (1986). Investigation of the development of the recrystallization textures in deep drawing steels by ODF analysis. Acta Metallurgica, 34(11), 2105-2117.

61. Kestens, L., & Jacobs, S. (2008). Texture control during the manufacturing of nonoriented electrical steels. Texture, Stress, and Microstructure, 2008.

62. He, Y., & Hilinski, E. J. (2016). Texture and magnetic properties of non-oriented electrical steels processed by an unconventional cold rolling scheme. Journal of Magnetism and Magnetic Materials, 405, 337-352.

63. He, Y., Hilinski, E., & Li, J. (2015). Texture evolution of a non-oriented electrical steel cold rolled at directions different from the hot rolling direction. Metallurgical and Materials Transactions A, 46(11), 5350-5365.

64. He, Y., & Hilinski, E. J. (2017). Skew rolling and its effect on the deformation textures of non-oriented electrical steels. Journal of Materials Processing Technology, 242, 182-195.

65. He, Y., Sanjari, M., & Hilinski, E. J. (2017). Processing Non-oriented Electrical Steels Using Inclined/Skew Rolling Schemes. In Energy Materials 2017 (pp. 51-59). Springer, Cham.

66. Yoshinaga, N., Kestens, L., & De Cooman, B. C. (2005). α→ γ→ α transformation texture formation at cold-rolled ultra low carbon steel surfaces. In Materials Science Forum (Vol. 495, pp. 1267-1272). Trans Tech Publications.

67. Tomida, T. (1996). A new process to develop (100) texture in silicon steel sheets. Journal of Materials Engineering and Performance, 5(3), 316-322.

68. Li, H. Z., Liu, H. T., Liu, Z. Y., & Wang, G. D. (2015). Microstructure, texture evolution and magnetic properties of strip-casting non-oriented 6.5 wt.% Si electrical steel doped with cerium. Materials Characterization, 103, 101-106.

69. Liu, H., Liu, Z., Cao, G., Li, C., & Wang, G. (2011). Microstructure and texture evolution of strip casting 3 wt% Si non-oriented silicon steel with columnar structure. Journal of Magnetism and Magnetic Materials, 323(21), 2648-2651.

70. Liu, H. T., Liu, Z. Y., Sun, Y., Gao, F., & Wang, G. D. (2013). Development of λ-fiber recrystallization texture and magnetic property in Fe–6.5 wt% Si thin sheet produced by strip casting and warm rolling method. Materials Letters, 91, 150-153.

71. Liu, H. T., Schneider, J., Li, H. L., Sun, Y., Gao, F., Lu, H. H., ... & Wang, G. D. (2015). Fabrication of high permeability non-oriented electrical steels by increasing< 0 0 1> recrystallization texture using compacted strip casting processes. Journal of Magnetism and Magnetic Materials, 374, 577-586.

Chapter 3 The Formation of the Cube ({100}<001>) Texture in Non-oriented Electrical Steels

3.1 Introduction

Electrical steels are widely used as soft magnetic cores in transformers, generators and electric motors [1-7]. Depending on the crystallographic texture and application, electrical steels can be classified as: (i) grain-oriented electrical steel (GOES), which is primarily used in transformers, and (ii) non-oriented electrical steel (NOES), which is mostly used in rotating machines [3]. The GOES is normally processed to contain large grains of essentially one single orientation, i.e. the Goss ({011}<100>), which gives rise to excellent magnetic properties in the rolling direction (RD). The properties of GOES in the transverse direction (TD) are much poorer than in the RD, i.e. there is apparent anisotropy. The NOES, on the other hand, is usually composed of grains with various orientations featuring the γ-fibre (<111>//ND) and α-fibre (<110>//RD) textures, i.e. similar to those of low carbon steels after conventional rolling and annealing. Although with much less anisotropy, the overall magnetic properties in all the directions are usually inferior to those of the GOES in the rolling direction.

It is well known that the magnetic properties of electrical steels are highly dependent on the chemical composition (e.g. the silicon content and the cleanness of the steel), the thickness of the sheets, the grain size and the crystallographic texture [3-7]. Currently, manufacturing electrical steel sheets (silicon content up to ~3.5%) with thickness in the range of 0.2~0.5 mm is very common even in mass production. With the same sheet thickness, the magnetic properties are mainly determined by the grain size and the crystallographic texture. An optimal grain size is normally required depending on the application, e.g. the excitation frequency. The dependence of

magnetic properties on the crystallographic texture is due to the magnetocrystalline anisotropy of bcc iron, which shows an easy magnetization direction in the <100> crystal axis, and a hard magnetization direction in the <111> direction [1-3]. As a result, it is preferable to producing final electrical steel sheets with a strong θ-fibre (<001>//ND) texture, which has easy <100> axis in all the directions of the sheet, the latter being the magnetization directions of rotating machines (electric motors) [3-7]. Of the θ-fibre, the cube texture ({001}<100>) is a highly desired orientation since it has two <100> axes lying in the sheet plane. Although the cube texture is the final annealing texture in fcc metals (e.g. aluminum), it has been proven to be very difficult to be produced in bcc iron after conventional cold rolling and annealing.

Many investigations have shown that the final annealing texture of low carbon steel essentially resembled the cold-rolling texture before annealing [8, 9], while the texture under plain-strain deformation (rolling) was usually characterized by a γ-fibre and an α-fibre, with particularly strong intensities at {001}<110> (rotated cube), {112}<110>, {111}<110>, and {111}<112>. After annealing, the texture normally also consisted of a γ-fibre and an α-fibre, with the {001}<110> component completely eliminated or largely weakened. The major texture component was the {111}<112> orientation on the γ-fibre [8, 9]. Thus, except using unconventional processing technologies [9], it was rarely able to produce the desired <100>//ND texture in non-oriented electrical steels, especially those with a high silicon content, e.g. 3.2 wt% or more.

The formation mechanisms of specific orientations (e.g. the Goss orientation) in electrical steels have been the subject of many studies, e.g. those on the nucleation and growth of the Goss ({110}<001>) orientation during primary and secondary recrystallization [10-13]. Dillamore et al. [14] attributed the formation of shear bands to the geometric softening of grains with high Taylor factors. It was believed that these grains had high resistance to plain-strain compression, and were

more prone to plastic instability which resulted in geometric softening through the formation of localized shear bands. Several models have been suggested for the retention of the Goss orientation during cold rolling [10-13]. On the other hand, many researchers [10, 12] have connected the formation of the Goss orientation during annealing to the shear bands formed in {111}<112> grains. Ushioda and Hutchinson [10] observed two kinds of shear bands formed in Si-Fe silicon steel with different inclination angles to the rolling direction. These subsequently led to the preferential nucleation of Goss orientation during recrystallization. This preferential nucleation was attributed to the advantage of sharp lattice curvature [10, 15] and low dislocation density locally inside the shear bands [16].

The formation of the cube texture in electrical steel has been linked to the rotated Goss {110}<110> orientation [17, 18]. The origin of this orientation has not been fully understood. A tentative proposition was that it was retained during hot rolling as a consequence of phase transformation [19]. Vanderschueren et al. [17] observed a fishbone-like shear banding structure in rotated Goss grains in IF steels using optical microscopy. Nguyen-Minh et al. [19] examined the internal structure of the shear bands in rotated Goss grains, and observed the existence of ideal cube orientation within the deformation bands. On the other hand, He et al. [9] observed a strong cube texture in an electrical steel containing 0.88% silicon after inclined cold rolling at an angle of 60° to the hot rolling direction, but the cube texture did not appear in a high silicon steel (2.8 wt%) after the same inclined rolling.

The objective of this study is to evaluate the possibility of obtaining the ideal cube {100}<001> texture in non-oriented electrical steels. For this purpose two steels (2.8% Si and 3.2% Si) were prepared using conventional thermomechanical processing. The cube texture was tracked at all thermomechanical stages using electron backscattered diffraction (EBSD) analysis. Emphasis was

placed on the formation of the cube texture during cold rolling and the effect of shear bands and crystal fragmentations on the recrystallization behaviour.

3.2 Experimental

The chemical compositions of the two non-oriented electrical steel are shown in Table 3.1. The first steel (2.8% Si) was melted using a vacuum furnace and subsequently cast into ingots with a cross-section area of 200 × 200 mm^2. A first hot rolling was performed at a nominal temperature of 1040°C, with 80% thickness reduction (to ~25 mm). The surface oxides were machined before second hot rolling, which was again at a nominal temperature of 1040 °C, and reduced to ~2.5 mm. The surface oxides generated during the hot rolling process were removed through pickling in an HCl solution. The steel plates were then annealed at 840°C for 60 hours in a 100% dry hydrogen atmosphere. The steel plates were finally cold rolled to a thickness of ~0.5 mm (~85% reduction). The second steel (3.2% Si) was also melted in a vacuum furnace and subsequently cast into ingots with a cross-section area 265 × 200 mm^2. It was then processed using similar procedures but with slightly different parameters. A detailed description of the processing steps of both steels are compared in Fig. 3.1.

In previous studies, it has been shown that there are strong brass, copper and Goss textures in the surface layers of electrical steels after hot rolling. To obtain the rotated Goss texture, the top 1 mm of the hot-rolled plate was machined and used to conduct inclined rolling, in which a strip was cut from the hot-rolled plate (top layer) at an angle of 55° from the hot rolling direction (HRD) and cold rolled in the longitudinal direction (Fig. 3.2). In this way, the brass component in the hot-rolled plate became the rotated Goss orientation which was not produced directly from hot rolling. The plate was cold rolled along the new rolling direction (RD) to a final thickness of 0.5 mm (50% reduction).

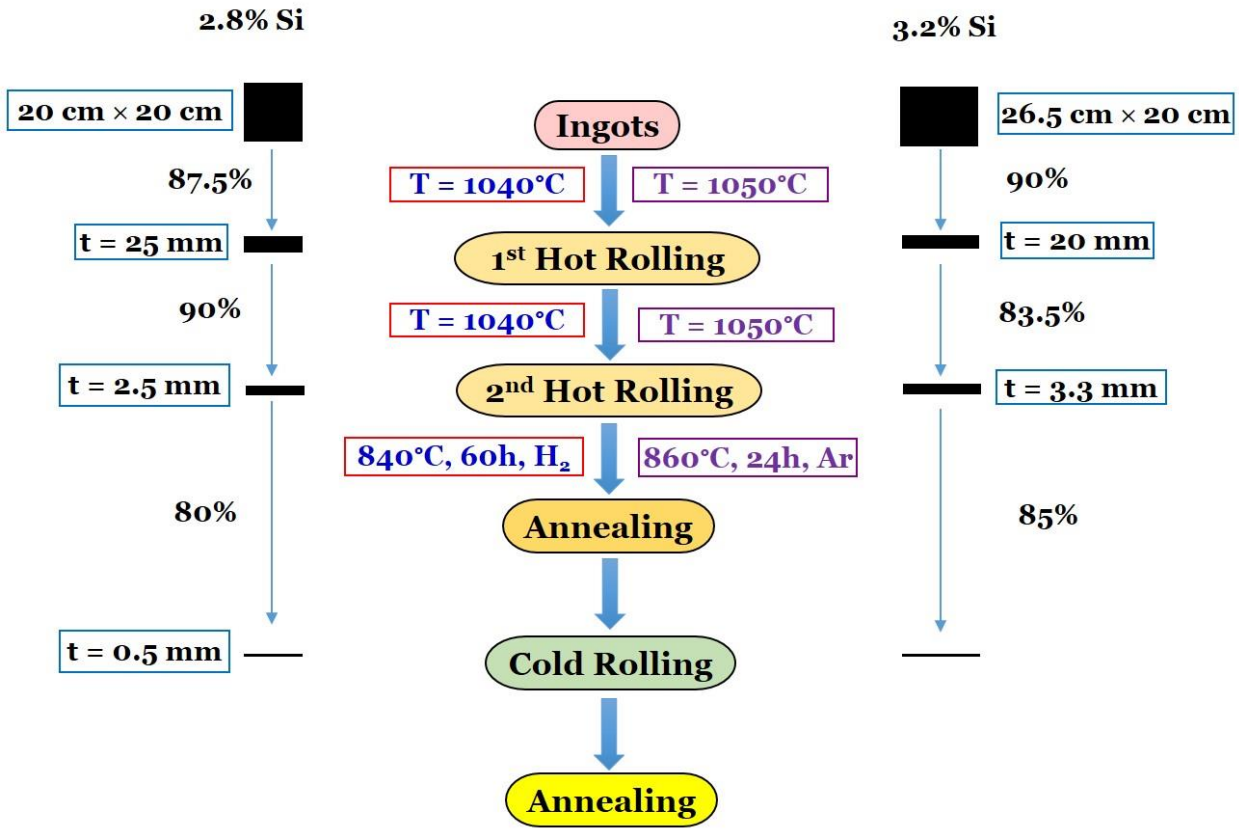

Fig. 3.1. Schematic illustration of the processing steps and parameters used for the two electrical steels.

EBSD characterization was carried out at all thermomechanical stages in a field emission gun scanning electron microscope (Nova NanoSEM, FEI) equipped with an EDAX Orientation Imaging Microscopy system (OIM 6.2). The EBSD scans were performed on the cross section (ND-RD plane) of the samples, which covered essentially the entire thickness of the plate or sheet. Orientation distribution functions (ODFs) were calculated from the measured Euler angles using a harmonic series expansion method with a Gaussian half-width of 5° and a series rank of 22. The textures were plotted on the $\varphi_2 = 45°$ section of the Euler space (Bunge notation). Full constraint Taylor theory was used to calculate the Taylor factors of different crystal orientations using a

family of slip systems for bcc metals, i.e. {110}<111> , {211}<111> and {321}<111>, and with plane-strain deformation gradients given by $\varepsilon_{11}=1, \varepsilon_{12}=\varepsilon_{13}=\varepsilon_{23}=\varepsilon_{21}=\varepsilon_{31}=\varepsilon_{32}=0$, and $\varepsilon_{33}=-1$.

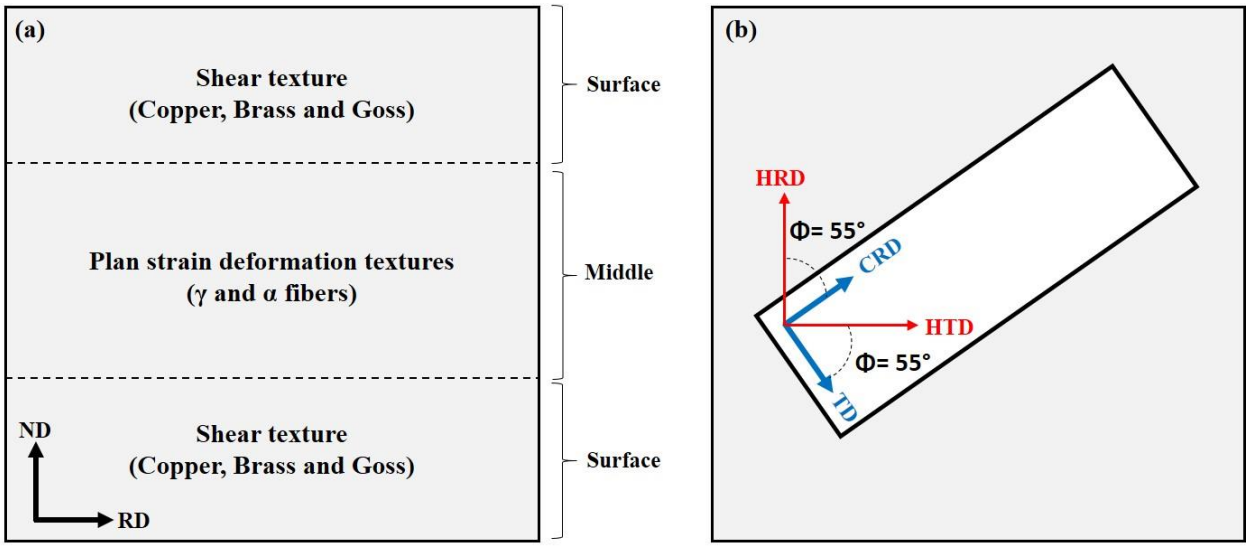

Fig. 3.2. Schematic illustration of the hot band textures and inclined rolling. (a) different textures developed during hot rolling, (b) rotating the cold rolling direction by Φ= 55° from the hot rolling direction (HRD).

Table 3.1. Chemical compositions of the investigated steels (wt%).

C	Mn	P	S	Si	Al	N	O	Fe
0..003	0.3	0.01	0.01	2.8	0.52	0.0008	0.0021	balance
0.004	0.40	0.0095	0.0027	3.20	0.58	0.0034	0.0037	balance

3.3 Results

3.3.1 Hot rolling

The textures and microstructures of the two electrical steels after hot rolling are shown in Fig. 3.3. It can be seen that the microstructures and the textures are heterogeneous across the thickness of the plates for both steels. The textures of the central regions resembled the typical textures of low carbon steels after plane-strain deformation, which were composed of elongated deformed grains that have crystal orientations belonging to the γ and α fibres. On the other hand, the surface region consisted of small equiaxed grains as a result of static and/or dynamic recrystallization during the hot rolling process. The crystal orientations were similar to those obtained under shear strain, with Goss, brass and copper as the major components. It can be seen from the inverse pole figure (IPF) maps and the image quality (IQ) maps that, the cube orientation exists in a very small volume fraction in the 2.8% Si sample, and is predominantly found as fragmented grains in the central region of the plate. On the other hand, the intensity of the cube is much higher in the 3.2% Si steel, and it is also primarily observed in the central region, but with small fractions in the recrystallized regions. There are traces of the rotated Goss orientation in both of the steels at both the central and surface layers.

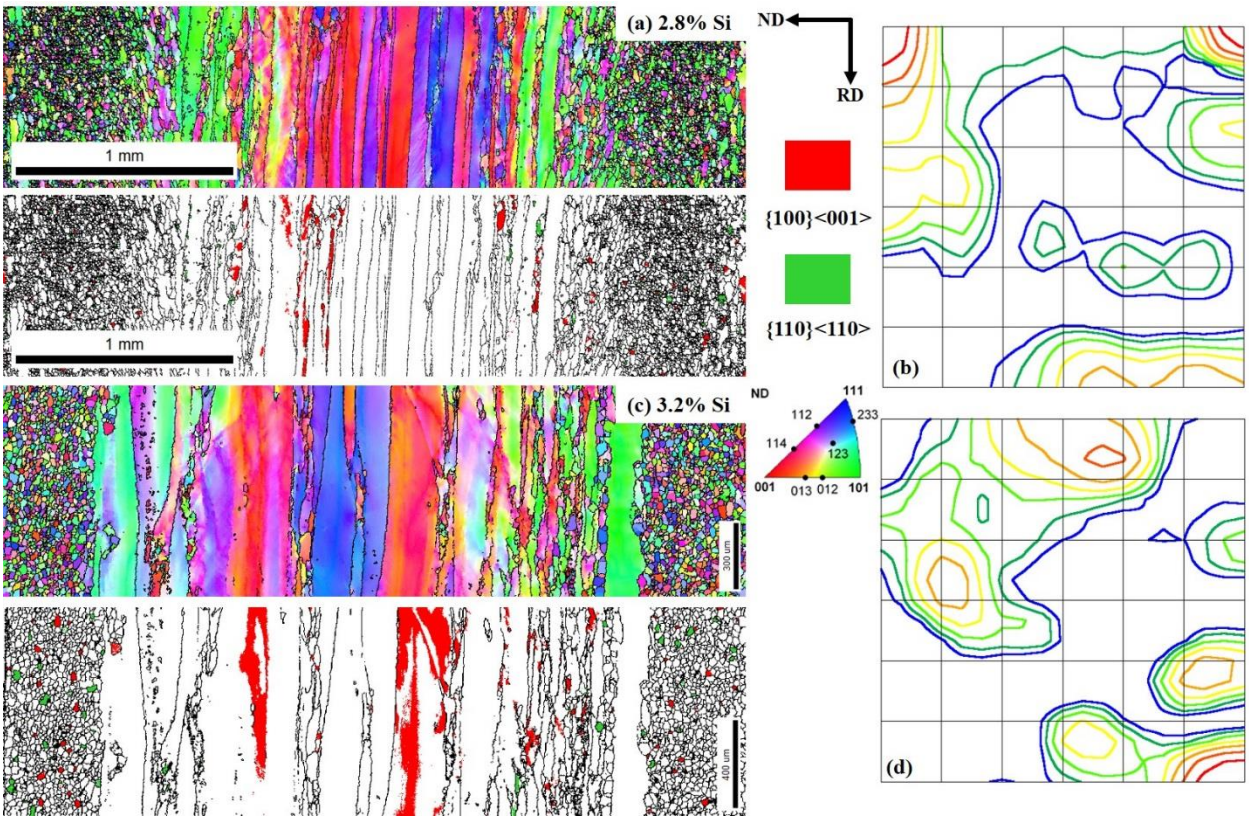

Fig. 3.3. The microstructures and textures of the hot-rolled 2.8% Si and 3.2% Si electrical steels: (a) EBSD IPF and IQ maps of the cross-section of the 2.8% Si steel, (b) φ_2 =45° section of the ODFs (Bunge notation) of the sample in (a), (c) EBSD IPF and IQ maps of the cross-section of the 3.2% Si steel, (d) φ_2 =45° section of the ODFs of the sample in (c).

3.3.2 Hot band annealing

The microstructure and texture of the 2.8% Si steel after hot band annealing are shown in Fig. 3.4. The texture was considerably randomized because of recrystallization. The average grain size is ~205 μm, with variations between ~25 and ~700 μm. The IPF map reveals that the <110>//ND grains were most located at the top and bottom layers of the plate (similar to the hot-rolled plate shown in Fig. 3.3). On the other hand, the central region is essentially composed of <100>//ND

and <111>//ND grains. The cube orientation is extremely rare after hot band annealing, and only two very small grains can be noted. No rotated Goss is found throughout the plate thickness.

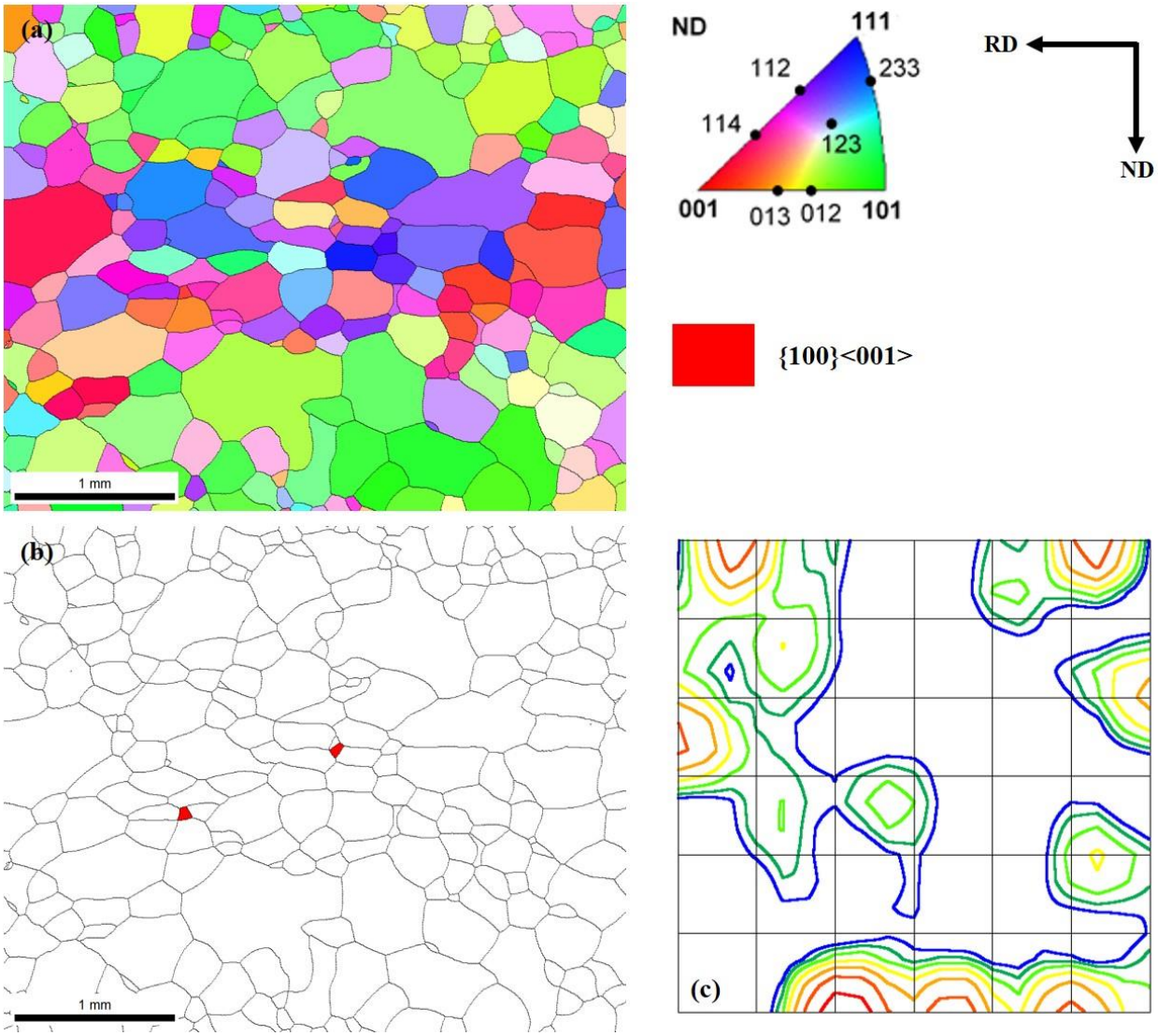

Fig. 3.4. The microstructure and texture of the hot-rolled 2.8% Si steel after annealing: (a) EBSD IPF map, (b) grain unique color map showing the location of the cube orientation, and (c) φ_2 =45° section of the ODFs (Bunge notation) of the sample.

The microstructure and texture of the 3.2% Si steel after hot band annealing (Fig. 3.5) show quite different features. The central region is mainly composed of large "elongated" grains, although they are recrystallized, which is different from the 2.8% Si steel where the central grains are mostly equiaxed. The average grain size was ~118 μm with variations between ~18 and ~590 μm. There is no apparent <110>//ND texture in the surface layers and the <100>//ND components are moved towards the cube orientation. Both cube and rotated Goss grains are observed within the microstructure. It is evident that the different annealing parameters (i.e. 60h at 840°C in H_2 vs. 24h at 860°C in Ar) have led to significantly different microstructure and texture in the annealed hot bands.

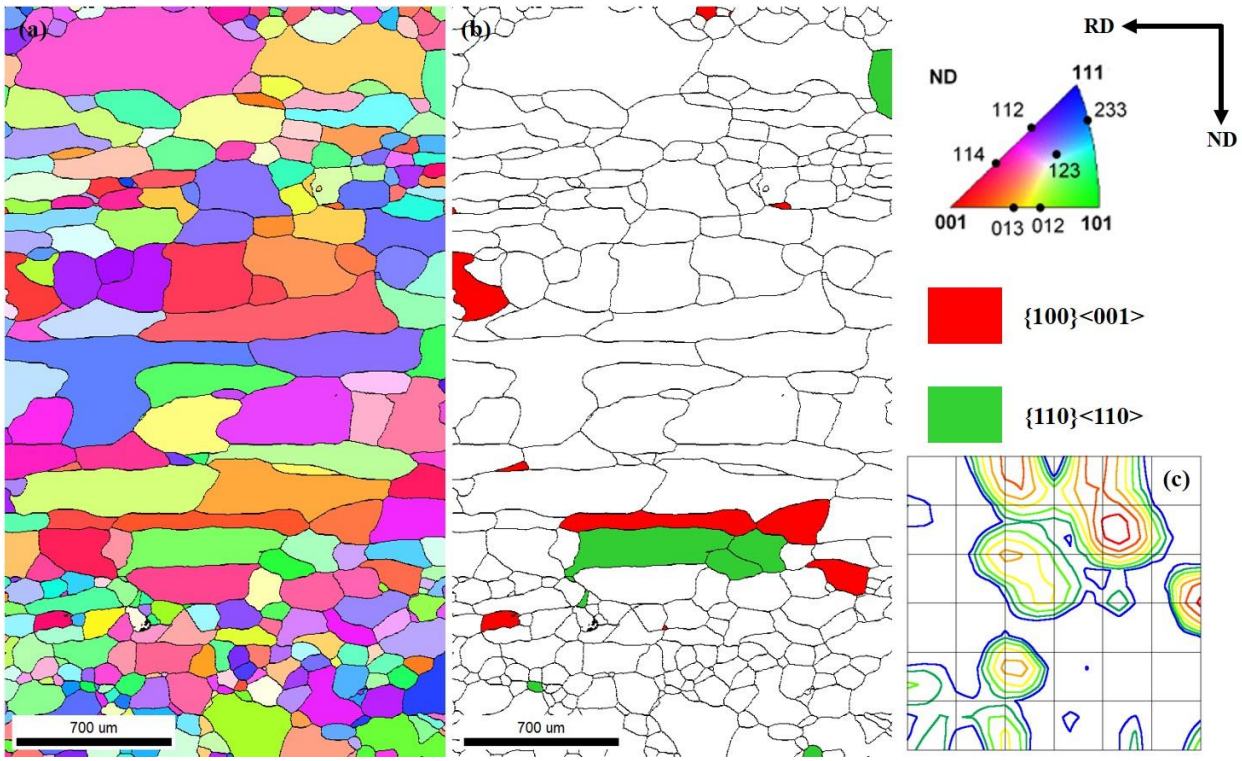

Fig. 3.5. The microstructure and texture of the hot-rolled 3.2% Si steel after annealing: (a) EBSD IPF map, (b) grain unique color map showing the location of the cube and rotated Goss orientations, (c) φ_2 =45° section of the ODFs (Bunge notation) of the sample.

3.3.3 Cold rolling

The microstructure and texture of the 2.8% Si steel after cold rolling to a final thickness of 0.5 mm are shown in Fig. 3.6. The major textures are the γ and α fibres, with the strongest intensity at rotated cube. The microstructure is composed of large elongated grains, which is the typical microstructure after cold rolling. The black regions in Fig. 3.6a were points not successfully indexed, which indicate high stored energy and high dislocation density as a result of heterogeneous plastic deformation. Only a very small volume fraction of the cube orientation is present after cold rolling, and it is mainly located near the surface of the sheet. Essentially no rotated Goss grain is found after cold rolling in the area shown in Fig. 3.6. Several scans with smaller step sizes were performed around regions of high stored energy (high dislocation density), and some rotated Goss grains were observed in these regions, as shown in Fig. 3.7. It is seen that the deformed rotated Goss has clear shear bands that are at ~28° from the rolling direction (RD), and within these shear bands very small volumes of the cube orientation are observed (Fig. 3.7c).

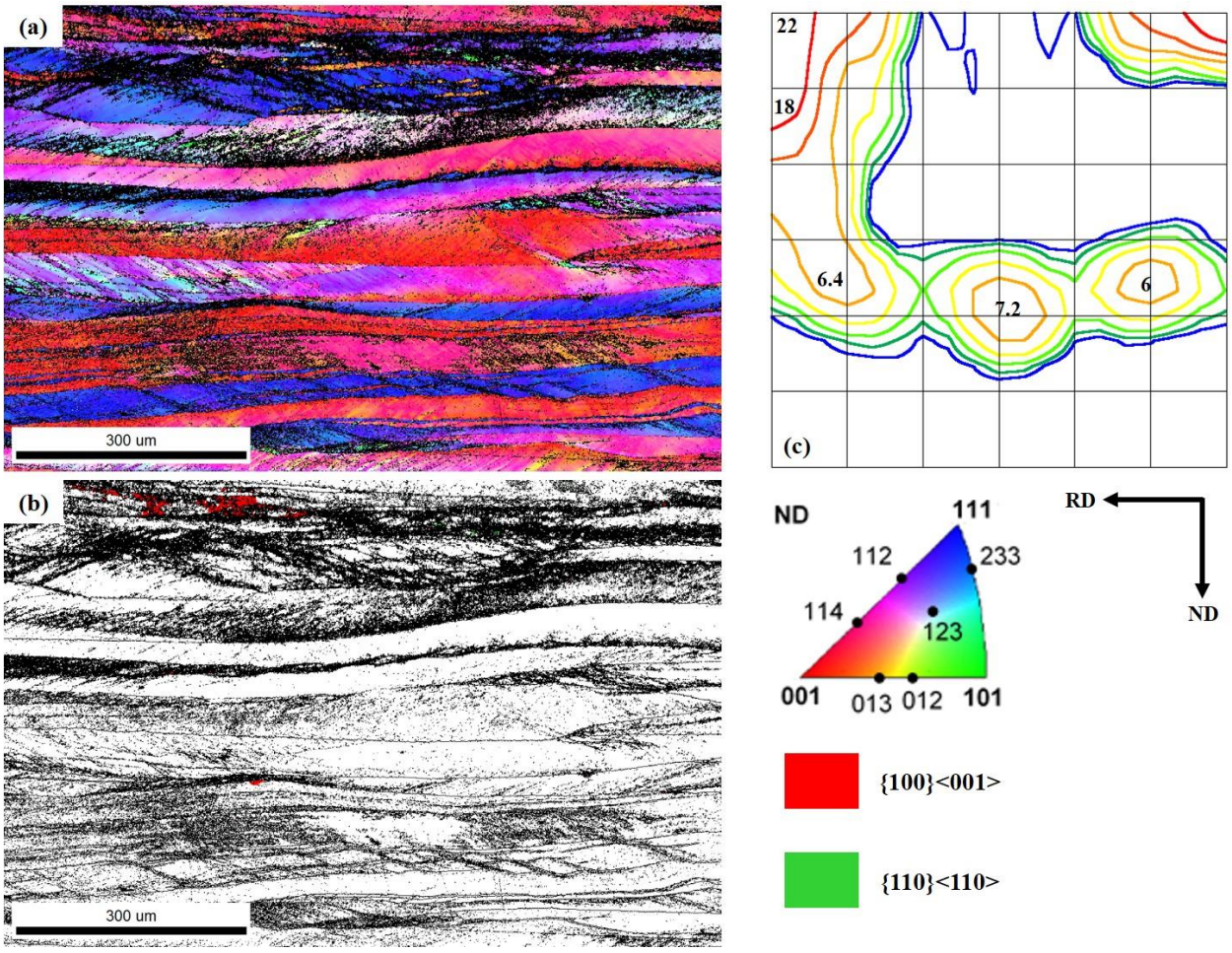

Fig. 3.6. The microstructure and texture of the cold-rolled 2.8% Si steel: (a) EBSD IPF map, (b) IQ map showing the location of the cube and rotated Goss orientations, and (c) φ_2 =45° section of the ODFs (Bunge notation) of the sample.

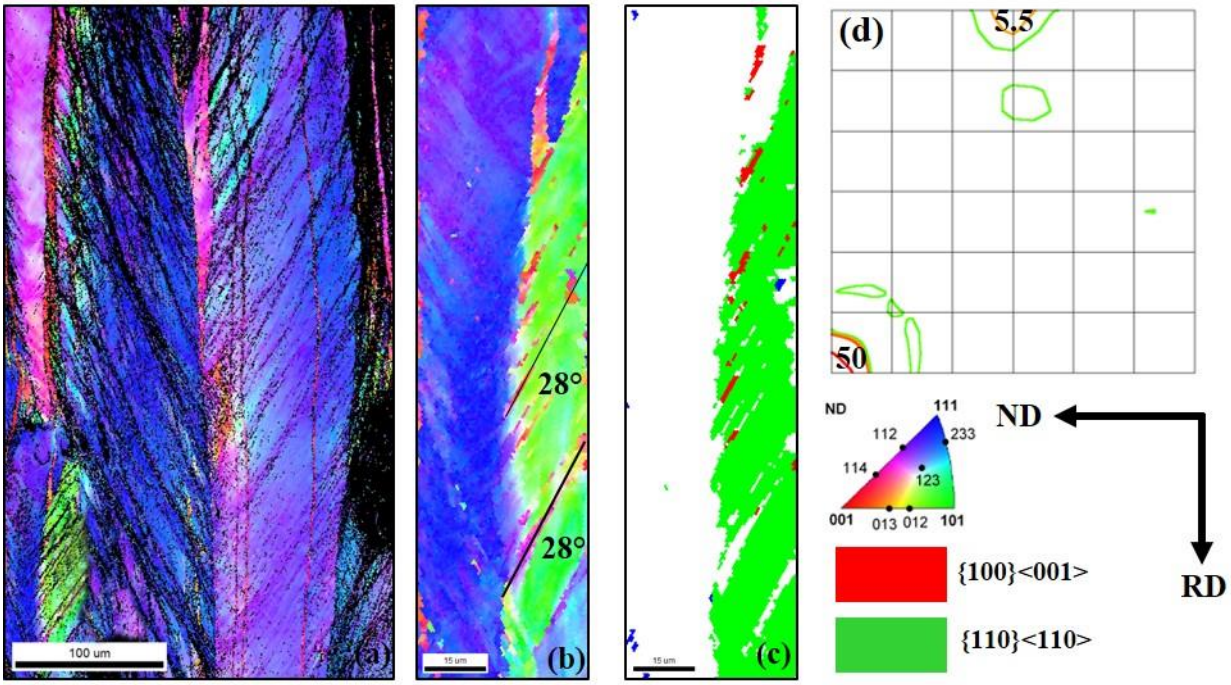

Fig. 3.7. An example of the cube {100}<001> orientation observed in the shear bands of a deformed rotated Goss {110}<110> grain in the 2.8% Si steel: (a) inverse pole figure map, (b) IPF map at a higher magnification, (c) grain unique color map showing the cube and rotated Goss orientations, and (d) φ_2 =45° section of the ODFs (Bunge notation).

The microstructure and texture of the 3.2% Si steel after cold rolling are shown in Fig. 3.8. The microstructure is composed of elongated grains containing numerous shear bands and grain fragmentations throughout the thickness. The texture reveals much stronger rotated cube {001}<110> and {113}<110> components than the 2.8% Si steel. The γ-fibre has a slightly lower intensity with major components at {111}<110> and {111}<112>. Two regions showed volumes of cube orientation, which were labelled as A and B, respectively, in the IPF map. Both regions were examined under a finer step size of 200 nm and the results are shown in Fig. 3.9.

As shown in Fig. 3.9, Region A was composed of heavily deformed areas that contained a few orientations distributed over a very small area. The heavily deformed region between Grain 1 ({111}<110>) and Grain 2 ({001}<110>) shows significant strain heterogeneity which leads to the formation of grain fragmentations as well as microbands. The main orientations include the cube {001}<100> and rotated Goss {110}<110> as indicated in the grain unique colour map (Fig. 3.9b). Apparently, the cube orientation in the 3.2% Si was able to survive in the proximity of the rotated Goss grain in the microbands and in fragmented regions during cold rolling. It is worth noting that it is difficult to find a grain with only the cube orientation during cold rolling, while grains with the rotated cube orientation can be readily observed, as shown in Fig. 3.9 (Grain 2).

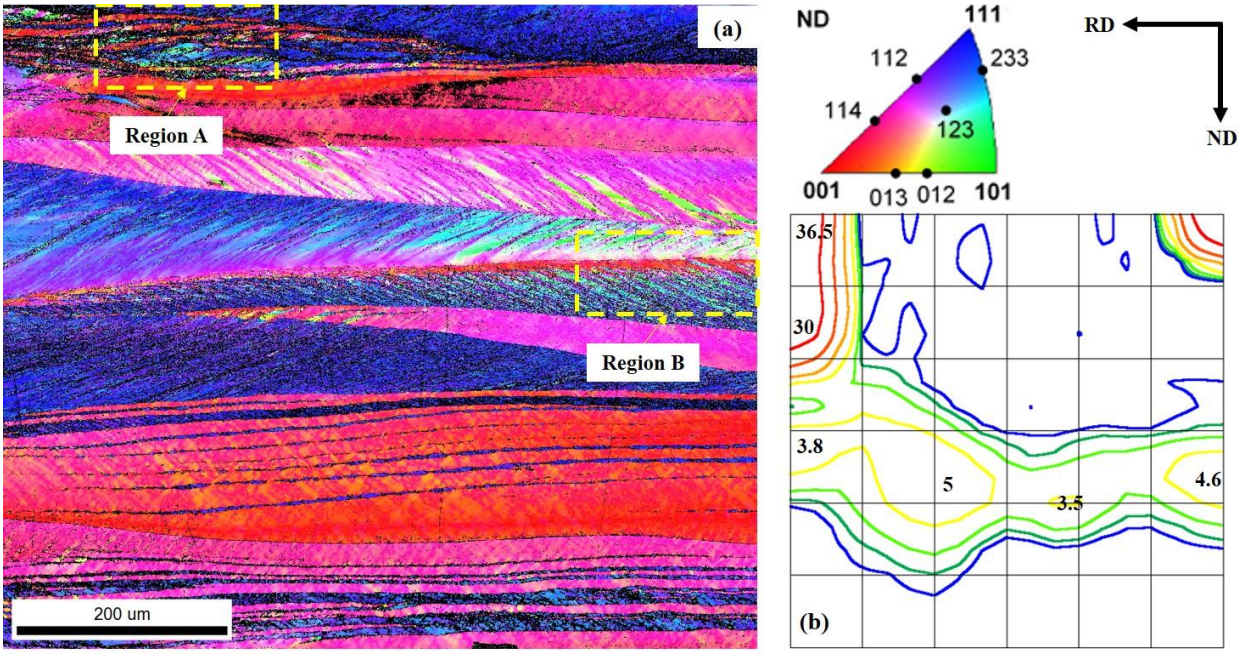

Fig. 3.8. The microstructure and texture of cold-rolled 3.2% Si electrical steel: (a) EBSD IPF map, (b) φ_2 =45° section of the ODFs (Bunge notation) of the sample.

A close examination of region B in Fig. 3.8 reveals that cube orientation may exist at the grain boundaries after cold rolling. The scanned region shows an uncommon texture for bcc steel, i.e. the cube and three other components as shown in Fig. 3.10c. The color variation in the IPF map (Fig. 3.10a) shows significant crystal fragmentation in this region. The upper grain is mainly composed of the {225}<7 12 2> orientation with shear bands at ~24° to the rolling direction (RD). The orientations in the shear bands are significantly different from those of the surrounding matrix and are predominantly composed of the {110}<11 11 9> orientation which is 15° away from the rotated Goss {110}<110>. On the other hand, the bottom grain is composed of three major orientations, {112}<8 18 5>, {331}<563> and the cube (at the grain boundary). It can also be seen that the deformed cube volumes form high angle grain boundaries with respect to both the upper and lower regions. The high angle grain boundaries would facilitate the growth of recrystallized cube nuclei in that region into the surrounding deformed matrix due to high mobility.

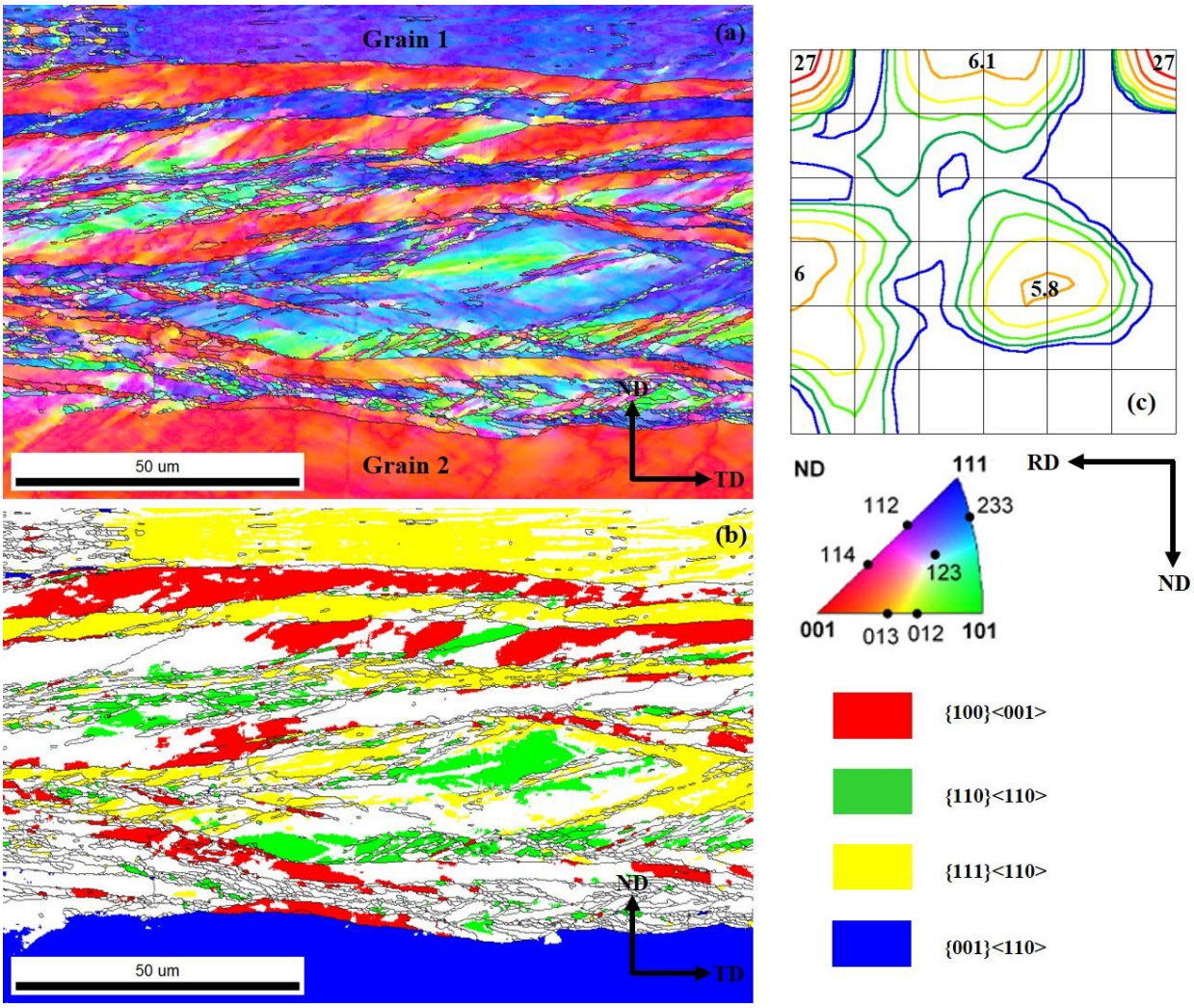

Fig. 3.9 A fine scan of Region A shown in Fig. 3.8: (a) EBSD IPF map , (b) grain unique colour map, (c) φ_2 =45° section of the ODFs (Bunge notation).

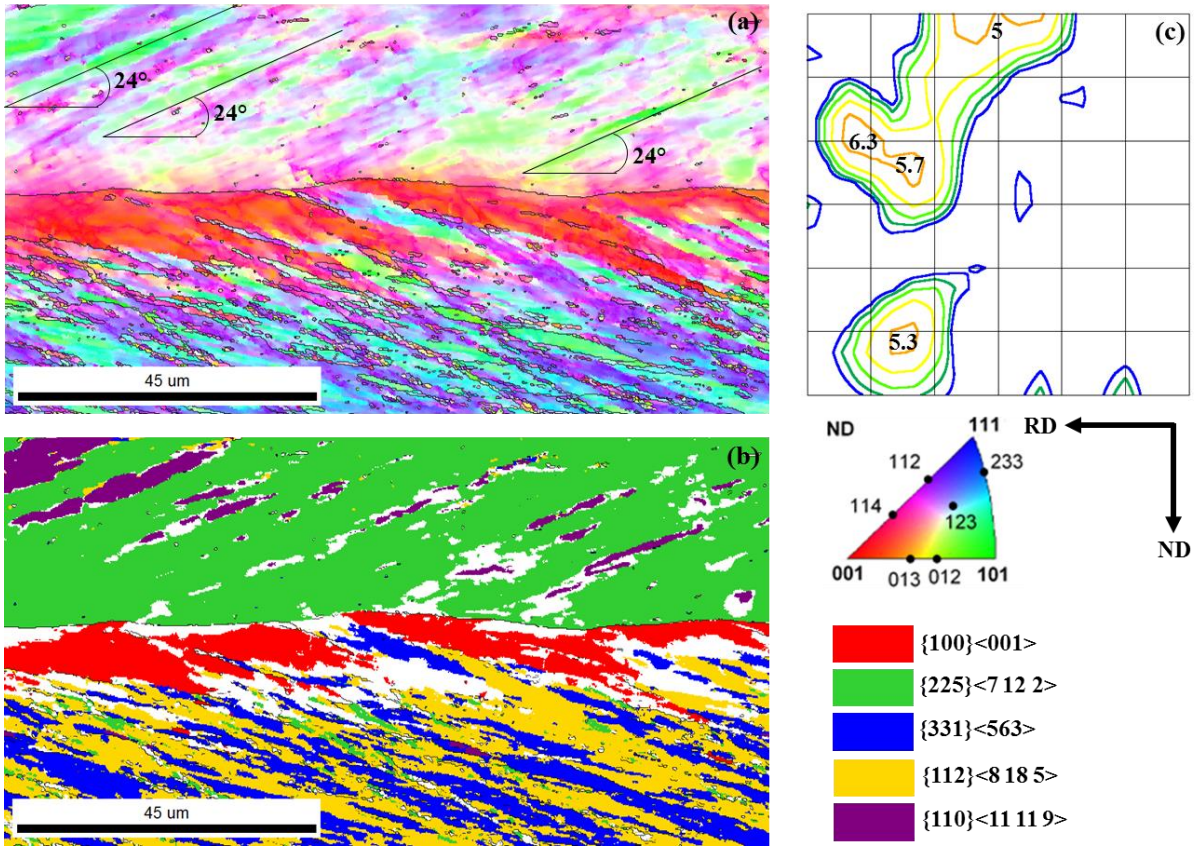

Fig. 3.10 A fine scan of Region B in Fig. 3.8: (a) EBSD IPF map, (b) grain unique colour map, (c) φ_2 =45° section of the ODFs (Bunge notation).

3.3.4 Recrystallization

When the deformed material is heated up to a temperature above recrystallization temperature, new grains are formed in the material, in order to reduce the overall stored energy. These grains are stress free, and they nucleate at microbands, shear bands or grain boundaries during the early stages of the annealing process. The driving force for the growth of these nuclei is the reduction of the stored energy of the surrounding deformed matrix. When the two steel sheets were partially annealed for 5 minutes at 750 °C then water quenched, the cube texture was not present at all in

the 2.8% Si sheet. On the other hand, the 3.2% Si steel sheet showed several regions in the microstructure with the cube orientation (Fig. 3.11). All of the cube nuclei formed during partial annealing were found to be close to the grain boundaries. It can be seen that the cube grains nucleate along with various other crystal orientations. The misorientations between the cube nuclei and their surrounding deformed matrix are almost all high angle grain boundaries (labelled as HA in Fig. 3.11).

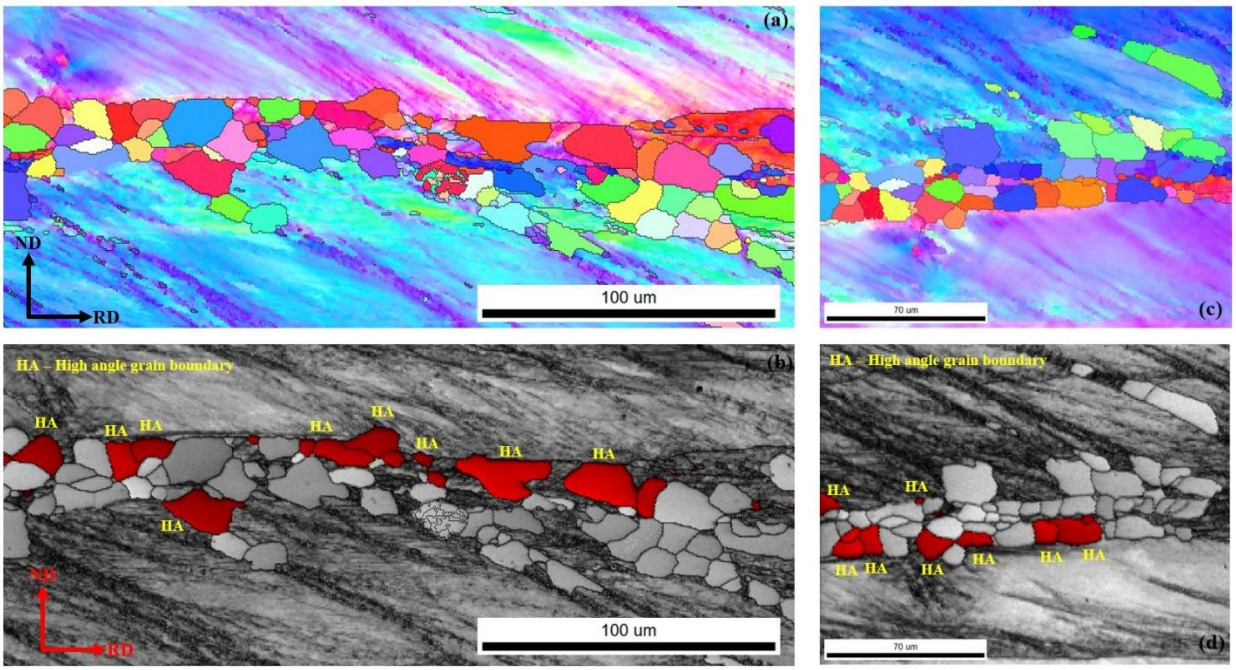

Fig. 3.11. Examples of cube grains at the grain boundaries during partial recrystallization in a 3.2% Si electrical steel: (a) and (b) EBSD IPF map of two different regions, (c) and (d) the corresponding grain unique colour maps showing the formation of high angle grain boundaries with respect to the surrounding matrix. Red grains are cube.

3.3.5 Inclined rolling

It is worth noting that, due to the fact that it is very difficult to find rotated Goss grains in high silicon electrical steels after conventional rolling, it is difficult to track or link the nucleation of the cube texture to the shear bands that were formed inside the {110}<110> grains which were previously illustrated in Fig. 3.7. In order to study the nucleation of the cube texture in deformed rotated Goss grains, a special controlled experiment, i.e. inclined rolling, was carried out.

As shown in Fig. 3.12, the surface layer (top 1 mm) of the hot-rolled and annealed 2.8% Si steel contained a high amount of shear textures including copper and brass. By rotating the plate around the ND for 55°, the brass orientation was brought to the rotated Goss orientation (Fig. 3.12c). With this initial texture, the steel sheet was cold rolled to a thickness of 0.5 mm (50% reduction). The microstructure and texture after inclined cold rolling are shown in Fig. 3.13. It can be seen that the texture produced after cold rolling consists of rotated cube, {114}<9 13 1>, {110}<110> and {111}<112>. Two regions contain rotated Goss orientation, while the remaining volumes in these regions are mainly the {335}<273> orientation, the latter being one of the metastable crystal orientations of the rotated Goss grains produced during cold rolling. It can also be seen that the rotated Goss grains have numerous shear bands inclined to the rolling direction (RD). Two regions (C and D) in the rotated Goss grains were closely analyzed (scanned with a smaller step size) in order to identify the crystal orientations within the shear bands, and to link them to the nuclei during the subsequent annealing.

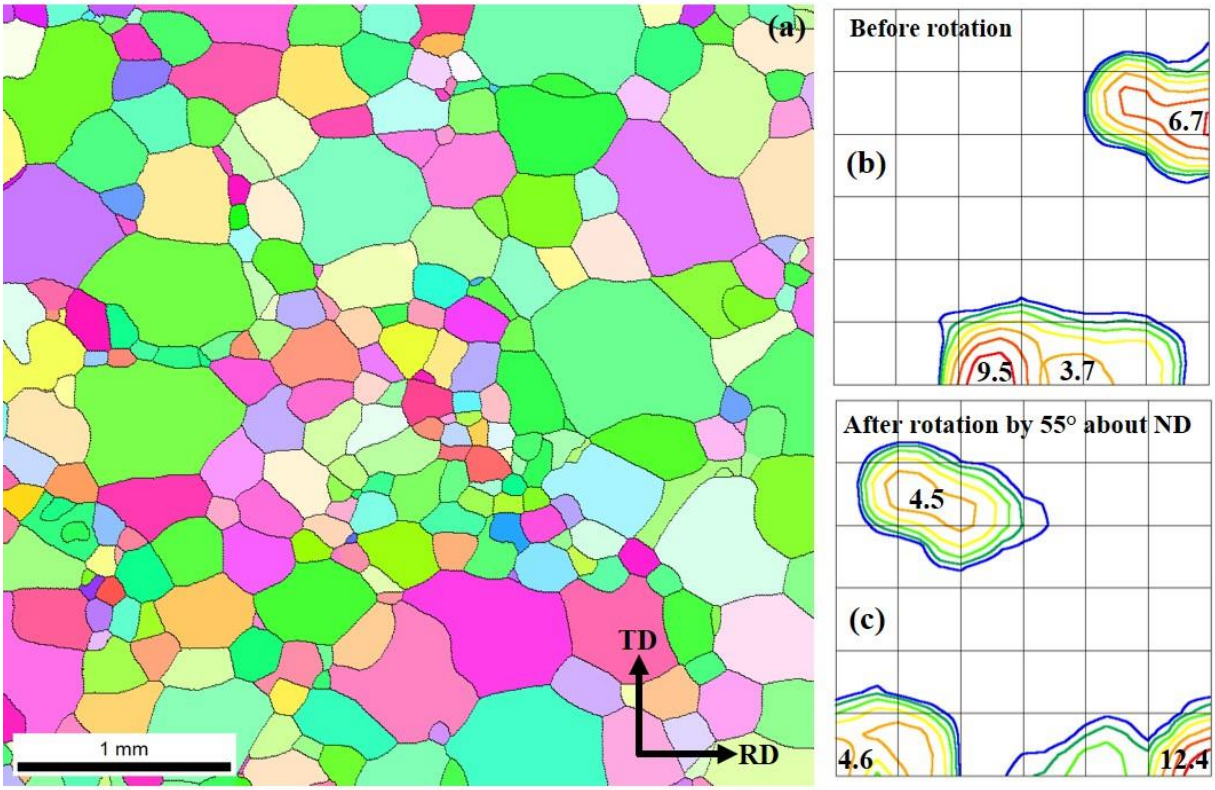

Fig. 3.12. The microstructure and texture of the top layer of the 2.8% Si sheet after hot rolling and annealing: (a) EBSD IPF map, (b) φ_2 =45° section of the ODFs, (c) φ_2 =45° section of the ODFs after rotation by 55° around ND.

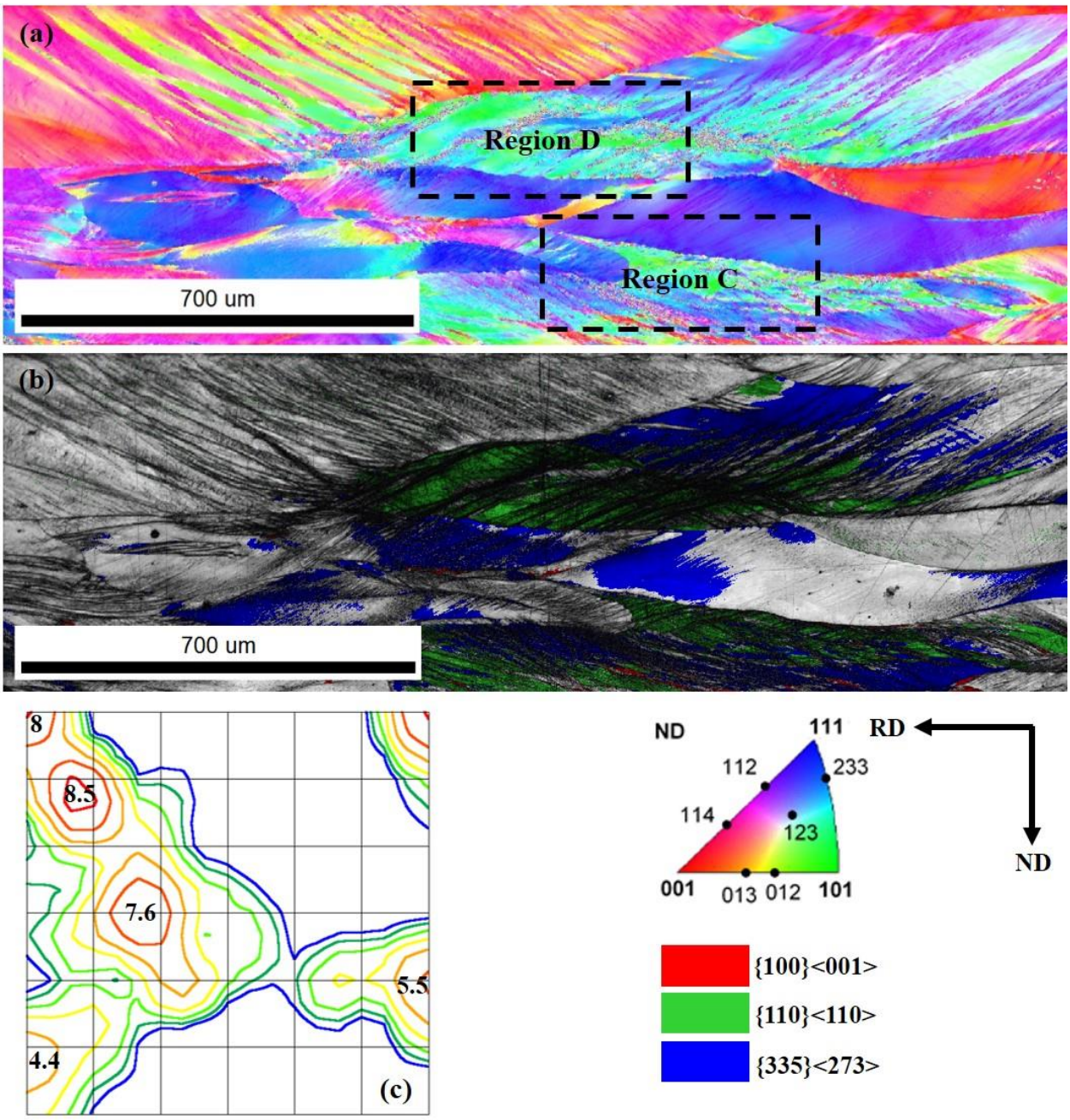

Fig. 3.13. The microstructure and texture of incline cold rolled 2.8% Si electrical steel after 50% thickness reduction: (a) EBSD IPF map of the full cross-section (RD-ND plane), (b) grain unique color map showing the locations of the cube and rotated Goss orientations, (c) φ_2 =45° section of the ODFs of the sample.

As shown in Fig. 3.14, Region C is predominantly composed of {110}<110> and {335}<273> orientations. Cube grains are also found in the shear bands, along grain boundaries and in the microbands of the rotated Goss grain. It is worth noting that microbands with a high concentration of cube orientation were formed after 50% inclined cold rolling. The intensities of the rotated Goss and {335}<273> are 13 and 5.5, respectively, while that of the cube is 2.7. Similarly, Region D was also mainly composed of the rotated Goss {110}<110> orientation as shown in Fig. 3.15. Again, the grain undergoes grain fragmentation during plastic deformation, as evidenced by the various colors within the deformed grain (Fig. 3.15a). Microbands and shear bands also developed. It is seen that there are cube grains along the shear bands and microbands.

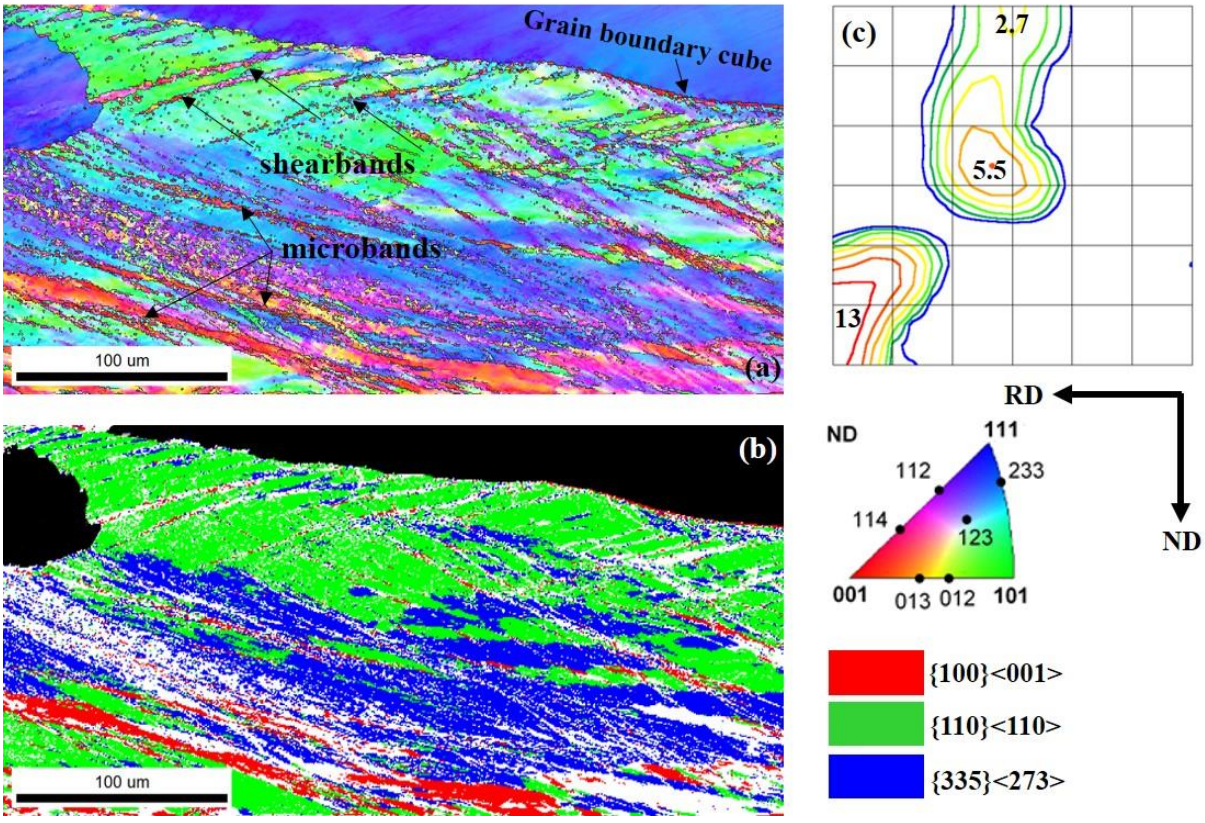

Fig. 3.14. Region C of Fig. 3.13 showing a deformed rotated Goss grain after 50% cold rolling reduction: (a) EBSD IPF map, (b) grain unique color map showing the locations of the cube and rotated Goss orientations, (c) φ_2 =45° section of the ODFs (Bunge notation).

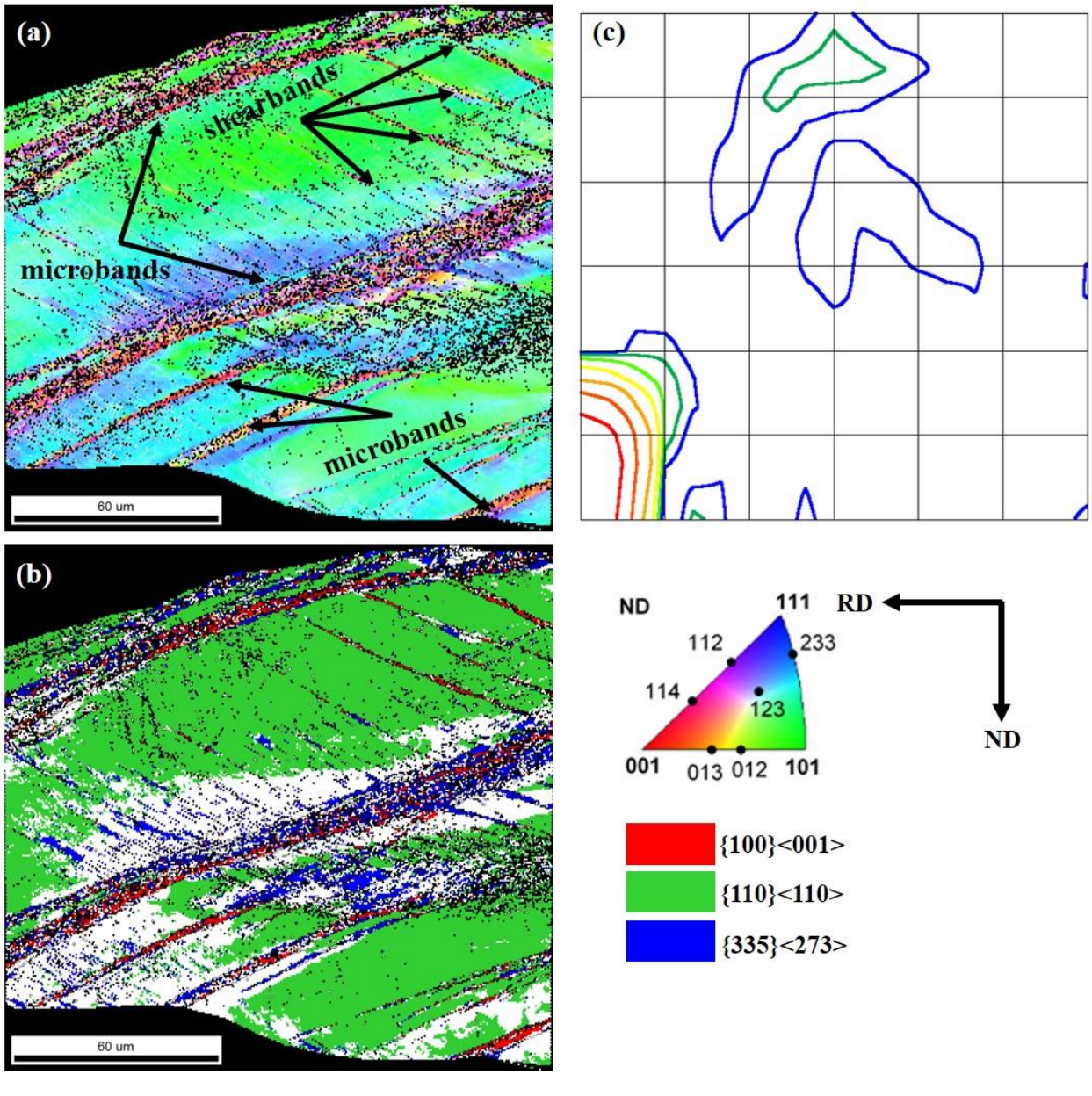

Fig. 3.15 Region D of Fig. 3.13 showing a second deformed rotated Goss grain after 50% inclined cold rolling reduction: (a) EBSD IPF map, (b) grain unique colour map showing the locations of the cube and rotated Goss orientations, (c) φ_2 =45° section of the ODFs (Bunge notation).

Furthermore, two fine EBSD scans were carried out around two shear bands using a very fine step size of 50 nm in order to examine the internal structure. As shown in Fig. 3.16, cube grains exist inside the shear bands of the deformed {110}<110> grains. It was also found that the shear bands are inclined at an angle of 20°-25° to the rolling direction (RD). The unique colour maps (Fig. 3.16c. and d) reveal that the shear bands are essentially composed of the cube grains exclusively.

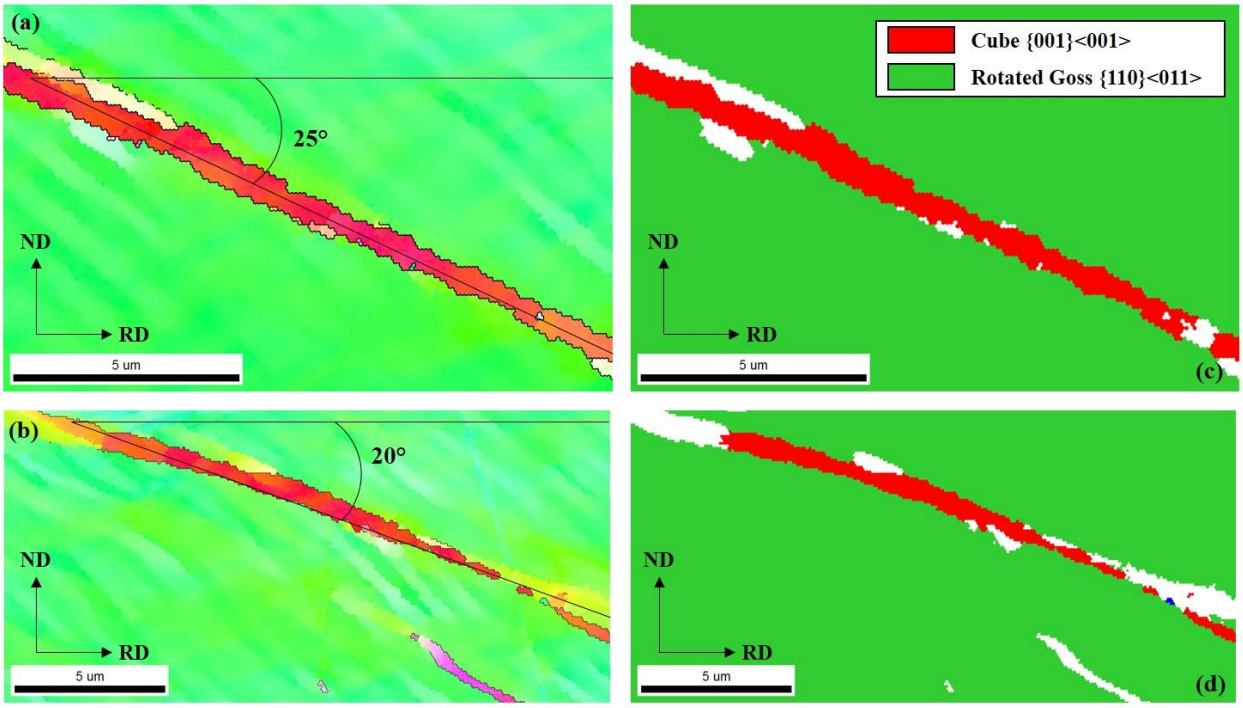

Fig. 3.16. High resolution EBSD scans (steps size =50 nm) around shear bands: (a), (b) EBSD IPF maps, and (c), (d) grain unique color map showing the locations of the cube and rotated Goss orientations.

3.3.6 Partial recrystallization after inclined rolling

In order to track the recrystallization of the cube texture within the shear bands of the deformed rotated Goss grains, the 2.8% Si electrical sheet after inclined cold rolling was annealed at 750 °C for 5 minutes and then water quenched. This process allowed nucleation only at high stored energy regions (shear bands and microbands), which enabled direct observation of the orientation relationship between the nuclei and the deformed grains. One example of the nucleation of the cube grain along the shear bands of the rotated Goss is illustrated in Fig. 3.17. These nuclei were formed at shear bands inclined at 25° to the rolling direction (RD). The deformed matrix is essentially the rotated Goss orientation with fragmented {335}<273> orientation. Another example of the cube nucleation is observed at the grain boundary of a deformed rotated Goss grain (Fig. 3.18). Because the cube nuclei were very small in size after partial annealing, this EBSD scan was performed using a much smaller step size (50 nm). Two cube grains are clearly seen nucleated beside a deformed rotated Goss grain.

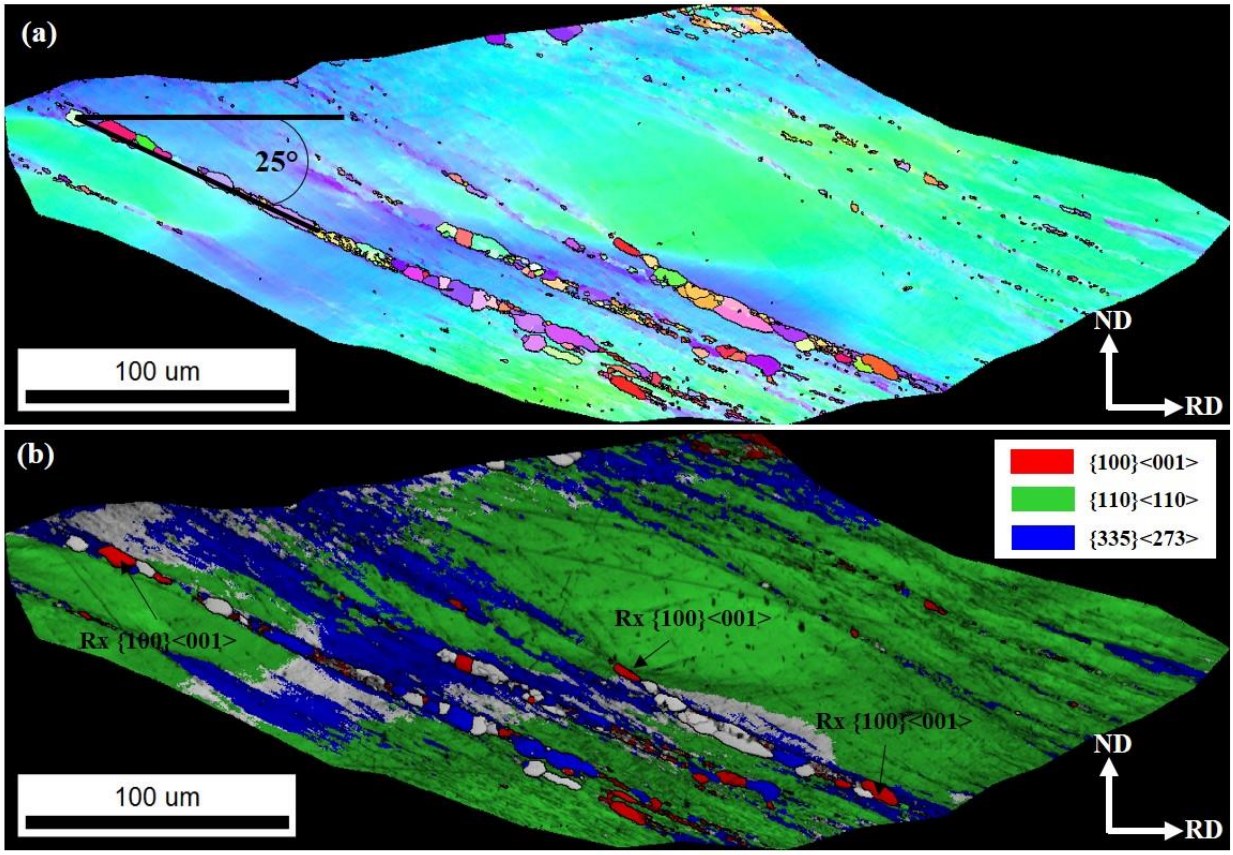

Fig. 3.17. Nucleation of cube grains inside the shearbands of rotated Goss grains during partial recrystallization of the 2.8% Si steel after inclined cold rolling: (a) EBSD IPF maps, and (b) grain unique color map showing the locations of the cube and rotated Goss orientations.

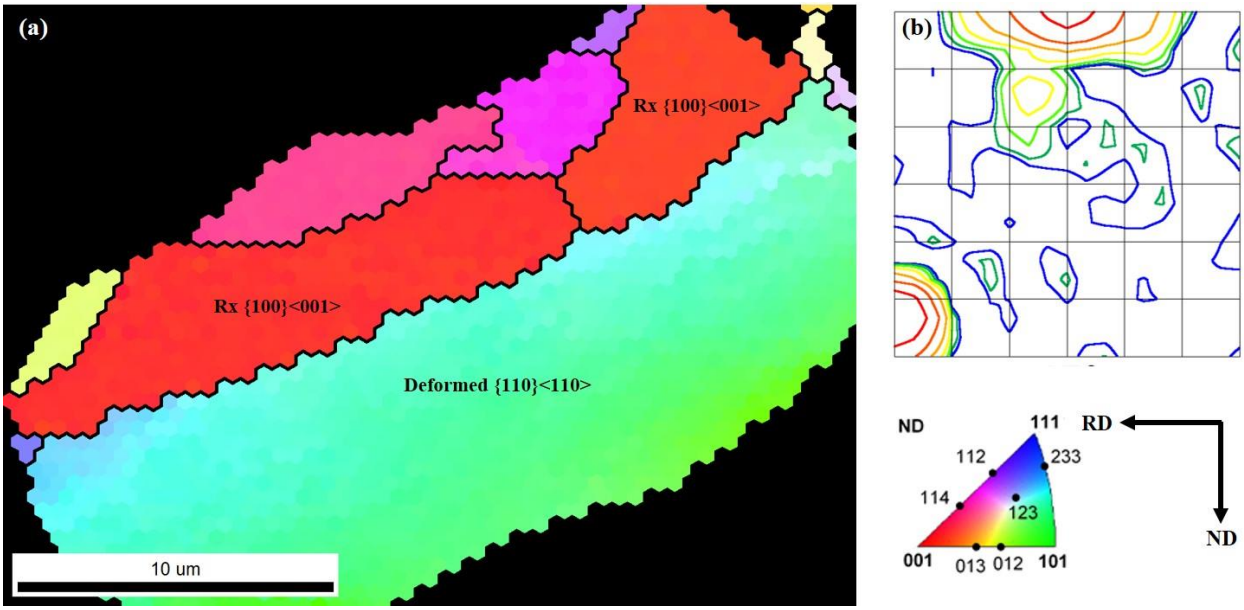

Fig. 3.18. Example of the nucleation of the cube grains at grain boundary of a rotated Goss grains during partial recrystallization of a 2.8% Si steel after inclined cold rolling: (a) EBSD IPF map, (b) φ_2 =45° section of the ODFs.

3.4 Discussion

It was mentioned before that the ideal cube texture was extremely difficult to be produced in the final electrical steel sheets using conventional rolling and annealing procedures. Many researchers [20-24] have developed unconventional processing techniques in order to promote the formation of this texture or other orientations along the θ-fibre (<100>//ND). To form the cube nuclei during recrystallization, volumes of the cube orientation must exist within the deformed grains, either at the grain boundaries or within the shear bands. The formation of these cube volumes is believed to be closely related to the fragmentation of the crystals during plastic deformation.

One possible origin of the cube volumes for nucleation during annealing was the fragmentation of the cube grains during cold deformation, i.e. in order to form the final recrystallization cube

texture, the initial texture before cold rolling should contain cube orientation. Similar to the formation mechanisms of the Goss texture during primary recrystallization [10-12], the fragmentation of the cube grain during plane-strain compression leaves traces of the original cube orientation at the grain boundaries. These undeformed cube volumes have low stored energy and form high-angle boundaries with respect to their deformed neighbours. During annealing, they can nucleate and grow to the deformed matrix (Fig. 3.11). The experiments conducted in this research have shown that by conventional rolling, the cube texture can only recrystallize in the final sheet at the grain boundaries (Fig. 3.11). This was only found in the 3.2% Si steel and not in the 2.8% Si steel, which may be due to the absence of the cube orientation in the 2.8% Si steel after hot band annealing.

Another origin of the cube recrystallization texture is the cube volumes within the shear bands of the rotated Goss grains, as have been shown in the incline rolled 2.8% Si steel (Fig. 3.16). After inclined cold rolling, a large number of the rotated Goss grains were found in the microstructure and numerous shear bands were formed at 20°~25° to the rolling direction. Shear bands are regions of plastic instability in a material. Dillamore et al. [14] has attributed the formation of shear bands to geometric softening of the crystal. The condition of crystal instability is given by:

$$\frac{1}{\sigma}\frac{d\sigma}{d\varepsilon} \leq 0 \tag{3.1}$$

where σ is the stress and ε is the strain. Geometric softening is given by the following condition

$$\frac{dM}{d\varepsilon} \leq 0 \tag{3.2}$$

where M is the Taylor factor of a given orientation. Geometric hardening would occur if $dM/d\varepsilon$ is positive.

During rolling, the material's resistance to plane strain compression increases due to geometric hardening and work hardening. However, grain boundaries make homogenous deformation essentially impossible, thus the strain is restricted in inclined bands, resulting in local geometric changes within the grain. This is usually accompanied by changing the crystal orientation within the shear bands, such that the resistance to deformation in these local regions is much less than the rest of the grain [14].

Crystal plasticity calculations have been used to demonstrate that the rotated orientations within the shear bands exhibit a lower Taylor factor than the surrounding orientation for the {111}<112> orientations [18]. It is well known that the shear bands within the {111}<112> grains have crystallites oriented towards the Goss orientation and thus act as preferential nucleation sites for the Goss nucleation during recrystallization. By analogy, the shear bands formed inside the rotated Goss grains would have a lower Taylor factor than the surrounding orientation, i.e., geometric softening. This can be demonstrated by calculating the Taylor factors using full constraint Taylor model for all possible orientations and superimposing them on the φ_2 =45° section of the ODFs as shown in Fig. 3.19. In this calculation the {110}<111>, {112}<111> and {123}<111> slips were taken into account for the deformation of the bcc crystals, corresponding to a pencil glide. Since the rotated Goss has the highest resistance to plane strain compression due to the highest Taylor factor of all the orientations (M=4.24), it is an ideal crystal orientation for the formation of shear bands to lead to geometric softening. The formation of the cube orientation inside the shear bands lowers the Taylor factor from 4.24 (rotated Goss) to 2.45 (cube).

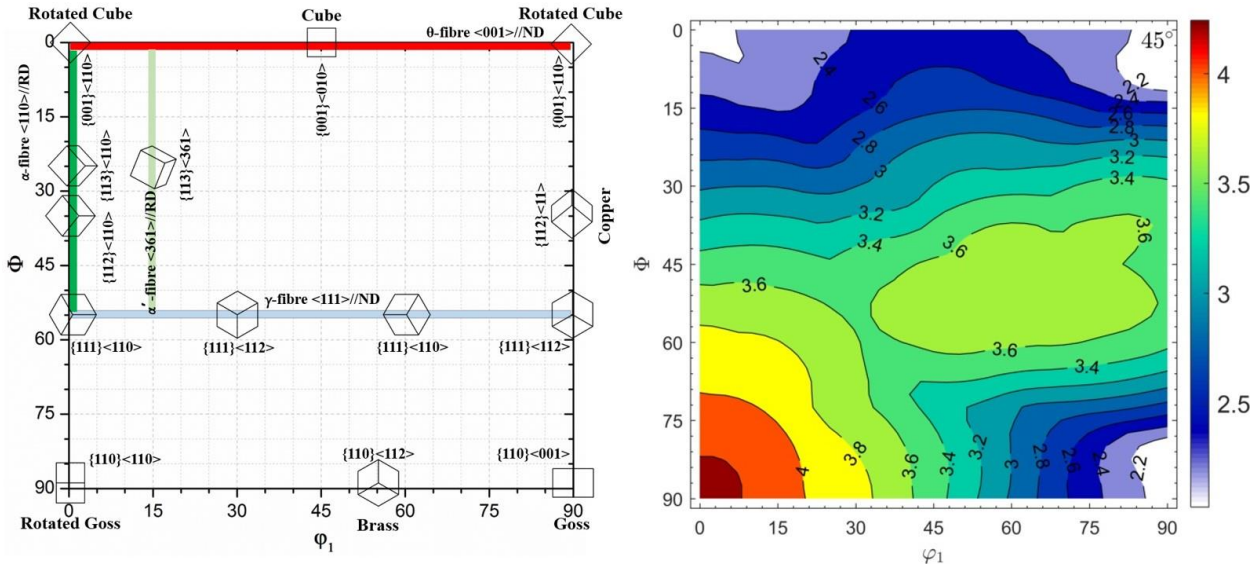

Fig. 3.19 The calculated Taylor factors (under plane strain compression) superimposed on the φ_2 =45° section of the ODFs (Bunge notation).

To further illustrate this point, the change of the Taylor factor with the second Euler (Bunge notation) angle (Φ) is plotted Fig. 3.20. The rotated Goss orientation is defined by the three Eulerian angles {90°, 45°, 0°} and the cube orientation {90°, 0°, 0°} on the Φ_2=0° section . A rotation of 45° around the TD or [010] (Φ) will bring the rotated Goss to the cube orientation. Due to cubic symmetry, this rotation could be either positive or negative leading to the symmetrically equivalent cube orientations {0°, 0°, 0°} or {90°, 0°, 0°}. This gives rise to a fishbone like structure due to the two symmetrically inclined shear bands [16]. It is seen that as the Φ angle changes from Φ=45° to Φ=0°, the Taylor factor decreases gradually, i.e. geometric softening occurs. It can also be seen that the minimum Taylor factor is obtained when the grain orientation changes from rotated Goss to cube. Further rotation away from the cube is considered energetically unfavourable and would result in geometric hardening rather than softening.

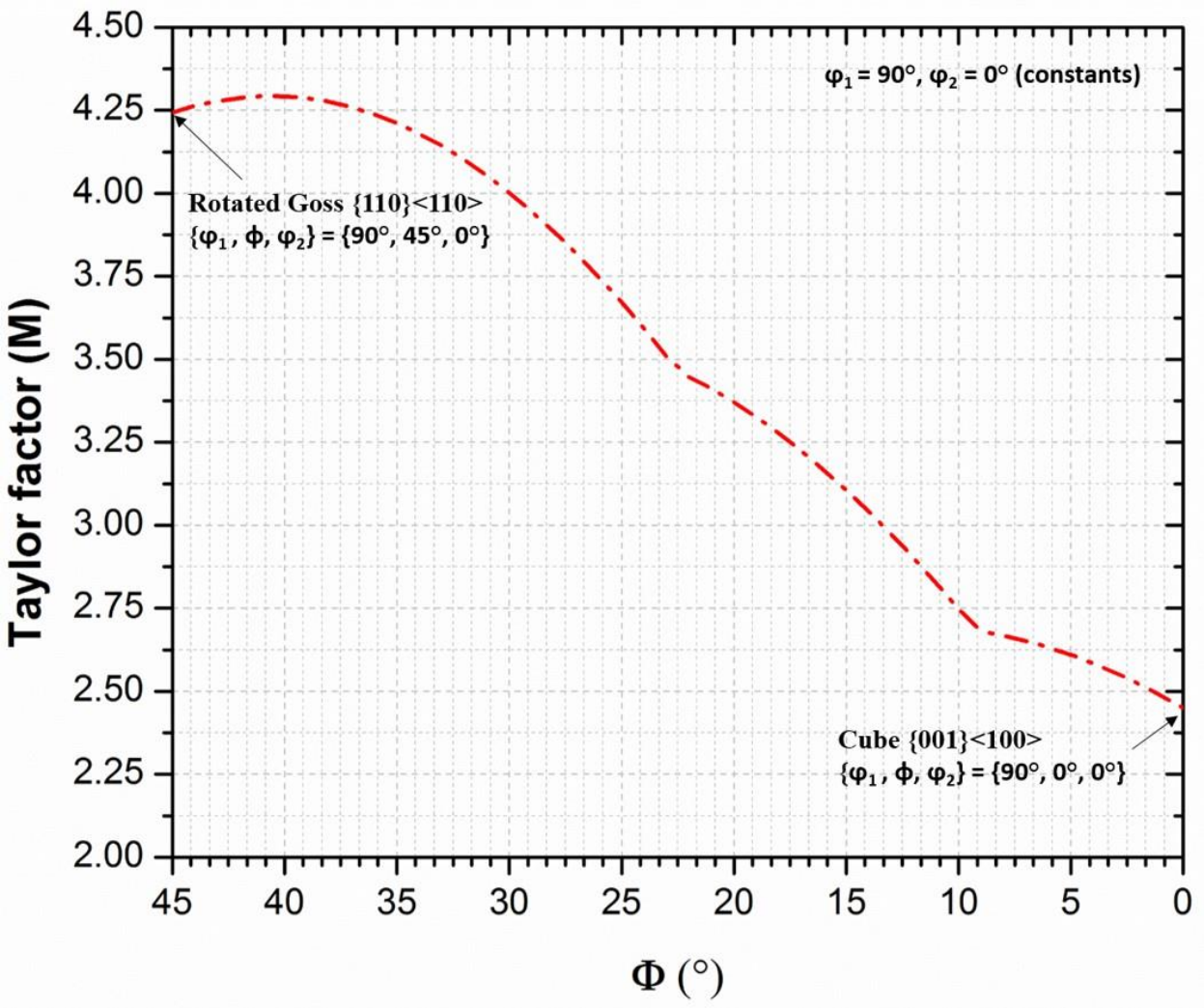

Fig. 3.20. The change of the Taylor factor (M) when the rotated Goss orientation changes to the cube.

Nucleation of new grains during annealing occurs at high stored energy sites such as grain boundaries, shear bands, microbands, deformation twins as well as precipitates [8, 10]. It is thus vital to control the heterogeneities within the material in order to preferentially nucleate certain crystal orientations during the annealing process. It is generally believed that the orientation of the nucleus is the same as the residual volume that has been left behind during heterogeneous deformation. Nevertheless, controversy still exists when explaining the recrystallization textures

in different materials under different conditions. For example, the nucleation of the Goss texture in the shear bands of {111}<112> grains has been attributed to the Goss crystallites having the sharpest lattice curvature as well as having a low dislocation density locally [10, 15, 16]. Park, Jong-Tae, and Jerzy A. Szpunar [12] suggested that the formation of the Goss grains in the shear bands of {111}<112> deformed grain is a clear indication of oriented nucleation. Nguyen-Minh et al. [18] reported that the nucleation of the cube texture inside the rotated Goss shear bands could be facilitated by the fast rotation rate which results in sharp lattice curvatures. They found that the cube orientation exhibits the largest lattice curvature within the shear bands of the rotated Goss grain. In this paper it was shown that the cube texture can indeed recrystallize in the shear bands as illustrated in Fig.3.16 and Fig. 3.17. The growth of the cube orientation after nucleation in the shear bands is further facilitated by the high angle grain boundary between the cube orientation and its surrounding matrix.

3.5 Conclusions

i. The cube texture is present during hot rolling in fragmented grains in the central region of the plate, as well as in the recrystallized grains in the top region.

ii. During hot band annealing, the cube texture is significantly reduced in volume fraction in the 2.8% Si steel, while few grains survived in the 3.2% Si steel.

iii. During cold rolling the 2.8% Si steel had a very small volume fraction of the cube orientation inside the shear bands of deformed rotated Goss grain. On the other hand, the 3.2% Si had the cube orientation preserved at the grain boundaries (fragmented grain), as well as in heavily deformed regions adjacent to the rotated Goss.

iv. During recrystallization, the cube orientation nucleated at the grain boundaries in the 3.2% Si steel, and these nuclei formed high angle boundaries with respect to the surrounding matrix.

v. Inclined rolling clearly demonstrated the formation of the cube texture inside the shear bands, microbands as well as the grain boundaries of the deformed rotated Goss grains.

vi. The development of the cube volumes inside the shear bands of the rotated Goss was due to geometric softening, resulting in lowering the Taylor factor from 4.24 (for rotated Goss) to 2.46 (for the cube).

vii. The heavily deformed shear bands acted as preferential nucleation sites for the cube orientation during primary recrystallization. This was explained using oriented nucleation theory as well as the result of high lattice curvature of the cube orientation.

References

1. Cullity, B. D., & Graham, C. D. (2011). Introduction to magnetic materials. John Wiley & Sons.

2. Chen, C. W. (2013). Magnetism and metallurgy of soft magnetic materials. Courier Corporation.

3. Fiorillo, F., Bertotti, G., Appino, C., and Pasquale, M.: Soft magnetic materials. In Wiley Encyclopedia of Electrical and Electronics Engineering, Peterca, M., ed. (Wiley, Hoboken, New Jersey, 2016)

4. Moses, A. J. (1990). Electrical steels: past, present and future developments. IEE Proceedings A (Physical Science, Measurement and Instrumentation, Management and Education), 137(5), 233-245.

5. Lyudkovsky, G., Rastogi, P. K., & Bala, M. (1986). Nonoriented electrical steels. JOM, 38(1), 18-26.

6. Mehdi, M., He, Y., Hilinski, E. J., & Edrisy, A. (2017). Effect of skin pass rolling reduction rate on the texture evolution of a non-oriented electrical steel after inclined cold rolling. Journal of Magnetism and Magnetic Materials, 429, 148-160.

7. Petrovic, D. S. (2010). Non-oriented electrical steel sheets. Materiali in tehnologije, 44(6), 317-325.

8. Humphreys, F. J., & Hatherly, M. (2012). Recrystallization and related annealing phenomena. Elsevier.

9. Kestens, L., & Jacobs, S. (2008). Texture control during the manufacturing of nonoriented electrical steels. Texture, Stress, and Microstructure, 2008.

10. Ushioda, K., & WB, H. (1989). Role of shear bands in annealing texture formation in 3% Si–Fe (111)[112] single crystals. ISIJ International, 29(10), 862-867.

11. Haratani, T., Hutchinson, W. B., Dillamore, I. L., & Bate, P. (1984). Contribution of shear banding to origin of Goss texture in silicon iron. Metal Science, 18(2), 57-66.

12. Park, J. T., & Szpunar, J. A. (2003). Evolution of recrystallization texture in nonoriented electrical steels. Acta Materialia, 51(11), 3037-3051.

13. Dorner, D., Zaefferer, S., & Raabe, D. (2007). Retention of the Goss orientation between microbands during cold rolling of an Fe3% Si single crystal. Acta materialia, 55(7), 2519-2530.

14. Dillamore, I. L., Roberts, J. G., & Bush, A. C. (1979). Occurrence of shear bands in heavily rolled cubic metals. Metal Science, 13(2), 73-77.

15. Barnett, M. R. (1998). Role of in-grain shear bands in the nucleation of< 111>//ND recrystallization textures in warm rolled steel. ISIJ international, 38(1), 78-85.

16. Murakami, K., Morishige, N., & Ushioda, K. (2012). The effect of cold rolling reduction on shear band and texture formation in Fe-3% Si alloy. In Materials Science Forum (Vol. 715, pp. 158-163). Trans Tech Publications.

17. Vanderschueren, D., Yoshinaga, N., & Koyama, K. (1996). Recrystallisation of Ti IF steel investigated with electron backscattering pattern (EBSP). ISIJ international, 36(8), 1046-1054.park

18. Nguyen-Minh, T., Sidor, J. J., Petrov, R. H., & Kestens, L. A. I. (2012). Occurrence of shear bands in rotated Goss ({1 1 0}< 1 1 0>) orientations of metals with bcc crystal structure. Scripta Materialia, 67(12), 935-938.

19. Toth, L. S., Jonas, J. J., Daniel, D., & Ray, R. K. (1990). Development of ferrite rolling textures in low-and extra low-carbon steels. Metallurgical Transactions A, 21(11), 2985-3000.

20. Kovac, F., Dzubinský, M., & Sidor, Y. (2004). Columnar grain growth in non-oriented electrical steels. Journal of Magnetism and Magnetic Materials, 269(3), 333-340.

21. Yoshinaga, N., Kestens, L., & De Cooman, B. C. (2005). α→ γ→ α transformation texture formation at cold-rolled ultra low carbon steel surfaces. In Materials Science Forum (Vol. 495, pp. 1267-1272). Trans Tech Publications.

22. Tomida, T. (1996). A new process to develop (100) texture in silicon steel sheets. Journal of Materials Engineering and Performance, 5(3), 316-322.

23. He, Y., & Hilinski, E. J. (2016). Texture and magnetic properties of non-oriented electrical steels processed by an unconventional cold rolling scheme. Journal of Magnetism and Magnetic Materials, 405, 337-352.

24. He, Y., Hilinski, E., & Li, J. (2015). Texture evolution of a non-oriented electrical steel cold rolled at directions different from the hot rolling direction. Metallurgical and Materials Transactions A, 46(11), 5350-5365.

Chapter 4 The Origins of the Goss Orientation in Non-oriented Electrical Steel and the Evolution of the Goss Texture during Thermomechanical Processing

4.1 Introduction

Electrical steels (also known as silicon steels) are indispensable soft magnetic materials for the generation, transportation and conversion of electricity [1-6]. While *grain-oriented* electrical steels were widely used in transformers, *non-oriented* silicon steels were the material choice for electric motors and generators. Almost all the current technologies used to process grain-oriented electrical steels have been developed based on the method patented by Goss [2,7] in 1934, i.e. producing the so-called Goss ({011}<100>) texture in the final steel sheets. Although technically the developed processes were successful in producing the desired Goss texture for transformers, the theory behind the formation of the Goss orientation during thermomechanical processing is still under debate. On the other hand, although the Goss texture is not necessarily an ideal orientation for non-oriented electrical steels (where the <100> crystal axes are desired in all the directions in the sheet plane, instead of only in the rolling direction as in grain-oriented electrical steel), the Goss texture does frequently appear during steel processing [1-6]. Thus, it is of interest to study the origin and the evolution of this orientation in non-oriented electrical steel for better control of the final texture.

The origin of the Goss ({110}<001>) orientation in grain-oriented electrical steel has been a subject of many studies [8-11] since this is the texture of the finished product that results in high magnetic induction and low magnetic loss. It has been shown that the Goss orientation is first developed in the hot rolling process near the surfaces of the steel plate due to the shear strain

induced by the friction between the rolls and the steel [9]. However, the Goss texture is not stable under plane-strain compression, thus only a small fraction (around 1% volume fraction) is retained after cold rolling [8, 9]. Primary recrystallization allows the Goss grains to recrystallize, resulting in a slight increase in the overall intensity. Secondary recrystallization in grain-oriented electrical steels causes the Goss grains to grow abnormally, leading to a sharp Goss texture and very large grain sizes (i.e. in the order of centimetres) in the final sheet [10].

Dorner et al. [9] identified two origins of the Goss orientations in a cold-rolled Fe-3.2% Si *single crystal*. The first type (Type I) appeared in the shear bands of the deformed matrix, and the second type (Type II) was observed within microbands of the deformed grains. On the other hand, Ushioda and Hutchinson [11] reported that two shear bands (a wide one ~35° to RD and a narrow one ~17° to RD) were observed after cold rolling of 3% Si-Fe {111}<112> single crystals. The Goss orientation (with some dispersion) nucleated preferentially along and within the shear bands and eventually grew into the surrounding matrix. Park and Szpunar [8] illustrated that the Goss grains in a recrystallized non-oriented electrical steel nucleated within shear bands in the {111}<112>, {111}<110> and {112}<110> deformed grains. The recrystallized Goss grains have a high-angle grain boundary (~30°<110>) with respect to the surrounding deformed matrix, which may give them an advantage to preferentially grow during early stage of annealing. This agrees with the oriented growth theory, which assumes that high-angle grain boundaries exhibiting a specific orientation relation like ~30°<110> in bcc metals have a faster migration rate than other boundaries [10, 12-14]. It should be noted that this mechanism is still highly controversial among researchers, thus over-reliance or exaggerated confidence should be avoided [15].

In this research, the origin and the evolution of the Goss orientation in a 2.8 wt% Si non-oriented electrical steel was investigated by EBSD. The formation of this orientation during hot

rolling, hot band annealing, cold rolling and final annealing was analyzed against existing theories. The rotation of the Goss orientation during cold rolling was tracked using a quasi *in situ* EBSD technique, in which the rotations of individual grains during plane-strain compression were traced. In addition to the known origins of the Goss orientation observed in cold-rolled electrical steels, a new origin of the Goss orientation is observed at the grain boundaries between {111}<112> and {113}<361> grains. The volume fraction change of the Goss orientation during each stage of the processing is also evaluated, which shows the evolution of the Goss texture during steel processing.

4.2 Material and Methods

A non-oriented electrical steel with a composition (wt%) of: 2.8 Si, 0.52 Al, 0.3 Mn, 0.01 P and 0.003 C was melted in a vacuum furnace and cast into a 200 mm × 200 mm (cross section) ingot. It was then reheated to a temperature of ~1038°C and hot rolled to a thickness of ~2.5 mm in a reversing rolling mill. The steel plates were pickled using an HCl solution at a temperature of 82°C to remove surface oxides. The hot band was subsequently annealed in a 100% dry hydrogen atmosphere at 840°C for ~60 hours. The annealed plates were then cold rolled to a final thickness of ~0.5 mm. The cold-rolled sheets were finally annealed at 750°C in an argon-protected atmosphere. In order to investigate the nucleation of the Goss grains, a few samples were annealed for 5 minutes and quenched in water to obtain partially recrystallized microstructure. Other samples were annealed for 10 minutes to obtain fully recrystallized structure. Microtexture and microstructure characterization was conducted on the normal direction (ND)-rolling direction (RD) sections of the samples in a field emission gun scanning electron microscope (FEG-SEM) equipped with an OIM 6.2 EBSD system. A tolerance of 20° was allowed for orientation

calculations, i.e. for volume fraction or the isolation of specific grains. The step size used for the EBSD scans ranged from 0.25 µm to 2 µm.

In order to investigate the deformation characteristics of the Goss grains during cold rolling, a quasi *in situ* EBSD technique was utilized to track the rotations of individual grains during plane-strain rolling. As shown in Fig. 4.1, a piece (2.5 cm × 1 cm) of the non-oriented electrical steel after hot rolling and annealing was cut from a steel plate. One surface (ND-RD plane) of the steel piece was ground and polished using conventional metallographic methods, and a final polishing step using a 0.05 µm colloidal silica suspension was applied to prepare the surface for EBSD scans. An area was then marked by micro-hardness indents and the initial grain orientations of the area were obtained from EBSD scan. The scanned sample was then inserted into a larger sample holder made of the same material (i.e. the same thickness and same processing history), which was then subjected to cold rolling. After each rolling reduction, the same surface was slightly polished using the colloidal silica suspension, and the same area was examined again under EBSD, which enabled the tracking of the orientation changes of individual grains under rolling. The evolution of the Goss orientation during cold rolling was then evaluated.

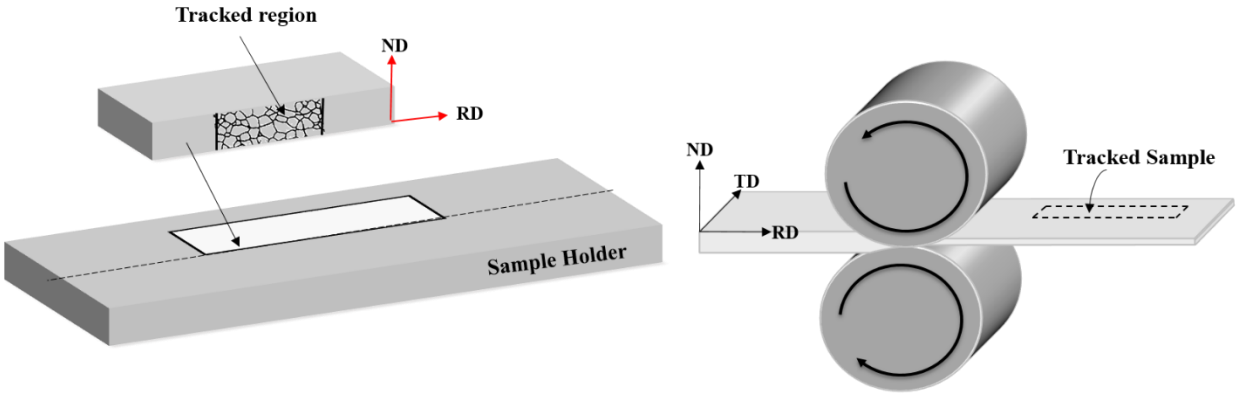

Fig. 4.1. Experimental setup for the tracking of individual crystal rotation during cold rolling.

4.3 Results and Discussion

4.3.1 Hot Rolling

Fig. 4.2 shows the cross-section microstructure, crystal orientations and texture of the steel after hot rolling. The grain morphology, size and orientation are significantly different across the thickness of the plate (Fig. 4.2a). The surface region is ~800 μm thick on each side and essentially consists of recrystallized grains of {110} (green) and {112} (pink-purple) orientations, while the central region is mainly composed of elongated {100} (red) and {111} (blue) orientations. As a result, the textures of the different regions (Fig. 4.2b) are significantly different, i.e. Goss ({110}<001>), brass ({110}<112>) and copper ({112}<111>) in the surface regions, and α- (<110>//RD) and γ- (<111>//ND) fibres in the central region. The surface texture is formed due to the shear strain resulting from the friction between the rolls and the steel plate during hot rolling. The texture in the central region is very similar to typical bcc texture after plane-strain compression (hot or cold rolling). From the isolated Goss orientations shown in Fig. 4.2c, it is seen that the Goss grains form in both the recrystallized and deformed microstructures across the thickness. Large elongated Goss grains are observed near the interface between the surface and the central regions. It is noted that in the central deformed region only some small traces of the Goss grains are found (e.g. A, B, C and D in Fig. 4.2c). The overall volume fraction of the Goss grains after hot rolling is ~10%.

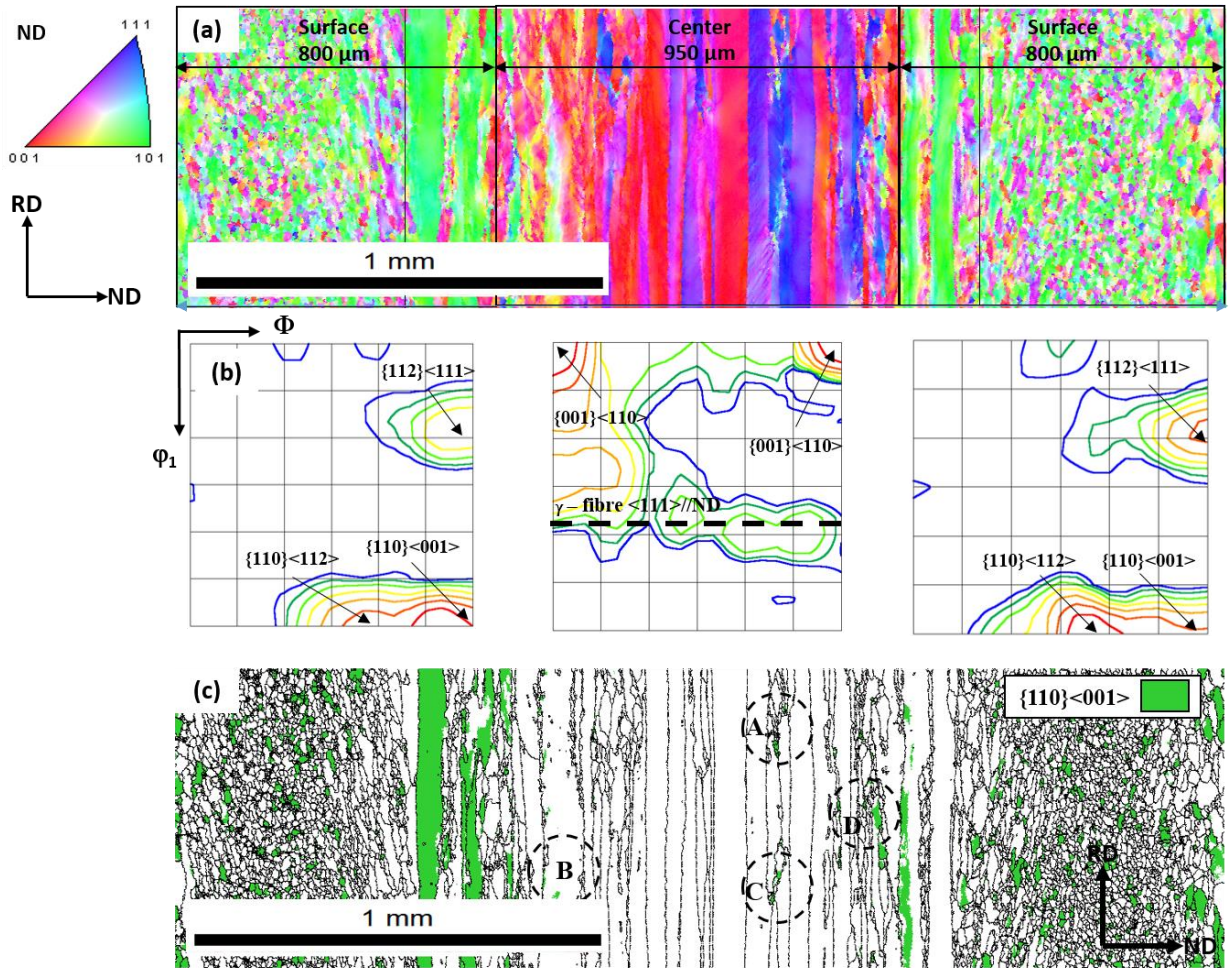

Fig. 4.2. Hot rolling texture and microstructure of a 2.8 wt% Si non-oriented electrical steel: a) inverse pole figure map showing different regions across the thickness of the plate, b) orientation distribution functions (φ_2 = 45° sections, Bunge notation) of different regions, and c) location of the Goss grains in the hot-rolled plate (with a 20° tolerance).

Fig. 4.3 shows a fine scan of the surface region using a small step size of 0.25 µm. It is clearly seen that large elongated Goss grains appear in the top surface region (Region Z), where dynamically recrystallized crystals were simultaneously deformed during hot rolling. Elongated Goss grains also appeared in the transition area (Region X) between the surface and the central regions. The transition area may still undergo shear deformation, which results in the formation of

the Goss orientation, but the shear strain is not large enough to enable the recrystallization of these Goss grains. In between these two regions (Region Y), the Goss grains are recrystallized and equiaxed. The total volume fraction of the Goss grains in the surface region is ~30%, which is much higher than the overall volume fraction (~10%) across the thickness.

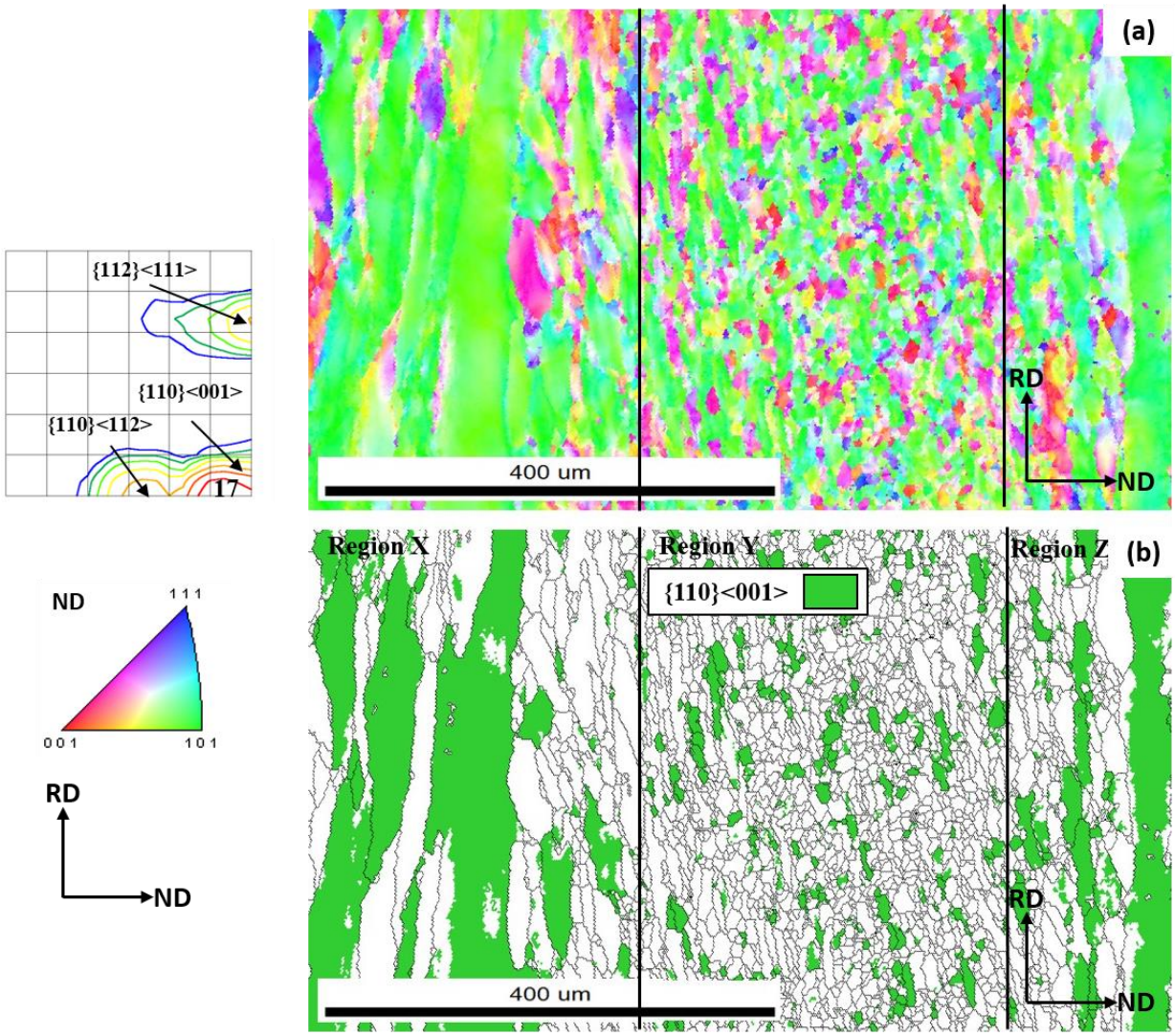

Fig. 4.3. Surface region (top of 1050 µm of the sample) of hot rolled steel: a) inverse pole figure map and the texture, and b) location of the {110}<001> orientation showing both deformed and equiaxed Goss grains.

4.3.2 Hot Band Annealing

After annealing at 840°C for ~60 hours, a considerable amount (~9 %) of *recrystallized* Goss grains (Fig. 4.4) is observed across the thickness of the steel plate (not just the surface region). These Goss grains are the result of the nucleation and grain growth during the long time holding of the sample in a relatively high temperature. Apparently, the originally large amount of Goss grains has disappeared after annealing, especially the elongated Goss grains at the surface and the transition areas. It should be noted that, the preferred nucleation sites for the Goss orientation in (cold) deformed non-oriented electrical steel were believed to be the shear bands of the {111}<112>, {111}<110> or {112}<110> grains. However, in the hot-rolled steel, no shear bands was observed in the deformed microstructure (central region in Fig. 4.2a). Thus the formation of the Goss orientations in the central region is believed to be the nucleation and growth of the traces of Goss grains (Fig. 4.1c) initially existing in the hot-rolled microstructure. It is also noted that, despite the long annealing time, the banded structures in the hot-rolled plate and the difference in texture across the thickness still exist after hot band annealing. The surface region still has a <110>//ND texture (including brass and Goss) and a copper component, while the central region is dominated by a {001}<120> texture together with an α-fibre and a γ-fibre.

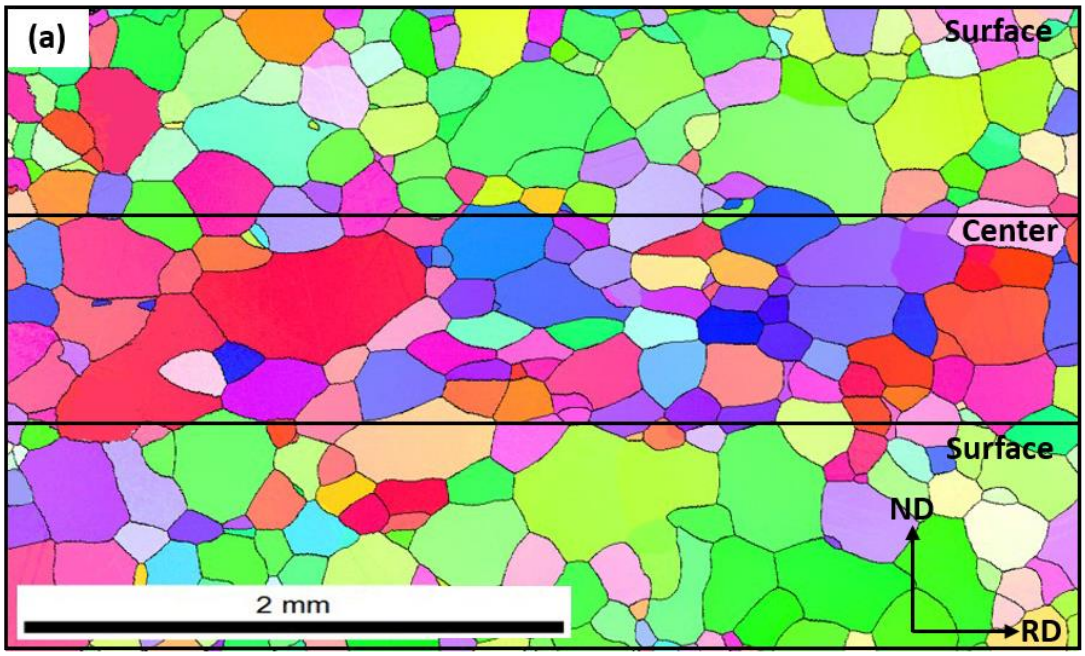
(a)
Surface
Center
Surface
ND
RD
2 mm

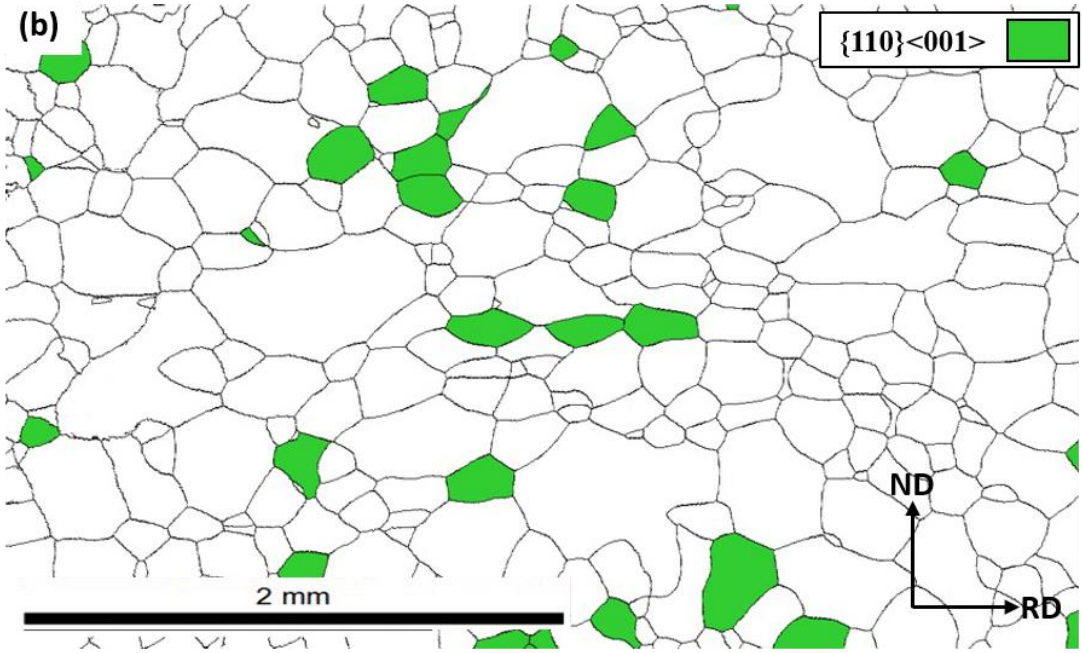
(b)
{110}<001>
ND
RD
2 mm

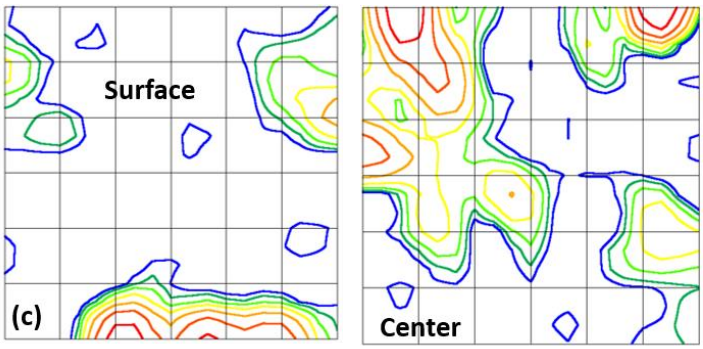
Surface
(c)
Center

Fig. 4.4. Microtexture and microstructure after hot rolling and annealing: a) inverse pole figure map, b) Goss grains present within the microstructure, and (c) textures at the surface and center regions.

4.3.3 Cold Rolling

Fig. 4.5 shows the rotation of a Goss grain during cold rolling under different thickness reductions. It is seen that under plane-strain compression, not only was the shape of the grain changed (elongated), but the orientation of the crystal was also altered. With the increase of the reduction rate from 10% to 20%, the maximum deviation of the final orientations from the Goss orientation changes from ~13° to ~22°, and the rotation was 8° to 15° around the <110> axis (due to the {110}<111> and {112}<111> slip systems). The apparent increase in grain area was probably due to the fact that the slight polishing before EBSD scan after each rolling reduction shifted the sectioning plane, which resulted in a different cross-section area of the grain. It is noted that cold rolling rotates the Goss orientation towards the {11 11 8}<4 4 11> and {111}<112> orientations. The {11 11 8}<4 4 11> orientation is the theoretically stable orientation of the Goss after plane-strain compression [10], which is slightly deviated (~8°) from the {111}<112> orientation [9, 10]. It is also noted that, the rotation of the crystal occur gradually, i.e. when the reduction rate was small (10%), about 35% of the crystal was rotated; when the reduction rate increased to 20%, about 90% of the crystal was rotated.

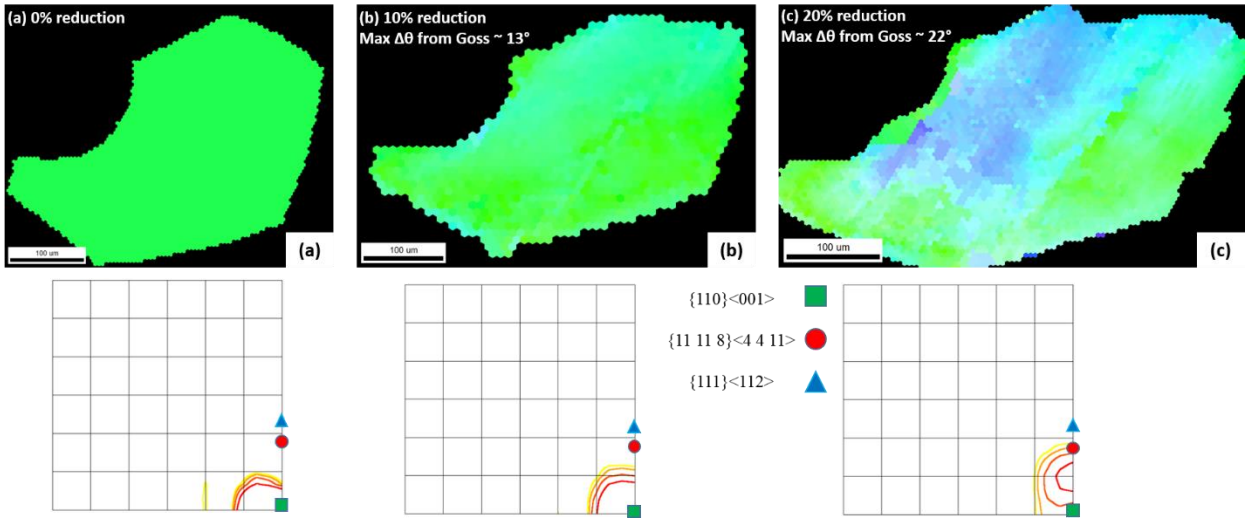

Fig. 4.5. The rotation of a Goss grain during cold rolling: a) before rolling, b) after 10% reduction (first pass), and c) after 20% reduction (second pass). The deformation rotates the Goss grains about the <110> axis toward {11 11 8}<4 4 11> and {111}<112>.

Apparently, the rotation of the Goss grain during cold rolling significantly reduces the amount of Goss orientations. Thus, after cold rolling, the volume fraction of the Goss grains was reduced to only ~1%. Examples of some discrete Goss grains observed within the cold-rolled steel are shown in Fig. 4.6. Depending on the location where they are observed, different types of Goss grains can be discerned. An example of the first type Goss grain (Type I) is shown in Fig. 4.6c, where a small Goss grain (green) and its neighbouring grains with two distinguished colors (blue and red) are shown in the inverse pole figure (IPF) map. The Goss grain is observed between two {111}<112> grains having symmetrically equivalent orientations, i.e. $\{111\}[\bar{1}\bar{1}2]$ (blue) and $\{111\}[1\bar{2}1]$ (red). The formation of this type of Goss grains can be explained by the transition band model proposed by Dillamore et al. [16] based on the study of single crystals, where it was

assumed that a residue of an initial metastable orientation was retained if the orientation splits into two symmetrically oriented grains [16]. Based on this model, during plane-strain deformation, the metastable Goss grain (originated from the annealed hot band, Fig. 4.4) splits into two symmetrical orientations: $\{111\}[\bar{1}\bar{1}2]$ and$\{111\}[1\bar{2}1]$, leaving traces of the original grain behind. The splitting of the Goss grain into the {111}<112> grains was due to the rotation of the {110}<001> orientation around the transverse direction (TD, or the <110> direction in the crystal). This rotation was caused by the shear deformation near the surfaces of the material during cold rolling. It has already been shown by Dorner et al [9] that very small deviations from the Goss orientation is unstable under plane-strain deformation, and it rotates ~35° around the TD to give rise to the two symmetrical $\{111\}[\bar{1}\bar{1}2]$ and $\{111\}[1\bar{2}1]$ orientations with Euler angles (φ_1, ϕ, φ_2) of (90°, 54.7°, 45°) and (30°, 54.7°, 45°), respectively (Bunge's notation). The crystallographic relationship between the Goss orientation and the two {111}<112> orientations is shown in Rodrigues space in Fig. 4.6e, where it is clear that these two orientations have the same rotation angle (35.26°) but different rotation axes of the <110> type with respect to the Goss orientation (the origin of the Rodrigues space).

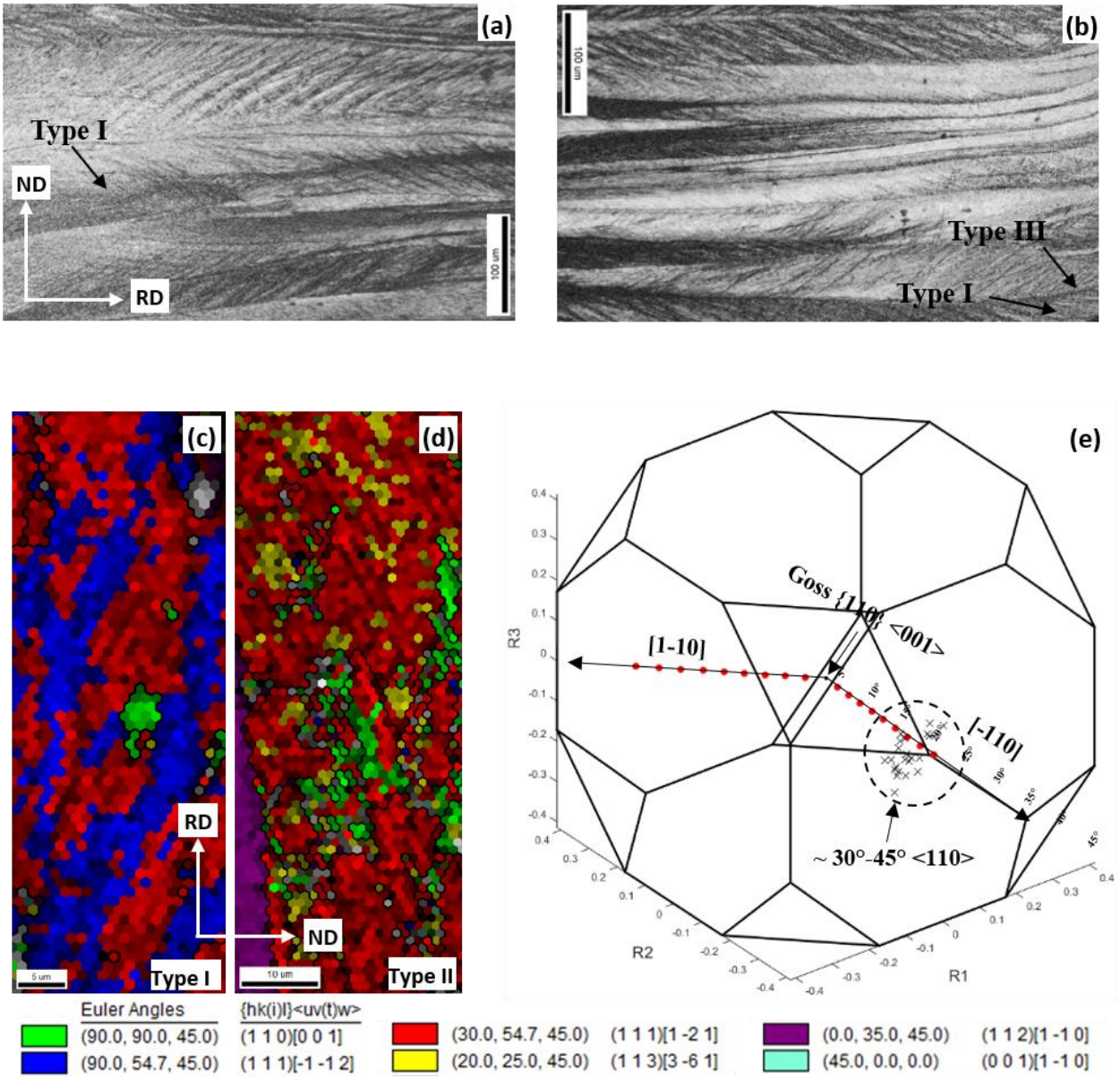

Fig. 4.6. Goss grains observed in a 2.8 wt% Si electrical steel after cold rolling: (a) and (b) image quality maps showing the contrast in dislocation density, (c) and (d) inverse pole figure maps showing the variation in grain orientations for Type I and Type II Goss grains, respectively, (e) Rodrigues space showing the misorientations between the Goss orientation and the {111}<112> neighbouring grains.

Examples of the second type of Goss orientation (Type II) are shown in Fig. 4.6d. These grains are embedded within one of the {111}<112> grains ($(111)[1\bar{2}1]$ in these examples), and the Goss grains are usually elongated and dispersed. Apparently, the formation of this type of Goss grains cannot be explained by the transition band model mentioned before. Dorner et al. [9] proposed that a rigid inclusion model can be used to explain it. The proposed model suggests that, although mathematically the exact {110}<001> is stable under perfect plane-strain deformation conditions due to the compensation of the two symmetrically equivalent {111}<112> orientations, small deviations from the perfect plane-strain conditions or from the exact {110}<001> orientation could significantly alter the deformation conditions, and force the Goss orientation to rotate into only one of the final stable orientations. In this case, a small volume of the Goss grain would have a different set of active slip systems from the surrounding matrix, i.e. the Goss grains within the deformed {111}<112> matrix can be considered as a rigid inclusion that has a net rotation of zero [9]. It should be noted that the above two types of Goss grains are very small in volume fraction and usually they are sparsely distributed in the shear bands or microbands *within* deformed grains. Ushioda and Hutchinson associated the formation of the Goss orientation with the sharpest lattice curvature within the shear bands, which can be applied successfully to the wide shear bands in {111}<112> but not the narrows ones [11].

In addition to the two types of Goss grains mentioned before, a new type of Goss grain (Type III) is observed in this study, i.e. *bands* of the Goss grains are found at the *grain boundaries* between deformed {111}<112> and {113}<361> grains (Fig. 4.7a). The {113}<361> orientation (yellow) is on the α*-fibre ({1 1 h} <1 2 1/h>) which is parallel to the α-fibre (<110>//RD) on the $\varphi_2 = 45°$ section of the orientation distribution function (ODF). Gobernado et al. [20] observed this orientation in deformed IF steel (60% cross-rolled), and attributed the formation of this orientation

to the fragmented α-fibre grains (especially {001}<110> orientations) due to inhomogeneous deformation and the formation of intra-grain deformation bands. In this research, the {113}<361> orientations (Fig. 4.7a) are observed within the {112}<110> grains (on the α-fibre), thus their formation may be explained by the fragmentation of the {112}<110> grains during deformation. Similar to the {111}<112> grains, there are also shear bands within the {113}<361> grains, which are inclined approximately 35° to the rolling direction. The image quality (IQ) map (Fig. 4.7b) and the kennel average misorientation (KAM) map (Fig. 4.7c) show that, at the grain boundaries between {111}<112> and {113}<361> where the Goss grains are observed, the density of geometrically necessary dislocations (GNDs) and thus, the stored energy, are high.

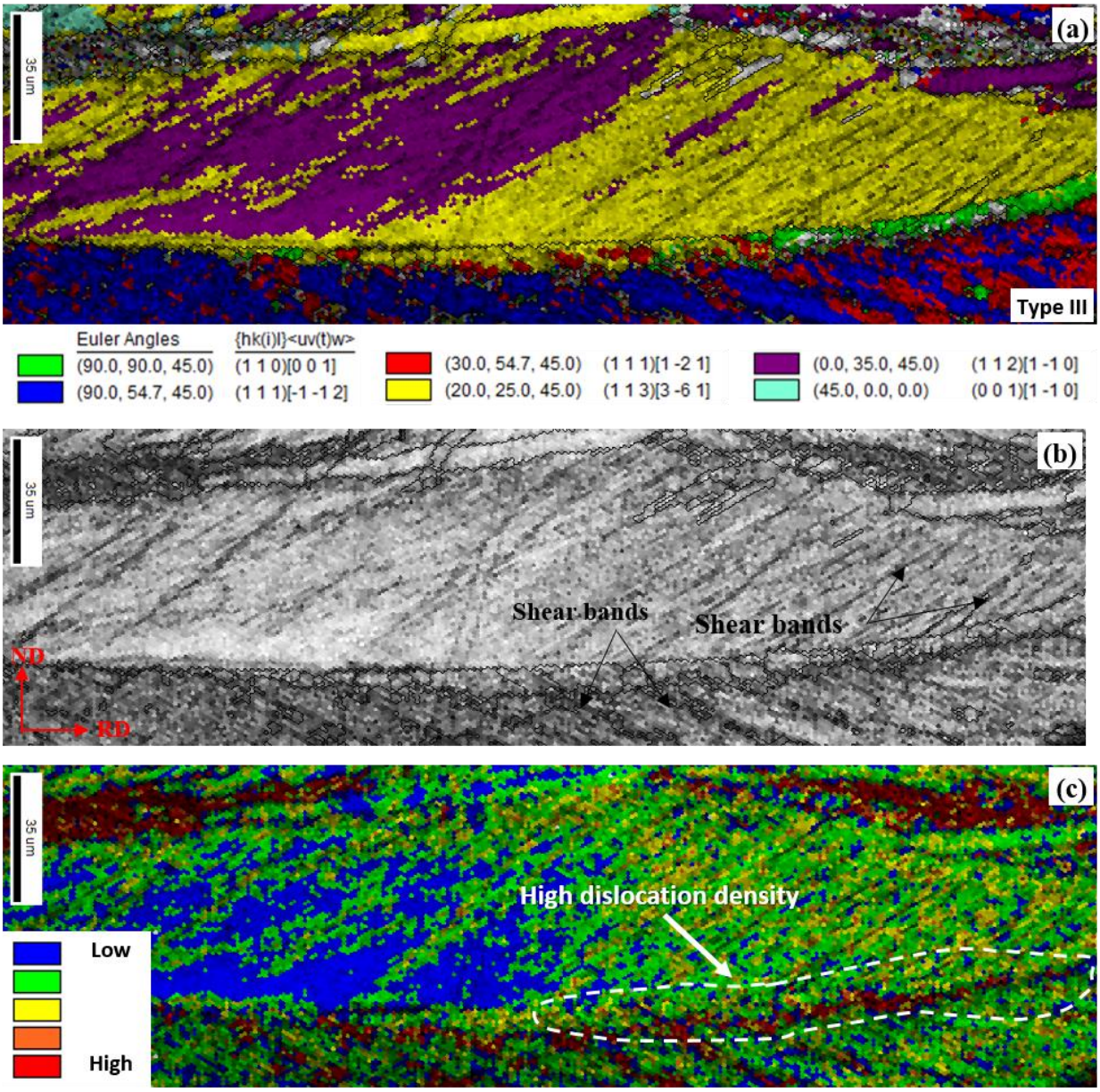

Fig. 4.7. Goss grains in a cold-rolled 2.8 wt% Si electrical steel: (a) IPF map showing the Type III Goss grains at the grain boundary, (b) image quality map illustrating the variation of dislocation density, and (c) kernel average misorientation map showing the inhomogeneity of deformation and the variation of stored energy.

The misorientations between the Goss grains and the surrounding {111}<112> and {113}<361> orientations are represented in Rodrigues space in Fig. 4.8a, taking the Goss orientation as the reference [20]. The magnitude of the Rodrigues vector between {110}<001> and {111}<112> is $\|\vec{\mathcal{R}}\| = 0.327$, while that between {110}<001> and {113}<361> is $\|\vec{\mathcal{R}}\| = 0.318$. It is seen that the misorientation angles (~36.2° and ~35.2°) between the {110}<001> and the two surrounding orientations ({111}<112> and {113}<361>) are essentially identical. In addition, the axes of both misorientations are approximately <110>, which means that the Goss grain at the {111}<112> and {113}<361> grain boundary has essentially the same crystallographic relationship with respect to its neighbours. The mechanism that forms this special misorientation can be described below using the transition band model [9].

It has been shown that, at high strains and due to inhomogeneity of deformation, the Goss grain may split into {111}<112> orientations upon plane-strain compression [9, 10], which gives rise to two symmetrically equivalent grains [9, 16], or to a single {111}<112> grain [9], leaving behind residual Goss orientations. The origin of the Type III Goss grains may also be explained using the transition band model [9], i.e. during plastic deformation, the original Goss grain may split into fragments that have the same misorientation relationship with respect to the original Goss orientation. In this case, the {113}<361> grains have a misorientation of ~35°<110> to the Goss grain, which is the same as the misorientation between the {111}<112> and {110}<001> grains. Thus, a part of the Goss orientation is retained while forming the two neighbouring grains with the same misorientation to the original grain. The identical misorientation between the two neighbouring grains and the Goss grain leads to a zero rotation because of the activation of different slip systems in the Goss grain (similar to [9]).

However, it should be noted that the above explanation is only a tentative induction about the origin of Type III Goss grains. This is due to the inexistence of any adequate theory accounting for the formation of the {113}<361> orientation during cold rolling, which means that the use of any crystal plasticity model would require highly exotic conditions to rotate the {110}<001> to {113}<361>. A summary of the governing conditions for the existence of Type III Goss grains is shown in Fig. 4.8b. There exists an approximately identical ~35°<110> relationship between the Goss orientation and its neighbouring {113}<361> and {111}<112> grains. Since the ~35°<110> misorientation has been reported [10, 24] to exhibit a high mobility, it could be the growth direction between the Goss grain and the surrounding deformed matrix.

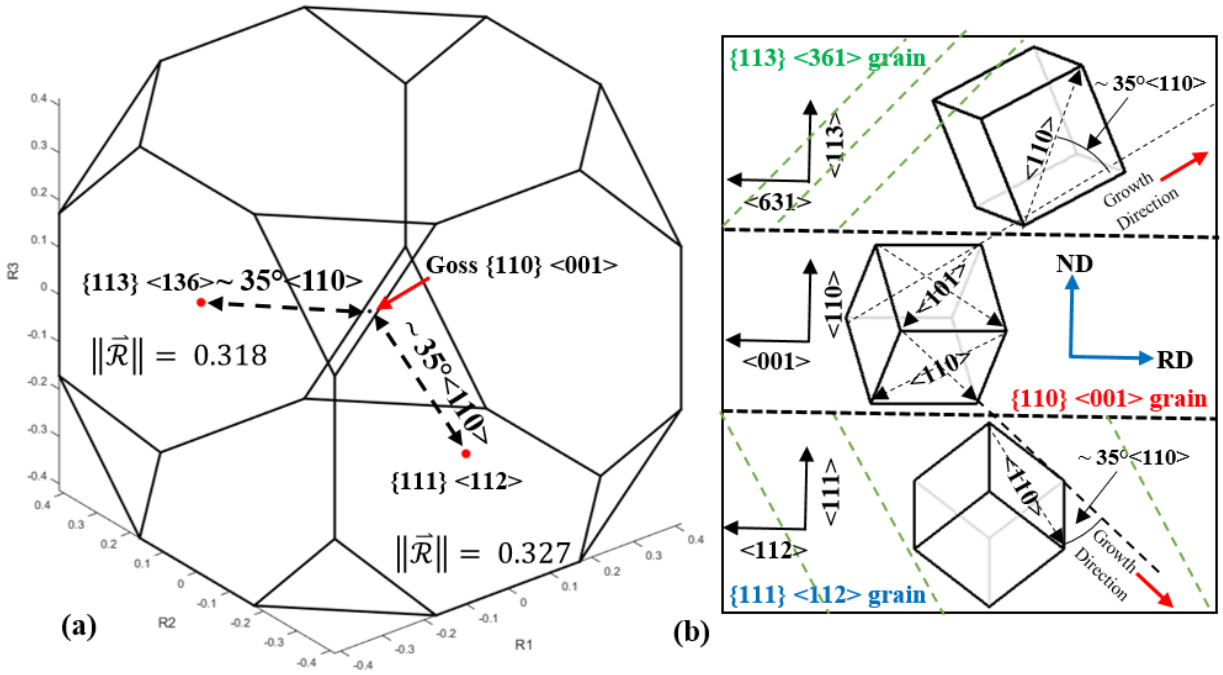

Fig. 4.8. Type III Goss orientation observed in a cold-rolled 2.8 wt% Si electrical steel: (a) Rodrigues space representation of Type III Goss orientation with respect to the deformed matrix, (b) a schematic illustration of the crystallographic relations between {110}<001> and its {113}<361> and {111}<112> neighbours.

4.3.4 Final Annealing

It has been shown that the first two types of Goss orientations (Types I and II) exist only inside the {111}<112> grains. Since Type I is located in a high stored energy region (shear bands), this would explain why the Goss grains recrystallize first during the annealing process [8, 9]. On the other hand, both types of Goss grains have a ~30°-45°<110> misorientation with respect to the surrounding matrix as seen from the Rodrigues space illustration (Fig. 4.6e), which is known to exhibit a high migration mobility. According to oriented growth theory, such a boundary will promote the growth of the Goss nuclei to the surrounding matrix (the {111}<112> grains).

Fig. 4.9 shows the microstructure and grain orientations after partial recrystallization (50%). It is seen that the Goss grains preferentially formed at the shear bands within the {111}<112> grains at angles ranging from 20° to 35° with respect to the rolling direction (RD). This has been explained in the literature as a direct result of the high mobility of ~35°<110> boundary between the {110}<001> and the {111}<112> deformed matrix (Fig. 4.6e) [8, 24]. These Goss grains belong to Types I and II as mentioned before. The volume fraction of the Goss grains increased from ~1% (after cold rolling) to ~8% after partial recrystallization. The Goss grains account for ~17% of all the *recrystallized* grains, which means that the Goss orientation is one of the favourable orientations during early recrystallization.

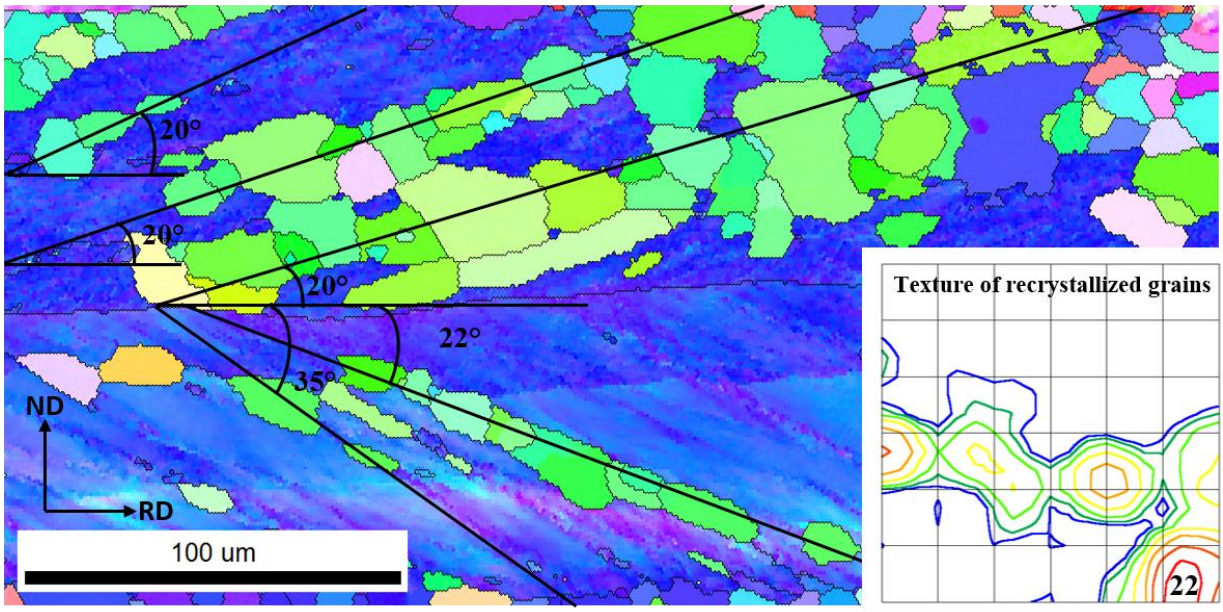

Fig. 4.9. Goss grains nucleating at the shear bands of the <111>//ND deformed grains after annealing at 750 °C for 5 minutes followed by water quenching. The Goss grains are formed at 20°-35° to the rolling direction (RD).

The Goss grains are also observed to nucleate from the elongated grain boundaries (those parallel to the rolling direction) as shown in Fig. 4.10. These Goss grains are closely clustered to each other, suggesting a common preferential nucleation site. They are formed parallel to the rolling direction (RD) and surrounded by highly deformed (elongated) grains. It has been shown that residual Goss grains retained after cold rolling, like the ones seen in Fig. 4.7. These residual Goss grains would be the most likely origin of the recrystallized Goss grains at the boundaries. Their low stored energy would allow them to preferentially consume the highly deformed surrounding matrix during the early stages of annealing.

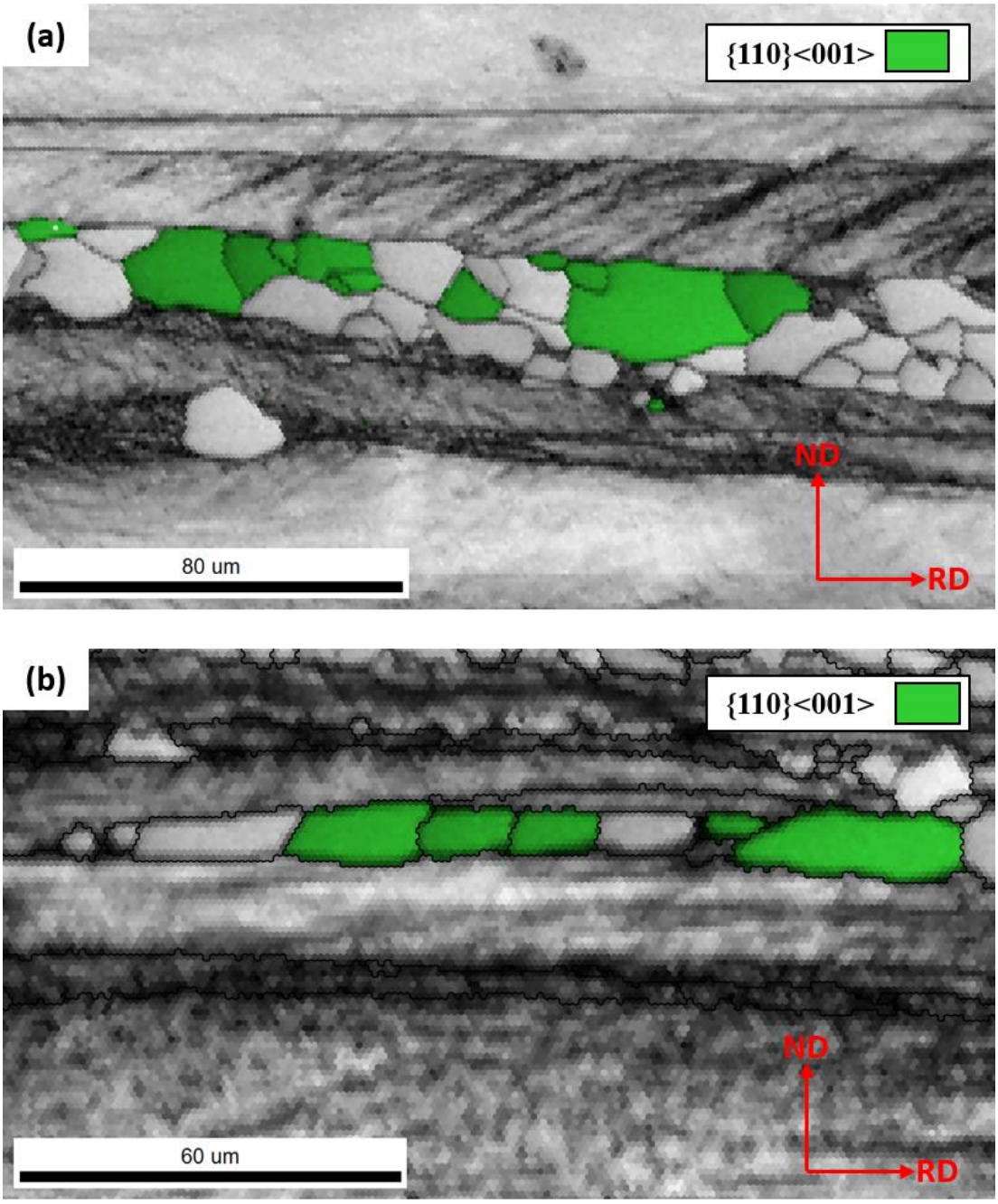

Fig. 4.10. Goss grains nucleating at the grain boundaries after annealing at 750 °C for 5 minutes followed by water quenching. The Goss grains are formed along the boundaries parallel to the rolling direction.

Thus, it is seen that the recrystallized Goss grains come from the initial Goss grains before cold rolling, i.e. after hot band annealing (Fig. 4.4). During cold rolling, a small fraction of these grains are *retained* because of the formation of fragments of the {111}<112> orientations. During annealing, these *residual* Goss grains serve as the initial nuclei since they did not undergo severe plastic deformation or crystal rotation, so the local stored energy is low as compared to its neighbours. This provides the driving force for them to grow into the heavily deformed neighbouring grains. On the other hand, the high mobility boundaries (30°-35°<110>) between the Goss and their neighbours make the Goss grains preferentially grow by consuming their neighbouring grains.

However, there might be other mechanisms that are responsible for the formation of the Goss grains in the annealed steel, especially for the Type III Goss grains that are located at the grain boundaries. Nucleation of randomly oriented grains may occur at the grain boundaries between the {111}<112> and {113}<361> grains. Of all the nuclei, those with the Goss orientation may preferentially grow into the deformed matrix due to the high mobility boundaries (~35°<110>) between the Goss nuclei and the neighbouring {111}<112> and {113}<361> grains.

As noted before, the Type III Goss grains that survive during cold rolling are located at the grain boundaries. During annealing, these grains could recrystallize and form clusters of recrystallized Goss grains as seen in Fig. 4.11a. This is again due to the fact that these Goss grains have ~35°<110> misorientations with respect to its neighbours ({111}<112> and {113}<361>), which are high mobility boundaries and thus favour the growth of these grains to their neighbours [10, 24]. This fact combined with the high stored energy (as seen in the IQ and KAM maps in Fig. 4.7) gives the Goss grains preferential conditions for the nucleation and growth during annealing.

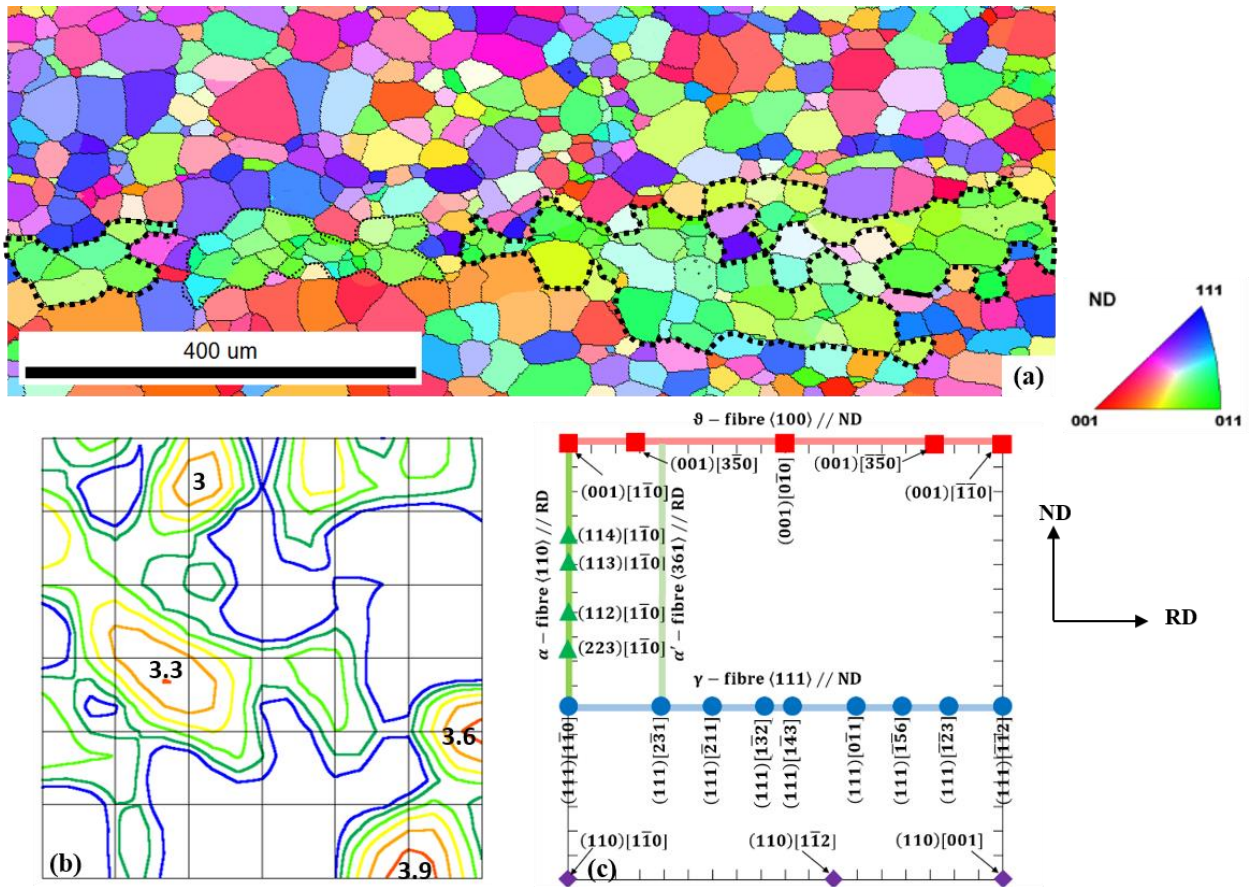

Fig. 4.11. Texture of the 2.8 wt% Si steel after annealing at 750 °C for 10 minutes: (a) EBSD IPF map, (b) ODF at the φ_2 =45° section of the Euler space, (c) the texture key showing the locations of major texture components and fibres including <001> //ND (θ fibre), <111 > //ND (γ-fibre), and < 110 > //RD (α-fibre).

The final texture of the completely recrystallized material after annealing at 750°c for 10 minutes is shown in Fig. 4.11b. The texture mainly consists of {111}<112> and {111}<231> components on the <111>//ND fibre, as well as a component ~10° away from the {001}<350> component on the <100>//ND fibre. An interesting feature to note here is the strong intensity of a component ~10°-15° away from the Goss orientation, which is the result of the clusters of near

Goss grains seen in the microstructure of Fig. 4.11a. Strong Goss texture during primary recrystallization was also noticed by Dunn [21] for Goss single crystals, while Mishra et al. [22] explained this for polycrystalline steel by comparing the hot-rolled plate to a Goss single crystal (due to the high intensity formed by shear deformation).

Table 4.1. Summary of the volume fraction change of the Goss grains during thermomechanical processing.

Processing stage	**Vol. fraction (%)**	**Observation/Explanation**
Hot rolling (across thickness)	~10%	-High volume fraction close to the surface due to shear strain. - Discrete grains and sub-grains in the central region due to grain fragmentation.
Hot rolling (surface)	~30%	- Elongated grains very close to the surface and between the surface and central regions. - Small equiaxed grains beneath the surface layer, recrystallization due to the high strain and high temperature.
Hot band annealing	~9%	- Scattered throughout the thickness with a higher volume fraction closer to the surface.
Cold rolling	~1%	- Within shear bands and microbands of {111}<112> deformed grains. - Fragmented grains close to grain boundaries.
Primary recrystallization (partial, 50%)	~8% of total, ~17% of Recrystallized grains	- Within shear bands and microbands of {111}<112> deformed grains. - At grain boundaries.
Primary recrystallization (complete)	~15%	- Clustered together with a high fraction of low angle boundaries.

4.4 Conclusions

The Goss orientation appears in large amounts during hot rolling, where the volume fraction of the Goss grains reaches ~30% in the surface region of the cross section. This is due to the shear strain induced by the friction between the rolls and the steel, and the dynamic recrystallization of the surface area during hot rolling.

After hot band annealing, the overall volume fraction of the Goss grains decreases to below ~10%; after cold rolling, the volume fraction is further reduced to around 1%. The rotation of the Goss orientation towards the {11 11 8}<4 4 11> and {111}<112> orientations leads to the significant reduction of the Goss volume fraction during cold rolling.

Three types of Goss grains were observed in the matrix of the cold-rolled steel. The first two types were embedded inside the {111}<112> grains, and their formation mechanisms had already been explained in the literature through a transition band model and a rigid inclusion model. The third type of Goss grains was observed at the grain boundaries between the {111}<112> and {113}<361> grains, and its origin was also explained using a rigid inclusion model.

Although observed in different locations, the existence of all these Goss grains may be attributed to the retention of a small fraction of the initial Goss grains during the deformation process. The specific misorientations (30°-35°<110>) between the Goss grains and the neighbouring {111}<112> or {113}<361> grains result in the preferential growth of the Goss grains to their neighbours during annealing, which form the final Goss texture.

References

1. Cullity, B. D., & Graham, C. D. (2011). Introduction to magnetic materials. John Wiley & Sons.

2. Fiorillo, F., Bertotti, G., Appino, C., and Pasquale, M.: Soft magnetic materials. In Wiley Encyclopedia of Electrical and Electronics Engineering, Peterca, M., ed. (Wiley, Hoboken, New Jersey, 2016)

3. Oda, Y., Kohno, M., & Honda, A. (2008). Recent development of non-oriented electrical steel sheet for automobile electrical devices. Journal of Magnetism and Magnetic Materials, 320(20), 2430-2435.

4. Petrovic, D. S. (2010). Non-oriented electrical steel sheets. Materiali in tehnologije, 44(6), 317-325.

5. Honma, K., Nozawa, T., Kobayashi, H., Shimoyama, Y., Tachino, I., & Miyoshi, K. (1985). Development of non-oriented and grain-oriented silicon steel. IEEE Transactions on magnetics, 21(5), 1903-1908.

6. Mehdi, M., He, Y., Hilinski, E. J., & Edrisy, A. (2017). Effect of skin pass rolling reduction rate on the texture evolution of a non-oriented electrical steel after inclined cold rolling. Journal of Magnetism and Magnetic Materials, 429, 148-160.

7.Goss, N. P. (1934). U.S. Patent No. 1,965,559. Washington, DC: U.S. Patent and Trademark Office.Park, J. T., & Szpunar, J. A. (2003). Evolution of recrystallization texture in nonoriented electrical steels. Acta Materialia, 51(11), 3037-3051.

9. Dorner, D., Zaefferer, S., & Raabe, D. (2007). Retention of the Goss orientation between microbands during cold rolling of an Fe3% Si single crystal. Acta materialia, 55(7), 2519-2530.

10. Humphreys, F. J., & Hatherly, M. (2012). Recrystallization and related annealing phenomena. Elsevier.

11. Ushioda, K., & WB, H. (1989). Role of shear bands in annealing texture formation in 3% Si–Fe (111)[112] single crystals. ISIJ International, 29(10), 862-867.

12. Ibe, G., & Lücke, K. (1968). Orientierungszusammenhänge bei der Rekristallisation von Einkristallen einer Eisen-Silizium-Legierung mit 3% Si. Archiv für das Eisenhüttenwesen, 39(9), 693-703.

13. Hölscher, M., Raabe, D., & Lücke, K. (1991). Rolling and recrystallization textures of bcc steels. steel research, 62(12), 567-575.

14. Hu, H. (1974). Texture of metals. Texture, Stress, and Microstructure, 1(4), 233-258.

15. Kestens, L. A. I., & Pirgazi, H. (2016). Texture formation in metal alloys with cubic crystal structures.

16. Dillamore, I. L., Morris, P. L., Smith, C. J. E., & Hutchinson, W. B. (1972). Transition bands and recrystallization in metals. Proc. R. Soc. Lond. A, 329(1579), 405-420.

17. Hutchinson, W. B. (1974). Development of textures in recrystallization. Metal Science, 8(1), 185-196.

18. Samajdar, I., Cicale, S., Verlinden, B., Van Houtte, P., & Abbruzzesse, G. (1998). Primary recrystallization in a grain oriented silicon steel: On the origin of Goss {l_brace} 110 {r_brace}< 001> grains. Scripta materialia, 39(8).

19. Haratani, T., Hutchinson, W. B., Dillamore, I. L., & Bate, P. (1984). Contribution of shear banding to origin of Goss texture in silicon iron. Metal Science, 18(2), 57-66.

20. Gobernado, P., Petrov, R. H., & Kestens, L. A. I. (2012). Recrystallized {3 1 1}< 1 3 6> orientation in ferrite steels. Scripta Materialia, 66(9), 623-626.

21. He, Y., Godet, S., & Jonas, J. J. (2005). Representation of misorientations in Rodrigues–Frank space: application to the Bain, Kurdjumov–Sachs, Nishiyama–Wassermann and Pitsch orientation relationships in the Gibeon meteorite. Acta materialia, 53(4), 1179-1190.

22. Dunn, C. G. (1954). Cold-rolled and primary recrystallization textures in cold-rolled single crystals of silicon iron. Acta Metallurgica, 2(2), 173-183.

23. Mishra, S., Därmann, C., & Lücke, K. (1984). On the development of the Goss texture in iron-3% silicon. Acta Metallurgica, 32(12), 2185-2201.

24. G. Ibe and K. Lücke (1966). In Recrystallization, Grain Growth and Textures. Ed. H. Margolin, ASM, 434-447.

Chapter 5 Texture Evolution of a 2.8% Si Non-oriented Electrical Steel and the Elimination of the <111>//ND Texture

5.1 Introduction

Non-oriented electrical steels (also known as silicon steels) are soft magnetic materials that are widely used in the manufacturing of magnetic cores for electric motors and generators [1-6]. For optimal energy efficiency, the magnetic properties of the core material should be optimized, i.e. the losses should be minimized and the magnetic permeability be maximized [1-6]. These properties are strongly dependent on the material chemistry, the processing routes and the operational parameters employed, which lead to specific microstructure and texture in the final steel sheets. Both the grain size and the crystallographic orientations of the recrystallized grains have strong effects on the iron loss and the magnetic permeability [4-6]. To improve the properties of the electrical steel, the magnetically favourable <001>//ND (normal direction) texture should be promoted, while the magnetically unfavourable orientations, e.g. <111>//ND, should be eliminated [4-6].

During thermomechanical processing of non-oriented electrical steels, various textures develop at every processing stages, e.g. hot rolling, hot band annealing, cold rolling, final annealing, etc. [4-6], and the control of the final texture in the thin steel sheet has proven to be very challenging. For steels containing a high amount of silicon (e.g. 2 wt% or more) the final texture in the steel sheet is usually composed of a strong γ-fibre (<111>//ND) and an α-fibre (<110>//RD, rolling direction), while the desired θ-fibre (<100>//ND) is usually weak [2, 3]. Many authors also studied the effect of grain size on the overall magnetic properties of electrical steels, and suggested that there is an optimum grain size that favors low loss for steels containing different

amounts of silicon [7, 8], which is closely related to the grain growth during the final annealing process.

The evolution of texture in electrical steel has been extensively studied, and a number of theories and models have been proposed and employed to analyze and predict the formation of texture during annealing [9-11]. Most of these theories, however, are concerned with the initial (primary) recrystallization stage, i.e. the nucleation from the deformed matrix and early grain growth at the beginning of the recrystallization, while theories for grain growth after the completion of primary recrystallization and models for the prediction of texture evolution during grain growth remained controversial, and sometimes even contradictory [10, 11]. It is known that the driving force for grain growth is the reduction of grain boundary energy [9, 10], and the mobility of the grain boundaries depends on the misorientation between the growing grains and their neighbours [8, 9]. Some authors have suggested that the <111>//ND fibre texture, especially the {111}<112> and {111}<110> components are strengthened during grain growth [11], while others have found the opposite [12].

The grain boundaries that are responsible for the development of the magnetically favourable Goss texture ({011}<100>) in grain-oriented electrical steels have also been subjected to debate in the literature [13]. Some have attributed the formation of the Goss orientation to special coincidence site lattice (CSL) boundaries, including the Σ5, Σ7 and Σ9 individually, or a collection of other CSL boundaries [14, 15]. Others challenged this by citing that the fraction of the CSL boundaries for the Goss orientation is only ~3% higher than the other orientations [13, 16, 17], and this small difference could not account for the selective growth of the Goss grains during secondary recrystallization. It was also found [13, 16, 17] that the Goss grains had a large fraction of high angle boundaries (20°~45°) which were believed to have high mobility and thus

allowed them to move more rapidly as compared to the low angle (<20°) or ultra-high angle (>45°) boundaries [13, 16, 17].

During the processing of non-oriented electrical steels, it was also noted that Goss texture developed during hot band annealing, and the volume fraction of the Goss component decreased during primary recrystallization and grain growth [9]. This decrease has been attributed to the formation of a large fraction of low angle boundaries around the Goss grains [9]. These low angle boundaries had low migration mobility and the driving pressure was very low during grain growth [9, 10], which resulted in the hindrance of the growth of the Goss grains when compared to the {111}<112> grains, which were surrounded by a large amount of high-angle boundaries and a small fraction of low-angle boundaries [9].

To understand the evolution of texture of non-oriented electrical steels during thermomechanical processing, especially the formation mechanism of the final texture during grain growth, a 2.8 wt% Si non-oriented electrical steel was processed using conventional routes such as hot rolling, hot band annealing, cold rolling and final annealing. The final annealing was carried out at a fixed temperature (750°C) but with different holding times to evaluate the effect of annealing time on texture. The evolution of texture was characterized using EBSD techniques, and the grain boundary character (i.e. misorientation) and the grain size of the major components appearing in the microstructure were statistically analyzed, which confirmed that during grain growth, both the grain boundary mobility and the grain sizes of the grains across the boundary affect the growth process, i.e. the existence of high mobility boundaries decides the tendency for growth, while the relative grain sizes between a grain and its neighbors determines the direction of the growth. It was found that, after annealing for certain times at a fixed temperature, the

unfavorable <111>//ND texture may be eliminated, while the desired <100>//ND texture was enhanced.

5.2 Experimental

The non-oriented electrical steel processed in this research contains (wt %): 2.8 Si, 0.52 Al, 0.3 Mn, 0.01 P, and 0.003 C. It was melted in a vacuum furnace and cast into ingots with a cross-section area of 200 × 200 mm^2. The material was then reheated to a nominal temperature of ~1040°C and hot rolled to a thickness of 25 mm in six passes in a reversing rolling mill. The surface oxides were then machined before carrying out a second hot rolling process, in which the steel plates were reheated again to ~1040°C and rolled to a final thickness of ~2.5 mm (~90% reduction). The plates were then pickled in a HCl solution to remove surface oxides generated during the second hot rolling. These plates were annealed in a 100% dry hydrogen atmosphere at 840°C for 60 hours.

The annealed hot bands were then cold rolled to a final thickness of ~0.5 mm (~85% reduction). Five smaller strips were cut from the cold-rolled sheets and subsequently annealed at 750°C for different times (10, 30, 60, 90, and 120 minutes) in an argon-protected atmosphere. The furnace was first heated up to 750°C and the samples were quickly inserted into the furnace and held for the specific times. In this way, the annealing occurred at a high heating rate, which has been reported in the literature [18] to have a positive effect on the texture development, i.e. enhancing the magnetic properties. The samples were finally furnace cooled.

EBSD characterization was carried out in a field emission gun scanning electron microscope (Nova NanoSEM, FEI) equipped with an EDAX Orientation Imaging Microscopy system (OIM 6.2). The EBSD scans were performed on the cross section (ND-RD plane) of the steel plate or sheet, which covered essentially the entire thickness of the plate or sheet. Orientation distribution

functions (ODFs) were calculated from the measured Euler angles using a harmonic series expansion method with a Gaussian half-width of 5° and a series rank of 22. The textures were plotted on the $\varphi_2 = 45°$ section of the Euler space (Bunge notation).

For grain boundary character analysis, specific crystal orientations (e.g. Goss, θ-fibre or γ-fibre) were isolated (with a tolerance of 15°) and the misorientations between these grains and their immediate neighbours were calculated and classified into low angle (0°-20°), high angle (20-45°), ultrahigh angle (>45°) and CSL (up to Σ29) boundaries. The volume fraction of a specific boundary group was then compared to that of all the other grains at various annealing times. The average grain sizes of specific orientations appearing in the microstructure (e.g. {011}<100>, {001}<350>, {111}<112>, etc.) were also calculated and compared to the average grain sizes of all the other grains, which gave an indication of which grains had a size advantage during grain growth.

5.3 Results

5.3.1 Hot Rolling Texture

Fig. 5.1 shows the cross-section microstructure and microtexture of the steel after hot rolling. The microstructure is featured by significantly different bands of grains with various morphologies and grain sizes across the thickness, i.e. large, elongated grains in the center, and small, recrystallized grains near the surfaces. Within the elongated (deformed) grains, apparent orientation variation is observed, which is due to the inhomogeneous plastic deformation during the rolling process. The difference in microstructure is caused by the non-uniform stress/strain and temperature distributions across the thickness [19]. The surface regions may be further divided into two sub-regions: near the surface are small *equiaxed* grains, and adjacent to the center region

are relatively large and *elongated* grains, the latter being the result of plastic deformation on the dynamically or statically recrystallized grains during the hot rolling process.

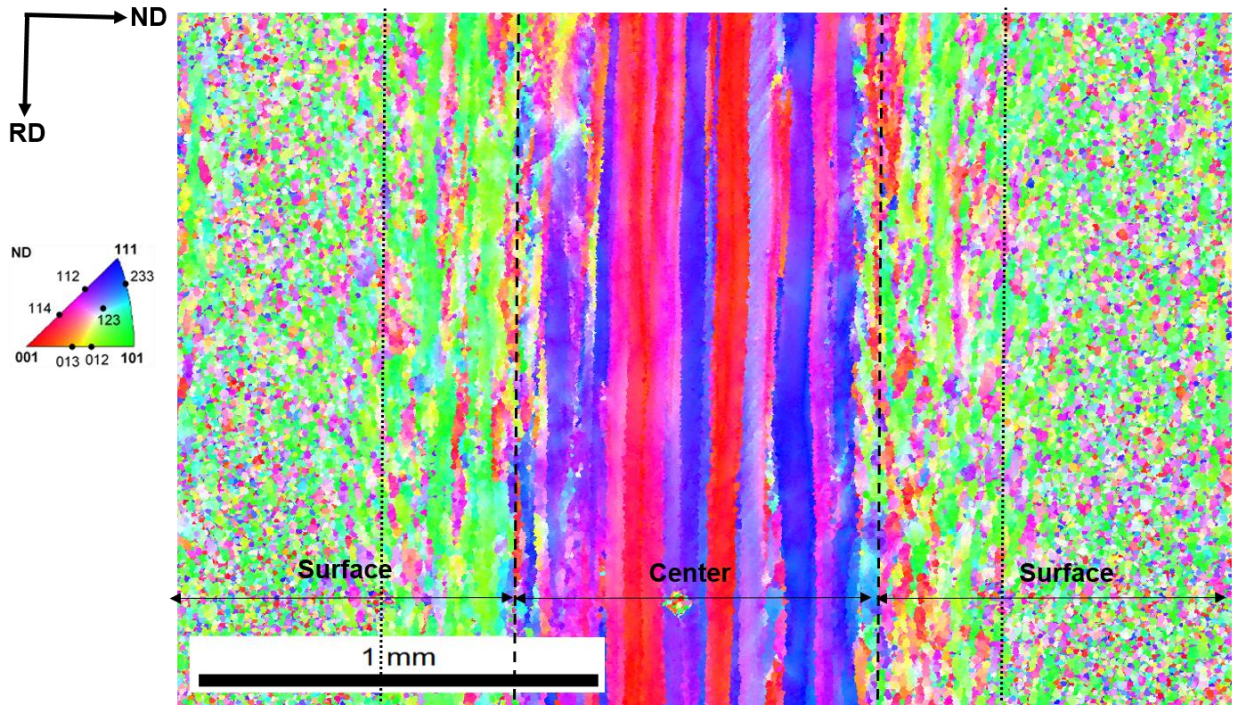

Fig. 5.1. EBSD inverse pole figure (IPF) map showing the cross-section microstructure and microtexture of the 2.8% Si non-oriented electrical steel after hot rolling. The ND-RD section shows banded microstructures and apparent texture inhomogeneity across the sheet thickness.

The texture of the surfaces is dominated by <110>//ND and <112>//ND grains (green and purple, respectively, in the inverse pole figure map), which form the Goss ({110}<001>)/brass ({110}<112>) and copper ({112}<111>) textures, respectively, as shown in Fig. 5.2a. These are known to be the shear textures in bcc metals developed due to strong shear stress generated by the friction between the rolls and the surfaces of the material [10, 18]. These textures are the result of slip symmetry arising from a slip system with a Schmid factor starting from 0 and turning into the

maximum when a rotation of the lattice occurs by 45° [20], and they are strengthened at higher rolling temperatures. It should be noted that the development of the Goss texture at the surface regions is critical to the formation of the final Goss texture in the subsequent cold rolling and annealing processes [21, 22].

On the other hand, the central region in the hot-rolled plate is mainly composed of a strong rotated cube ({001}<110>) and two fibre textures (Fig. 5.2b): <110>//RD (α-fibre) and <111>//ND (γ-fibre). These textures are typical of bcc metals after plane-strain compression (rolling) and are very similar to the *cold rolling* textures of non-oriented electrical steels [20]. The overall texture across the thickness is a combination of the textures from both the surface and central regions (Fig. 5.2c). Although all the components present in the combined texture, the intensities are much weaker than in the individual regions. It is worth noting that the shear textures on the surfaces and the rolling textures in the central region are related to each other by a 90° rotation about the sample's transverse direction [20]. This is because the shear stresses acting on the surfaces are in the rolling direction, thus leading the crystals to rotating around the transverse direction.

The difference in texture between the central and surface regions is because the central region is not in direct contact with the rolls and the shear stress is essentially negligible. In addition, the cooling rate at the central region is slower than the surface regions. The large shear strain on the surfaces results in rapid recrystallization of the heavily sheared crystals, which forms typical recrystallization textures, while the much smaller or non shear strain in the central region causes dynamic recovery instead of recrystallization. Thus, the central region still has a deformation microstructure and texture. The quick drop of the temperature on the surfaces due to the direct contact with the rolls prohibits the growth of the newly recrystallized grains, thus these grains are usually small.

During hot rolling, both dynamic and static recrystallizations may occur at the surface regions (due to high shear strains). The nuclei come from small regions of the deformed microstructure, i.e. the orientations of the nuclei are the same as the deformed grains [10], thus the small equiaxed grains observed at the surface regions show similar texture to the deformed material, i.e. Goss, copper and brass. Recrystallized grains formed *during* hot rolling are subjected to simultaneous plastic deformation, thus they may be elongated and show considerable orientation variations. The grain orientation spread (GOS) map shown in Fig. 5.2e clearly indicates that the "equiaxed" grains in the surface regions actually contain both deformed (GOS ≥ 5°) and non-deformed (GOS < 2.5°) crystals, although their orientations are essentially the same, i.e. Goss, copper and brass. The non-deformed grains are the result of static recrystallization *after* hot rolling, while the deformed grains are due to the deformation of the recrystallized crystals *during* hot rolling.

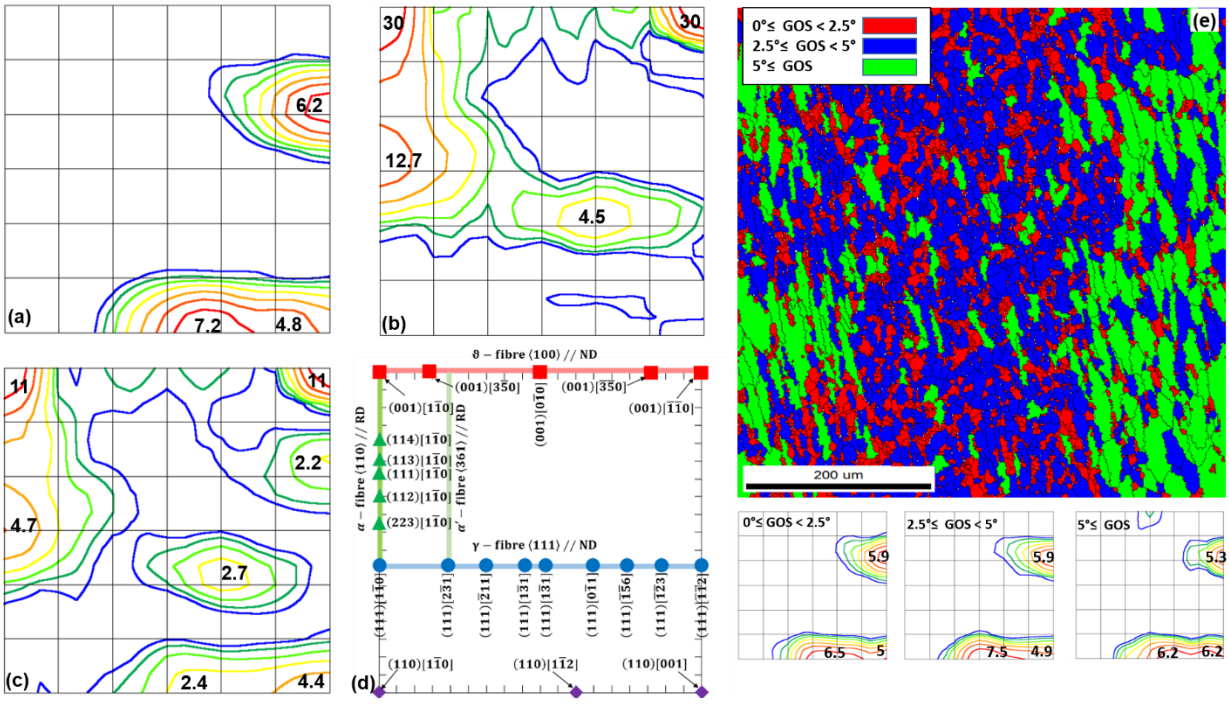

Fig. 5.2. φ_2=45° sections of the orientation distribution functions (Bunge notation) showing the textures after hot rolling: (a) texture of the surface regions, (b) texture of the central region, (c) overall texture across the thickness, (d) texture key showing the major fibres and components, (e) an area close to the surface showing the grain orientation spread and the textures associated with the grains of various spread angles.

5.3.2 Texture after Hot Band Annealing

Fig. 5.3a shows the EBSD inverse pole figure (IPF) map of the hot-rolled steel after annealing at 840°C for 60 hours. Although with a long holding time at a relatively high temperature, the microstructure remains heterogeneous as evidenced by the large variation in grain size: the average grain size is ~305 μm, but grains with diameters ranging from tens of microns to hundreds of microns are all present. The annealing process significantly weakened the overall texture (Fig. 5.3b) when compared to the hot rolling texture (Fig. 5.2c). Even though annealing usually randomizes the texture, discrepancy in texture between the surface and the central regions still persists. Apparently, the banded structures in the hot-rolled state recrystallized differently during annealing, which resulted in different textures.

The surfaces again consist of numerous {110} grains (green), and the texture (Fig. 5.3c) is similar to that after hot rolling (Fig. 5.2a), i.e. the shear texture components such as brass, Goss and copper are essentially retained. In addition, two weak components ({001}<350> and {110}<110>) formed, which were not seen in the hot-rolled steel. The central region shows a significantly different texture (Fig. 5.3d). Compared to the hot-rolled steel (Fig. 5.2b), the originally very strong rotated cube ({001}<110>) has been largely weakened, while a strong

{113}<110> component on the α-fibre develops. Again, a component near {001}<350> on the θ-fibre is produced. The γ-fibre is weakened and a Goss and a rotated Goss start to appear.

As mentioned before, after hot rolling, the surface regions contain both deformed and non-deformed crystals with mainly three orientations, i.e. Goss, copper and brass (Fig. 5.2e). During hot band annealing, recrystallization starts from the existing non-deformed grains through grain growth (since nuclei already formed due to static recrystallization after hot rolling), i.e. these grains would grow into their surrounding matrix that has been deformed and has higher stored energies. Since the non-deformed grains (the nuclei) have the Goss, copper and brass orientations, the resulted final texture would resemble the starting texture before annealing (Fig. 2a). However, during hot band annealing, new grains may also nucleate and grow, and these form the {001}<350> and {110}<110> textures as shown in Fig. 5.3c. The central region, on the other hand, has experienced a different recrystallization process, i.e. the recrystallization starts from nucleation in the dynamically recovered matrix since there is no existing nuclei after hot rolling. The final texture formed after annealing is the result of the common recrystallization process consisting of both nucleation and grain growth.

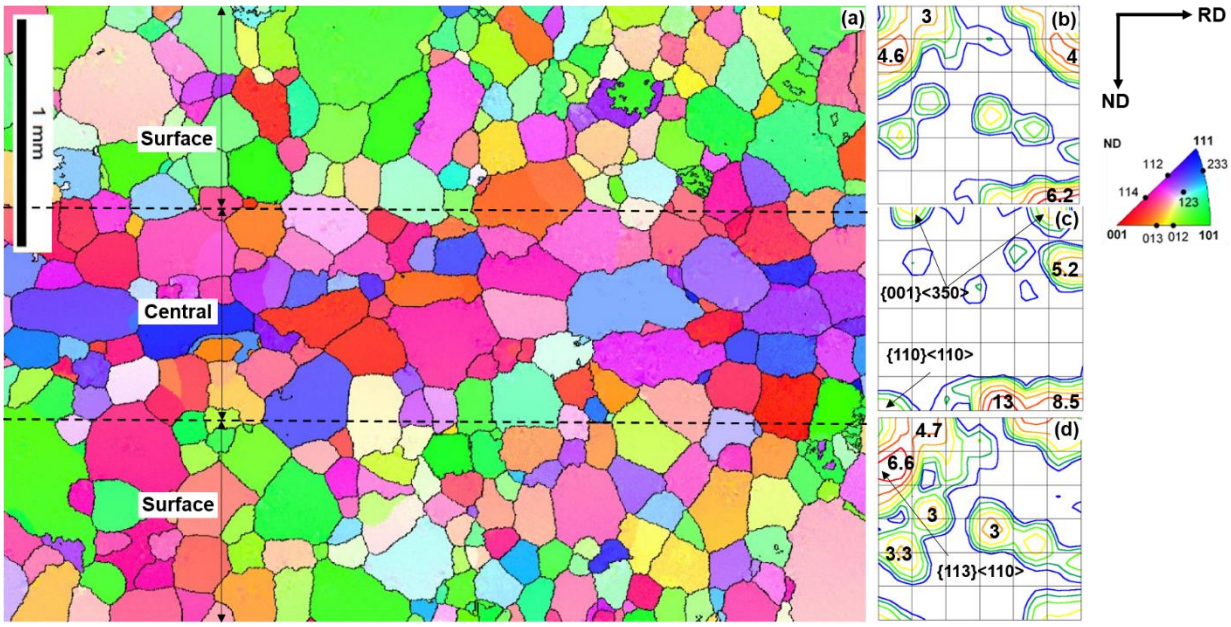

Fig. 5.3. Texture after hot band annealing: (a) EBSD IPF map showing the microstructure and variation of crystal orientations, (b) overall texture across the thickness, (c) texture of the surface regions, and (d) texture of the central region.

5.3.3 Cold Rolling Texture

The microstructure and microtexture of the steel after cold rolling (~85% reduction) are shown in Fig. 5.4. The deformed material exhibits a typical rolling microstructure featuring elongated grains containing numerous shear bands or deformation bands within these grains (Fig. 5.4a). The individual grains show substantial heterogeneity (or grain fragmentation) as evidenced by the large in-grain misorientations (variation in grain color). Some regions (black) could not be indexed due to the accumulation of dislocations and the distortion of the lattice.

Typical bcc rolling textures, i.e. α- and γ-fibres, are produced after cold rolling (Fig. 5.4b) [10], which are very similar to that in the central region of the hot-rolled material (Fig. 5.2b). The dominant texture components include {112}<110>, {111}<110>, {001}<110> and {001}<350>, and the maximum intensity was observed at {112}<110>. For bcc iron, rotated cube {001}<110>

(on both the α-fibre and the θ-fibre) is usually the strongest orientation after rolling with intermediate reductions (<80%), while the {112}<110> (on α-fibre) and {111}<110> orientations (on α- and γ- fibres) are the dominant textures after large rolling reductions (>80%) [10]. In addition, the γ-fibre is usually continuous and uniform after low and intermediate reductions, while after large rolling reductions, the {111}<110> component dominates and the {111}<112> is relatively weak. The variations of the texture components on the three common fibres are shown in Fig. 5.4c, where it is clear that the {111}<110> and {112}<110> components have the largest volume fractions, while the {001}<110> and their neighbours also show relatively strong intensities.

The {001}<350> texture that was present after hot band annealing (Fig. 5.3b) was retained and strengthened after cold rolling. Compared to the textures in Fig. 5.3b, the γ-fibre, in particular the {111}<110> component, has been significantly intensified during plane-strain compression. On the other hand, the originally strong Goss texture in the hot-rolled and annealed plate disappeared after cold rolling. This is because Goss is not a stable orientation under plane-strain compression [23, 24], and it rotates around the transverse direction towards the {111}<112> orientation. By calculating the active slip systems using a full constraint Taylor model, Dorner et al. [24] explained this by a concentration of the dislocation activity about a single slip system for smaller rotations which then transition to other slips systems at higher rotations. A very small volume fraction (~1%) of the Goss orientation may be retained after cold rolling within the microbands or shear bands of the {111}<112> grains [24, 25]. This has been explained by Dillamore et al. [23] using a transition band model and by Dorner [24] using a rigid inclusion model.

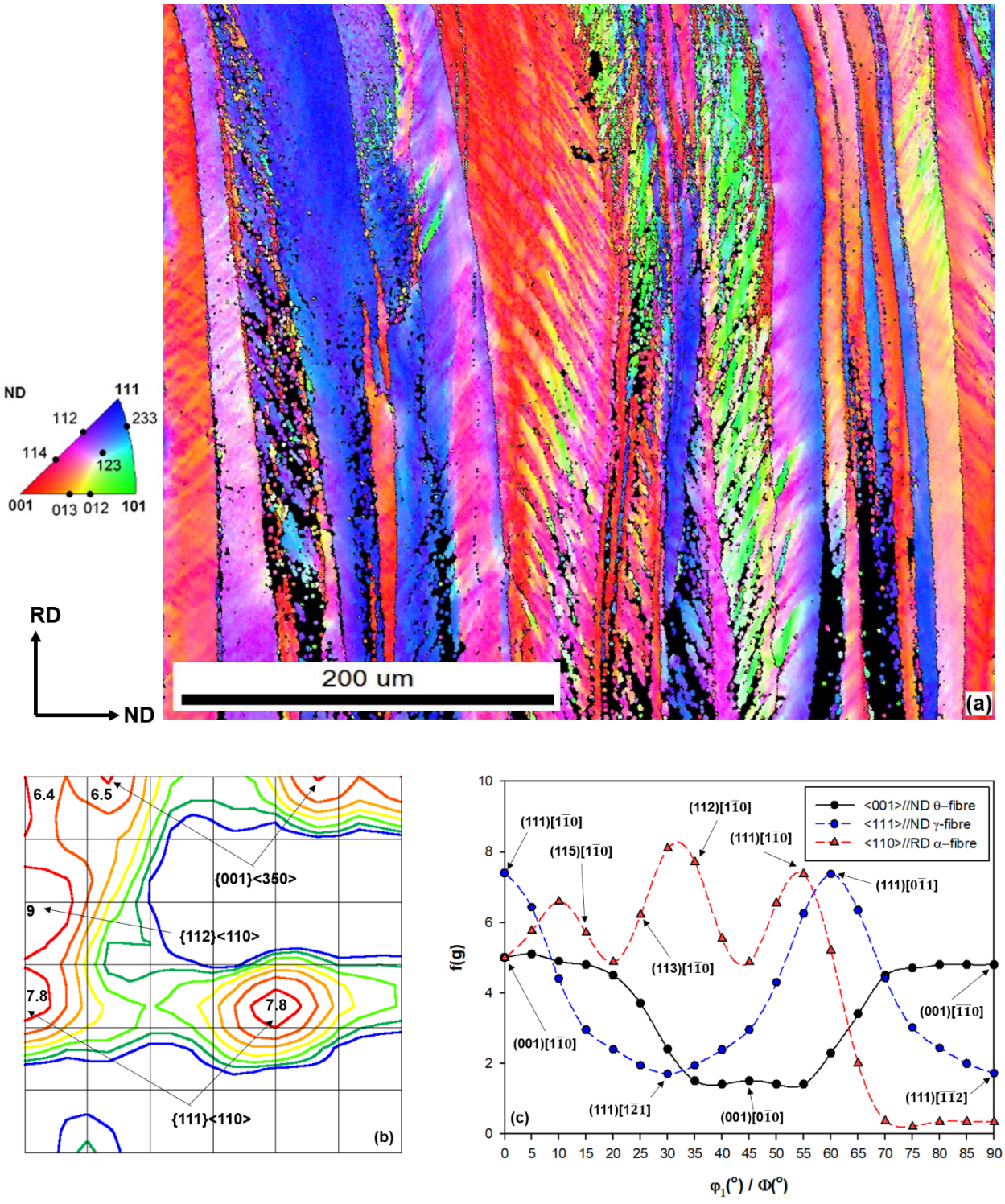

Fig. 5.4. Microstructure and texture after cold rolling: (a) EBSD IPF map showing the microstructure and orientations of the deformed grains, (b) φ_2 =45° section of the ODF, (c) comparison of the volume fractions of various components along the α-, θ- and γ-fibres.

5.3.4 Final Annealing Texture

The microstructures and grain orientations of the cold-rolled and annealed steel are shown in Fig. 5.5. After 10 minutes (Fig. 5.5a), recrystallization has already completed, and all deformed grains have been replaced by recrystallized (equiaxed) crystals. With the increase of the annealing time, the grain orientations (textures) change (Fig. 5.5b-5e) and the grain size gradually increases (Fig. 5.5f). At short annealing times (e.g. 10 and 30 minutes), some clusters of grains with close orientations (A, B, C in Fig. 5.5a, and D, E in Fig. 5.5b) are visible. Further increasing the annealing time, these clusters disappear.

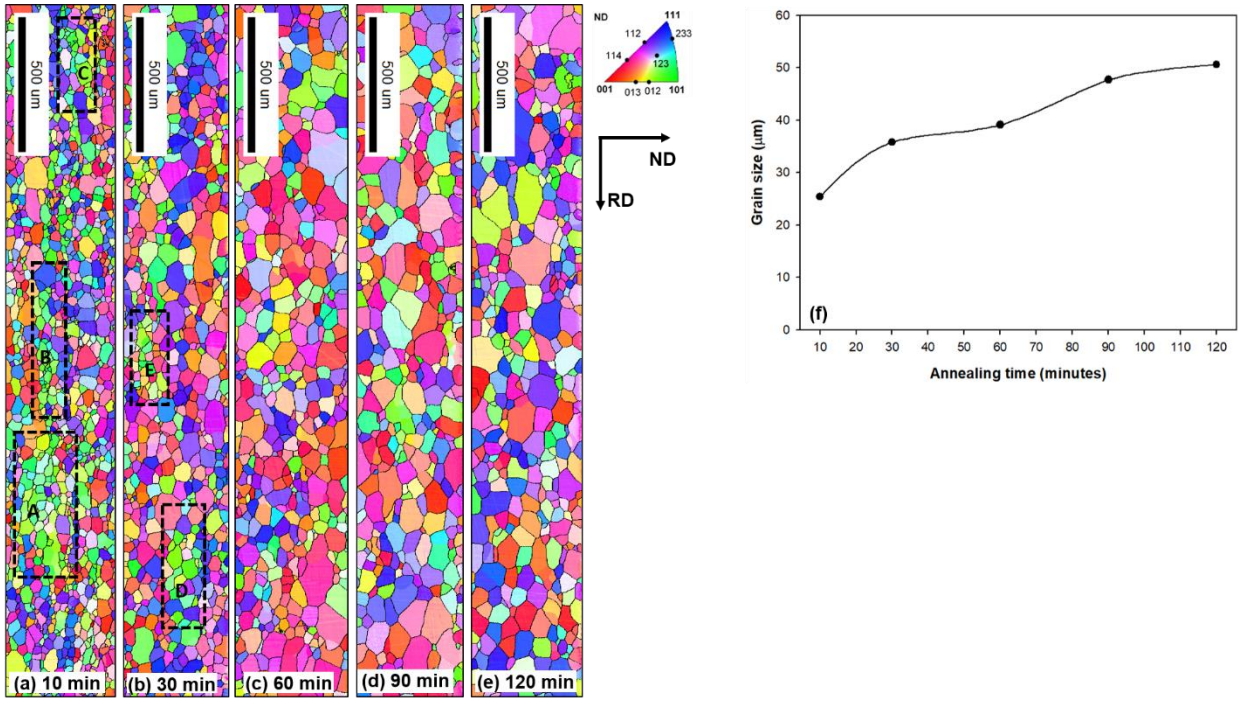

Fig. 5.5. EBSD IPF maps after annealing at 750 °C for different times: (a) 10 minutes, (b) 30 minutes, (c) 60 minutes, (d) 90 minutes, (e) 120 minutes, and (f) grain size vs. annealing time.

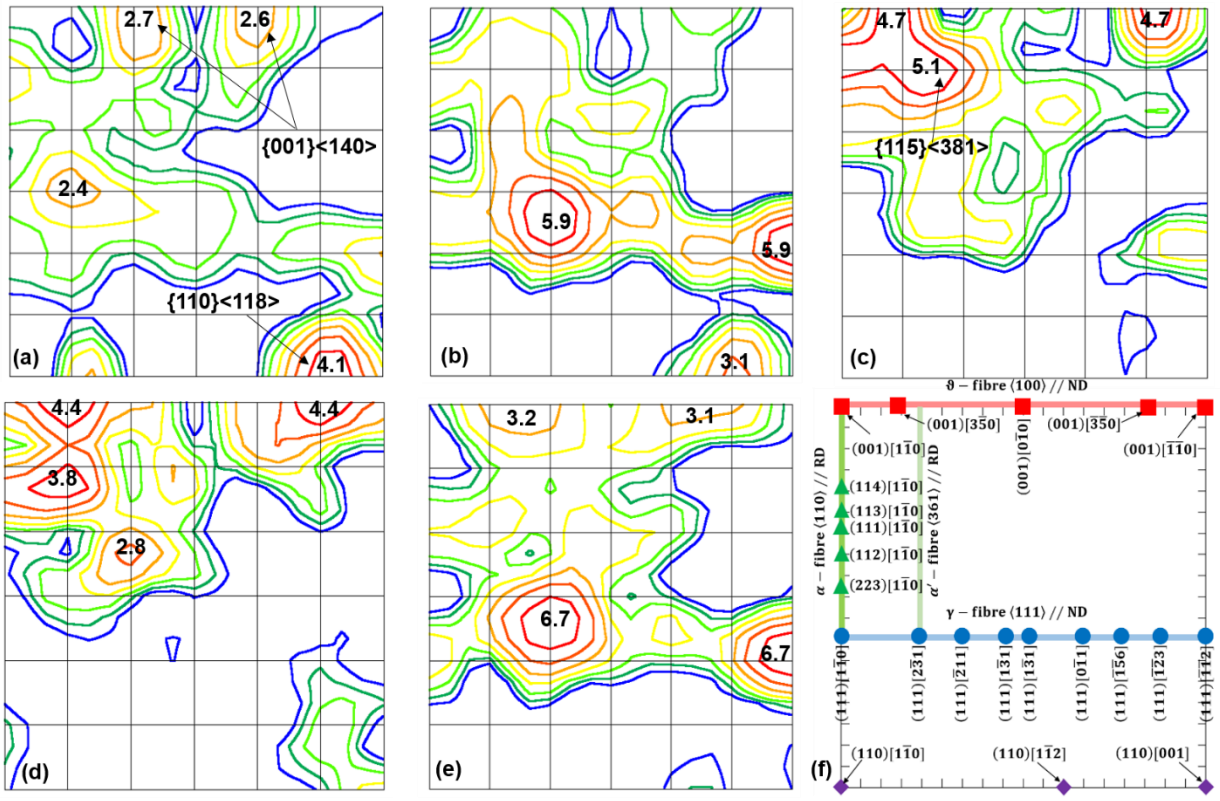

Fig. 5.6. Textures after annealing at 750 °C for different times: (a) 10 minutes, (b) 30 minutes, (c) 60 minutes, (d) 90 minutes, (e) 120 minutes, (f) texture key for the φ_2=45° section of the ODF.

The corresponding textures of the samples after annealing at different times are shown in Fig. 5.6. After 10 minutes (Fig. 5.6a), the texture is considerably weakened and randomized as compared to the cold rolling texture (Fig. 5.4b). The dominant texture is a {110}<118> orientation which is ~10° away from the Goss. There are also some minor components near {001}<140> on the θ-fibre and a weak but continuous γ-fibre. When the annealing time increases to 30 minutes (Fig. 5.6b), a major γ-fibre component, i.e. {111}<112>, develops, while the θ-fibre components and the {110}<118> texture are weakened. After 60 minutes (Fig. 5.6c), the {110}<118> component disappears and the γ-fibre is significantly weakened, while a strong {001}<350> component (~14° from the rotated cube) on the θ-fibre develops. A strong {115}<381> component

(which is close to the {001}<350>) orientation is also seen. As the annealing time increases to 90 minutes, the γ-fibre essentially disappears, while the {001}<350> and {115}<381> components persist. A weak Goss texture is also present. After 120 minutes, the γ-fibre appears again and the {111}<112> component becomes the strongest texture. In the meantime, the {001}<350> orientation on the θ-fibre is weakened.

A major difference between the γ-fibre of the cold rolling texture and the annealing texture (30 and 120 minutes) is the dominant component in this fibre, i.e. the maximum intensity of the {111}<110> component in the deformed state (Fig. 5.4b) is shifted to {111}<112> in the recrystallized state, as shown in Fig. 6b and 6e. This has been explained by several authors [10, 27-29] as a consequence of the oriented nucleation of the {111}<112> grains at a ~30°<110> misorientation with respect to the {112}<110> deformed grains, which preferentially grow due to the existence of high-mobility grain boundaries (~30°<110>) between the {111}<112> recrystallized grains and the dominant {112}<110> deformed grains. This misorientation is very close to the ideal CSL Σ19a (26.5°<110>), which is known to have high mobility in Fe-Si [10, 30].

The appearance of the {001}<350> texture during annealing has been reported by Liu et al. in non-oriented steel processed by strip casting [31]. The authors have found that the {001}<350> orientation preferentially nucleated in the shear bands of the deformed α-fibre grains, especially those ranging from {110}<110> to {115}<110>, as well as in the grain boundaries between the {112}<110> and {001}<150> deformed grains [31]. In this research, the {001}<350> grains are observed at the grain boundary of the deformed {112}<351> grains, as shown in Fig. 5.7. A small volume of the deformed {001}<350> grain was noticed at the boundary of a {112}<351> grain. During annealing, the {001}<350> grain may preferentially nucleate at the grain boundary of the {112}<351> grain or within the {001}<350> deformed grain due to an in-

situ nucleation mechanism [31]. After nucleation, the {001}<350> grain can grow into the deformed {112}<351> matrix due to the ~35°<110> (close to Σ19a) high mobility boundary [10, 30]. However, it is also possible that the {001}<350> grains randomly nucleate within the shear bands (as shown in the IPF map in Fig. 5.7a) in the {112}<351> grains and then preferentially grow into the deformed matrix, again due to the ~35°<110> misorientation between these two grains.

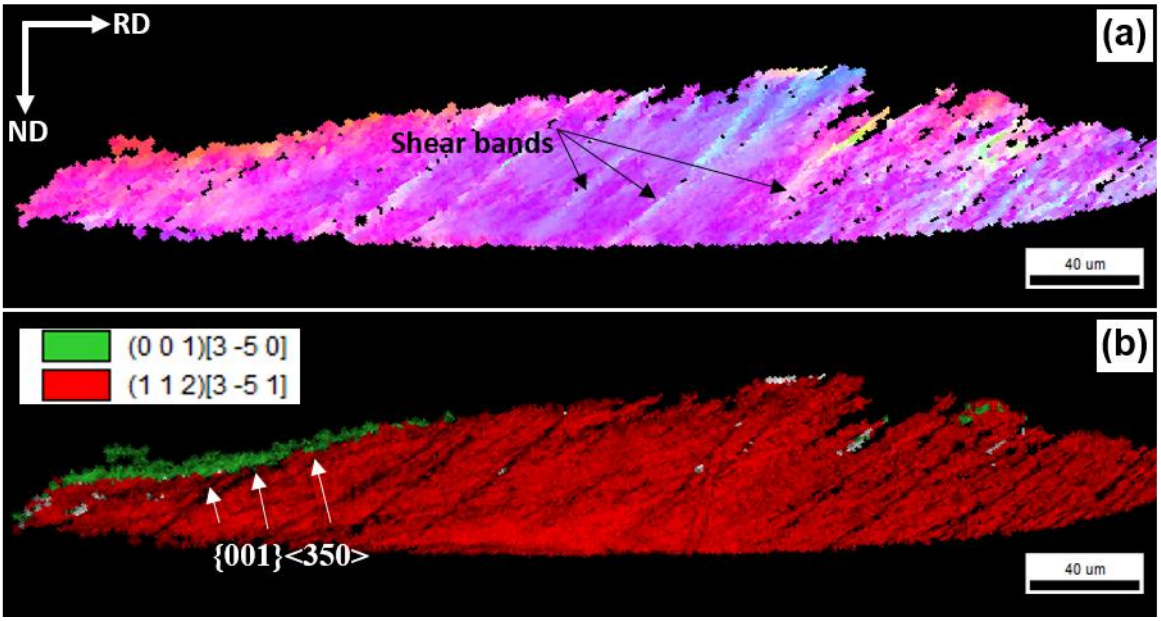

Fig. 5.7. An example of the {001}<350> deformed grain observed at the {112}<351> grain boundary: (a) inverse pole figure map, (b) grain unique color map.

The origin of the Goss orientation has been investigated by several authors using EBSD techniques. Park and Szpunar found that Goss grains nucleate within shear bands in the {111}<112>, {111}<110> and {112}<110> deformed grains [25]. The recrystallized Goss grains form high-angle grain boundaries with respect to the surrounding matrix. This gives them an advantage to preferentially grow during the early stage of recrystallization (hence, the strong Goss

texture after 10 minutes in this study). The Goss again shows a very close to the high mobility Σ19a boundary with respect to the {111}<112> deformed matrix. On the other hand, Dorner et al. [25] proposed two origins for the Goss orientation in an electrical steel in the cold-rolled sheet. The first type appeared in the shear bands of the {111}<112> exclusively, while the second type was found between microbands. Thus, the Goss could be considered already existing in the cold-rolled microstructure, and due to the Σ19a relation to the matrix, it grows preferentially at the initial stages of recrystallization.

The variations of major texture components on the θ-, α- and γ-fibres with respect to the annealing time are shown in Fig. 5.8. The {001}<350> component on the θ-fibre has the largest volume fraction after 60 minutes of annealing (Fig. 5.8a), and it also shows a relatively large fraction after 90 minutes. The cube component ($\varphi_1 = 45°$) has the smallest fraction (among the θ-fibre components) at all the times (except after 60 minutes, where the cube is slightly higher than the {001}<140>). The rotated cube orientation – a major texture in the cold-rolled steel – also shows small volume fractions after annealing at all the times.

On the α-fibre (Fig. 5.8b), the {114}<110> and {556}<110> components show relatively high volume fractions when the annealing time is short, i.e. 10 and 30 minutes. When the annealing time increases to 60 minutes, the {117}<110> component (which is ~10° from the rotated cube) shows a much higher volume fraction than other components. Further increasing the annealing time to 90 and 120 minutes, the largest component moves to {114}<110> and {665}<110>, respectively.

The components on the γ-fibre show significantly different volume fractions after annealing at different times (Fig. 5.8c). After 30 and 120 minutes, the γ-fibre components illustrate very similar trends, i.e. with very strong peaks at {111}<112> and all the other components being

weak. At all the other times, the volume fraction of the γ-fibre is very small, especially when the annealing time is 90 minutes (close to 0). Apparently, the strong γ-fibre developed in cold rolling (Fig. 5.4c), in particular the {111}<110> components, may be changed to the {111}<112> component or be *eliminated*, depending on the annealing time. Annealing for 30 or 120 minutes will give rise to the {111}<112> texture, while annealing for 60 or 90 minutes leads to the *elimination* of the <111>//ND textures.

The variations of the overall volume fractions of the three texture fibres with respect to the annealing time are shown in Fig. 5.8d. When the annealing time is short (i.e. 10 minutes), the difference among the three fibres is quite small, although the γ-fibre is slightly weaker than the θ- and α-fibres. After 30 minutes, the γ-fibre volume fraction increases considerably from ~16% to ~25% and becomes the largest, while those of the θ- and α-fibres essentially do not change or slightly decrease. When the annealing time is 60 minutes, the γ-fibre drops again to ~15%, while the θ-fibre increases from ~19% to ~27%. The α-fibre only shows a small change from ~18% to ~21%. At this time, the ratio of the θ-fibre to γ-fibre is the largest, i.e. 27/15 = 1.8. Increasing the annealing time to 90 minutes reduces the volume fractions of both the θ- and γ-fibres, and slightly increases the α-fibre volume fraction. The ratio of the θ-fibre to γ-fibre is also ~1.8. After 120 minutes, the γ-fibre increases to ~25%, while the θ-fibre drops to ~19%, which gives rise to a ratio of θ/γ = 0.76, being significantly smaller than those after 60 and 90 minutes. Apparently, during the annealing process, the holding time is a very important parameter that affects the magnetic quality of texture.

It is thus seen that at the same annealing temperature, with the variation of annealing time, the recrystallization texture changes significantly. At some times a strong θ-fibre (i.e. 60 and 90 minutes) develops, while at other times a strong γ-fibre forms (30 and 120 minutes). For the 2.8

wt% Si electrical steel studied in this paper, to obtain the desired θ-fibre and avoid the unfavorable γ-fibre, annealing for 60 or 90 minutes at 750°C would be preferred, as this would promote the θ-fibre and suppress the γ-fibre. Annealing for 90 minutes could essentially *eliminate* the detrimental γ-fibre.

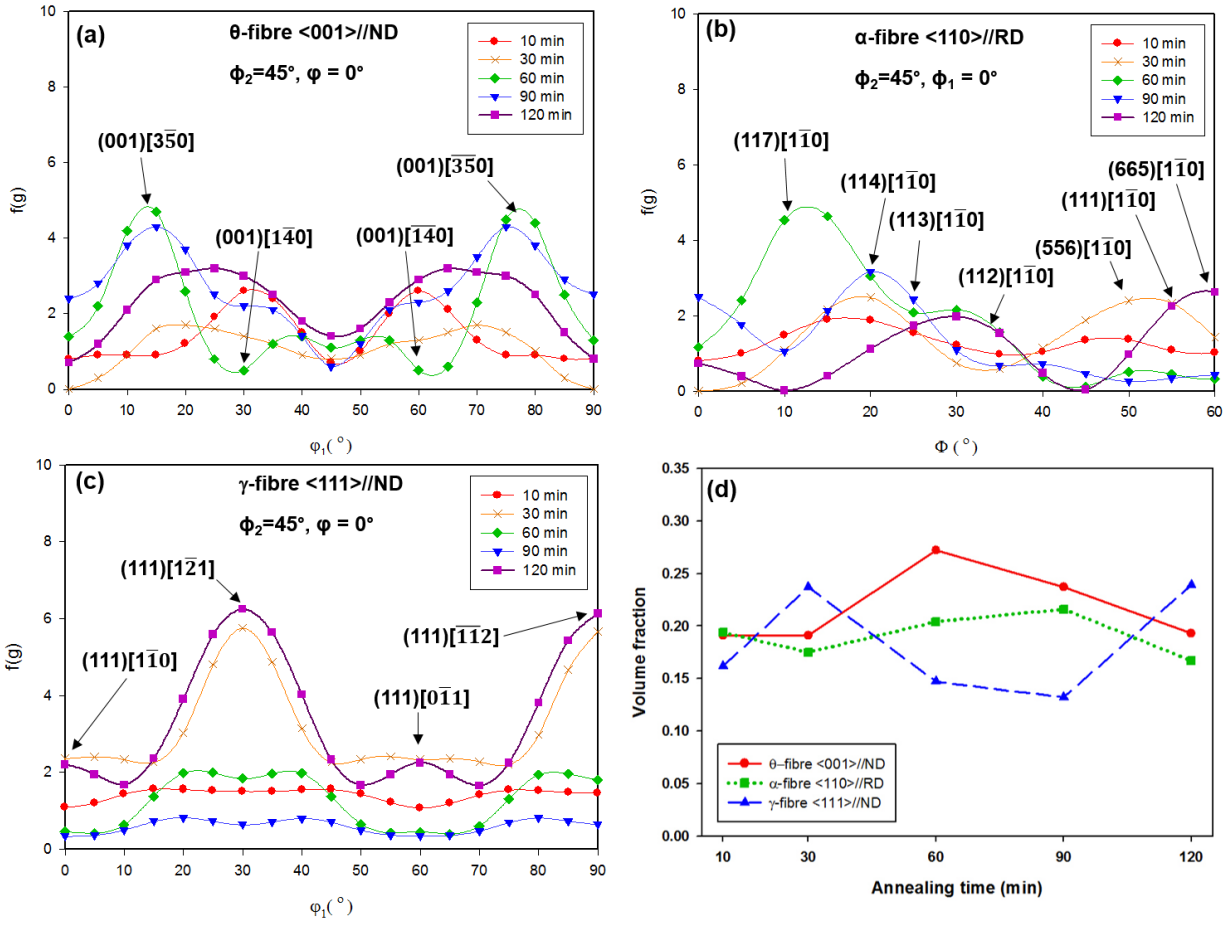

Fig. 5.8. Variations of the main texture components on the common texture fibres during the annealing process: (a) θ-fibre <001>//ND, (b) α-fibre <110>//RD, (c) γ-fibre <111>//ND, (d) overall volume fractions of the three fibres vs. annealing time.

5.4 Discussion

Many authors have tried to explain the relationship between the cold rolling texture and the subsequent annealing texture using two competing theories, i.e. oriented nucleation and oriented growth. However, it is now generally accepted that the "artificial distinction" between "nucleation" and "growth" is meaningless [10], since in the early stage of recrystallization, nucleation is always accompanied by growth. It should be noted that, once the recrystallization is complete, i.e. all deformed grains have been replaced by recrystallized grains, and the annealing process continues, the final texture is essentially controlled by the subsequent growth process, in which some grains may grow by consuming other grains, and the growth mechanism will determine which grains grow and which are consumed. Nevertheless, the evolution of texture during grain growth is very complicated and it is relatively unexplored [10]. In this research, two microstructural characters of the material, i.e. grain boundary misorientation and grain size, were statistically analyzed, from which the formation of textures at different annealing times was attempted to be related to the grain boundary mobility and the grain size advantage during grain growth.

When recrystallization starts, deformed grains with the highest stored energy usually nucleate first. It has been shown [10] that, the stored energy is dependent on the crystal orientation, i.e. $E_{110} > E_{111} > E_{112} > E_{100}$, thus the {011} and {111} deformed grains may nucleate first and the new grains will rapidly grow into their neighbors if the neighboring grains are still in the deformed state and have higher energies [33]. Thus, the variation in stored energy (because of the variation in crystal orientation) of the initially deformed grains will lead to significant differences in grain size and crystal orientations upon recrystallization.

During grain growth after the completion of recrystallization, the mobility of the grain boundary and the grain boundary energy may govern which grains will grow (by consuming their

neighbouring grains) and finally determine the texture. This, again, is closely related to the orientations of the grains, especially the misorientation between the grains across the boundaries. The driving force for grain growth is the reduction of energy, which requests that the growth process reduce the overall energy through grain boundary migration [10, 11]. As has been shown in many investigations [10, 11], during grain growth, grain size may play an important role, i.e. grains with a larger size may have an advantage over a smaller grain during growth [10, 11].

In order to understand why some of the crystal orientations, e.g. Goss, {001}<350> and {111}<112>, preferably form during grain growth at some annealing times, e.g. 60 and 90 minutes for {001}<350> , 10 and 30 minutes for Goss, and 30 and 120 minutes for {111}<112>, the *misorientations* ($\Delta\theta$) between these grains and their neighbouring grains in the sample were calculated and compared to those between the other grains and their neighbours. These misorientations are grouped into: i) low angle ($0° \leq \Delta\theta < 20°$), ii) high angle ($20° \leq \Delta\theta < 45°$), and iii) ultrahigh angle ($\Delta\theta \geq 45°$) [13, 16, 32]. It has been reported in many studies [13, 16, 17] that high angle boundaries have high mobility in bcc steel, while low angle and ultrahigh angle boundaries usually have low mobility. In addition, the abnormal grain growth of the Goss texture in grain-oriented electrical steel may be due to the high percentage of CSL boundaries that surround the Goss grain during the annealing process [14, 15]. However, it should be noted that only a few of the CSL boundaries were reported to have high mobility, e.g. Σ5, Σ7, Σ9 [32] and Σ19a [10, 29]. Thus, in this study the volume fractions of the high-angle boundaries (considered as high mobility boundaries) and the high-mobility CSL boundaries (Σ5, Σ7, Σ9 and Σ19a) are calculated and compared for samples annealed at different times. This is intended to elucidate the role grain boundary mobility plays during grain growth. Additionally, the average size of these grains and the average grain size of the entire sample are calculated and compared, which is

intended to show the importance of grain size advantage in the determination of the growth direction.

Goss ({110}<001>) Grains:

It has been shown that, at early stage of annealing (10 and 30 minutes, as shown in Fig. 5.5a and 5.5b), the Goss grains tend to form clusters in the microstructure. These are believed to be formed in the early grain growth stage in which small nuclei with some specific orientations (e.g. the Goss) grow into their neighboring (deformed) grains until they meet with each other [25]. As illustrated in Fig. 5.9a, nucleation of the Goss grains is usually observed in the shear bands within the deformed {111}<112> grains [27]. These Goss grains will grow into the deformed matrix, which has a ~35°<110> misorientation with respect to the Goss, until they meet with each other (Fig. 5.9b). Because these grains have very close orientations (near Goss), only low angle grain boundaries will form among these grains, which form the cluster structure shown in Fig. 5.9c and 5.9d. When the deformed matrix is completely replaced by the recrystallized grains, the recrystallized grains may further grow if enough energy is provided to drive the growth (e.g. high temperature holding during annealing). However, in this case, the grains have all recrystallized neighbours, so their growth is quite different from the initial crystal growth immediately after nucleation where the nuclei were essentially surrounded by the deformed matrix.

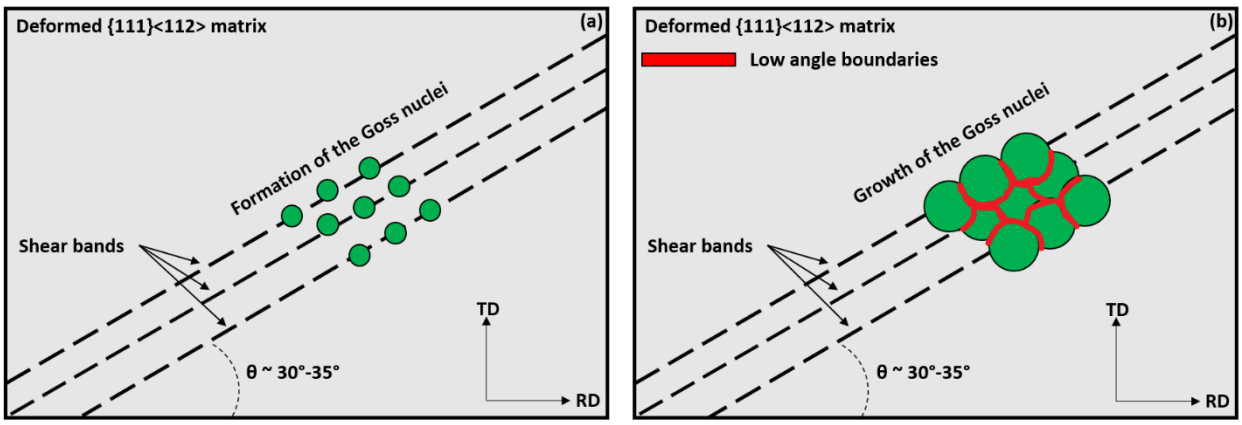

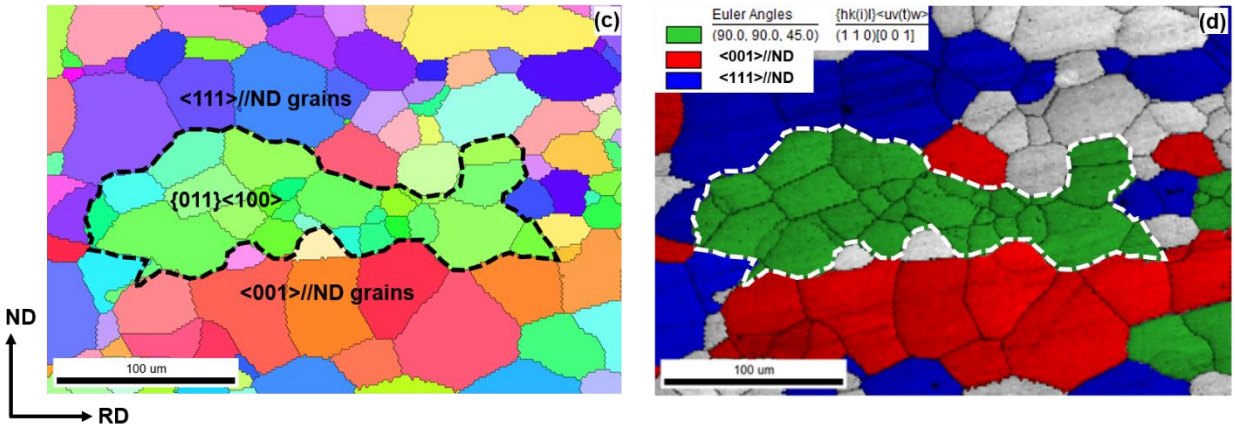

Fig. 5.9. Clustering of the Goss ({110}<001>) grains after annealing at 750 °C for 10 minutes: (a) schematic showing the nucleation of the Goss grains in shear bands, (b) the growth of the Goss nuclei, (c) EBSD IPF map showing the cluster of the Goss grains, (d) grain unique color map.

The volume fractions of the high-angle and high mobility CSL boundaries between the Goss grains and their *recrystallized* neighbours are calculated at different annealing times and compared in Fig. 5.10. These volume fractions are compared to those between the non-Goss grains and their neighbours for the same sample at the same annealing times. After 10 minutes, the volume fraction of the high-angle boundaries of the Goss grains is larger than that of the other grains (Fig. 5.10a), and that of the CSL boundaries is also slightly higher than that of the other grains (Fig. 5.10b), which means that the Goss grains (the clusters shown in Fig. 5.9c and 5.9d) are surrounded by a larger amount of high mobility boundaries than the other grains, thus having high tendency to migrate. However, the average grain size of the Goss grains is smaller than that of their neighbours (Fig. 5.11), thus the neighbouring grains have a size advantage, which results in the growth of the neighbouring grains into the Goss grains, leading to the disappearance of the Goss grains, and the weakening of the Goss texture (Fig. 5.6b and 5.6c). This process continues

until 60 minutes, at which the neighbouring grains grow to the largest and the grain size does not change with further increase of the annealing time. At this moment, the fractions of the high-angle and CSL boundaries of the Goss reach the highest. After that, the Goss grains essentially do not change, or only slightly fluctuate (Fig. 5.6d and 5.6e).

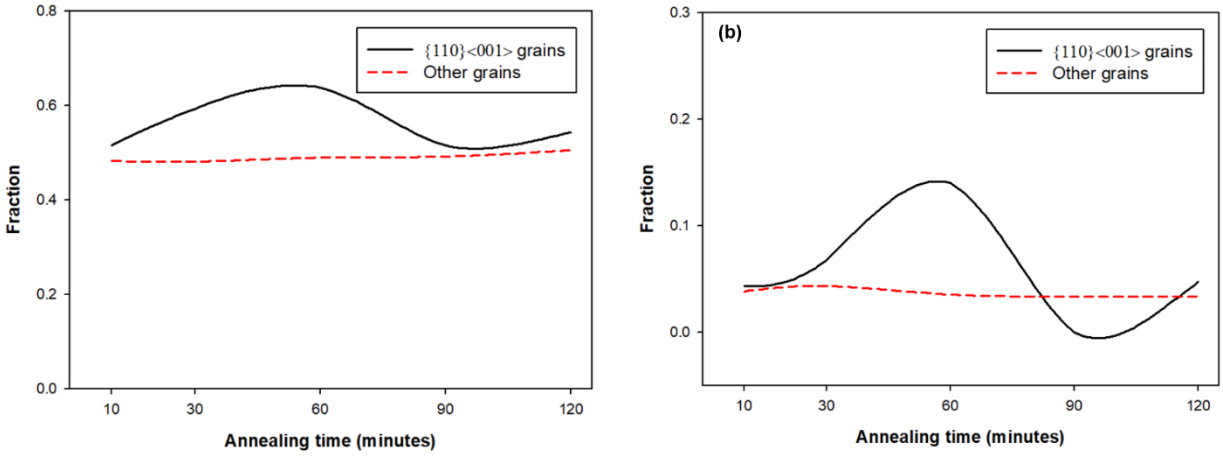

Fig. 5.10. Variations of the volume fraction of the main recrystallization texture components vs. annealing time: (a) high-angle boundaries, (b) CSL boundaries. The CSL boundaries include Σ5, Σ7, Σ9 and Σ19a.

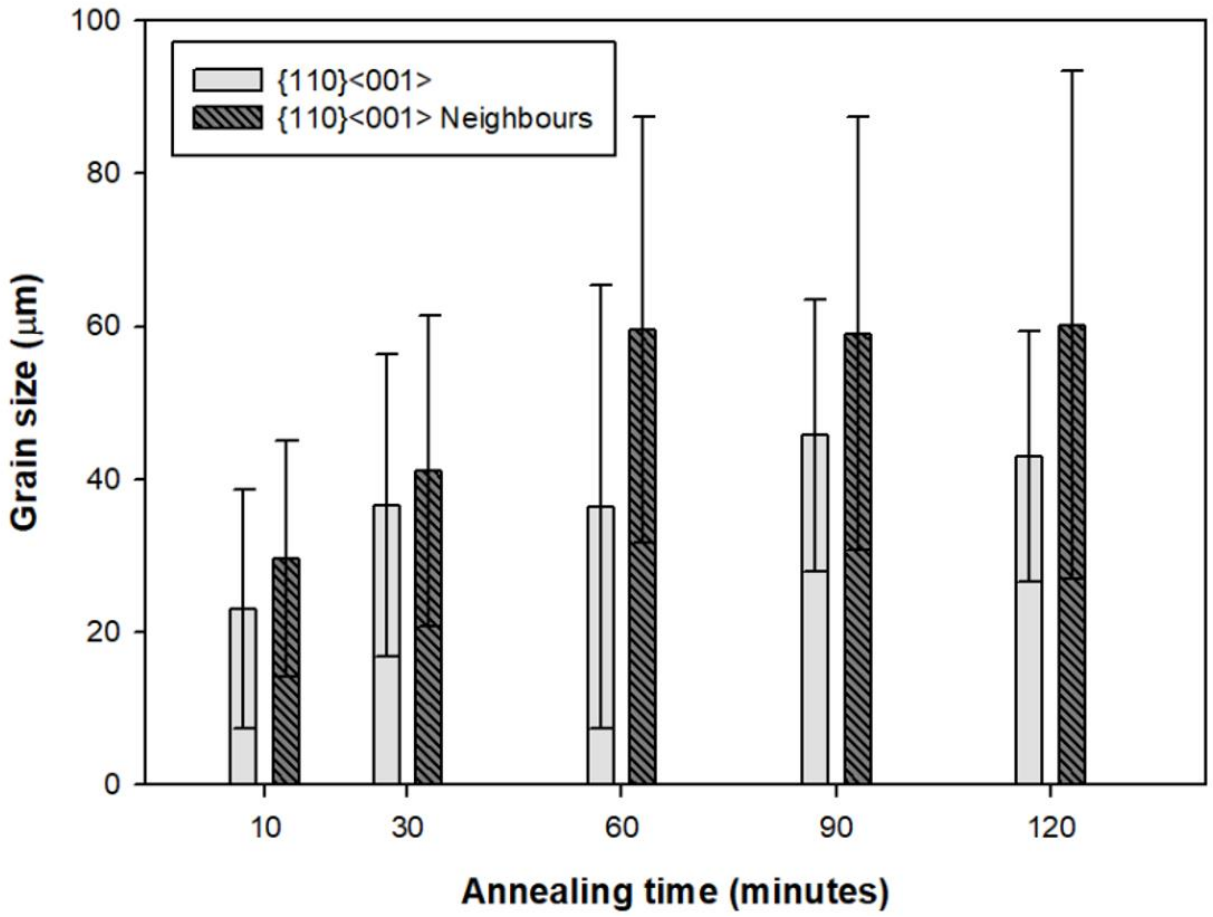

Fig. 5.11. Comparison of the average grain sizes of the Goss grains and their neighbours at different annealing times.

{001}<350> Grains:

The variation of the grain boundary character of the {001}<350> grains with respect to the annealing time is shown in Fig. 5.12. Similar to the Goss grains, the {001}<350> grains also have higher fractions of high-angle ($20° \leq \Delta\theta < 45°$) and CSL boundaries at the beginning of annealing (10 minutes). The average grain size of the {001}<350> grains is essentially the same as that of their neighbours (Fig. 5.12), i.e. there is essentially no grain size advantage of the {001}<350> grains. Thus, essentially no grain growth is expected for the {001}<350> grains after 30 minutes

except for some grains with larger sizes than their neighbours (because of the difference in grain size of individual grains). As a result, the {001}<350> texture is rather weak at the beginning of annealing.

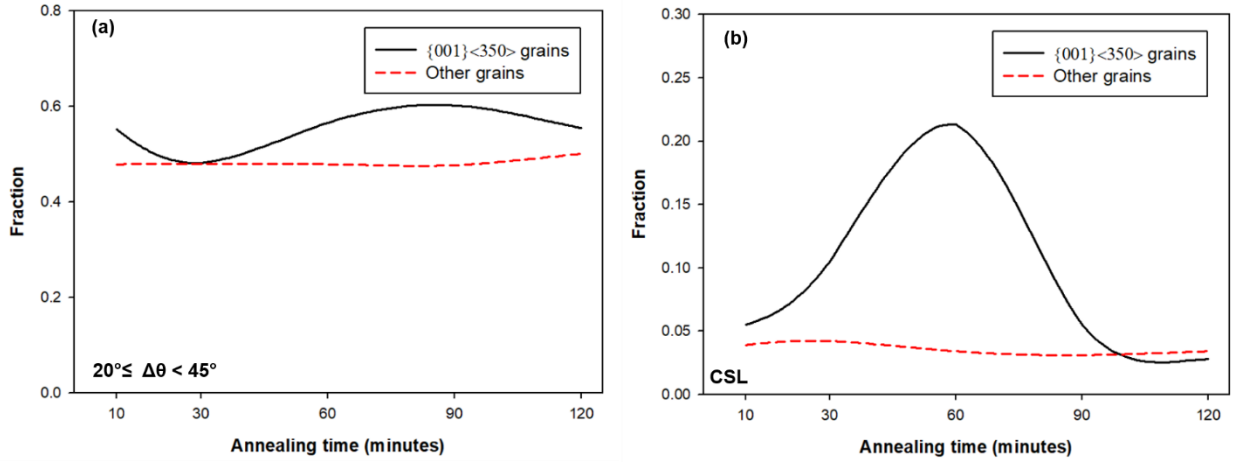

Fig. 5.12. Variations of grain boundary character of the {001}<350> grains and the other grains: (a) high-angle boundaries, (b) CSL boundaries.

After 60 minutes, the fraction of the high-angle boundaries of the {001}<350> grains becomes considerably higher than that of other grains, and the fraction of the high-mobility CSL boundaries is significantly higher than that of the other grains (~6 times). In the meantime, the average grain size of the {001}<350> grains is larger than their neighbours, which favours the growth of the {001}<350> grains, thus a strong {001}<350> texture (Fig. 5.6c) is observed. After that (90 and 120 minutes), the fraction of high mobility CSL boundaries drops significantly to the level of other grains, while that of the high-angle boundaries is still higher than other grains. In the meantime, the average grain size of the {001}<350> grains is smaller than that of their neighbours, thus the {001}<350> grains are gradually consumed by their neighbours, resulting in the weakening of the {001}<350> texture (Fig. 5.6d and 5.6e).

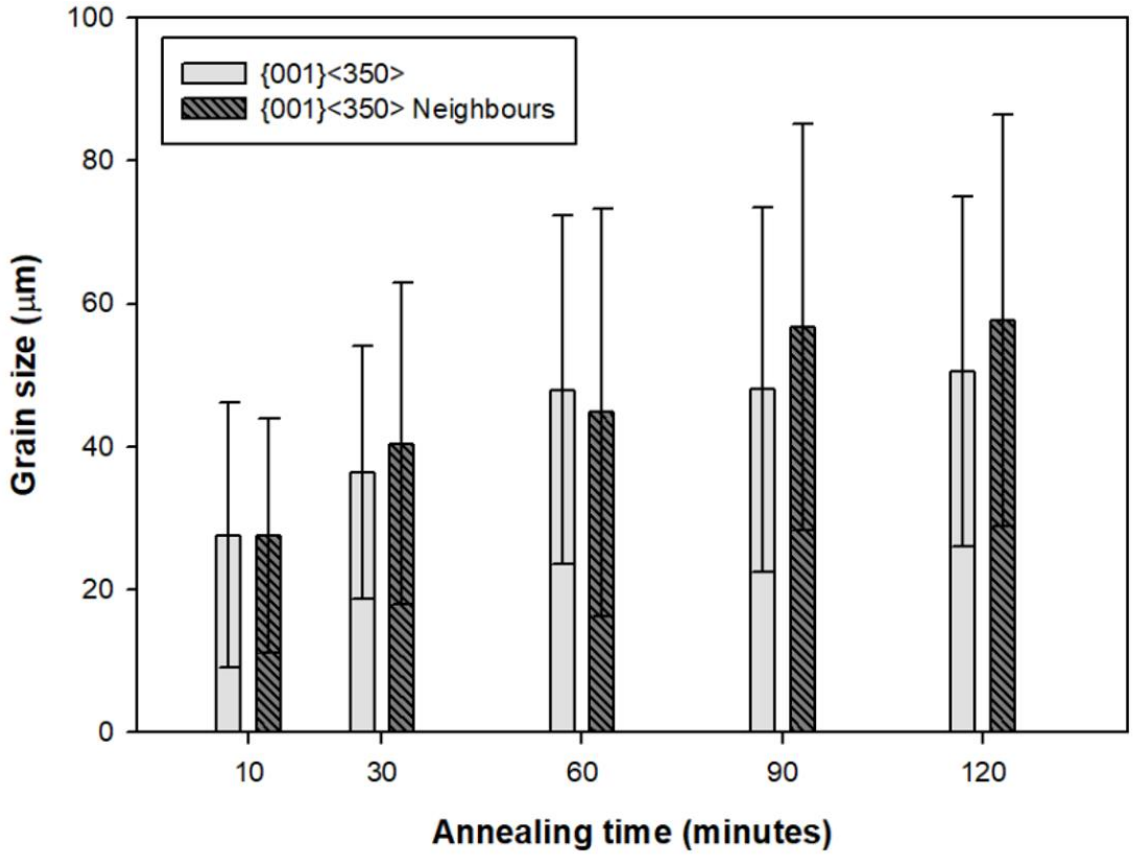

Fig. 5.13. Comparison of the average grain sizes of the {001}<350> grains and their neighbours grains at different annealing times.

The {111}<112> Grains:

Immediately after the completion of recrystallization (10 minutes), the {111}<112> texture is relatively weak (Fig. 5.6a), but the {111}<112> grains have higher fractions of high-angle boundaries (Fig. 5.14a) and CSL boundaries (Fig. 5.14b) than the other grains. Although the average grain size of these grains is slightly smaller than that of their neighbours, it should be noted that, the {111}<112> grains show a very heterogeneous grain size distribution, i.e. grains with sizes from ~3 μm to ~77 μm are all observed in the microstructure, and some of the {111}<112> grains may have a larger grain size than their neighbors. These grains can grow

because of the size advantage and the high mobility grain boundaries surrounding them. As a result, the {111}<112> texture is strengthened after 30 minutes of annealing.

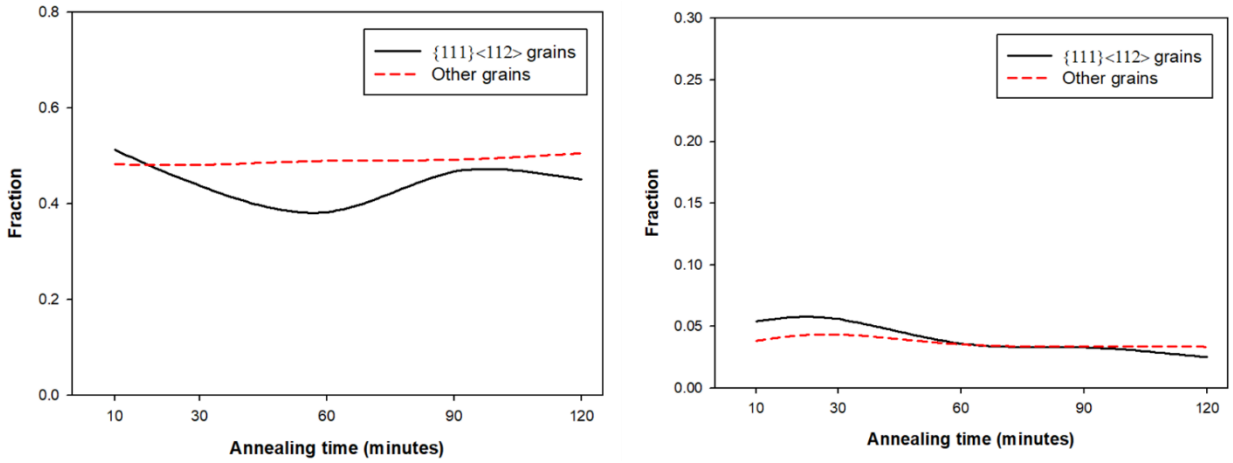

Fig. 5.14. Variations of grain boundary character of the {111}<112> grains and the other grains: (a) high-angle boundaries, (b) CSL boundaries.

With the increase of the annealing time (60 and 90 minutes), the fraction of high angle boundaries of the {111}<112> grains decreases, and it becomes lower than that of the other grains. Thus these grains have lower tendency to grow while the other grains have a higher fraction of high-mobility boundaries (Fig. 5.14a) and a larger grain size (Fig. 5.15). This results in the growth of the other grains (e.g. the {001}<350> grains discussed above) by consuming the {111}<112> grains. Thus, the <111>//ND texture is essentially *eliminated* when the annealing time was 60 or 90 minutes, while the θ-fibre grains grow considerably and dominate the texture.

After 90 minutes, the fraction of the high-mobility boundaries ($20° \leq \Delta\theta < 45°$ and CSL) of the {111}<112> grains is comparable to that of the other grains, while the average grain size of the {111}<112> grains is smaller than that of their neighbours. Again, due to the large variation in

grain size of these grains, some large than average grains may preferentially grow by consuming the surrounding smaller grains, which results in the strengthening of the {111}<112> texture again after annealing for 120 minutes. On the other hand, the {001}<350> texture is weakened.

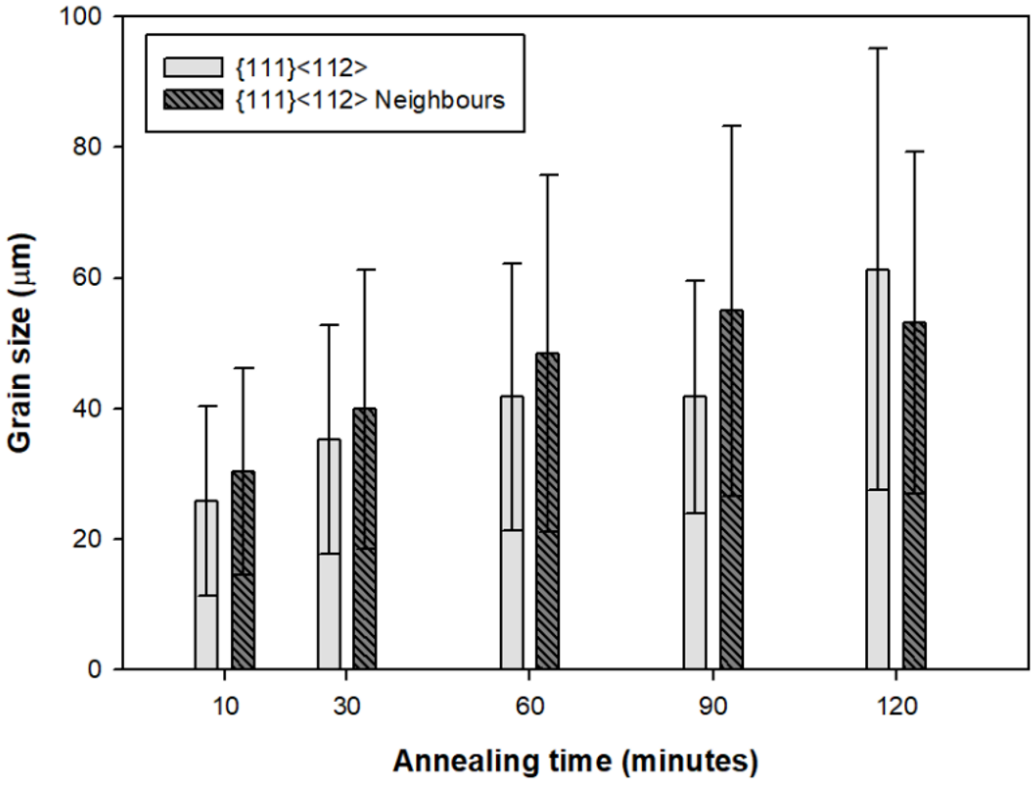

Fig. 5.15. Comparison of the average grain sizes of the {111}<112> grains and their neighbours at different annealing times.

It should be noted that, although the statistic analysis of the grain boundary character and grain size in the above discussion gives some *rough* explanations on the formation of the different textures during annealing at different times, it is still far from a complete understanding of the mechanisms involved in the grain growth process. It is well known that crystallographic texture is only one of the many factors that affect the grain growth process, and even in this aspect, the relationships between the mobility, energy and misorientation of grain boundaries are still not

known accurately [10]. One of the most important factors that affect the grain growth process is the Zener drag effect due to the presence of solutes and second phase particles in the matrix and the segregation of particles at the boundaries, which is not able to be investigated using the EBSD data. On the other hand, the statistic analysis of the grain boundary character inevitably ignored the grain boundary curvatures of individual grains, which is also an important factor influencing grain boundary migration [34-38]. Finally, the grain growth process itself changes the grain boundary character both globally and locally, and the local change of the character was overlooked during statistic analysis. Thus further work using advanced in-situ technologies are definitely needed to investigate the annealing process in a more elaborate way.

5.5 Conclusions

The evolution of texture of a 2.8 wt% Si non-oriented electrical steel was investigated during thermomechanical processing, i.e. hot rolling, hot band annealing, cold rolling and final annealing. The origins of the textures at every stage were analyzed against the theories/models existing in the literature. Focus was placed on the final annealing process where different final textures were obtained through the change of annealing time under the same annealing temperature.

Although started from the same cold rolling texture, annealing at the same temperature for different times gave rise to significantly different textures. After 60 or 90 minutes, the <111>//ND (γ-fibre) texture can be essentially eliminated, while the <001>//ND (θ-fibre) texture is considerably enhanced. On the other hand, annealing for 30 or 120 minutes promoted the γ-fibre texture while the θ-fibre is suppressed.

The presence of a higher fraction of high mobility grain boundaries (high angle and high mobility CSL) of some grains than that of their neighbours makes them tend to grow, but the direction of the growth is determined by the relative grain sizes across the boundary. A statistic analysis of the grain boundary character and grain size advantage roughly explained the formation of the different textures during annealing at different times.

References

1. Moses, A. J. (1990). Electrical steels: past, present and future developments. IEE Proceedings A (Physical Science, Measurement and Instrumentation, Management and Education), 137(5), 233-245.

2. Lyudkovsky, G., Rastogi, P. K., & Bala, M. (1986). Nonoriented electrical steels. JOM, 38(1), 18-26.

3. Mehdi, M., He, Y., Hilinski, E. J., & Edrisy, A. (2017). Effect of skin pass rolling reduction rate on the texture evolution of a non-oriented electrical steel after inclined cold rolling. Journal of Magnetism and Magnetic Materials, 429, 148-160.

4. He, Y., & Hilinski, E. J. (2016). Texture and magnetic properties of non-oriented electrical steels processed by an unconventional cold rolling scheme. Journal of Magnetism and Magnetic Materials, 405, 337-352.

5. Honda, A., Fukuda, B., Ohyama, I., & Mine, Y. (1990). Effects of magnetic properties of nonoriented electrical steel sheets on motor efficiency. Journal of Materials Engineering, 12(1), 41-45.

6. Kestens, L., & Jacobs, S. (2008). Texture control during the manufacturing of nonoriented electrical steels. Texture, Stress, and Microstructure, 2008.

7. Shimanaka, H., Ito, Y., Matsumara, K., & Fukuda, B. (1982). Recent development of non-oriented electrical steel sheets. Journal of Magnetism and Magnetic Materials, 26(1-3), 57-64.

8. PremKumar, R., Samajdar, I., Viswanathan, N. N., Singal, V., & Seshadri, V. (2003). Relative effect (s) of texture and grain size on magnetic properties in a low silicon non-grain oriented electrical steel. Journal of Magnetism and Magnetic Materials, 264(1), 75-85.

9. Park, J. T., & Szpunar, J. A. (2005). Texture development during grain growth in nonoriented electrical steels. ISIJ international, 45(5), 743-749.

10. Humphreys, F. J., & Hatherly, M. (2012). Recrystallization and related annealing phenomena. Elsevier.

11. Hutchinson, W. B., & Nes, E. (1992). Texture development during grain growth-a useful rule-of-thumb. In Materials Science Forum (Vol. 94, pp. 385-390). Trans Tech Publications.

12. Balke, P. (2002). Dynamics of microstructures in metal sheets: an orientation imaging microscopy study Groningen: s.n.

13. Rajmohan, N., & Szpunar, J. A. (2001). An analytical method for characterizing grain boundaries around growing goss grains during secondary recrystallization. Scripta materialia, 44(10), 2387-2392.

14. Harase, J., Shimizu, R., & Dingley, D. J. (1991). Texture evolution in the presence of precipitates in Fe− 3% Si alloy. Acta metallurgica et materialia, 39(5), 763-770.

15. Lin, P., Palumbo, G., Harase, J., & Aust, K. T. (1996). Coincidence site lattice (CSL) grain boundaries and Goss texture development in Fe-3% Si alloy. Acta Materialia, 44(12), 4677-4683.

16. Hayakawa, Y., & Szpunar, J. A. (1997). A new model of Goss texture development during secondary recrystallization of electrical steel. Acta materialia, 45(11), 4713-4720.

17. Rajmohan, N., Szpunar, J. A., & Hayakawa, Y. (1999). A role of fractions of mobile grain boundaries in secondary recrystallization of Fe–Si steels. Acta materialia, 47(10), 2999-3008.

18. Jian, W. A. N. G., Jun, L. I., Wang, X. F., Tian, J. J., Zhang, C. H., & Zhang, S. G. (2010). Effect of heating rate on microstructure evolution and magnetic properties of cold rolled non-oriented electrical steel. Journal of iron and steel research, international, 17(11), 54-61.

19. Hu, H. (1974). Texture of metals. Texture, Stress, and Microstructure, 1(4), 233-258.

Raabe, D., & Lücke, K. (1993). Textures of ferritic stainless steels. Materials science and technology, 9(4), 302-312.

20. Hölscher, M., Raabe, D., & Lücke, K. (1994). Relationship between rolling textures and shear textures in fcc and bcc metals. Acta metallurgica et materialia, 42(3), 879-886.

21. Mishra, S., Därmann, C., & Lücke, K. (1984). On the development of the Goss texture in iron-3% silicon. Acta Metallurgica, 32(12), 2185-2201.

22. Böttcher, A., & Lücke, K. (1993). Influence of subsurface layers on texture and microstructure development in RGO electrical steel. Acta metallurgica et materialia, 41(8), 2503-2514.

23. Kim, J. K., Lee, D. N., & Koo, Y. M. (2014). The evolution of the Goss and Cube textures in electrical steel. Materials Letters, 122, 110-113.

24. Dillamore, I. L., Morris, P. L., Smith, C. J. E., & Hutchinson, W. B. (1972, September). Transition bands and recrystallization in metals. In Proceedings of the Royal Society of London A: Mathematical, Physical and Engineering Sciences (Vol. 329, No. 1579, pp. 405-420). The Royal Society.

25. Dorner, D., Zaefferer, S., & Raabe, D. (2007). Retention of the Goss orientation between microbands during cold rolling of an Fe3% Si single crystal. Acta materialia, 55(7), 2519-2530.

26. Park, J. T., & Szpunar, J. A. (2003). Evolution of recrystallization texture in nonoriented electrical steels. Acta Materialia, 51(11), 3037-3051.

27. Lücke, K. (1993) The orientation dependence of grain boundary motion and the formation of recrystallization textures. Can. Metall. Q. 13, 261–265.

28. Hölscher, M., Raabe, D., & Lücke, K. (1991). Rolling and recrystallization textures of bcc steels. steel research international, 62(12), 567-575.

29. Ibe, G. E. R. H. A. R. D., & Lücke, K. (1966). Growth selection during recrystallization of single crystals. Recrystallization, Grain Growth and Textures, 434.

30. Liu, H. T., Liu, Z. Y., Sun, Y., Qiu, Y. Q., Li, C. G., Cao, G. M., ... & Wang, G. D. (2012). Formation of {001}< 510> recrystallization texture and magnetic property in strip casting non-oriented electrical steel. Materials Letters, 81, 65-68.

31. Liu, H., Liu, Z., Cao, G., Li, C., & Wang, G. (2011). Microstructure and texture evolution of strip casting 3wt% Si non-oriented silicon steel with columnar structure. Journal of Magnetism and Magnetic Materials, 323(21), 2648-2651.

32. Sanjari, M., He, Y., Hilinski, E. J., Yue, S., & Kestens, L. A. (2016). Development of the {113}< uvw> texture during the annealing of a skew cold rolled non-oriented electrical steel. Scripta Materialia, 124, 179-183.

33. Hayakawa, Y., Muraki, M., & Szpunar, J. A. (1998). The changes of grain boundary character distribution during the secondary recrystallization of electrical steel. Acta materialia, 46(3), 1063-1073.

34. Zener, C. (1949). Private communication to CS Smith. Trans. AIME, 175(15), ll.

35. Lücke, K., & Detert, K. (1957). A quantitative theory of grain-boundary motion and recrystallization in metals in the presence of impurities. Acta Metallurgica, 5(11), 628-637.

36. Lucke, K., & Stuwe, H. (1963). Recovery and recrystallisation. New York, Interscience, 9, 118-124.

37. Cahn, J. W. (1962). The impurity-drag effect in grain boundary motion. Acta metallurgica, 10(9), 789-798.

Chapter 6: Effect of skin pass rolling reduction rate on the texture evolution of a non-oriented electrical steel after inclined cold rolling

6.1 Introduction

Non-oriented electrical steels have been widely utilized as a core lamination material for electric motors, generators, alternators, etc. to amplify magnetic flux, and have thus found many applications in general appliances, wind mills, electric vehicles (EVs), etc. [1-5]. Superior magnetic properties are desired in traction motors in EV, since high torque is required when accelerating, which needs a high magnetic flux density for the winding core, while at regular driving speeds, core loss is desired to be minimum to reduce the energy loss, which requires the core material to have low iron loss [4]. It is well known that the magnetic properties of non-oriented electrical steels are influenced by a number of factors such as chemical composition, sheet thickness, grain size, residual stress, crystallographic texture, etc. [1-3, 5]. In order to improve the magnetic permeability and reduce core loss, a <001>//ND texture (θ-fibre), which comprises the cube, rotated cube, and all orientations with the {001} planes parallel to the sheet plane, is desired since it contains the most number of the easy magnetization axes <001> in the sheet plane. The <111>//ND (γ-fibre) texture has the hard magnetization axes <111> in the sheet plane, and thus needs to be suppressed in the final steel sheets [6, 7].

For electrical steel with a given chemical composition, the final texture of the sheet is highly dependent on the manufacturing processes that usually include casting, hot rolling, cold rolling and annealing. During crystallization (solidification), plastic deformation, phase transformation and recrystallization, the orientations of the crystals will be altered several times, and the final texture will be affected by all these processes [8-10]. Although numerous investigations have

already been carried out to optimize the operational parameters (e.g. temperature, rolling reduction rate, annealing conditions, etc.), very limited improvement in the final texture has been achieved. This is mainly due to the fact that, in conventional rolling, the θ-fibre formed in hot rolling generally changes to the γ- and α-fibres after cold rolling and annealing. A number of unconventional processing techniques, e.g. cross rolling [6, 11], two-stage cold rolling [12-15], columnar grain growth [16], phase transformation annealing [17, 18], etc., have also been developed to optimize the texture of non-oriented electrical steels. However, these techniques are usually difficult to be implemented in industry for mass production.

In a recent study, He et al. [19, 20] investigated the influence of initial texture on the final annealing texture of non-electrical steels, in which the cold rolling direction was intentionally inclined at an angle between 0° and 90° to the hot rolling direction (also known as *inclined rolling*). It was shown that inclined rolling was able to significantly enhance the cube texture in the final sheets when the inclination angle was 60°. Although the inclined rolling process was not feasible to be implemented in a continuous production line either, it was proven that by simply changing (rotating) the initial texture before cold rolling, the final annealing textures could be significantly altered. An advantage of inclined rolling was that the chemistry, microstructure and processing history can all be kept the same, while only the initial texture was changed. In this way, it was able to investigate the effect of initial texture on the deformation and annealing textures without the influence of other parameters such as microstructure, chemistry and processing history. In inclined rolling, by simply cutting the sample at an angle to the hot rolling direction and rolling the material conventionally, the initial texture can be altered in a wide range, and this makes it possible to examine how different initial textures affect the deformation and final annealing textures. Inclined cold rolling does not require special heat treatments after deformation, while the proposed

alternatives in the literature such as phase transformation annealing, columnar grain growth, etc., usually need long holding times at high temperatures to achieve the optimal texture, which is both energy and time consuming.

Since in non-oriented electrical steel processing the annealed thin sheets are usually subjected to final skin pass rolling in order to flatten and straighten the sheets, it is of interest to investigate the effect of skin pass rolling on the texture of the annealed steel. Also, skin-pass-rolled sheets need to be final annealed to release the stress introduced during the final rolling pass, thus it is also interesting to examine if the skin pass rolling has an effect on the final annealing texture. In this paper, a non-oriented electrical steel was first incline rolled to a thickness of 0.5 mm (with ~78% reduction) and annealed. It was then skin pass rolled (without applying tension) to various reduction rates up to 20%. The textures before skin pass rolling, after skin pass rolling, and after final annealing were evaluated by electron backscatter diffraction (EBSD) techniques. The effect of the rolling reduction rate on the deformation and final annealing textures was examined.

6.2 Material and Experimental Procedures

The material investigated was a low silicon (0.88 wt%) non-oriented electrical steel, and its chemical composition is given in Table 6.1. The steel was melted in a vacuum furnace and cast into 200 × 200 × 300 mm^3 (width × thickness × length) ingots. The steel was then heated up to a nominal temperature of 1311 K (1038 ˚C) and hot rolled to a thickness of 25 mm (from 200 mm) with ~90% reduction. After removing the oxides from the surfaces, a second hot rolling (at the same reheat temperature of 1038 °C) was carried out in order to further reduce the thickness to 2.5 mm (also with ~90% reduction). The steel was then pickled at 355 K (82 ˚C) using a hydrochloric acid solution. The material was subsequently annealed at 1113 K (840 ˚C) for 60 hours in a dry 100% hydrogen atmosphere.

Table 6.1. Chemical composition of the investigated steel (wt%).

C	Mn	P	S	Si	Al	Fe
0.002	0.31	0.01	0.001	0.88	0.46	balance

The annealed steel was then cut into small rectangular pieces (200 × 50 mm^2) at various angles (0˚, 30˚, 45˚, 60˚, 90˚) to the hot rolling direction (HRD), which were cold rolled to a final thickness of 0.5 mm (Fig. 6.1). The cold-rolled steel sheets were subsequently annealed at 1023 K (750 ˚C) for 5 minutes in argon protected atmosphere and furnace cooled. The texture after annealing was characterized by electron backscatter diffraction (EBSD). Two samples, i.e. those incline rolled at 45° and 60° to the HRD, were selected to undergo further skin pass rolling with various reduction rates (5%, 10%, 15% and 20%). The skin-pass-rolled samples were annealed again (final annealing) at 750°C for 5 minutes, and the textures were characterized.

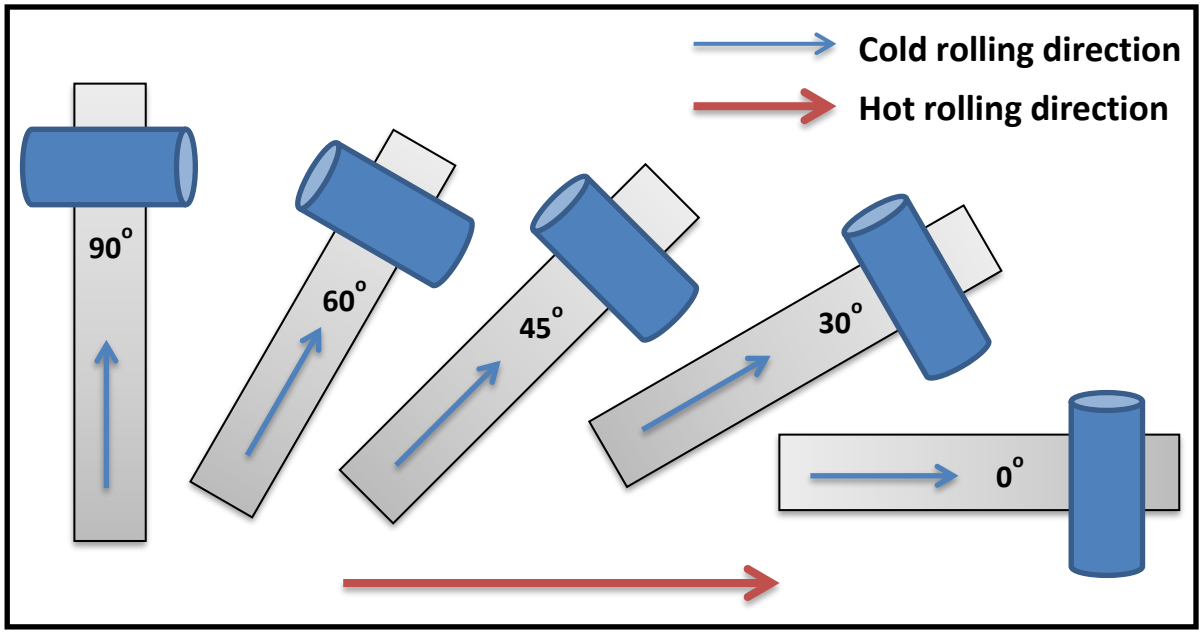

Fig. 6.1. Schematic of inclined cold rolling and sample cutting from the hot band with angles 0° to 90° to the hot rolling direction (HRD).

The microstructures of the steel after cold rolling, annealing and skin pass rolling were characterized by optical microscopy. The samples were prepared using conventional metallographic procedures and etched with a 2% nital solution for 30 seconds. The grain size was measured according to ASTM standard (ASTM E112-96) [21]. For EBSD characterization, a final polishing step using a 0.05 μm colloidal silica solution was applied after the conventional metallographic preparation steps. EBSD scans were performed on the RD-ND cross-sections in a field emission gun scanning electron microscope (FEG-SEM) (Nova NanoSEM, FEI) equipped with an EDAX Orientation Imaging Microscopy system (OIM 6.2). The scanned areas (approximately 0.5×2.2 mm^2) usually covered almost the entire thickness of the steel sheets. Orientation distribution functions (ODFs) were then calculated using a harmonic series expansion method, in which the series rank and the Gaussian half-width were set 22 and 5°, respectively [22]. Typical texture components were plotted on the $\varphi_2 = 45°$ section of the Euler space (Bunge notation) [23, 24]. The volume fractions of ideal textures and fibres were calculated from the ODFs within a 15° tolerance from the exact orientation. Taylor factors were calculated for the major texture components using a family of slip systems for bcc metals, i.e. {110}<111>, {211}<111> and {321}<111>.

6.3 Results

6.3.1 Microstructure

After inclined cold rolling at various angles (0°, 30°, 45°, 60° and 90°) to the HRD, the microstructures were characterized and shown in Fig. 6.2. Three differently etched regions can be noticed in the optical micrographs of the deformed sheets: i) lightly etched regions (L) that essentially contain no shear/deformation bands, indicating relatively homogeneous plastic

deformation, ii) moderately etched regions (M) with visible shear bands in some areas within the grains, iii) heavily etched (dark) regions (H) with dense dislocations, implying highly inhomogeneous plastic deformation and high stored energy. These three regions are present in all the samples regardless of the rolling direction to the HRD. However, it is noted that rolling at 30°, 45° and 60° to the HRD produced more inhomogeneous regions (M and H) than those rolled at 0° and 90° angles.

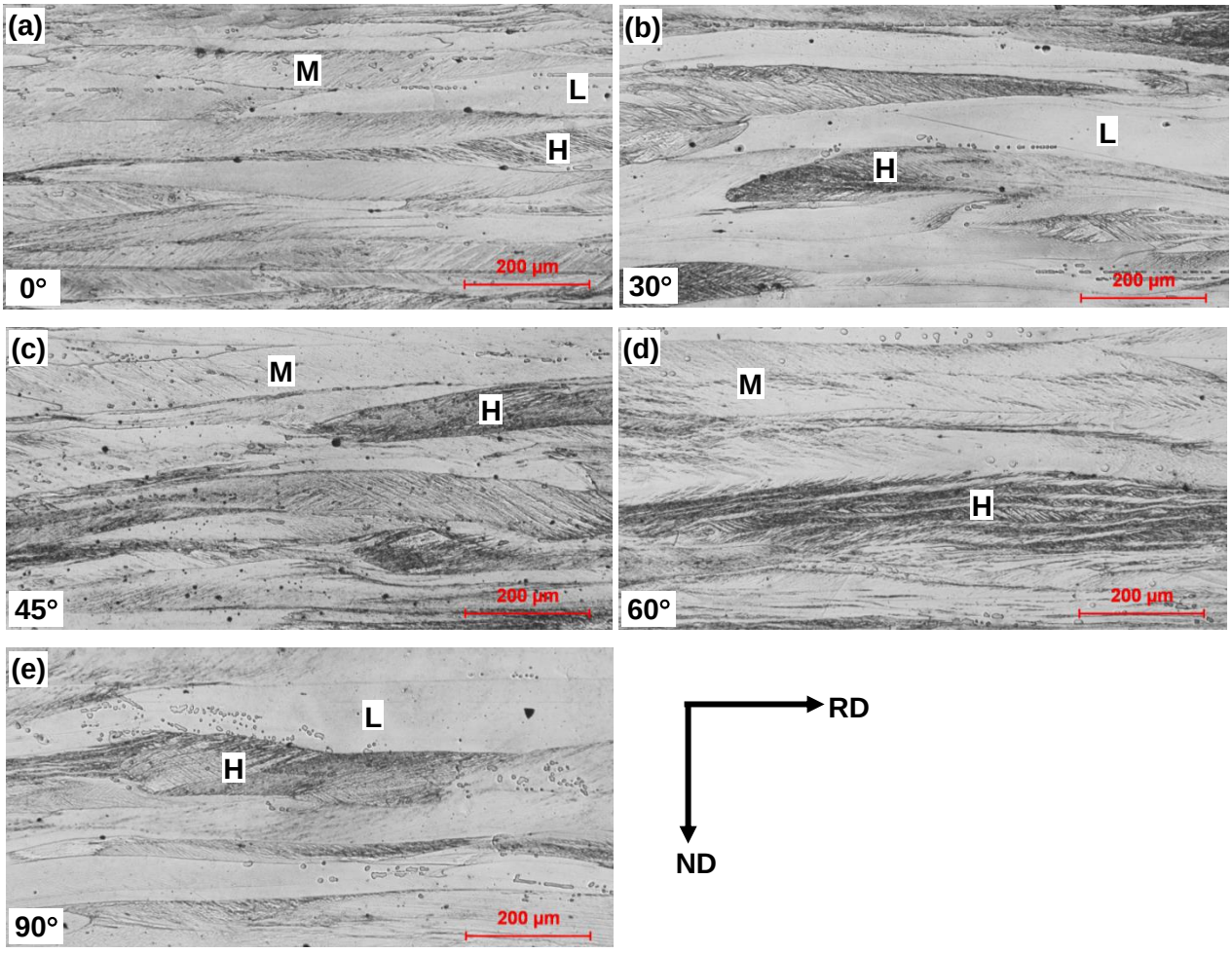

Fig. 6.2. Optical micrographs showing the microstructures of samples cold-rolled at various angles to the hot rolling direction: (a) 0°, (b) 30°, (c) 45°, (d) 60°, and (e) 90°.

The microstructures of the samples after annealing at 1023 K (750 ˚C) for 5 minutes are shown in Fig. 6.3. Although the cold rolling direction is at different angles to the HRD, the average grain sizes of all the samples after annealing are very close with each other, i.e. from ~28 µm to ~34 µm (Table 6.2). Rolling at 60° to the HRD produces the smallest average grain size (27.9 µm), while cross rolling (90°) results in the largest average grain size (33.9 µm). The microstructure is inhomogeneous at all the rolling angles, i.e. in each case, the grain diameters vary from a few microns to more than 100 µm.

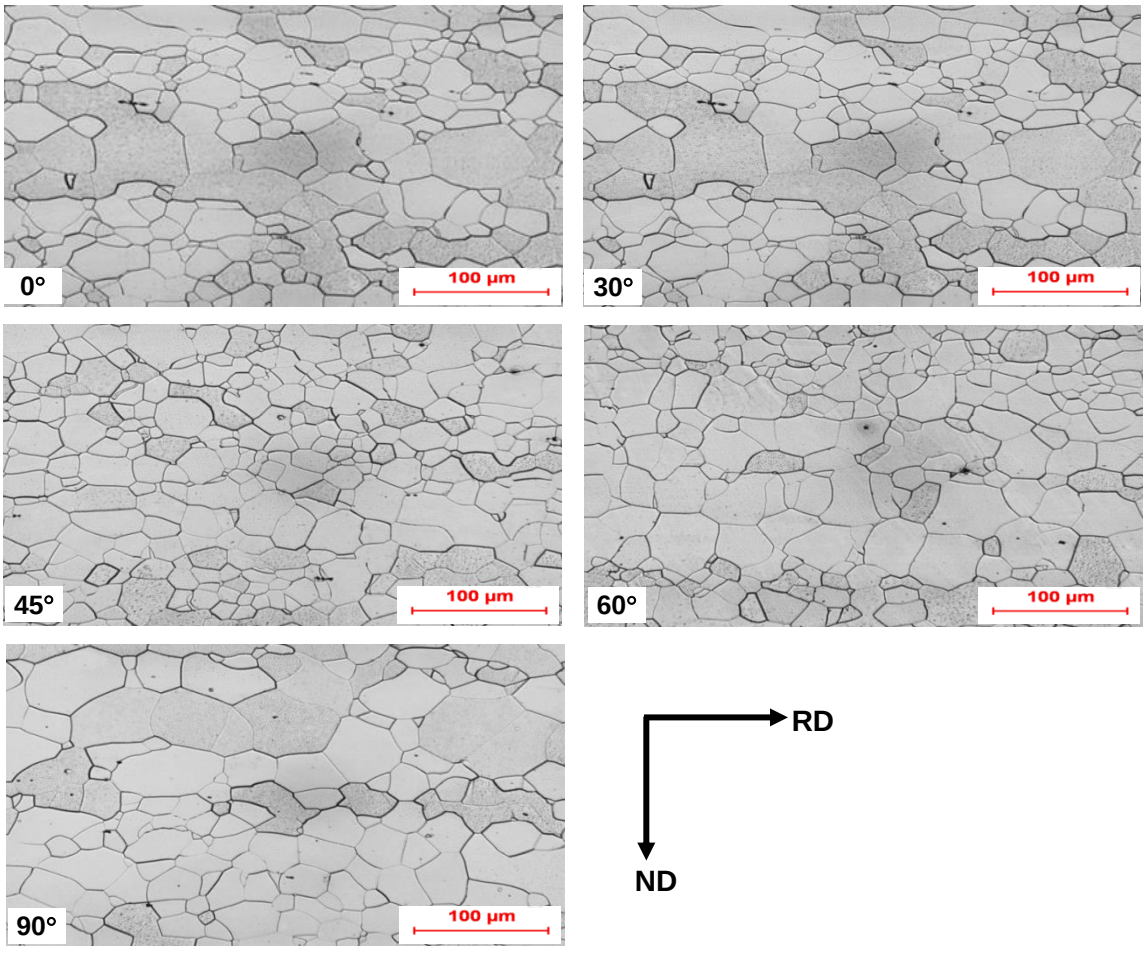

Fig. 6.3. Optical micrographs of the electrical steel samples (cold rolled at various angles to the HRD) after annealing at 1023 K (750 ˚C) for 5 minutes followed by furnace cooling.

Table 6.2. Average grain sizes of the annealed samples after inclined rolling.

Rolling angle	ASTM grain Number (n)	ASTM grain size (μm)
0°	7.12	28.2 ± 4
30°	7.04	32.5 ± 4
45°	6.98	32.1 ± 1
60°	7.40	27.9 ± 2
90°	6.57	33.9 ± 3

The EBSD inverse pole figure (IPF) maps of the samples after cold rolling and annealing are illustrated in Fig. 6.4. In all the maps, the dominant colors are red, orange and pink, indicating that most of the crystals have orientations close to <001>//ND. There is essentially no blue color, implying that there is almost no <111>//ND (γ-fibre) texture. Some purple grains are apparently shown in all the samples (especially in the sample rolled at 0° to the HRD), which indicates that a <112>//ND texture is present. Crystals in green color (<011>//ND) are also noticed in all the samples. In each case, the grain structure is inhomogeneous, i.e. grain sizes vary considerably from a few microns to more than 100 microns, which is similar to those observed in optical micrographs (Fig. 6.3). The small grains are usually distributed in bands parallel to the rolling direction. After conventional rolling (0°) and annealing, the grains near the sheet surfaces are generally smaller than those in the middle thickness. When the angle is 30°, the small grains are distributed near the middle thickness plane, but there are still some small grains near the bottom surface. At 45° and 60°, the small grains tend to move to the surfaces again. At 90° (cross rolling), the grain size is more uniform than those rolled at other angles, and the amount of small grains is also less (the average grain size is the largest). The grain size distributions of all the samples (calculated from the EBSD maps) are shown in Fig. 6.5. It is seen that, if the inclination angle is 0° or 30°, the

grains have two peaks at ~35 μm and 50 μm. When the angle is equal to or greater than 45°, there is only one peak at ~35 μm.

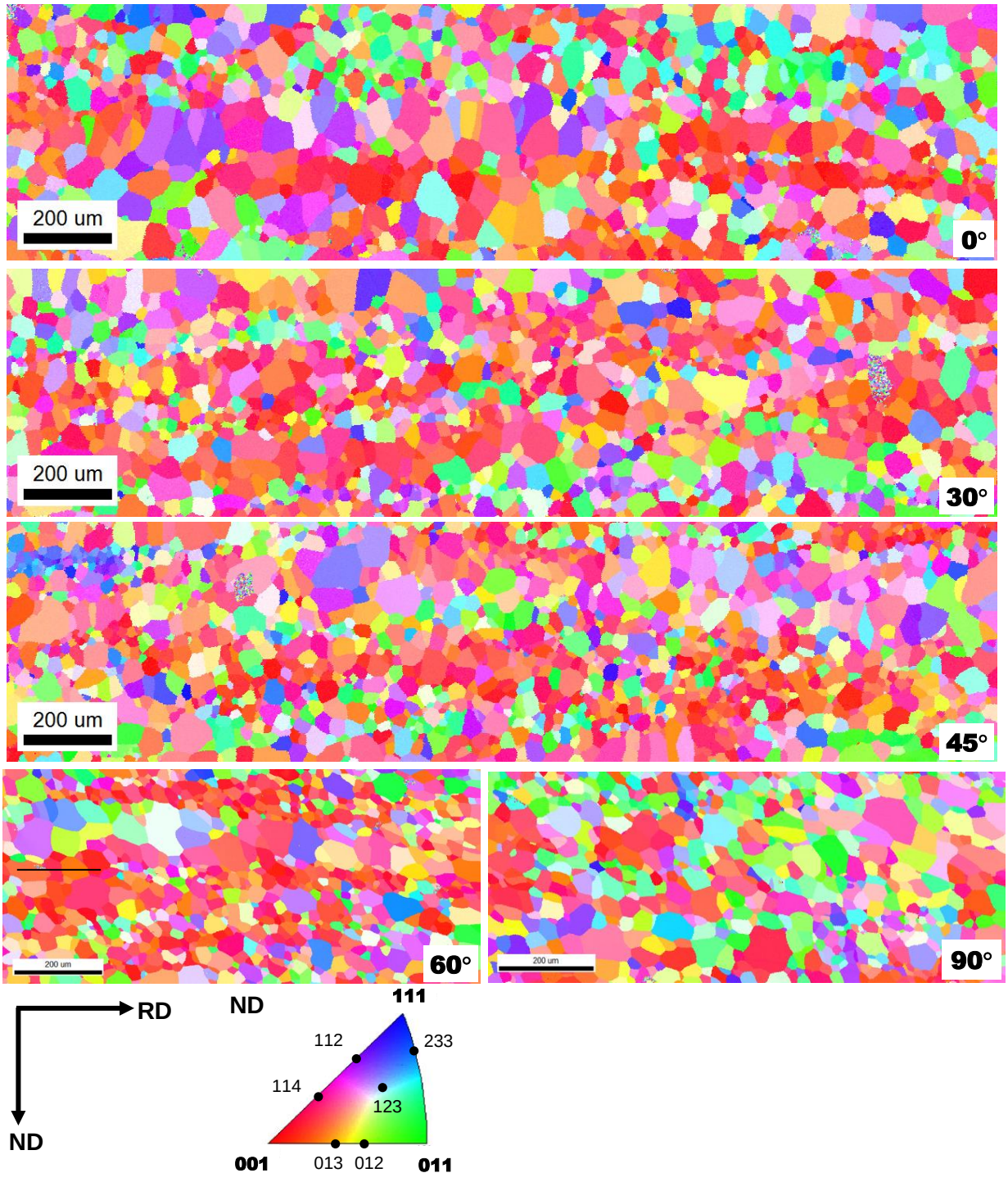

Fig. 6.4. Inverse pole figure maps of the electrical steel after annealing at 750°C for 5 minutes. The angle shown in each map was the angle between CRD and HRD during cold rolling.

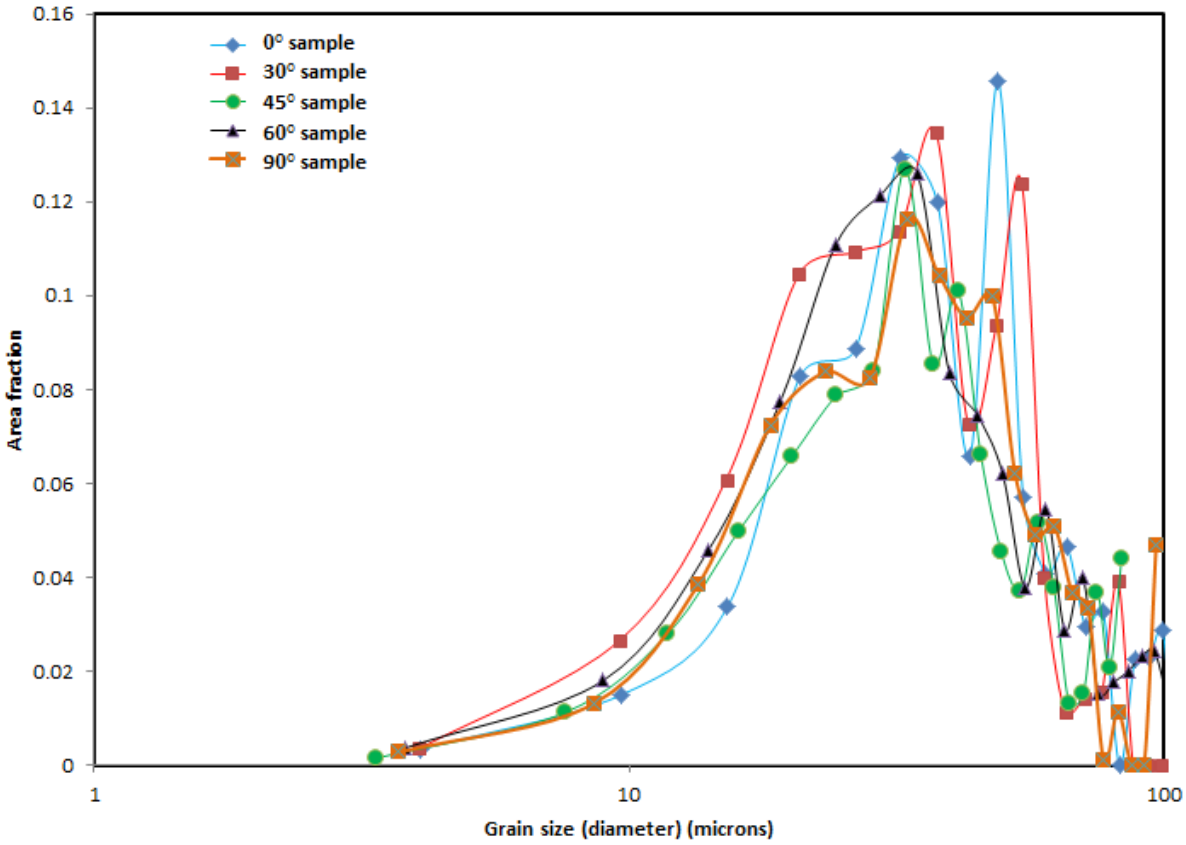

Fig. 6.5. Variation of the grain size distribution with respect to the angle between CRD and HRD. The average grain sizes for the 0°, 30°, 45°, 60°, and 90° samples are, 26.7, 23.6, 24.3, 24.4 and 25.2 microns respectively.

6.3.2 Textures before and after Inclined Cold Rolling

It is well known that the as-cast texture is primarily dependent on the solidification cooling rate and the dendrite columnar structure [25]. During cooling, there is a high temperature gradient in the direction perpendicular to the mould surface and towards the center of the ingots, which favors the growth of <001>//ND grains [26, 27]. After hot rolling, the texture was dominated by rotated cube, Goss, and cube components in our steel, as shown elsewhere [19].

Upon annealing, the texture was slightly randomized and the main texture component changed to {001}<$\frac{1}{2}$ $\frac{\sqrt{3}}{2}$ 0>, which was 15° from the rotated cube on the θ-fibre [20]. There were also some minor {111}<121> and {554}<225> components. With inclined cold rolling at different angles to the hot rolling direction, the cold-rolling textures all consisted of a similar overall range of preferred orientations typical of bcc metals after rolling, i.e. the <111>//ND and <110>//RD fibres [20]. However, the intensities of the different components within that range was considerably different. For conventional rolling, the texture was composed of strong {112}<110> and rotated cube components (maximum intensity of ~7), while for inclined rolling at all the angles, the maximum intensity was increased to ~10 or more. The rotated cube component was usually intensified (except for inclined rolling at 30° where the rotated cube was considerably weakened), while the {112}<110> component was decreased with the increase of the inclination angle.

6.3.3 Texture after Inclined Rolling and Annealing

The orientation distribution functions (ODFs) calculated from the EBSD maps (Fig. 6.4) are illustrated in Fig. 6.6. In all the cases, the textures are featured by a strong θ-fibre, and there is essentially no γ-fibre. This is significantly different from the textures usually observed in low carbon steels after conventional rolling and annealing [8, 25], where a strong α-fibre together with a γ-fibre are the most common components. If the inclination angle is 0° (conventional rolling), the texture is characterized by a maximum orientation at {115}<7 13 4>, and the cube and rotated cube are also strong. If the cold rolling is conducted at 30° to the HRD, the annealing texture is featured by components such as {001}<140> (15° from cube), {115}<8 13 1> and {118}<441>,

etc., which are either on the θ-fibre or are very close to it. A {112}<110> orientation is also noted. When the inclination angle is increased to 45°, the texture is characterized by a strong {114}<352> component together with a few orientations on the θ-fibre (cube and rotated cube). Some α- and α*-fibres ({11h}<1 2 1/h>) [26] are also noted. The maximum texture intensity at this angle is the lowest among all the samples. When the angle between the CRD and HRD is 60°, the annealing texture is very close to the ideal texture, i.e. a θ-fibre with a strong cube orientation, and the maximum intensity is also the highest among all the samples. Thus, at this angle the cube texture is considerably enhanced. When the inclination angle is increased to 90° (cross rolling), the texture is characterized by {114}<041> and {115}<552> components, which are about 20° and 15°, respectively, from the θ-fibre. There is also a θ-fibre and a cube component extending to the {1 1 16}<4 12 1> orientation. Three <011>//ND components, i.e. Goss, brass and rotated Goss, are also seen at the bottom of the ODF section, although the intensities are relatively low. A strong {112}<461> component is noticed as well.

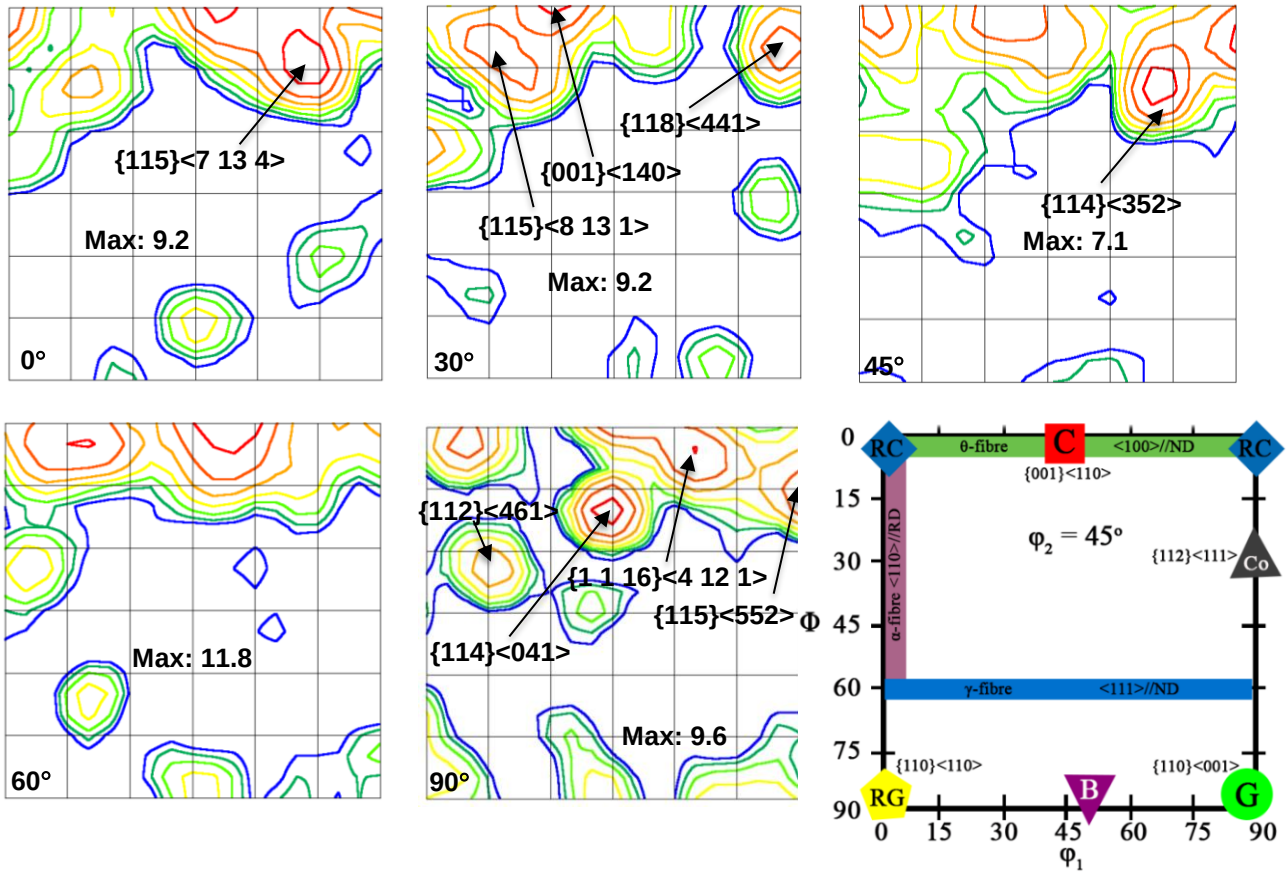

Fig. 6.6. Annealing (750°C for 5 minutes) textures of the electrical steel cold rolled at various angles with respect to the HRD. $\varphi_2 = 45°$ sections of the Euler space (Bunge notation). The texture key shows the locations of major texture components and fibres: C (Cube), G (Goss), B (Brass), Co (Copper), RC (Rotated cube), RG (Rotated Goss), <001>//ND (θ fibre), <111>//ND (γ-fibre), and <110>//RD (α-fibre).

It is thus seen that after inclined cold rolling and annealing, the textures are characterized by a strong θ-fibre or close to θ-fibre components. However, different inclination angles during cold rolling lead to different features of the annealing textures. To quantitatively compare the texture components obtained in each case, the volume fractions of the three typical fibres (i.e. α,

θ and γ) and the most important texture components in electrical steels (i.e. cube, rotated cube and Goss) are calculated and plotted against the inclination angle in Fig. 6.7. In all the cases, the γ-fibre has the lowest volume fraction, while the θ-fibre has the highest (Fig. 6.7a). When the inclination angle was increased from 0° to 30°, the γ- and α-fibres essentially do not change, while the volume fraction of the θ-fibre is slightly increased from ~0.25 to about ~0.275. If the inclination angle is further increased to 45°, the volume fraction of the γ-fibre is almost the same as those at 0° and 30°, but the fraction of the α-fibre is increased to ~0.20 from ~0.175, and that of the θ-fibre is decreased from ~0.275 to ~0.22. If the cold rolling is conducted at 60° to the HRD, both the γ- and α-fibres are considerably decreased, while the θ-fibre is significantly increased from ~0.25 (conventional rolling) to ~0.35. When the inclination angle is 90° (cross rolling), the γ-fibre increases slightly as compared to those at 0°, 30° and 45°, and the θ-fibre drops to approximately the same as that of 45°. The α-fibre essentially does not change as compared to that at 60°. Thus it is seen that cold rolling at an angle of 60° to the HRD leads to significant strengthening of the θ-fibre texture and considerable weakening of the γ- and α-fibres, thus giving rise to the best texture. Cold rolling at 45° to HRD leads to the lowest θ-fibre and highest α-fibre.

It is noted from Fig. 6.7b that increasing the inclination angle from 0° to 90° gradually decreases the volume fraction of the rotated cube component, although there is a slight increase at 60°. The Goss texture is very low in most of the cases, but when the inclination angle is 60° or 90°, the volume fraction is considerably increased. The cube component is increased slightly from about 0.06 at 0° to about 0.08 at 30° and 45°, but is significantly increased to more than 0.12 when the inclination angle is 60°. Further increasing the angle to 90° decreases the cube component

again to about 0.09, but it is still higher than conventional rolling. Thus inclined rolling at 60° promotes both the cube and Goss textures, and essentially does not affect the rotated cube texture.

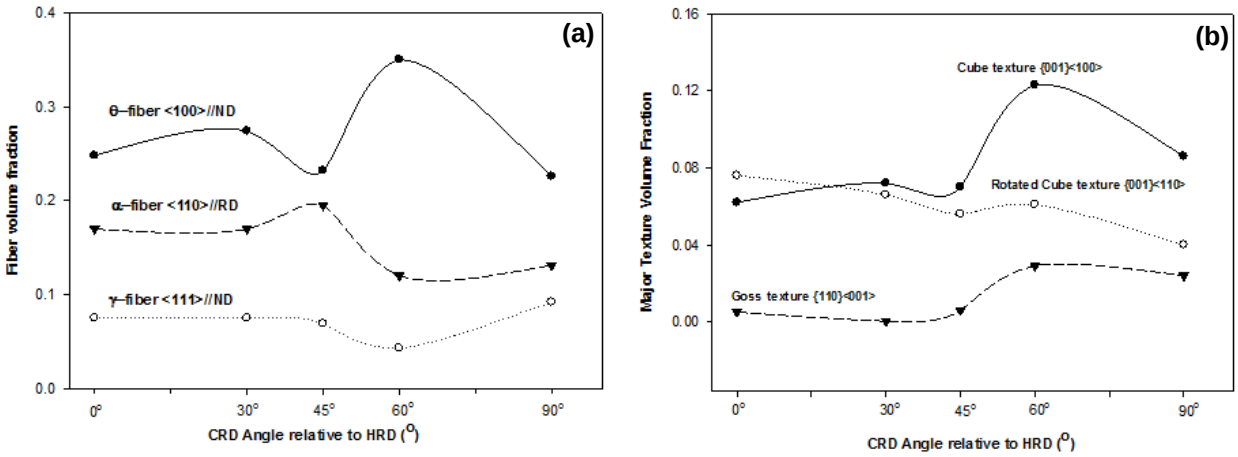

Fig. 6.7. Variation of the major texture fibres and components with respect to the angle between the CRD and HRD during cold rolling: (a) typical fibres, (b) texture components. The samples were annealed at 750°C for 5 minutes after cold rolling.

6.3.4 Texture after Skin Pass Rolling

In steel processing, it is a common practice that the cold-rolled and annealed steel sheet is subjected to a final skin pass (or temper rolling) to achieve good surface finish and flatness. The reduction rate of skin pass rolling is usually less than ~2% in order to minimize the change of the sheet thickness. In electrical steel processing, however, it is generally desired that the skin pass rolling not only straightens/flattens the steel sheet, but it also applies a certain amount of surface strain, which induces grain growth during the final annealing process [27]. The amount of strain is critical to the final microstructure/texture as insufficient strain will not provide enough driving

force for grain growth, while too much strain may lead to recrystallization instead of grain growth and change the final texture. The current research is intended to study the effect of the amount of plastic deformation during skin pass rolling on the formation of the final texture, thus the skin pass reduction rate is intentionally increased up to 20% to cover a wide range of strains.

It has been seen (Fig. 6.7a) that after inclined cold rolling and annealing, the magnetically favourable θ-fibre could be significantly enhanced at some inclination angles (e.g. 60°) or slightly weakened at other angles (e.g. 45°). Apparent changes on texture were noted when the inclination angle reached 45° (Fig. 6.7a). When the inclination angle was 60°, a significant difference was noticed. As the θ-fibre is the desired final texture in the sheet, it is thus of interest to examine if the subsequent skin pass rolling has an effect on this texture. Since the 45° and 60° samples have the lowest and highest, respectively, volume fractions of the θ-fibre, they are selected to undergo further 5% to 20% skin pass rolling to elucidate the effect of rolling reduction rate on the final texture.

Fig. 6.8 shows the IPF maps and textures of the 45° sample after skin pass rolling with various reduction rates. The initial sample contains ~22% of the θ-fibre after inclined rolling and annealing. Compared to the initial texture (Fig. 6.6), the main feature of the textures after skin pass rolling remains essentially the same, i.e. all the textures are still dominated by the θ-fibre, but there are apparent differences among the textures obtained at different reduction rates. With 5% reduction, the original {114}<352> orientation in the annealed steel is eliminated, while the rotated cube texture is strengthened. After 10% reduction, a {001}<140> component is produced, while the cube texture is considerably weakened. A strong {112}<461> orientation and a couple of <113>//ND components are also noted. Further increasing the reduction rate to 15% greatly reduces the cube texture, while the rotated cube is extended considerably towards the copper ({112}<111>) orientation. When the reduction rate reaches 20%, a typical {112}<110> orientation

on the α-fibre is produced, which becomes the strongest component in the texture. This orientation has been predicted to be a stable final orientation for plane-strain compression [9]. On the other hand, the cube component is slightly increased. Thus it is seen that, when the skin-pass reduction rate is increased up to 15%, the cube texture is gradually weakened, but it is slightly increases when the reduction rate reaches 20%. In the meantime, the originally weak {112}<461> component is gradually intensified and shifted towards the α-fibre, and finally forms a strong {112}<110> component.

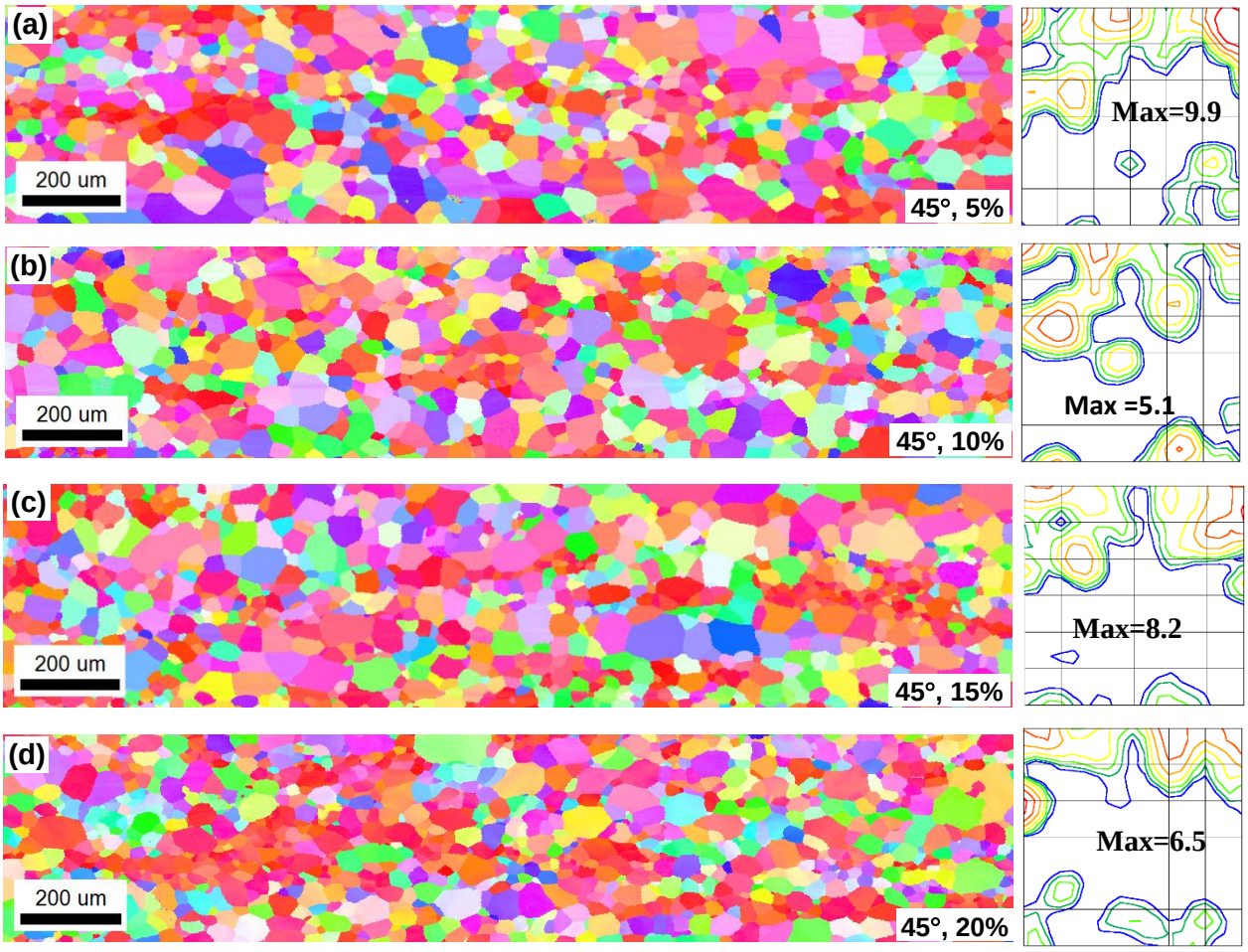

Fig. 6.8. IPF maps (left) and calculated ODFs (right) of the 45° sample after skin pass rolling at different thickness reduction rates: (a) 5%, (b) 10%, (c) 15%, and (d) 20%. φ_2=45° sections of the ODF's (Bunge notation).

The textures of the 60° sample (which contains ~35% of the θ-fibre in the annealed state) after skin pass rolling are shown in Fig. 6.9. Similarly to the 45° sample, increasing the reduction rate gradually intensifies the {112}<110> component on the α-fibre and weakens the cube texture. However, the cube texture is not significantly reduced even if the reduction rate reaches 15% and 20%. The rotated cube component is intensified first with 5% reduction, and weakened after 10% reduction. It is intensified again with 15% reduction and considerably weakened once more after 20% reduction.

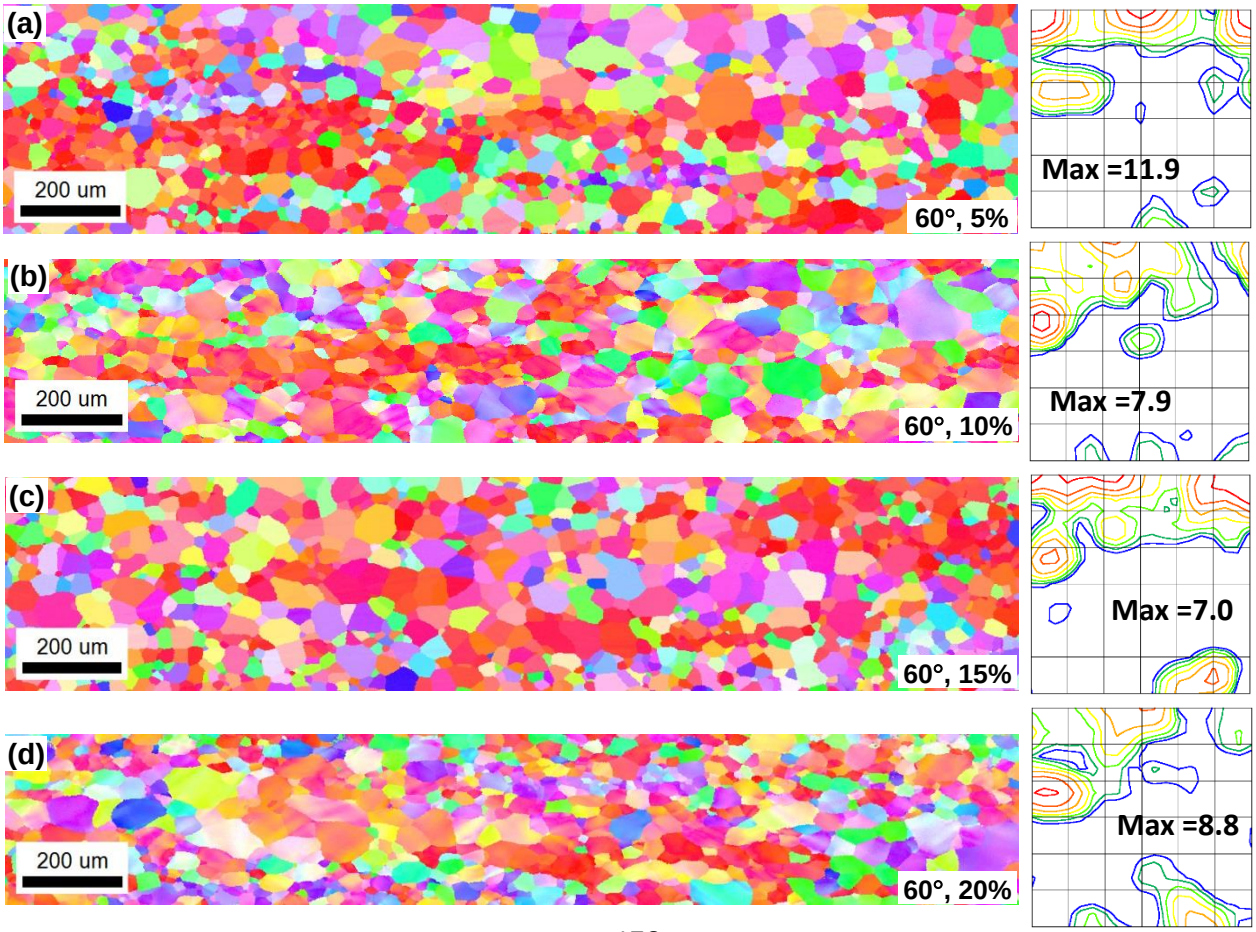

Fig. 6.9. IPF maps (left) and calculated ODFs (right) of the 60° sample after skin pass rolling at different thickness reduction rates: (a) 5%, (b) 10%, (c) 15%, and (d) 20%. φ_2=45° sections of the ODF's (Bunge notation).

The variations of the volume fractions of the textures with respect to the skin pass rolling reduction rate are compared in Fig. 6.10. It is seen from Fig. 6.10a that, although the 45° and 60° samples have considerably different volume fractions of the cube and rotated cube components after annealing, with the increase of the reduction rate, they change very similarly: the cube component is gradually decreased when the reduction rate increases, and it drops to a minimum when the reduction rate is 15% (further increasing the reduction rate to 20% slightly increases it again); the volume fraction of the rotated cube approximately follows a sine curve with respect to the reduction rate, i.e. two maxima are found at 5% and 15% reductions, and three minima are located at the 0%, 10% and 20% reductions. The Goss component has very small volume fractions in all the cases, and its variation with respect to the reduction rate is very small.

The variations of the fibre textures with respect to the reduction rate (Fig. 6.10b) are different in individual fibres. The θ-fibre decreases with the increase of reduction rate until 10%, where a minimum is noticed in both samples. Further increasing the reduction rate to 15% increases the volume fraction again. When the reduction rate reaches 20%, the θ-fibre essentially does not change in the 45° sample, while that of the 60° sample is considerably decreased (this decrease is mainly due to the decrease of the rotated cube as seen in Fig. 6.10a). The variations of the α-fibre and γ-fibre with respect to the reduction rate are much smaller than that of the θ-fibre, and the differences between the 45° and 60° samples are also small. After a 20% reduction, the α-

fibre is strengthened in both samples, but the 60° sample shows a larger increase than the 45° sample if compared to the initial annealing texture.

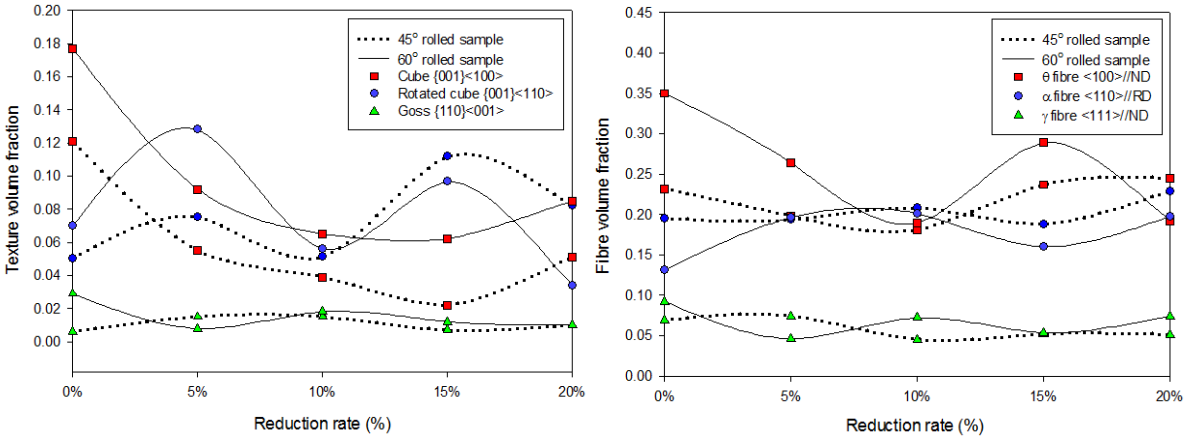

Fig. 6.10. Variations of the main texture components (a) and fibre textures (b) with respect to the reduction rate during skin pass rolling.

6.3.5 Texture after Final Annealing

For semi-processed electrical steels the final annealing treatment is usually carried out by the customer and not the steel supplier. It is typically performed after skin pass rolling or after punching, to increase grain size and eliminate residual stress. In this study, final annealing was accomplished for the skin-pass-rolled samples using the same conditions as for the annealing after inclined rolling, i.e. at 750 °C for 5 minutes. The IPF maps and their corresponding ODFs are shown in Fig. 6.11 and 12, respectively, for the 45° and 60° samples.

For the 45° sample (Fig. 6.11), final annealing restores the cube texture that has been reduced during skin pass rolling, i.e. the cube component that has been significantly reduced at 15% and 20% skin pass reduction appears again after final annealing. The rotated cube still remains

a main component for all the cases after annealing. It is noted that at all the reduction rates, a close to θ*-fibre texture (<113>//ND, with Φ≈25°) forms, although it is relatively weak and usually only has a few peaks along the fibre. The originally strong {112}<110> texture formed after 20% reduction is eliminated after annealing, but a partial fibre stretching from {112}<111> to {332}<113> along φ_1 = 90° is formed. It is also noted that the maximum texture intensity of the sample with a 10% reduction is significantly increased after annealing, i.e. from 5.1 to 12.8, while at all the other reduction rates, the variation of the maximum texture intensity is small.

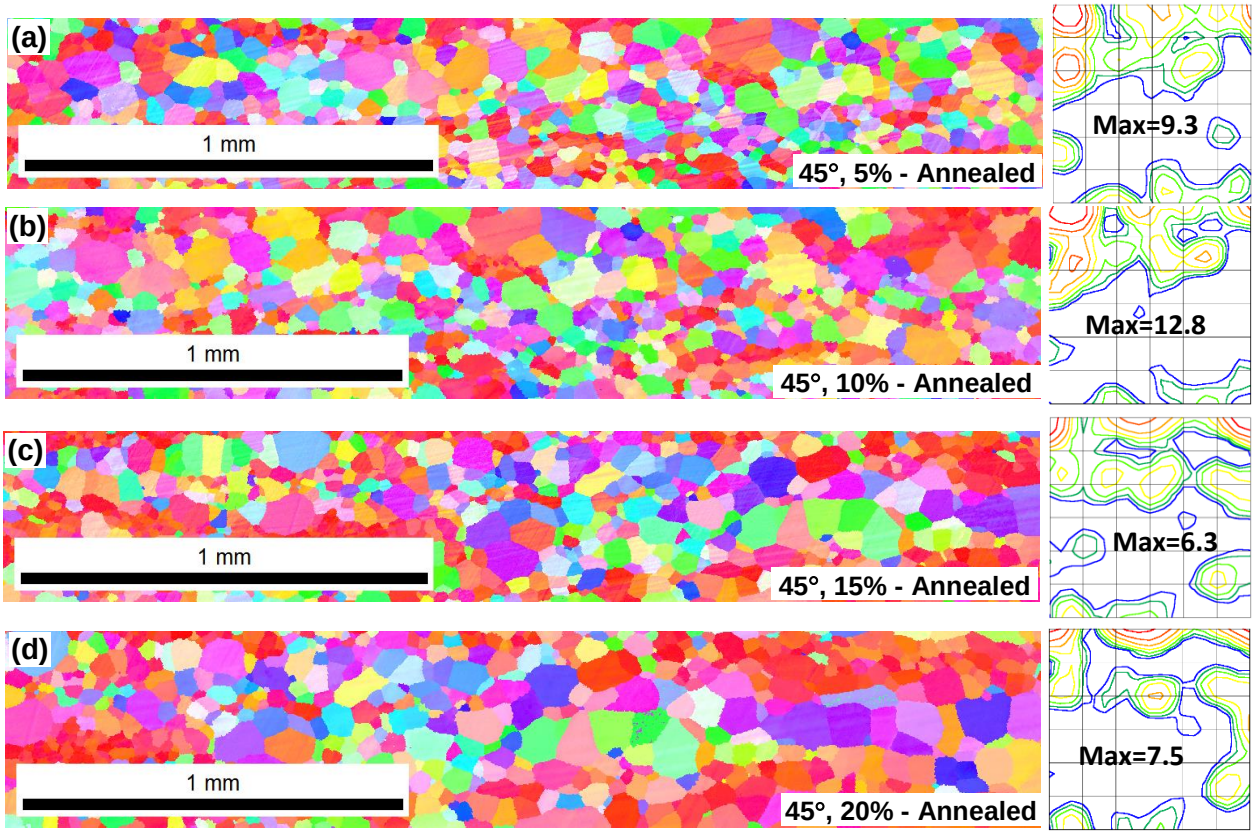

Fig. 6.11. Final annealing textures of the 45° sample after skin pass rolling at different thickness reduction rates: (a) 5%, (b) 10%, (c) 15%, and (d) 20%. φ_2=45° sections of the ODF's (Bunge notation).

The 60° sample behaves similarly to the 45° sample after final annealing, i.e. the θ-fibre still dominates the texture in all the cases. The initially strong cube component after 5% reduction is weakened after final annealing, while the rotated cube is considerably strengthened. For the 10% reduced sample, both the cube and rotated cube components are intensified after annealing, while the originally strong {112}<110> texture is significantly weakened. The θ-fibre texture of the 15% reduced sample is considerably weakened after annealing, so is the 20% reduced sample. Also noted is the much larger grain size of the 20% reduced sample after final annealing which was calculated to be ~51 μm and ~34 μm for the 60° and 45° samples respectively.

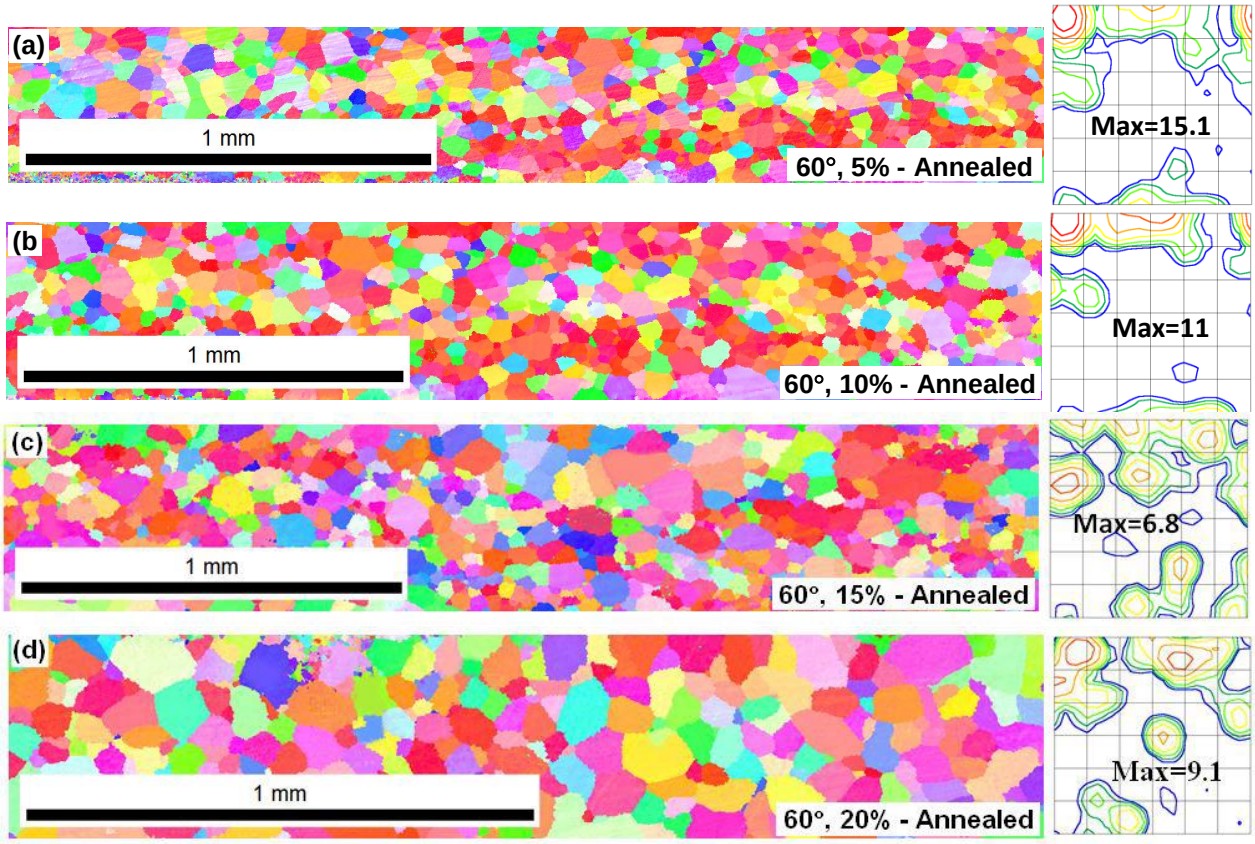

Fig. 6.12. Final annealing textures of the 60° sample after skin pass rolling at different thickness reduction rates: (a) 5%, (b) 10%, (c) 15%, and (d) 20%. φ_2=45° sections of the ODF's (Bunge notation).

The variations of volume fractions of major texture components (cube, rotated cube and Goss) during skin pass rolling/final annealing are compared in Fig. 6.13. Generally, applying 5% to 20% reduction during skin-pass rolling results in significantly weakening of the *cube texture* in all the cases, and this is similar for both the 45° and 60° samples. Upon final annealing, the cube component is slightly restored for samples subjected to 10% or more reductions, but the final volume fraction is considerably lower than that before skin pass rolling. The 5% reduced sample shows further decrease of the cube texture after final annealing. Thus skin pass rolling will weaken the cube texture, and it is not beneficial to the final texture.

The *rotated cube* component varies similarly for both the 45° and 60° samples if the reduction rate is 5% or 10%: skin pass rolling and final annealing gradually increase the volume fraction, so the volume fraction of the final rotated cube texture is higher that before skin pass rolling. If the skin pass reduction rate is 15% or 20%, the rotated cube is also strengthened during the deformation for both samples, but they behave differently after annealing: the rotated cube texture of the 60° sample is considerably weakened, while that of the 45° sample is increased.

The Goss component has very small volume fractions in both samples before skin-pass rolling, and its variation with respect to the rolling reduction is generally small. A general trend is that with the application of the skin pass rolling and final annealing, this component is weakened, and it drops nearly to zero after final annealing.

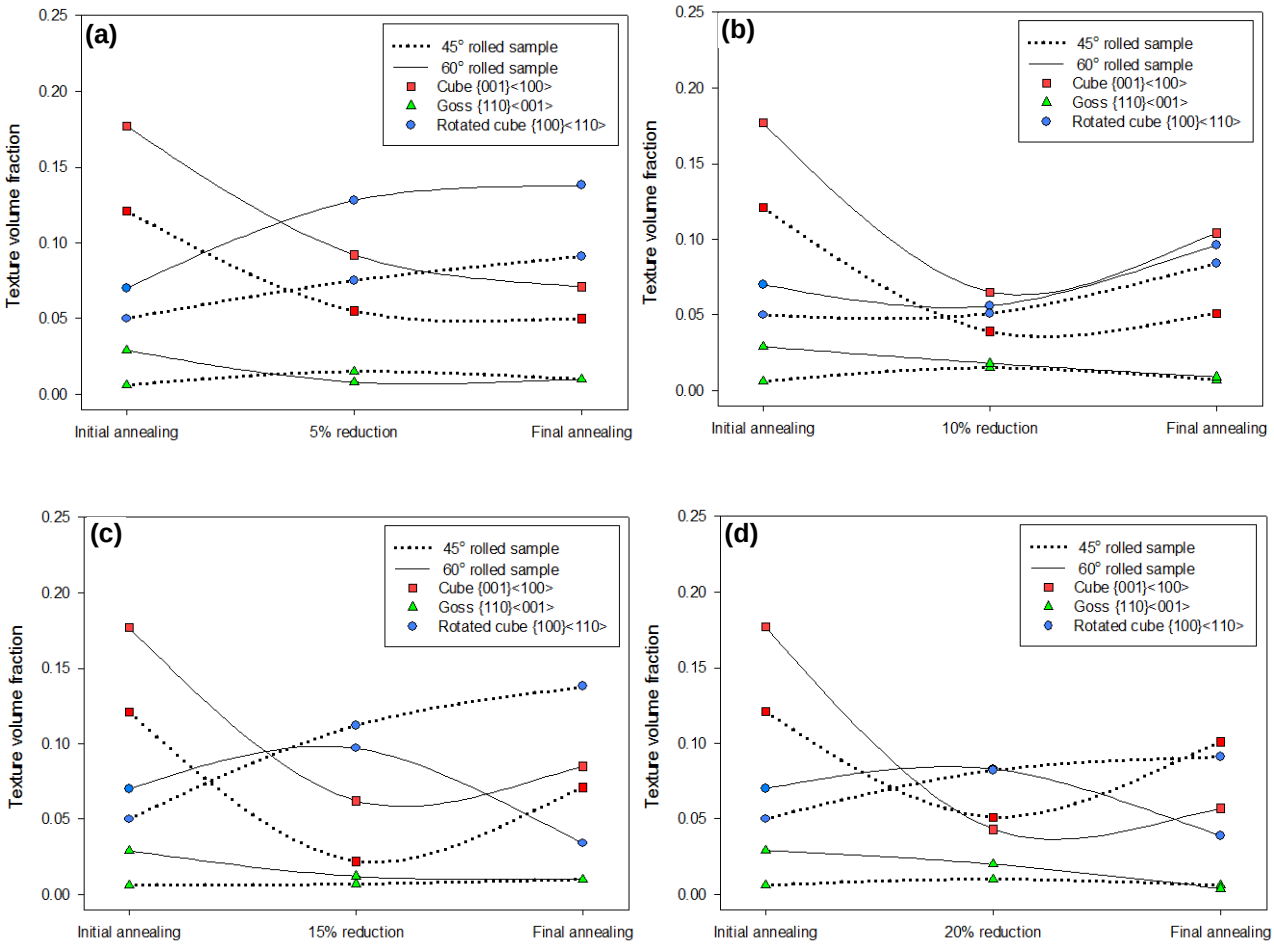

Fig. 6.13. Comparison of the changes of volume fractions of the main texture components after initial annealing (before skin pass rolling), after skin pass rolling, and after final annealing with (a) 5%, (b) 10%, (c) 15%, and (d) 20% reduction during skin pass rolling.

The effect of skin pass rolling and final annealing on the volume fractions of the typical fibre textures is shown in Fig. 6.14. The θ-fibre, which is composed of the cube, rotated cube and other <001>//ND components, approximately follows a trend that is the result of a combined effect of the cube and rotated cube components. For the 45° sample, skin pass rolling slightly weakens (after 5% or 10% reduction) or essentially does not change (after 15% or 20% reduction) the θ-fibre.

Upon final annealing, the θ-fibre is slightly strengthened (after ≤15% reduction) or essentially does not change (after 20% reduction). The final volume fraction (after final annealing) of the θ-fibre is almost the same as that in the initial steel, thus skin pass rolling seems not to alter this fibre. For the 60° sample, skin-pass rolling significantly (after 10% or 20% reduction) or slightly (after 5% or 15% reduction) weakens the θ-fibre. After final annealing, the volume fraction of the θ-fibre is almost the same as (after 5% or 10% reduction) that before skin pass rolling or is considerably lower (after 15% or 20% reduction). Thus skin pass rolling essentially deteriorates the θ-fibre.

For the 45° sample, skin pass rolling generally strengthens the α-fibre at all the reduction rates. Upon final annealing, however, the α-fibre either stays essentially the same (after 10% and 15% reduction) or is slightly decreased (after 5% reduction) or considerably increased (after 20% reduction). For the 60° sample, the volume fraction of the α-fibre is essentially not affected by skin pass rolling regardless of the reduction rate. The final volume fraction of this fibre is almost the same as before skin pass rolling.

The initial γ-fibre volume fraction is relatively small in both samples, and their variation with the application of skin pass rolling is also small. Generally, skin-pass rolling and the final annealing slightly weaken the γ-fibre if the reduction rate is ≤15%, and slightly strengthen it if the reduction rate is 20%.

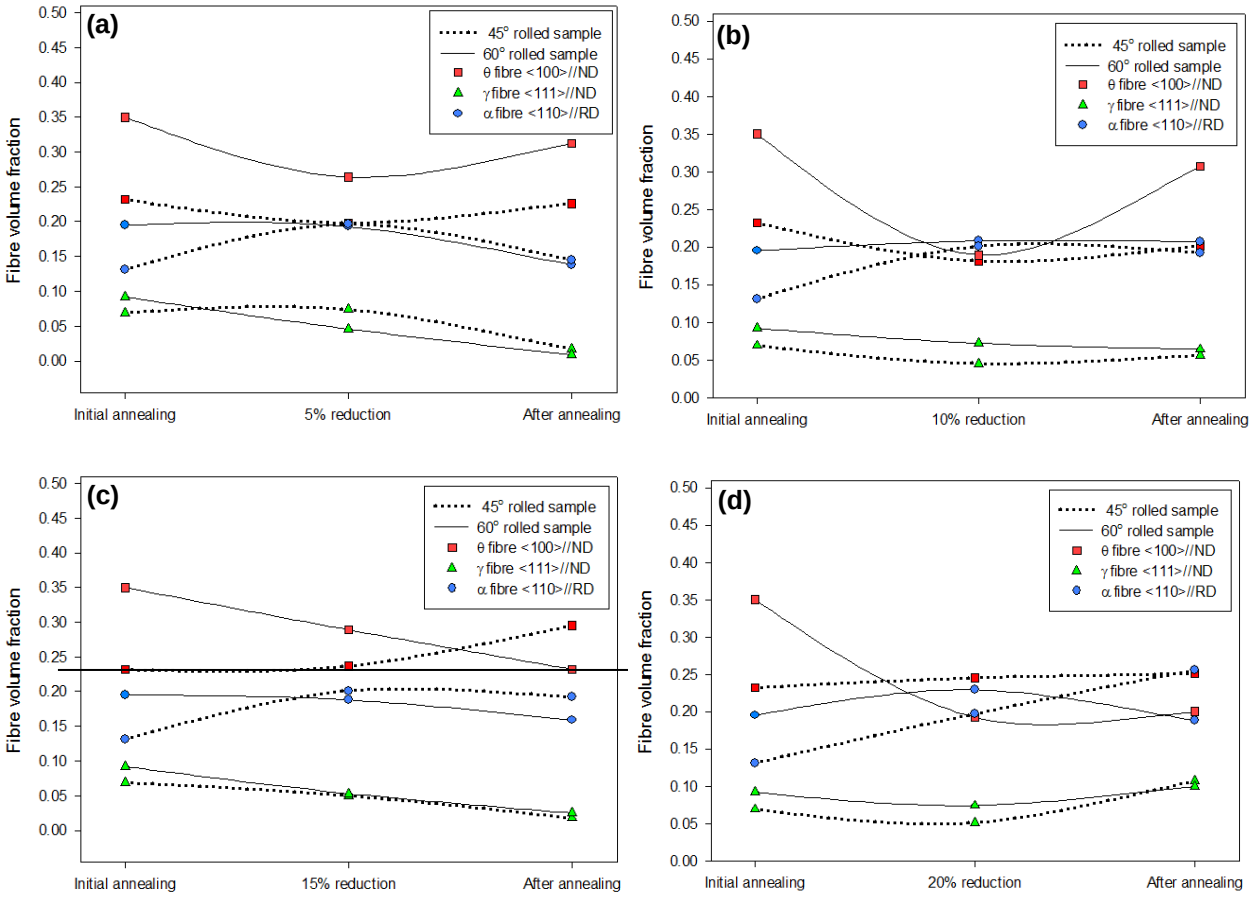

Fig. 6.14 Comparison of the changes of volume fractions of the fibre textures after initial annealing (before skin pass rolling), after skin pass rolling, and after final annealing with (a) 5%, (b) 10%, (c) 15%, and (d) 20% reduction during skin-pass rolling.

6.4 Discussion

From the above analysis it was seen that, the initial samples in this study, i.e. those after 45° and 60° inclined cold rolling and annealing, all had a major θ-fibre texture, and there was essentially no γ-fibre or α-fibre. Thus skin-pass rolling showed a profound effect on the cube and rotated cube components, which were both on the θ-fibre. Skin-pass deformation (regardless of the reduction rate) significantly weakened the cube texture, and slightly strengthened the rotated cube component. The reason for this can be explained by calculating the Taylor factors of the crystals with different orientations under plane strain deformation.

Taylor factors of the originally annealed 45° and 60° samples (Fig. 6.4) were calculated using a family of slip systems for bcc metals, i.e. {110}<111>, {211}<111>, and {321}<111>, and with a plane strain deformation (rolling) gradient given by $\varepsilon_{11}=1$, $\varepsilon_{12}=\varepsilon_{13}=\varepsilon_{23}=\varepsilon_{21}=\varepsilon_{31}=\varepsilon_{32}=0$, and $\varepsilon_{33}=-1$. It was found that the Taylor factors of various orientations spread from 2.4 to 4.1, i.e. ~2.4 for {001}<100> (cube), ~2.5 for {110}<001> (Goss), ~3.1 for {112}<110>, and ~4.1 for {110}<110> (rotated Goss). It should be noted that the real rolling deformation is more complicated than plane-strain deformation since the friction between the rolls and the workpiece surfaces will induce shear deformation on the material, especially in the surface layers. Nevertheless, the Taylor factors calculated using a simplified plane-strain compression mode are quite similar to those obtained using more complicated models. For example, Kestens and Jonas calculated the Taylor factors of IF steel using a full constraint model and obtained the following results: ~2.8 for {001}<100> (cube), ~2.8 for {110}<001> (Goss), ~3.1 for {112}<110>, and ~4.6 for {110}<110> (rotated Goss) [30]. Cheong et al. calculated the Taylor factors for a commercial non-oriented electrical steel (1.12% Si) and obtained: ~2.1 for {001}<100> (cube),

~2.1for {110}<001> (Goss), ~2.8 for {112}<110>, and ~3.7 for {110}<110> (rotated Goss) [31]. Finally, Kestens et al. calculated the Taylor factors for 0.395% Si non-oriented steel using a lath-type relaxed constrained model and the results were: ~2.5 for {001}<100> (cube), ~2.5 for {110}<001> (Goss), ~3.1 for {112}<110>, and ~4.0 for {110}<110> (rotated Goss) [32]. All of them showed very similar trend for these orientations.

Thus the cube orientation has the lowest Taylor factor and is the "softest" orientation during rolling. It has already been shown that during rolling, the {001}<100> crystals tend to rotate around the sheet normal direction (ND) by different angles depending on the amount of deformation and the constraints on the crystals, and the {001}<110> orientation (rotated cube) can be reached with the increase of the deformation. However, the {001}<110> orientation also rotates towards the {112}<110> orientation during rolling, thus when the cube texture is deformed, it may rotate (around the ND) to other components along the θ-fibre (including the rotated cube), while in the meantime the {001}<110> orientation changes to other orientations, e.g. {112}<110>. As a result, with the increase of the reduction rate, the cube orientation gradually reduces while the rotated cube component fluctuates (Fig. 6.10) with the reduction rate. A large reduction will finally lead to the formation of the stable {112}<110> texture.

Fig. 6.15a shows the EBSD IPF map of the 60° sample after 15% skin pass rolling reduction, and Fig. 6.15b is the distribution of the grains having the three typical fibre orientations (α, γ, and θ) in the map. Based on the orientations of the crystals, the Taylor factors (Fig. 6.15c) were calculated, which varied from ~2.0 to ~4.3 for the various orientations present in the microstructure. It is seen again that grains with the θ-fibre orientations show lower Taylor factors than those with other orientations. Thus the grains with the <001>//ND orientations are relatively

"soft", and are more easily deformed during skin pass rolling. The deformation of these crystals usually leads to the increase of the Grain Orientation Spread (GOS) as shown in Fig. 6.16. For the 60° sample after 20% skin pass rolling reduction, the calculated GOS varies between 0 and ~4.5, and the regions with the maximum GOS (Fig. 6.16c) correspond well to the <001>//ND regions (Fig. 6.16b) due to their low Taylor factors.

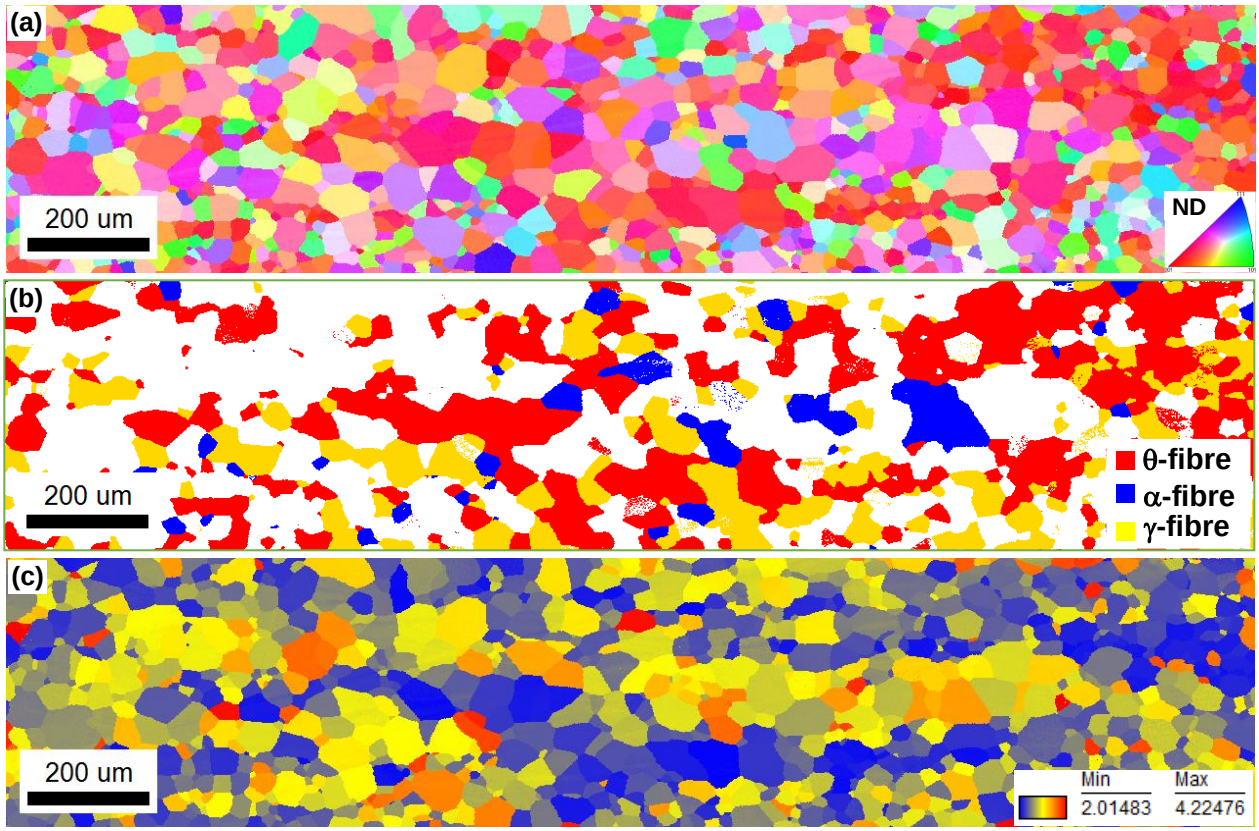

Fig. 6.15. Maps of the 60° sample after 15% skin-pass rolling: (a) EBSD IPF map, (b) distribution of the grains with typical fibre textures, and (c) Taylor factor map of the deformed sample.

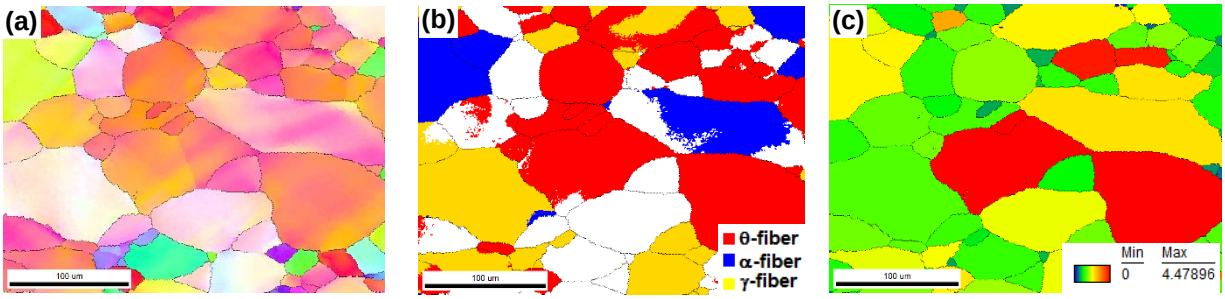

Fig. 6.16. Maps of the 60° sample after 20% skin-pass rolling: (a) EBSD IPF map, (b) distribution of the grains with typical fibre textures, (c) grain orientation spread map.

6.5 Conclusions

i. Inclined rolling at 60° to the HRD produced the strongest θ-fibre texture (35% volume fraction after annealing) among all the inclination angles, with the cube volume fraction reaching 12%, and the γ-fibre being only about 5%. After cold rolling at an inclination angle of 45°, the θ-fibre has the lowest volume fraction (22% after annealing), and the γ-fibre being about 8%.

ii. Skin-pass rolling deformation generally weakens the cube texture originally present in the steel, and promotes the formation of the {112} < 110 > texture (α-fibre). With the increase of the reduction rate, the volume fraction of the rotated cube fluctuates, i.e. the texture is intensified at 5% and 15% reductions, and is weakened at 10% and 20% reductions.

iii. With the application of skin pass rolling, the overall volume fractions of the γ- and α-fibres only show minor changes. However, the θ-fibre texture of the 60° sample has been significantly altered, i.e. the volume fraction drops from ~35% to ~20% after 10% or

20% reduction. The θ-fibre of the 45° sample, on the other hand, essentially does not change.

iv. After final annealing, the cube texture is considerably weakened (at all reduction rates) as compared to that before skin-pass rolling, while the rotated cube component is only intensified for the 45° sample. For the 60° sample, the rotated cube texture is strengthened if the reduction rate is ≤10%, and is weakened if the reduction rate is ≥15%.

v. Compared to the original textures, the volume fraction of the γ-fibre is slightly decreased (after 5% or 15% reduction) or essentially does not change (after 10% or 20% reduction). The volume fraction of the θ-fibre shows apparent differences from the initial textures only if the skin pass reduction rate is ≥15% (for the 60° sample only), i.e. it is considerably reduced from ~35% to 20–23% after final annealing. The volume fraction of the θ-fibre for the 45° sample and the volume fraction of the α-fibre for both samples only show slight changes after final annealing.

vi. The low Taylor factor of the cube orientation makes these grains easy to deform, and they rotate towards other orientations, e.g. rotated cube. Thus, the cube texture is reduced during skin pass rolling. In the meantime, the rotated cube also rotates towards the stable {112}< 110 > orientation, resulting in the fluctuation of this texture with respect to the reduction rate.

References

1. Moses, A. J. "Electrical steels: past, present and future developments."Physical Science, Measurement and Instrumentation, Management and Education, IEE Proceedings A 137.5 (1990): 233-245.

2. Lyudkovsky, Grigory, P. K. Rastogi, and M. Bala. "Nonoriented electrical steels." JOM 38.1 (1986): 18-26.

3. Ghosh, Pampa, et al. "Effect of crystallographic texture on the bulk magnetic properties of non-oriented electrical steels." Journal of Magnetism and Magnetic Materials 365 (2014): 14-22.

4. Oda Y, Kohno M, Honda A. Recent development of non-oriented electrical steel sheet for automobile electrical devices [J]. Journal of Magnetism and Magnetic Materials, 2008, 320(20): 2430-2435.

5. Honda A, Fukuda B. Effects of magnetic properties of non-oriented electrical steel sheets on motor efficiency [J]. Journal of Materials Engineering, 1990, 12(1): 41-45.

6. Kestens, Leo, and Sigrid Jacobs. "Texture control during the manufacturing of nonoriented electrical steels." Texture, Stress, and Microstructure 10.2008 (2008): 173083.

7. A. D. Rollett, M. L. Storch, E. J. Hilinski, and S. R. Goodman,“Approach to saturation in textured soft magnetic materials,” Metallurgical and Materials Transactions A, vol. 32, no. 10, pp. 2595–2603, 2001.

8. L. Kestens and J.J. Jonas: ASM Handbook, Part 1, ASM International,Materials Park, 2005, vol. 14, pp. 685–700.

9. B. Hutchinson, L. Ryde, and K. Tagashira: Mater. Sci. Eng., A,1998, vol. A257, pp. 9–17.

10. J.J. Sidor, K. Verbeken, E. Gomes, J. Schneider, P.R. Calvillo, andL.A.I. Kestens: Mater. Charact., 2012, vol. 71, pp. 49–57.

11. Y. Hayakawa and M. Kurosawa: Acta Mater., 2002, vol. 50, pp. 4527–34.

12. J. P. Anderson and B. A. Lauer, “Electrical steel with improved magnetic properties in the rolling direction,” US patent no.6,569,265, May 2003.

13. T. Shimazu, M. Shiozaki, and K. Kawasaki, “Effect of temper rolling on texture formation of semi-processed non-oriented steel,” Journal of Magnetism and Magnetic Materials, vol. 133, no. 1–3, pp. 147–149, 1994.

14. S. W. Cheong, E. J. Hilinski, and A. D. Rollett, “Effect of temper rolling on texture formation in a low loss cold rolled magnetic lamination steel,” Metallurgical and Materials Transactions A, vol. 34, no. 6, pp. 1311–1319, 2003.

15. E. J. Hilinski, “Recent developments in semiprocessed cold rolled magnetic lamination steel,” Journal of Magnetism and Magnetic Materials, vol. 304, no. 2, pp. 172–177, 2006

16. F. Kovac, M. Dzubinsky, and Y. Sidor: J. Magn. Magn. Mater.,2004, vol. 269, pp. 333–40. (column grain growth)

17. N. Yoshinaga, L. Kestens, and B. C. De Cooman, "α→γ→α transformation texture formation at cold-rolled ultra low carbon steel surfaces," Materials Science Forum, vol. 495-497,part 1-2, pp. 1267–1272, 2005. (phase)

18. T. Tomida: J. Appl. Phys., 1996, vol. 79, pp. 5443–45 (phase trans)

19. He, Youliang, Erik Hilinski, and Jian Li. "Texture Evolution of a Non-oriented Electrical Steel Cold Rolled at Directions Different from the Hot Rolling Direction." Metallurgical and Materials Transactions A 46.11 (2015): 5350-5365.

20. He, Youliang, and Erik J. Hilinski. "Texture and Magnetic Properties of Non-oriented Electrical Steels Processed by an Unconventional Cold Rolling Scheme." Journal of Magnetism and Magnetic Materials (2015).

21. ASTM E112-96: Standard test methods for determining average grain size.

22. Wright, Stuart I., Matthew M. Nowell, and John F. Bingert. "A comparison of textures measured using X-ray and electron backscatter diffraction."Metallurgical and Materials Transactions A 38.8 (2007): 1845-1855.

23. Suwas, Satyam, et al. "Effect of modes of rolling on evolution of the texture in pure copper and some copper-base alloys: Part I: Rolling texture."Zeitschrift für Metallkunde 93.9 (2002): 918-927.

24. H.-J. Bunge, Texture Analysis in Materials Science: Mathematical Models, Butterworths, London, UK, 1982.

25. A.D. Rollett and S.I. Wright: Typical Textures in Metals, CambridgeUniversity Press, Cambridge, 1998, pp. 179–237.

26. Xu, P. G., Yin, F. X., & Nagai, K. (2006). Solidification cooling rate and as-cast textures of low-carbon steel strips. Materials Science and Engineering: A, 441(1-2), 157-166.

27. Wu, S., Chen, A., Liu, H., Liu, Z., Li, H., & Wang, G. (2014). Microstructure and texture evolution of strip-cast and hot-rolled Fe-3% Si steel sheet. Metallography, Microstructure, and Analysis, 3(5), 390-396.

28. Chen, A. H., & Li, H. L. (2016). Microstructure and Texture of 0.75% Si Non-oriented Electrical Steel Fabricated by Strip Casting Process. Metallography, Microstructure, and Analysis, 5(5), 428-434.

29. P. Gobernado, R.H. Petrov, L.A.I. Kestens, Recrystallized {3 1 1}〈1 3 6〉 orientation in ferrite steels, Scripta Materialia 66(9) (2012) 623-626.

30. Cheong, S. W., Hilinski, E. J., & Rollett, A. D. (2003). Effect of temper rolling on texture formation in a low loss cold-rolled magnetic lamination steel. Metallurgical and Materials Transactions A, 34(6), 1311-1319.

31. Kestens, L., & Jonas, J. J. (1996). Modeling texture change during the static recrystallization of interstitial free steels. Metallurgical and Materials Transactions A, 27(1), 155-164.

32. Cheong, S. W., Hilinski, E. J., & Rollett, A. D. (2003). Grain growth in a low-loss cold-rolled motor-lamination steel. Metallurgical and Materials Transactions A, 34(6), 1321-1327.

33. Kestens, L., Jonas, J. J., Van Houtte, P., & Aernoudt, E. (1996). Orientation selective recrystallization of nonoriented electrical steels. Metallurgical and Materials Transactions A, 27(8), 2347-2358.

Chapter 7 Non-oriented Electrical Steel with Core Losses Comparable to Grain-oriented Electrical Steel

7.1 Introduction

Non-oriented electrical steels are the most widely used core materials for electric motors, generators and alternators, due to their high permeability, high magnetization saturation, and low cost and loss [1-11]. The magnetic properties of non-oriented electrical steels are highly dependent on the silicon content, the cleanliness of the melt, the thickness of the steel sheets, the grain size and the crystallographic texture. While most of these properties can be relatively readily controlled during the steel manufacturing processes, the producing of the desired crystallographic texture in these steels are proven to be challenging. This is because all the thermomechanical processing procedures used to manufacture the final thin sheets will alter the texture, and the mechanisms that control the formation of textures in some processes (e.g. recrystallization and phase transformation) are still not completely understood. The texture undergoes significant changes during solidification, phase transformation, plastic deformation as well as recrystallization (nucleation and grain growth) [6, 12]. Although many studies have been carried out to investigate the effect of thermomechanical processing on the crystallographic texture, and several models and theories [12, 13] have been developed to explain the underlying mechanisms, very limited improvement has been made to optimize the final texture of non-oriented electrical steels [13].

In this paper, a 3.2 wt% Si non-oriented electrical steel was processed using traditional manufacturing routes including casting, hot rolling, hot band annealing, cold rolling and final annealing. The texture and microstructure of the steel were characterized throughout all the processing stages. The final annealing was conducted at various temperatures for different times,

and it was found that the final textures are highly dependent on the annealing temperature and time. Generally, the higher the annealing temperature and the shorter the time, the weaker the magnetically unfavorable <111>//ND (normal direction) texture. The magnetic properties were evaluated using Epstein frame method as well as magnetic Barkhausen noise (MBN) analysis techniques. The relations among the microstructure, texture, core loss, and saturation magnetic induction were discussed. The magnetic properties (rolling direction) of the 3.20 % Si non-oriented electrical steel produced in this study is comparably to those of commercially available *grain-oriented* electrical steel with similar silicon content. The core losses at low frequencies (i.e. below 225 Hz) are even lower than the grain-oriented electrical steel.

7.2 Material and Experimental Procedures

The chemical composition of the non-oriented electrical steel investigated in this study is given in Table 7.1. The steel was melted in a vacuum furnace and cast into ingots with dimensions of 265 mm × 200 mm × 100 mm (length × width × thickness). The ingots were then heated up to 1050°C and hot rolled to a thickness of 20 mm (80% reduction) in a reversing rolling mill in six passes. The hot rolling entry temperature was ~945°C and the finishing temperature was ~865°C (the temperatures were measured on the surface of the steel plates using infrared thermometers). A second hot rolling step (heated to the same temperature of 1050°C) was applied to reduce the thickness of the steel plates from 20 mm to ~3.3 mm (~85% reduction) in six passes as well. In this case the entry and finishing temperatures were ~925 °C and ~680°C, respectively. The steel plates were then pickled in a hydrochloric acid solution to remove surface oxides and defects.

Table 7.1. Chemical composition of the investigated steel (wt%).

C	Mn	P	S	Si	Al	N	O	Fe
0.004	0.40	0.0095	0.0027	3.20	0.58	0.0034	0.0037	balance

The hot-rolled plates were subsequently annealed at 860 °C for 24 hours in argon protected atmosphere and furnace cooled. The annealed plates were cold rolled to a final thickness of 0.35 mm (~90% reduction). The cold-rolled sheets were then annealed at various temperatures (750, 850, 950, 1050 and 1150 °C) in argon protected atmosphere and furnace cooled. The samples were inserted into the furnace that has been heated to the designated temperatures so that the samples could be quickly heated up. The holding time was varied from 180 minutes at 750°C to 2 minutes at 1150°C, trying to reduce the variations in grain size.

The textures of the steel during all the thermomechanical processing stages were characterized by electron backscatter diffraction (EBSD) in a field emission gun scanning electron microscope (FEG-SEM) (Nova NanoSEM, FEI) equipped with an EDAX Orientation Imaging Microscopy system (OIM 6.2). Samples were prepared using conventional metallographic procedures plus a final polishing step using a 0.05 μm colloidal silica solution followed by thorough ultrasonic cleaning. The EBSD scans after hot rolling, hot-band annealing and cold rolling were performed on the cross-section plane, i.e. rolling direction (RD)-normal direction (ND) section, covering essentially the entire thickness of the plate/sheet. The EBSD scans after final annealing were performed on the middle thickness plane of the sheet. Large areas of ~3 mm × ~3 mm were scanned to ensure a good statistical representation of the textures (due to the large grain sizes). Orientation distribution functions (ODFs) were calculated using a harmonic series expansion method with a series rank of 22 and a Gaussian half-width of 5°. The φ_2=45° section of the Euler space (Bunge notation) was used to represent the typical bcc texture components. The

volume fractions of the three major texture fibres, i.e. θ-fibre (<100>//ND), α-fibre (<110>//RD) and γ-fibre (<111>//ND) were calculated from the ODFs with a tolerance of 15°. The grain sizes were calculated using the OIM software based on the grain orientation data.

Bulk magnetic properties of the processed steel were measured using standard Epstein frame method [14]. A total of 20 rectangular strips (305 mm × 30 mm) were cut from the steel sheets after final annealing, with the longitudinal axis parallel to the rolling direction. The magnetic properties were measured using a SMT-700 soft magnetic material testing system (Magnetic Instrumentation, Inc. [15]). Both direct current (DC) and alternating current (AC) tests were conducted. For DC measurements, a maximum current of 12A and a maximum induction of 2.5T were utilized. The DC core loss, saturation induction and maximum permeability were obtained. The AC tests were carried out at similar testing conditions with frequencies varying from 3 Hz to 300 Hz. A summary of the testing parameters used in the DC and AC tests is given in Table 7.2.

Table 7.2. Parameters used for the DC and AC Epstein frame tests.

Strip length	305 mm
Mass	~ 500 g
Density	7.65 g/cm^3
H coil turns	700 turns
B coil turns	74 turns
B coil resistance	0.6 Ω
B step size	0.02 T
Frequency	3 Hz – 300 Hz

Magnetic Barkhausen noise (MBN) measurements [16, 17] were carried out on the surfaces of the same final annealed steel strips using a Rollscan 350 MBN analysis system (Stresstech Oy, Finland [16, 17]). The measurements were conducted (Fig. 7.1) at 10 equally spaced locations in the rolling direction (RD) along the central line of the 305 mm × 30 mm each strip (Fig. 7.1a). The measured results from the 10 locations were then averaged and compared to the DC core loss results obtained from Epstein frame method (also measured in RD). All the MBN measurements were conducted at a magnetizing frequency of 125 Hz and a peak voltage of 5V. Each MBN measurement consists of 20 bursts of MBN signal, which was filtered to a range of 0.1-1000 kHz to reduce noise.

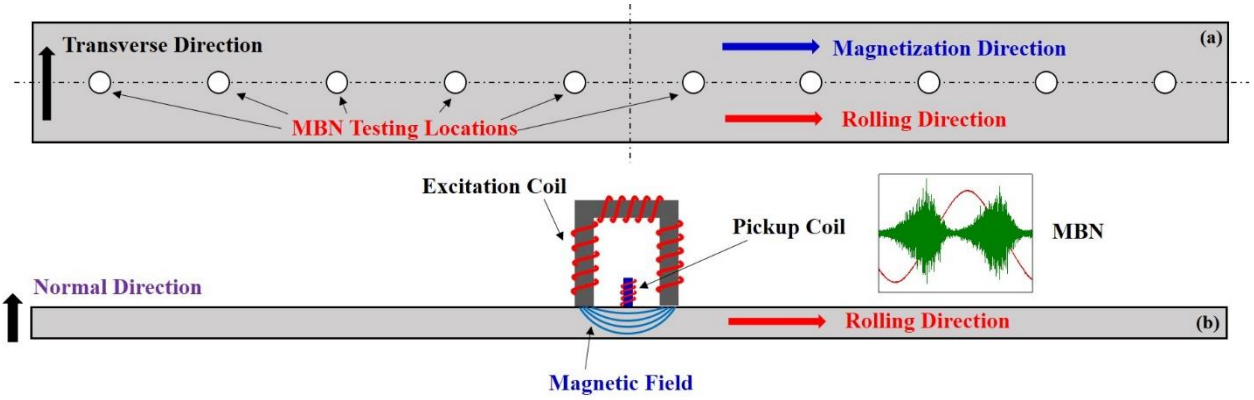

Fig. 7.1 Schematic illustration of the MBN measurements: (a) measurement locations along the rolling direction, (b) schematic of the MBN sensor and the magnetization of the sample.

7.3 Results

7.3.1 Hot rolling texture and microstructure

The cross-section (RD-ND) EBSD inverse pole figure (IPF) map of the 3.20% Si non-oriented electrical steel after hot rolling is illustrated in Fig. 7.2a. The microstructure and crystal orientations show significant heterogeneity across the thickness of the plate. The surfaces (approximately 1/3 of the thickness) are composed of small, equiaxed grains (average grain size

~13 µm), while the rest 2/3 of the microstructure consists of large, elongated grains. Different grain orientations can also be noticed in both regions: while the surface grains show a variety of different orientations (colors), the elongated grains only illustrate a few colors, i.e. red, green and blue. The elongated grains can be further divided into two sub-areas: the central area with mostly red and blue grains, and the transition area (between the surface and the central area) with mainly green grains.

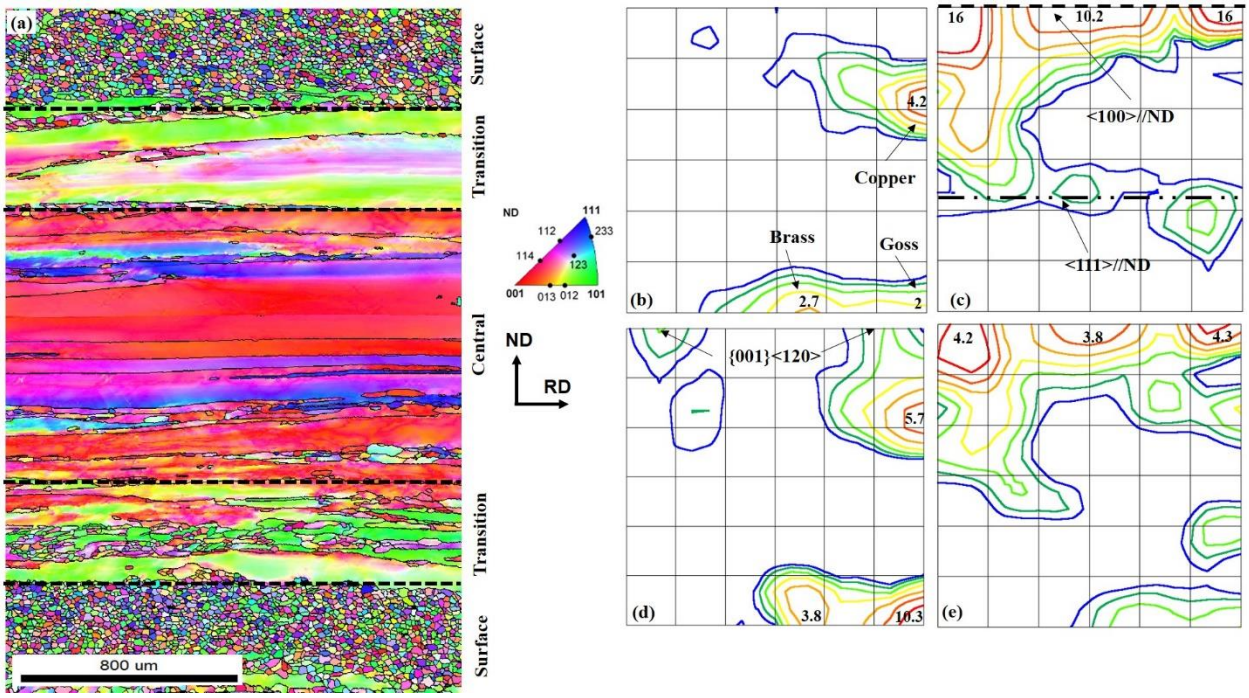

Fig. 7.2 Microstructure and microtexture of the 3.2% Si non-oriented electrical steel after hot rolling: (a) EBSD IPF map of the RD-ND cross section (b) texture of the surface regions, (c) texture of the central region, (d) texture of the transition region, (e) overall texture across the thickness, using φ_2 =45° sections of the ODFs (Bunge notation).

The texture of the surface regions (Fig. 7.2b) is mainly composed of brass ({110}<112>), copper ({112}<111>) and Goss ({110}<001>), which are common components induced by the friction (shear deformation) between the rolls and plate [18]. The central area (slightly more than

1/3 of the thickness) features a strong <100>//ND fibre (including cube and rotated cube) and a weak γ-fibre (<111>//ND) texture (Fig. 7.2c). The texture of the transition area (Fig. 7.2d) is mainly composed of a strong Goss, a copper and a brass. There is also a weak {001}<120> component. The overall texture of the cross section (Fig. 7.2e) is featured by a θ-fibre and some weak components such as brass, copper, Goss and γ-fibre. The intensities of these components, however, are much smaller than those in the individual regions. Both the texture and the microstructure of the hot-rolled non-oriented electrical steel are very similar to the rolling textures and microstructures of structural steels [12, 18-23].

7.3.2 Microstructure and texture after hot band annealing

After hot rolling and annealing, the microstructure and microtexture (Fig. 7.3a) changed significantly. Both the surface and central regions are occupied by recrystallized grains, but microstructural variation still exists across the thickness, i.e. the grains near the surface regions are generally smaller than those at the central region. The average grain size is approximately 123 μm, but the individual grains show large deviations, i.e. grains in the range of tens of microns to ~500 microns can all be seen in the microstructure. The variation in grain size is due to the fact that before annealing (Fig. 7.2a), the surface grains have already recrystallized during hot rolling, and they essentially only undergo grain growth during the subsequent annealing. The lack of stored energy in these grains limited their growth since all the neighboring grains were already recrystallized [12] and the driving force is relatively low. On the other hand, the central region is composed of deformed grains after hot rolling, which have higher stored energy as compared to the recrystallized grains near the surfaces. Once new grains nucleate from the deformed microstructure, the growth of these grains are fast since their growth was accomplished by

consuming the neighboring *deformed* matrix, the latter having high stored energy and the driving force being large [12].

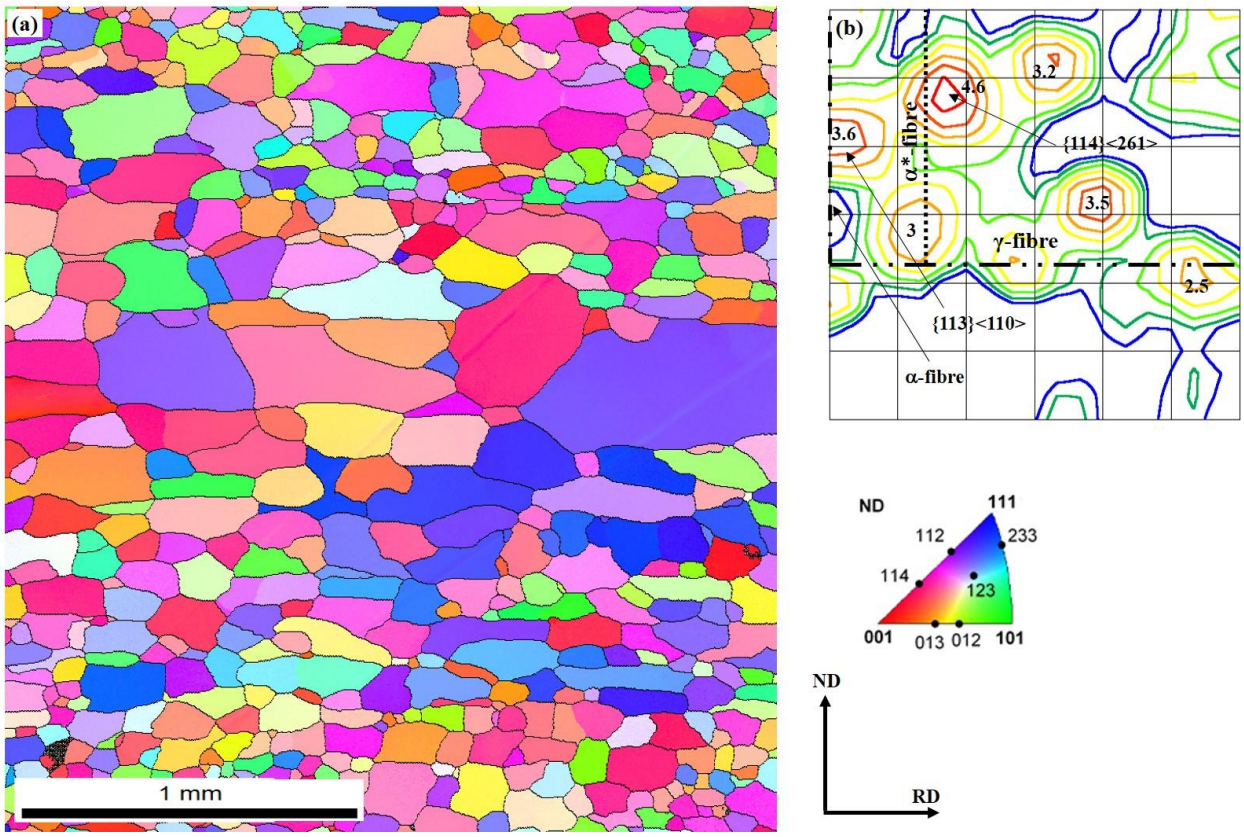

Fig. 7.3 Microstructure and microtexture after hot rolling and annealing: (a) EBSD IPF map of the cross section (RD-ND plane), (b) φ_2 =45° section of the ODFs (Bunge notation) showing the overall texture.

The texture of the steel plate after annealing is shown in Fig. 7.3b. It is seen that the texture is substantially altered after annealing at 860°C for 24 hours: the θ-fibre (<100>//ND) in the hot-rolled steel (Fig. 7.2e) essentially disappear, while a strong {114}<261> component is produced, which is close to the α*-fibre [24, 25]. There is also a {113}<110> component on the α-fibre. The

γ-fibre becomes essentially continuous after annealing. The copper, brass and Goss in the hot-rolled steel have been significantly weakened or completely eliminated.

It is worth noting that most of the recrystallized grains in the microstructure (Fig. 7.3a), especially those in the central region, show a large aspect ratio of the rolling direction to the transverse direction, i.e. they are not equiaxed, which indicates that the grain growth preferentially occurs in the rolling direction. In fact, the average intercept length measured from 200 horizontal lines parallel to the RD (i.e. the average grain diameter in RD) is ~190 μm, while that measured in the ND is only ~105 μm. This suggests that the newly formed nuclei in the central region more likely grow by consuming the elongated (deformed) grains in the rolling direction during grain growth. As have been shown in Fig. 7.2a, these elongated grains usually have grain boundaries essentially parallel to the RD. In other words, the growth of the new grains usually does not cross the boundaries of the elongated grains. The growth mechanism of these grains is schematically shown in Fig 7.4.

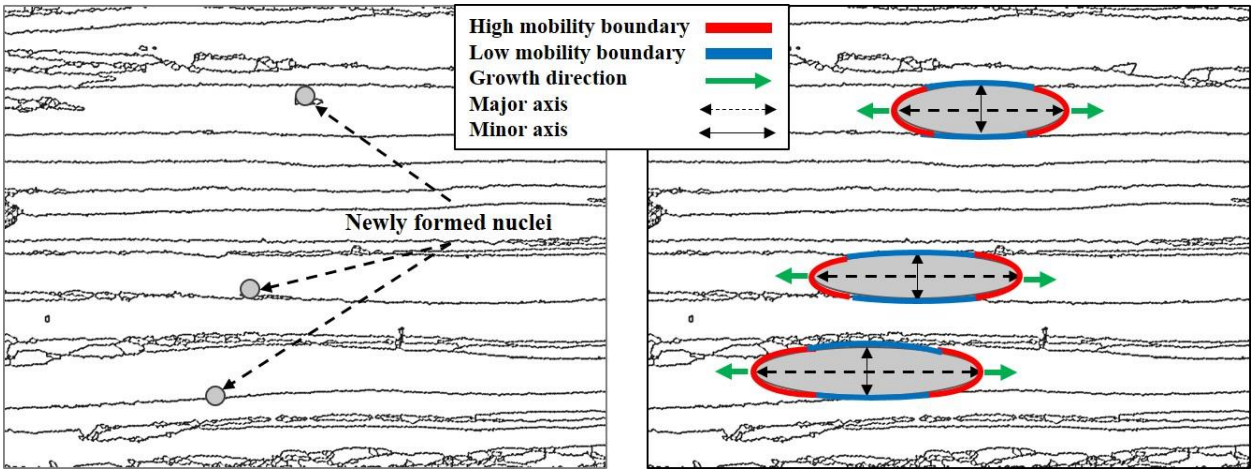

Fig. 7.4. Schematic illustration of the nucleation and growth of new grains in the central region of the hot-rolled plate during hot band annealing. The preferential growth in the rolling direction leads to elliptical-shaped grains as seen in Fig. 7.3a.

7.3.3 Cold rolling microstructure and texture

The microstructure and microtexture after cold rolling is shown in Fig. 7.5a. Cold rolling results in the elongation of the recrystallized grains in the annealed hot band (Fig. 7.3a). In some grains, a large amount of shear bands can be seen, and the accumulation of dislocations in these regions makes the indexing difficult, thus they may appear black in the IPF map. In other grains, the formation of shear bands is not obvious, but there are a lot of microbands showing different orientations (colors), which may be the result of grain fragmentation (intra-grain deformation) during heavy plastic deformation [24]. These locations are considered very important nucleation sites during the subsequent recrystallization process.

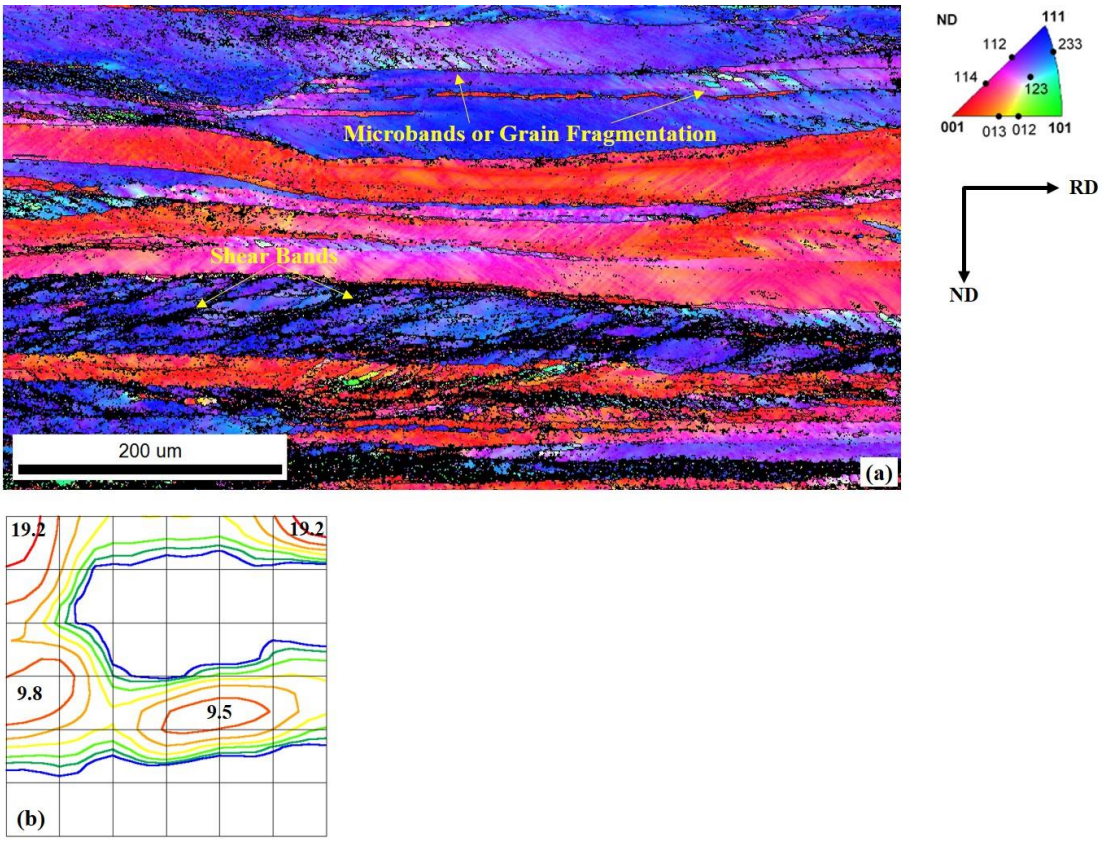

Fig. 7.5. Microstructure and texture of the cold-rolled 3.2% Si electrical steel: (a) EBSD IPF map of the RD-ND cross section, (b) φ_2 =45° section of the ODFs (Bunge notation) showing the overall texture across the thickness.

Although the crystal orientations in the annealed hot band show large variations, the texture after ~85% cold rolling reduction (Fig. 7.5b) is essentially composed of three fibres, i.e. <001>//ND (θ-fibre), <110>//RD (α-fibre) and <111>//ND (γ-fibre), which are typical fibre textures commonly observed in rolled bcc iron [12, 18-23]. The maximum intensity (19.2) is observed at the rotated cube as well as strong intensity at {111}<110> of 9.8.

7.3.4 Microstructure and texture after final annealing

As has been seen in Fig. 7.5a, the microstructure after cold rolling consists of a lot of shear bands and microbands, which are preferred nucleation sites during recrystallization. Upon annealing, nucleation occurs first at these deformation bands and at the grain boundaries, due to their high stored energies. The new grains grow by consuming the surrounding deformed matrix as the annealing process continues. The driving force for the growth of the newly formed grains is the reduction of the stored energy accumulated during plastic deformation. Depending on the annealing temperature and holding time, the annealed microstructure and texture show significant discrepancies (Fig. 7.6).

Fig. 7.6a shows the microstructure of the sample after annealing at 750°C for 180 minutes. The average grain size is ~82 μm, and there exists a large variation in the grain diameter, i.e. 10 ~250 microns. The texture (Fig. 7.6f) is featured by a strong γ-fibre and a relatively strong {001}<140> component on the θ-fibre. Compared to the cold rolling texture shown in Fig. 7.5b, the strong rotated cube and the α-fibre disappear, while the γ-fibre texture persist. A partial fibre close to the α*-fibre ({1 1 h}<1 2 1/h>) is noted stretching from the θ-fibre to the γ-fibre.

When the annealing temperature is increased to 850 °C and the holding time is reduced to 60 minutes, the average grain size is increased to ~103 μm (Fig. 7.6b), also with considerable

spread (20-300 μm). The prominent texture is now the {001}<140> component on the θ-fibre, with an intensity of 8.7 (Fig. 7.6g). The γ-fibre changes to only one weak {111}<112> component with an intensity of 2.8. Again, the rotated cube and the α-fibre in the cold-rolled steel essentially disappear. Similarly, a near α*-fibre is seen to extend from the θ-fibre to the γ-fibre.

When the annealing temperature is 950 °C and the holding time is 30 minutes, the average grain size increases to ~160 μm (Fig. 7.6c), with a spread between ~30 μm and ~500 μm. The texture (Fig. 7.6h) is again composed of a {001}<140> component (intensity 6.0) on the θ-fibre and a {111<112> (intensity 3.2) on the γ-fibre. A weak Goss texture ({110}<001>) starts to appear. The rotated cube and α-fibre are essentially eliminated, and there also exists a near α*-fibre.

If the annealing is conducted at 1050 °C for 10 minutes, the average gran size increases ~200 μm (Fig. 7.6d), with a spread of 38~550 μm. The texture (Fig. 7.6i) is also featured by a {001}<140> on the θ-fibre (intensity 5.0) , a {111}<112> on the γ-fibre (intensity 2.4), and an α*-fibre. The α-fibre and the rotated cube in the rolled steel are completely eliminated. If the annealing temperature is further increased to 1150 °C and the time is reduced to 2 minutes, the average gran size drops slightly to ~187 μm (Fig. 7.6e), with a spread of 35~525 μm. The decrease of the average grain size may be due to the formation of AlN precipitates at high temperatures [26], which hindered the growth of the grains. The main texture is still the {001}<140> component, but the intensity drops to 4.3 (Fig. 7.6j). However, the γ-fibre is essentially eliminated, and a cube texture (intensity 2.6) is observed, which is not seen in any of the samples annealed at lower temperatures. The rotated cube and the α-fibre are removed. Again, there is also an α*-fibre.

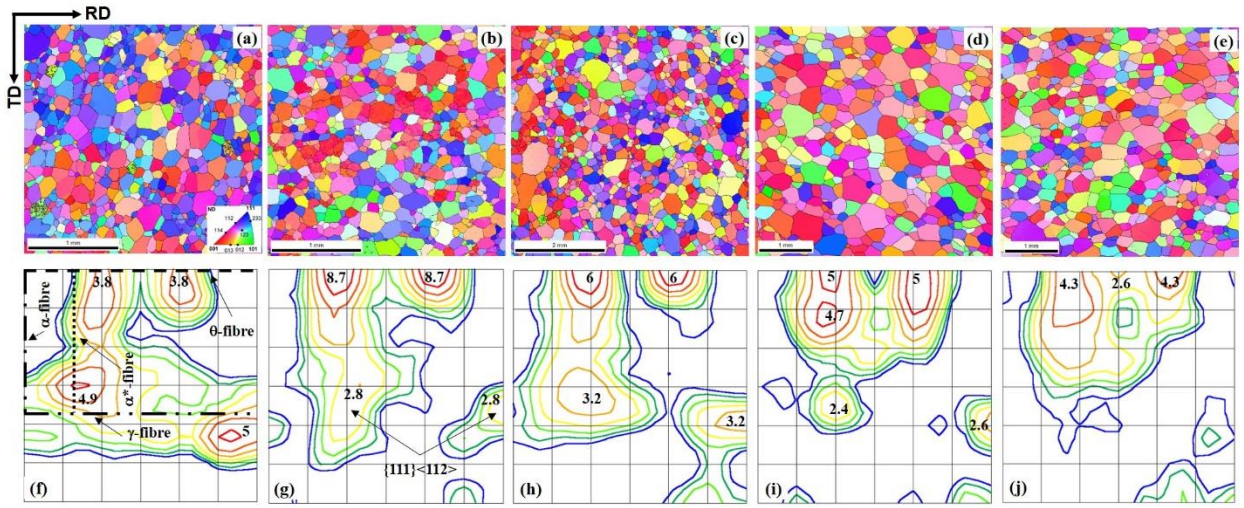

Fig. 7.6. Microstructure and texture of final annealed steel: (a)-(e) EBSD IPF maps showing the microstructure after annealing at 750 °C for 180min, 850 °C for 60 min, 950°C for 30 min, 1050 °C for 10 min and 1150 °C for 2 min, (f)-(j) the corresponding textures. The EBSD scans were performed on the sheet plane at the middle thickness.

It is seen that, although the annealing temperature and holding time are significantly different, the resulted recrystallization textures all contain a {001}<140> component, a {111}<112> component and a near α*-fibre texture [24, 25]. The differences among the textures are the relative intensities of the {001}<140> component on the θ-fibre and the {111}<112> component on the γ-fibre. Annealing at 750°C for 180 minutes produced the strongest γ-fibre and the weakest {001}<140> component, while annealing at 850°C for 60 minutes created the strongest {001}<140> component and a relatively weak {111}<112> component. Annealing at 1150°C for 2 minutes can essentially eliminate the magnetically detrimental γ-fibre, although the intensity of the {001}<140> component is also decreased.

The variations of the volume fractions of the three major fibre textures (α, θ and γ) with respect to the annealing temperature are summarized in Fig. 7.7a. It is seen that annealing at all

the temperatures significantly reduced the volume fraction of the α-fibre (compared to that after cold rolling), while the θ-fibre and γ-fibre may be strengthened or weakened depending on the annealing temperature. Annealing at 850°C and 1050°C can promote the θ-fibre texture, while annealing at other temperatures, the θ-fibre volume fraction essentially does not change, i.e. the same as the cold-rolled steel. The volume fraction of the γ-fibre, on the other hand, generally decreases with the increase of the annealing temperature. To evaluate the magnetic quality of the texture, a ratio of (volume fraction) the magnetically favourite <001>//ND fibre to the magnetically detrimental <111>//ND fibre may be calculated: the larger the ratio, the better the magnetic quality. Fig. 7.7b shows the variation of this ratio with respect to the annealing temperature. It is seen that annealing at 1050°C for 10 minutes produces the best texture as the ratio of the <001>//ND fibre to the <111>//ND fibre is the highest.

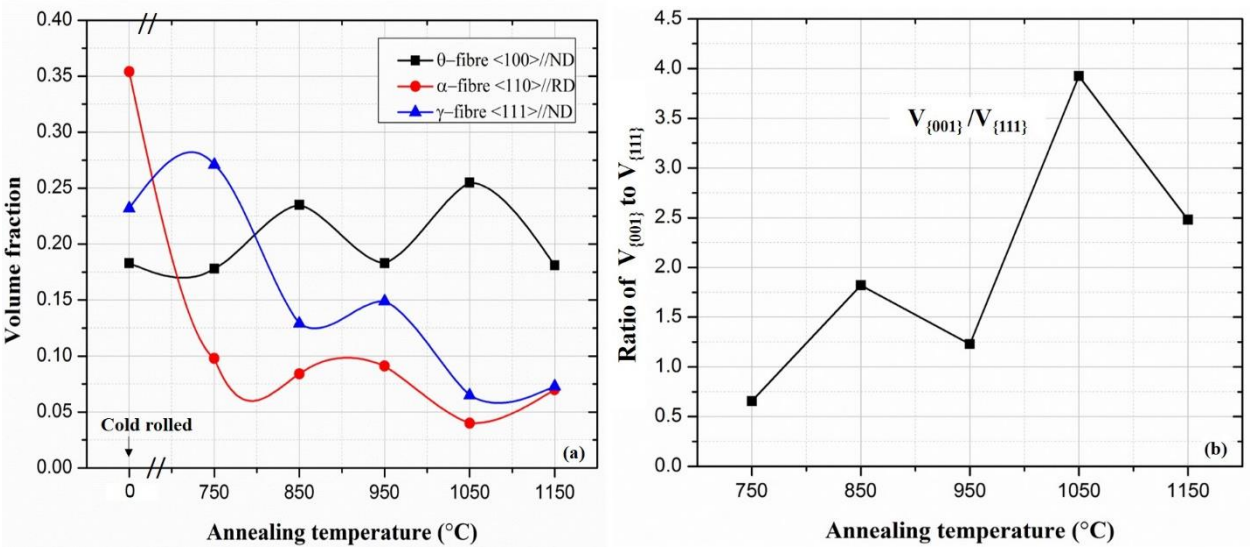

Fig. 7.7 Variations of the texture with respect to the annealing temperature: (a) volume fractions of the three major texture fibres (α, θ and γ), (b) the ratio of the <100>//ND volume fraction to the <111>//ND volume fraction.

7.3.5 Magnetic Properties

7.3.5.1 DC core loss

The measured DC core losses for samples annealed at different temperatures are illustrated in Fig. 7.8, where the losses are also compared to the average grain sizes of the steels. It is seen that with the increase of annealing temperature, the average grain size gradually increases until 1050°C, after which the grain size slightly drops when the annealing temperature is further increased. The DC core loss, on the other hand, gradually decreases with the annealing temperature. Again, at 1050°C, a minimum is reached, and further increasing the annealing temperature leads to a slight increase of the DC core loss. Thus the DC core loss generally decreases with the increase of the average grain size. This is due to the fact that grain boundaries act as pinning sites for the motion of domain walls during the magnetization and demagnetization processes. The smaller the grain size, the more the grain boundaries, thus the larger the core loss.

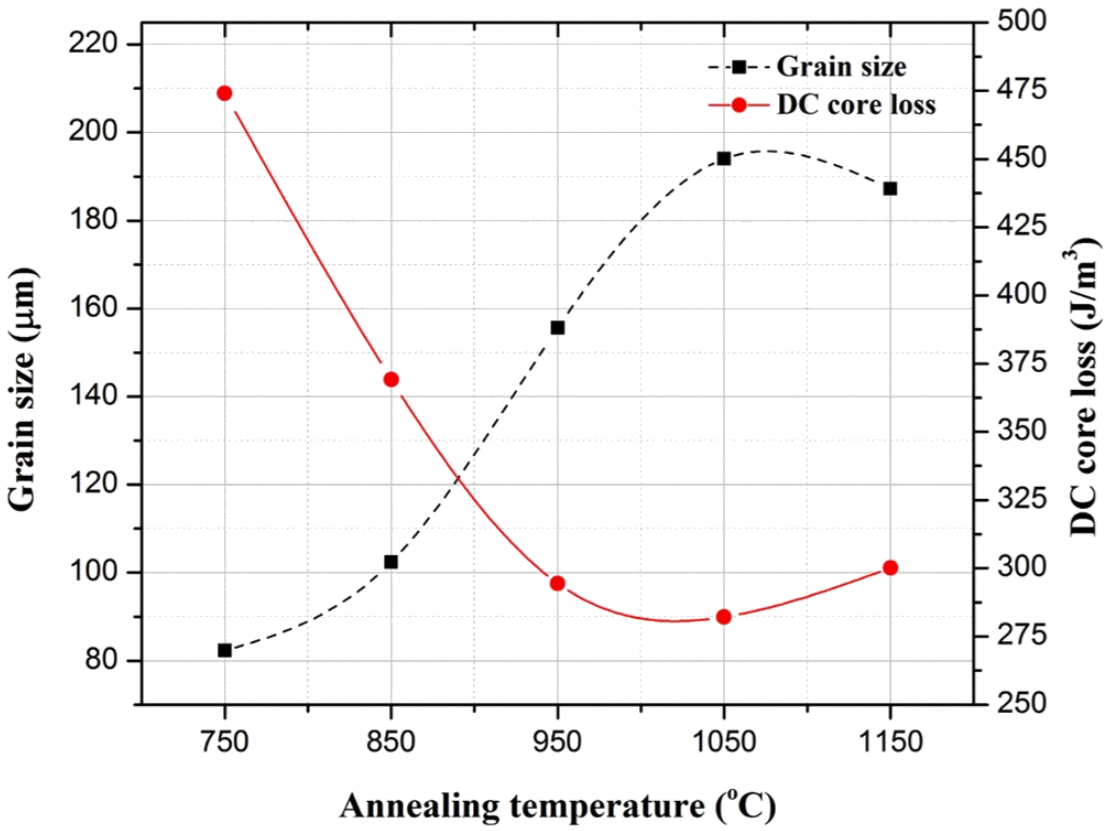

Fig. 7.8. Relation between the annealing temperature and the DC core loss.

7.3.5.2 AC magnetic properties

AC core losses were measured at two frequencies (50 and 250 Hz) and the steels were magnetized to saturation. Depending on the frequency, the saturation flux density is different: for the low frequency, the saturation magnetic flux density reaches ~1.68T, while that of the high frequency is only ~1.38 T. The results at a magnetic flux density of 1.0T for both frequencies are shown in Fig.7.9. The AC core losses at low (50 Hz) and high (250 Hz) frequencies behave slightly differently with respect to the annealing temperature: at low frequency, a minimum loss is observed at 850°C, and further increasing the annealing temperature gradually increases the core loss; at high frequency, the minimum loss is observed at 750°C, and it gradually increases with the

annealing temperature. The AC losses at 250 Hz are approximately an order of magnitude higher than those at 50 Hz.

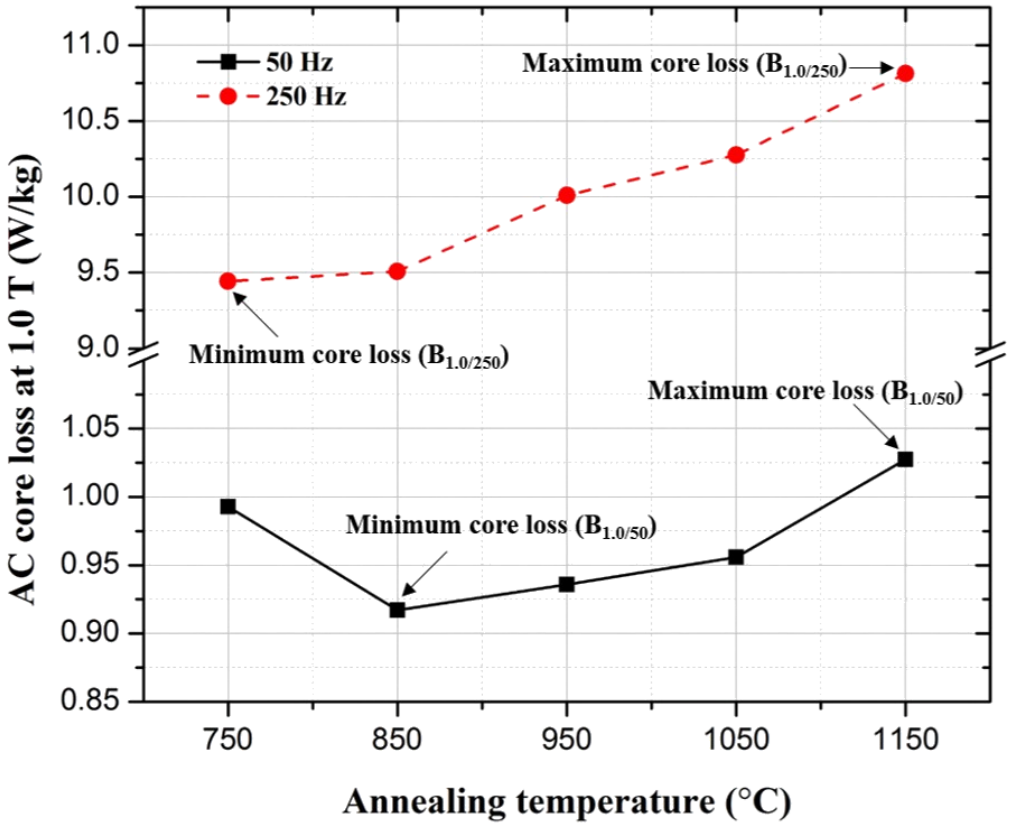

Fig. 7.9. The variations of AC core losses at a magnetizing frequency of 50 Hz and 250 Hz with respect to annealing conditions.

The saturation magnetic flux densities of all the annealed samples at DC and AC (50 Hz) magnetization conditions are shown in Fig. 7.10a. Generally, the DC saturation magnetization is consistently higher than the AC saturation magnetization at all the annealing temperatures, but both show essentially the same trend when the annealing temperature increases. In each case, a minimum saturation magnetization is observed at 850°C, and at all the other temperatures, the saturation magnetic flux densities are essentially the same. Thus, although the AC loss has a minimum after annealing at 850°C for 60 minutes (with the strongest θ-fibre texture), the

saturation magnetization is also the minimum. On the other hand, the relative permeability of the electrical steel (Fig. 7.10b) shows an opposite trend with respect to the annealing temperature, i.e. the relative permeability has a maximum at 850°C, where the magnetically favourite texture <001>//ND has the strongest intensity.

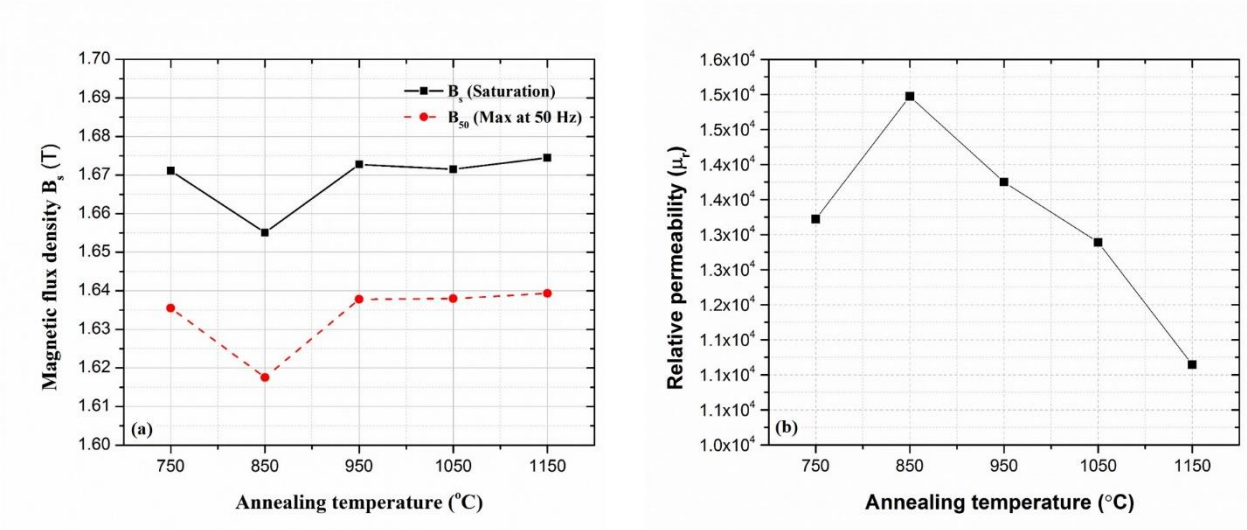

Fig. 7.10. The variation of maximum saturation flux and relative permeability with annealing conditions. (a) Maximum saturation flux at DC conditions (B_s) and maximum flux at 50 Hz (B_{50}) and (b) relative permeability (μ_r).

7.3.5.3 AC core loss compared to commercial grain-oriented electrical steel

The magnetic properties (rolling direction) of the non-oriented electrical steel produced in this study (annealed at 850°C for 60 minutes) are compared to those of commercially available *grain-oriented* electrical steel in Fig. 7.11. Both steels contain essentially the same amount of silicon (3.20%) and the thicknesses of the sheets are all ~0.35 mm. As can be seen from Fig. 7.11a, if the magnetic flux density is smaller than ~1.25T, the core losses of the non-oriented electrical steel are comparable (slightly higher than) to those of the commercial grain-oriented electrical

steel even in the *rolling direction*. When the magnetic flux density is greater than ~1.25T, the core losses of the non-oriented electrical steel are apparently higher than those of the grain-oriented steel. It is also noted that the grain-oriented electrical steel has apparent anisotropy between the rolling direction and the transverse direction, i.e. the core losses in the TD are considerably higher than in the RD.

The core losses of both steels at different frequencies (under a fixed magnetic flux density of 1.0T) are quite close with each other (Fig. 7.11b), i.e. the core losses of the non-oriented electrical steel produced in this study are also comparable to those of the grain-oriented electrical steel at all the frequencies if the magnetic flux density is relatively small (1.0T). In fact, the core losses are even slightly lower than those of the grain-oriented electrical steel (RD) when the frequency is less than 225 Hz.

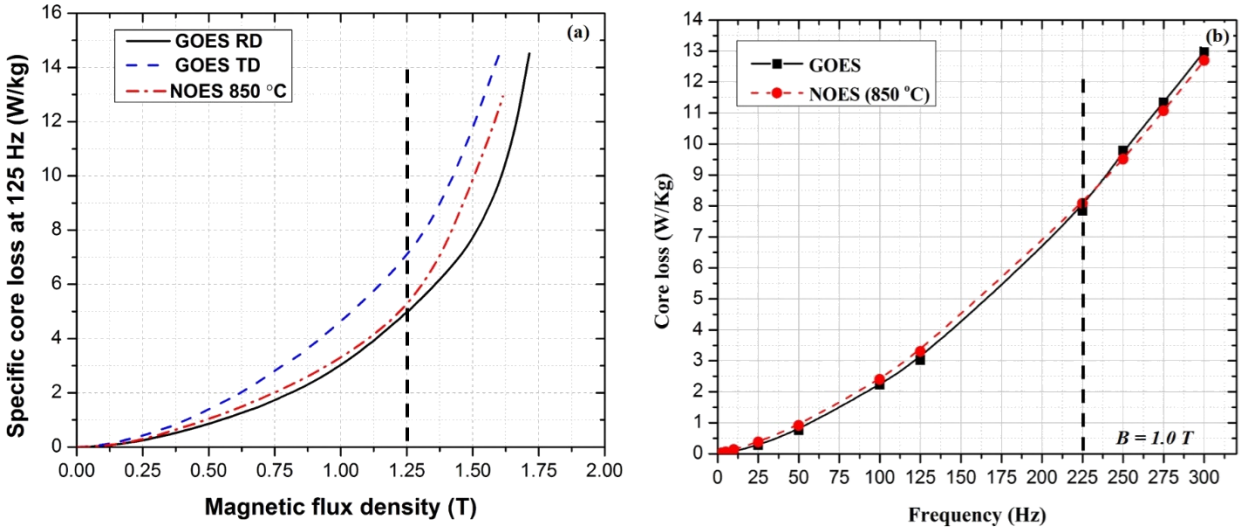

Fig. 7.11 Magnetic properties of the 3.2% Si non-oriented electrical steel produced in this study compared to commercial grain-oriented electrical steel: (a) core losses at different magnetic flux densities and directions (with a fixed frequency of 125 Hz), (b) core losses at various frequencies (with a fixed magnetic flux density of 1.0T).

7.3.5.4 Magnetic Barkhausen noise

The average MBN root mean square (rms) value [27] of the 10 measurements along the rolling direction (Fig. 7.1a) of each steel strip is plotted against the annealing temperature in Fig. 7.12a, where the MBN_{rms} values are also compared to the average grain diameters of the microstructure. It is seen that the MBN_{rms} drops significantly when the annealing temperature increases from 750°C to 1050°C. After that, the MBN_{rms} slightly increases with the increase of the annealing temperature. The grain size, on the other hand, shows an essentially opposite trend. If the MBN_{rms} is plotted against the square root of the average grain diameter *d* (Fig. 7.12b), a linear relationship is observed between the MBN_{rms} and the $d^{1/2}$, which is very similar to the well-known Hall-Petch relationship between the yield strength and the grain size observed in structural materials [12].

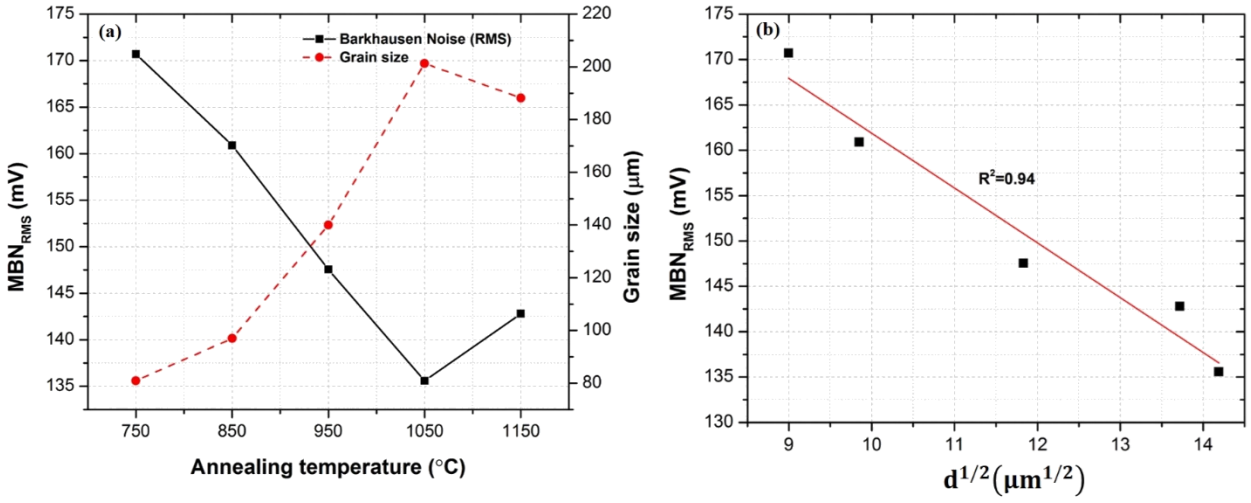

Fig. 7.12 The average MBN_{rms} values measured in the rolling direction of the steel strips: (a) relation between MBN_{rms} and annealing temperature, (b) relation between MBN_{rms} and the average grain size (d).

7.3.5.5 Magnetocrystalline anisotropy

The magnetocrystalline anisotropy of the electrical steel can be characterized using a texture factor [27-29] defined as the minimum angle between the magnetization direction $\overrightarrow{\boldsymbol{M}}$ and the three easy axes <100> of the crystal (Fig. 7.13) weighted by the intensity of the crystal orientation [27-29], which is expressed as:

$$A_\theta = \int f(g)\, A_\theta(g) dg \quad (1)$$

where $A_\theta(g)$ is the minimum angle between the magnetization vector and the three easy <100> axes of a given orientation g, θ is the angle between the magnetization direction and the sample coordinate system (RD in this study), and *f(g)* is the orientation distribution function [30]. For each angle θ, the texture factor can be readily calculated using Eq. (1) by rotating the ODF around the ND for θ angle. The average texture factor is then calculated from the texture factors at all the directions (θ = 0°-360°). Apparently, the smaller the texture factor, the closer the crystals' easy axes are to the magnetization vector.

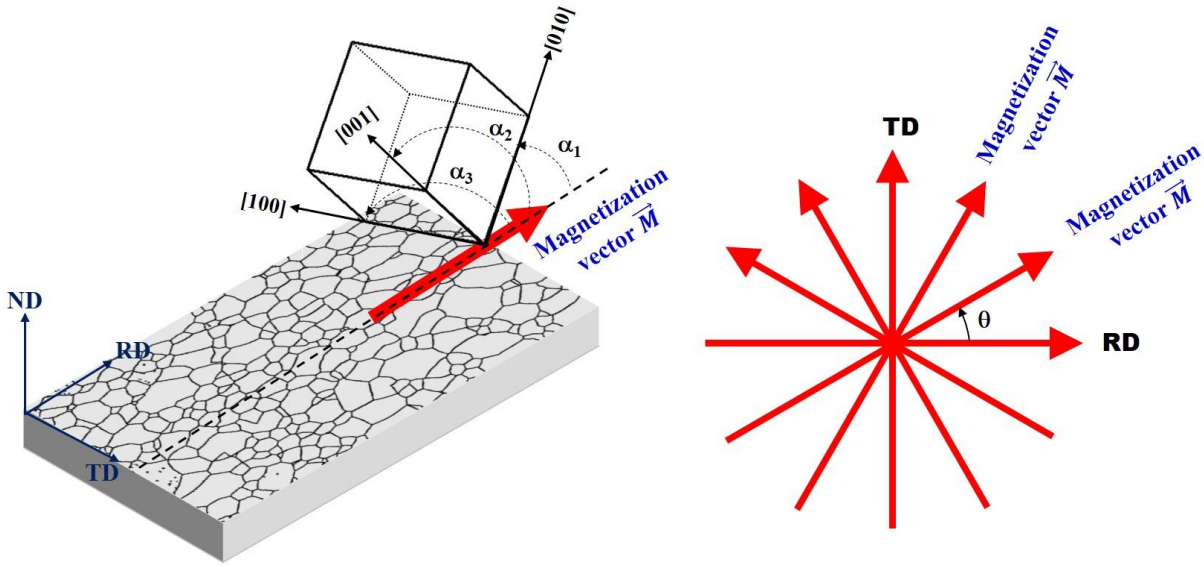

Fig. 7.13. Schematic illustration of the texture factor $A_\theta(g)$ defined as the minimum angle between the magnetization vector ($\vec{M}$) and the crystal easy magnetization axes [100], [010] and [001]. Since α_1 is the minimum angle in this example ($\alpha_1 < \alpha_2 < \alpha_3$) , $A_\theta(g)$ would be equal to α_1.

Fig. 7.14 shows the texture factors of the electrical steel sheets annealed at different temperatures. It is seen that the texture factors (Fig.7.14 a-e) for all non-oriented electrical steel sheets illustrate a similar quatrefoil shape, with the maximum values falling approximately half way between the RD and TD, i.e. at 45°/225° and 135°/315°. The minimums were seen close to RD and TD, i.e. 0°/180° and 90°/270°. The grain-oriented electrical steel (Fig. 7.14f), on the other hand, shows an hourglass shape with the narrow neck in the rolling direction. The very small texture factor (close to 0°) in the rolling direction is due to the unique Goss texture ({011}<100>) in this type of steel, i.e. the minimum angle between the magnetization vector (the RD) and the crystal <100> axes is zero. Apparently, the non-oriented electrical steel shows much less magnetocrystalline anisotropy than the grain-oriented steel since the variation of the texture factor in all the directions is much smaller than that of the grain-oriented steel.

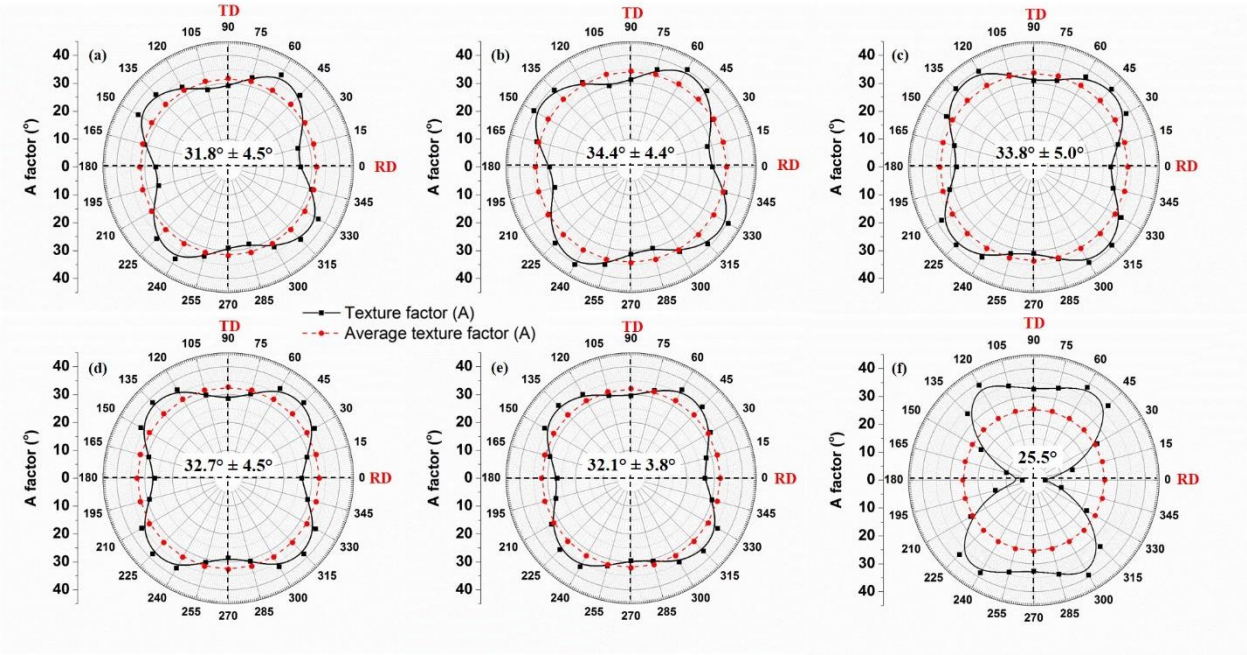

Fig. 7.14. The texture factors at various directions to the RD (0°) for steel sheets annealed under different conditions: (a) 750 °C for 180 min, (b) 850 °C for 60 min, (c) 950 °C for 30 min, (d) 1050 °C for 10 min, (e) 1150 °C for 2 min, and (f) grain-oriented electrical steel.

7.4 Discussion

It has been seen that the crystallographic texture of the 3.2% Si non-oriented electrical steel processed in this study has been considerably improved (i.e. the θ-fibre is strengthened and the γ-fibre is weakened or eliminated) by combining hot band annealing at 860 °C for 24 hours and final annealing at 850°C or higher. The prolonged hot band annealing leads to the formation of a heterogeneous microstructure across the thickness (Fig. 7.3a) and a randomized texture prior to cold rolling (Fig. 7.3b). Lee et al. [32] has reported that the coarse grains after hot band annealing can slow down the recrystallization process after cold rolling, which retards the formation of the <111>//ND orientations after final annealing and promotes the <001>//ND and <113>//ND

textures. On the other hand, de Dafe et al. [33] reported that coarse grains after hot band annealing promote the formation of magnetically favourable crystal orientations (i.e. <001>//ND), due to the increased amount of the shear bands in the deformed microstructure. It is well known that nucleation preferably starts at regions with microstructural heterogeneities (high stored energies), e.g. shear bands, microbands, etc. [12, 33-36]. This will supress the nucleation at grain boundaries that usually leads to the γ-fibre texture. Thus, increasing the amounts of shear bands, microbands or crystal fragmentations leads to the formation of the magnetically favorable θ-fibre components that are normally difficult to form from the nucleation in grain boundaries [31, 32].

On the other hand, the annealing in this study was conducted by inserting the samples into a furnace already heated to the designated temperature, so the heating rate is faster than that heating up with the furnace [37]. Since the <001>//ND grains have a lower stored energy than the <111>//ND grains [12, 25], their nucleation usually requires a higher temperature to occur [12, 25]. The rapid heating rate allows the material to reach the required temperature quickly before the deformed <001>//ND grains are consumed by other recrystallized grains, leading to the formation of the <001>//ND nuclei. Wang et al. [38] reported that a higher heating rate led to grain refinement as well as the weakening of the <111>//ND texture. A higher annealing temperature also promotes the nucleation of the θ-fibre grains. The results shown above (Fig. 7.6 and Fig. 7.7) indicate that the volume fraction of the γ-fibre decreased with the increase of the annealing temperature.

It is well known that the core loss (per hysteresis cycle) of electrical steel at a given frequency f is composed of three major parts [3, 39, 40]:

$$\frac{W(f)}{f} = W_h + W_{cl}(f) + W_{exc}(f) \quad (2)$$

where W_h is the quasi-static hysteresis loss, $W_{cl}(f)$ is the classical eddy current loss, and $W_{exc}(f)$ is the excess loss. The hysteresis loss W_h is independent of the frequency (*f*), while the other two losses are closely related to the frequency.

The hysteresis loss is directly related to the domain wall motion during the magnetization and demagnetization process under quasi-static conditions, which can be evaluated using the Steinmetz empirical formula [39-41].

$$W_h = \oint HdB \approx K_h(B_m)^x \quad (J/m^3) \tag{3}$$

where K_h and x are material-dependent parameters.

Eddy current loss is dependent on the thickness of the steel sheet *t*, the electrical resistivity ρ, the peak flux density B_m, as well as on the magnetizing frequency *f*, which can be calculated as [3, 39, 40]:

$$W_{cl}(f) = \frac{\pi^2}{k\rho} t^2 B_m^2 f \quad (J/m^3) \tag{4}$$

where *k* is a magnetization waveform dependent constant.

The origin of the excess loss remains a subject of debate in the literature. Some researchers have attributed the excess loss to the motion of large magnetic domains, and thus believing W_h and W_{exc} to have a similar origin. The excess loss can be evaluated as:

$$W_{exc}(f) = k_{exc}\sqrt{\sigma f} B_m^{3/2} \quad (J/m^3) \tag{5}$$

where k_{exc} is a material parameter related to the domain structure and the structural properties of the material [3, 39, 40].

The DC core loss shown in Fig. 7.8 confirmed that with the increase of the grain size, the grain boundaries decreased, which resulted in the decrease of the loss, since the pinning effect of the grain boundaries was reduced during the magnetization and demagnetization. This was also

reflected in the MBN response (Fig. 7.12), i.e. the less the grain boundaries, the less the pinning sites for domain wall motion, and the smaller the MBN.

Although Eq. 4 does not show an explicit relation between the eddy current loss and the grain size, it has been reported by a few researchers [3, 7, 39, 42] that the eddy current loss increases with grain size. Because of the opposite relation between the hysteresis loss and the grain size, there exists an optimal grain size at which the total loss induced by hysteresis and eddy current is minimum, e.g. the sample annealed at 850 °C for 60 minutes as shown in Fig. 7.9a. However, this is true only for low frequency excitations, since at high frequencies, the eddy current loss (which is proportional to f^2) will dominate the total loss, thus a smaller grain size would result in a smaller core loss [3, 39, 42]. The sample annealed at 750 °C for 180 minutes has the smallest grain size (~82 μm), thus it has the lowest core loss at 250 Hz.

Although it has been shown in Fig. 7.6 that, when the annealing temperature was increased, the texture could be optimized, i.e. the θ-fibre was promoted and the γ-fibre was weakened, the AC core loss does not show apparent improvement with the texture optimization, i.e. the variation of the core loss is quite small no matter what is the texture. As shown in Fig. 7.15, the texture factors (in RD) of the steels annealed at different temperatures vary from 26.0° to 29.3°, and the core losses of these steels vary from 0.94 W/kg to 1.025W/kg, but the lowest texture factor does not correspond to the lowest core loss. In fact, it is the opposite, i.e. the largest texture factor leads to the lowest core loss (annealing at 850°C for 60 minutes). Apparently, the dominant factor here is not the crystallographic texture, i.e. other microstructural features (e.g. grain size) may have controlled the core loss (e.g. the excess loss) [28].

Nevertheless, it has been shown that the core losses of the non-oriented electrical steel annealed at 850°C for 60 minutes were comparable to, or even better than, those of the

commercially available grain-oriented electrical steel if the magnetic flux density is smaller than 1.25T. It is well known that the grain-oriented electrical steel consists of essentially only one grain orientation (the Goss) with very large grain sizes (centimetres) [12]. Although it has very small texture factor in the rolling direction (which is beneficial to the core loss), the extremely large grain size will simultaneously deteriorate this, especially when the frequency is high. This is because the eddy current loss will dominate the total loss when the frequency is high, and the eddy current loss increases with grain size. Apparently, a good combination of the microstructure and the crystallographic texture of the non-oriented electrical steel produced in this study was the key to better core losses than the grain-oriented electrical steel.

7.5 Conclusions

i. The texture of 3.2% Si electrical steel can be improved through hot band annealing, faster heating rates as well as controlling the annealing temperature.

ii. Using an annealing temperature higher than 750 °C resulted in the increase of the magnetically favourable θ-fibre and suppressing the magnetically detrimental γ-fibre. This was due to the favourite nucleation at shear bands, microbands and fragmented grains, especially after obtaining coarse grains during hot band annealing.

iii. The DC core losses decreased with increasing grain size, which showed a good correlation with the MBN_{rms} measurements.

iv. The AC core loss was the lowest for the sample annealed at 850 °C for 60 minutes. This is due to the optimized texture and grain size obtained for this sample. In addition, the relative permeability was the highest for this sample.

v. For high frequency applications, it was shown that the grain size is the dominant factor, such that the lowest core loss is obtained for the sample with the smallest grain size, i.e. the one annealed at 750 °C for 180 minutes.

vi. The sample annealed at 850 °C for 60 minutes had an AC core loss that is slightly higher than GOES at low frequencies (<225 Hz) and lower AC core loss at higher frequencies (>225 Hz). The calculation of the texture factor reveals that the NOES sample is much more isotropic than the GOES.

References

1. Cullity, B. D., & Graham, C. D. (2011). Introduction to magnetic materials. John Wiley & Sons.

2. Chen, C. W. (2013). Magnetism and metallurgy of soft magnetic materials. Courier Corporation.

3. Fiorillo, F., Bertotti, G., Appino, C., and Pasquale, M.: Soft magnetic materials. In Wiley Encyclopedia of Electrical and Electronics Engineering, Peterca, M., ed. (Wiley, Hoboken, New Jersey, 2016)

4. Moses, A. J. (1990). Electrical steels: past, present and future developments. IEE Proceedings A (Physical Science, Measurement and Instrumentation, Management and Education), 137(5), 233-245.

5. Lyudkovsky, G., Rastogi, P. K., & Bala, M. (1986). Nonoriented electrical steels. JOM, 38(1), 18-26.

6. Mehdi, M., He, Y., Hilinski, E. J., & Edrisy, A. (2017). Effect of skin pass rolling reduction rate on the texture evolution of a non-oriented electrical steel after inclined cold rolling. Journal of Magnetism and Magnetic Materials, 429, 148-160.

7. Matsumura, K., & Fukuda, B. (1984). Recent developments of non-oriented electrical steel sheets. IEEE Transactions on Magnetics, 20(5), 1533-1538.

8. Oda, Y., Kohno, M., & Honda, A. (2008). Recent development of non-oriented electrical steel sheet for automobile electrical devices. Journal of Magnetism and Magnetic Materials, 320(20), 2430-2435.

9. Petrovic, D. S. (2010). Non-oriented electrical steel sheets. Materiali in tehnologije, 44(6), 317-325.

10. Hawezy, D. (2017). The influence of silicon content on physical properties of non-oriented silicon steel. Materials Science and Technology, 33(14), 1560-1569.

11. Moses, A. J. (2012). Energy efficient electrical steels: Magnetic performance prediction and optimization. Scripta Materialia, 67(6), 560-565.

12. Humphreys, F. J., & Hatherly, M. (2012). Recrystallization and related annealing phenomena. Elsevier.

13. Kestens, L., & Jacobs, S. (2008). Texture control during the manufacturing of nonoriented electrical steels. Texture, Stress, and Microstructure, 2008.

14. ASTM A343 / A343M-14, Standard Test Method for Alternating-Current Magnetic Properties of Materials at Power Frequencies Using Wattmeter-Ammeter-Voltmeter Method and 25-cm Epstein Test Frame, ASTM International, West Conshohocken, PA, (2014)

15. KJS Associates/Magnetic Instrumentation Inc, COMPUTER-AUTOMATED MAGNETIC HYSTERESIGRAPH FOR TESTING OF MAGNETICALLY SOFT MATERIALS MODEL SMT-700 TECHNICAL REFERENCE MANUAL, (July 2015) 1-74.

16. Stresstech Group, Rollscan 350 Operating Instructions, V1.0b (2013) 1-39.

17. Stresstech Group, MicroScan 600 Operating Instructions, V.5.4b (2015) 1-37.

18. Raabe, D. (2003). Overview on basic types of hot rolling textures of steels. steel research international, 74(5), 327-337.

19. Sidor, J. J., Verbeken, K., Gomes, E., Schneider, J., Calvillo, P. R., & Kestens, L. A. (2012). Through process texture evolution and magnetic properties of high Si non-oriented electrical steels. Materials characterization, 71, 49-57.

20. Raabe, D., & Lücke, K. (1994). Rolling and annealing textures of bcc metals. In Materials Science Forum (Vol. 157, pp. 597-610). Trans Tech Publications.

21. Hölscher, M., Raabe, D., & Lücke, K. (1991). Rolling and recrystallization textures of bcc steels. steel research, 62(12), 567-575.

22. Hu, H. (1974). Texture of metals. Texture, Stress, and Microstructure, 1(4), 233-258.

23. Ray, R. K., Jonas, J. J., & Hook, R. E. (1994). Cold rolling and annealing textures in low carbon and extra low carbon steels. International materials reviews, 39(4), 129-172.

24. Gobernado, P., Petrov, R. H., & Kestens, L. A. I. (2012). Recrystallized {311}< 136> orientation in ferrite steels. Scripta Materialia, 66(9), 623-626.

25. Sanjari, M., He, Y., Hilinski, E. J., Yue, S., & Kestens, L. A. (2016). Development of the {113}< uvw> texture during the annealing of a skew cold rolled non-oriented electrical steel. Scripta Materialia, 124, 179-183.

26. Jenkins, K., & Lindenmo, M. (2008). Precipitates in electrical steels. Journal of Magnetism and Magnetic Materials, 320(20), 2423-2429.

27. He, Y., Mehdi, M., Hilinski, E. J., Edrisy, A., Mukundan, S., Mollaeian, A., & Kar, N. C. (2018). Evaluation of Local Anisotropy of Magnetic Response From Non-Oriented Electrical Steel by Magnetic Barkhausen Noise. IEEE Transactions on Magnetics, (99), 1-5.

28. J.J. Sidor, K. Verbeken, E. Gomes, J. Schneider, P.R. Calvillo, L.A.I. Kestens, Through process texture evolution and magnetic properties of high Si non-oriented electrical steels, Materials Characterization. 71 (2012) 49-57.

29. He, Y., Mehdi, M., Hilinski, E. J., Edrisy, A., Mukundan, S., Mollaeian, A., & Kar, N. C. (2018). Evaluation of Local Anisotropy of Magnetic Response From Non-Oriented Electrical Steel by Magnetic Barkhausen Noise. IEEE Transactions on Magnetics, (99), 1-5.

30. Bunge, H. J. (2013). Texture analysis in materials science: mathematical methods. Elsevier.

31. Lee, K. M., Huh, M. Y., Lee, H. J., Park, J. T., Kim, J. S., Shin, E. J., & Engler, O. (2015). Effect of hot band grain size on development of textures and magnetic properties in 2.0% Si non-oriented electrical steel sheet. Journal of Magnetism and Magnetic Materials, 396, 53-64.

32. De Dafe, S. S. F., da Costa Paolinelli, S., & Cota, A. B. (2011). Influence of thermomechanical processing on shear bands formation and magnetic properties of a 3% Si non-oriented electrical steel. Journal of Magnetism and Magnetic Materials, 323(24), 3234-3238.

33. Park, J. T., & Szpunar, J. A. (2003). Evolution of recrystallization texture in nonoriented electrical steels. Acta Materialia, 51(11), 3037-3051.

34. Dorner, D., Zaefferer, S., & Raabe, D. (2007). Retention of the Goss orientation between microbands during cold rolling of an Fe3% Si single crystal. Acta materialia, 55(7), 2519-2530.

35. Nguyen-Minh, T., Sidor, J. J., Petrov, R. H., & Kestens, L. A. I. (2012). Occurrence of shear bands in rotated Goss ({1 1 0}< 1 1 0>) orientations of metals with bcc crystal structure. Scripta Materialia, 67(12), 935-938.

36. Dillamore, I. L., Roberts, J. G., & Bush, A. C. (1979). Occurrence of shear bands in heavily rolled cubic metals. Metal Science, 13(2), 73-77.

37. Sanjari, M., Mehdi, M., He, Y., Hilinski, E. J., Yue, S., Kestens, L. A., & Edrisy, A. (2017). Tracking the Evolution of Annealing Textures from Individual Deformed Grains in a Cross-Rolled Non-oriented Electrical Steel. Metallurgical and Materials Transactions A, 48(12), 6013-6026.

38. Jian, W. A. N. G., Jun, L. I., Wang, X. F., Tian, J. J., Zhang, C. H., & Zhang, S. G. (2010). Effect of heating rate on microstructure evolution and magnetic properties of cold rolled non-oriented electrical steel. Journal of iron and steel research, international, 17(11), 54-61.

39. Moses, A. J. (2012). Energy efficient electrical steels: Magnetic performance prediction and optimization. Scripta Materialia, 67(6), 560-565.

40. Goodenough, J. B. (2002). Summary of losses in magnetic materials. IEEE Transactions on magnetics, 38(5), 3398-3408.

41. Steinmetz, C. P. (1984). On the law of hysteresis. Proceedings of the IEEE, 72(2), 197-221.

42. Bertotti, G., Di Schino, G., Milone, A. F., & Fiorillo, F. (1985). On the effect of grain size on magnetic losses of 3% non-oriented SiFe. Le Journal de Physique Colloques, 46(C6), C6-385.

Chapter 8 Summary and Conclusions

In this work, non-oriented electrical steels with various silicon contents (0.9%, 2.8% and 3.2%, weight percentage) were thermomechanically processed using both conventional and unconventional rolling schemes. The evolution of texture during these processing stages was investigated using electron backscatter diffraction techniques. The formation mechanisms of specific crystallographic orientations that are of particular importance to the magnetic properties of the steel sheets, e.g. the cube and Goss, were examined considering the effects of hot rolling, hot band annealing, cold rolling and final annealing on the final texture. New insights and contributions to the scientific/technological fields and knowledge are summarized as follows:

The cube texture was normally very difficult to develop in non-oriented electrical steels through conventional rolling and annealing. Using inclined rolling, this research successfully "generated" the rotated Goss texture, which was also very rare in electrical steel after conventional rolling, and through cold deformation (plane-strain compression) of this texture, cube crystallites were produced within the shear bands of the rotated Goss and cube texture was subsequently nucleated from these volumes during annealing. This provides new insights into the formation mechanisms of the cube texture, which is of particular interest in both scientific research and practical implementation. It also highlighted the importance of producing specific textures before cold rolling in order to obtain the final desired texture after annealing.

A new origin of the Goss orientation was observed at the grain boundaries between the {111}<112> and {113}<361> orientations. The Goss crystallites were believed to be retained from original Goss grains during plane-strain compression, where the Goss was split into two orientations, {111}<112> and {113}<361>, that have essentially identical orientation relationship

with respect to the Goss, i.e. ~35°<110>. The residual Goss crystallites essentially do not undergo plastic deformation and would nucleate preferentially during subsequent annealing. The high mobility of the ~35°<110> boundary facilitates the growth of the Goss into the deformed matrix. The same mechanism may be applied to the cube crystallites observed at the cube grain boundaries in the 3.2 wt% Si steel.

By simply varying the annealing time, significantly different recrystallization textures were obtained in a 2.8 wt% Si non-oriented electrical steel. Annealing for 60 or 90 minutes at 750°C can essentially eliminate the magnetically unfavourable <111>//ND texture while promoting the desired <001>//ND texture; annealing at the same temperature for 30 or 120 minutes strengthens the <111>//ND texture and weakens the favourable <001>//ND texture. The formation mechanisms of the specific textures were reasonably well explained in terms of the grain boundary character and relative grain sizes through statistical analysis of the grain boundary misorientations.

A 3.2 wt% Si non-oriented electrical steel was optimized through appropriate hot band annealing and controlled final annealing. The final steel sheets annealed at 850°C for 60 minutes showed AC core losses comparable to, or even better than, those of commercially available grain-oriented electrical steel (with the same silicon content and sheet thickness), even in the rolling direction. This processing route may be readily applicable to mass production for the manufacturing of high quality electrical steel laminations.

Skin-pass rolling and final annealing were applied to incline-rolled and annealed non-oriented electrical steel to investigate the effect of the final small plastic deformation on the final texture. A 5% to 20% reduction of the annealed thin sheet may slightly or moderately alter the final annealing texture, depending on the original texture and the amount of reduction applied. The

cube texture is generally weakened while the rotated cube component may be strengthened or weakened depending on the amount of skin-pass reduction. The γ-fibre is slightly weakened or essentially does not change, again depending on the amount of reduction applied. The results of these experiments may be used to guide the practical application of the temper rolling process in the production of electrical steel laminations.

8.1 Future work

Some of the future work that I would like to pursue and investigate in the near future include:

1. Promoting the growth of the cube grains that were developed after inclined cold rolling inside the rotated Goss grains, in a similar way to the method used in the development of GOES. This can be done by examining whether abnormal grain growth can be induced once the cube nuclei are formed during primary recrystallization.
2. Investigate whether there exists a correlation between the core losses obtained from the Epstein frame tests and the MBN_{RMS} measurements obtained from magnetic Barkhausen noise analysis. This would be extremely beneficial and would have many research and practical applications. In order to do this, a careful experimental procedure has to be designed such that all microstructural and chemical parameters would be the same, and the only difference would be crystallographic texture.
3. Tracking texture evolution during recrystallization is also very essential to understanding the recrystallization dynamics of electrical steels. This can be done by identifying the nucleation sites and measuring the growth rates of different orientations. I have completed most of the experimental work related to this work, by tracking a region along the RD-ND plane of a hot rolled plate using quasi-in-situ EBSD technique at various recrystallization stages.

8.2 Contributions

1. M. Mehdi, Y. He, E. J. Hilinski, L. A. Kestens, A. Edrisy, The Formation of the Cube ({100}<001>) Texture in Non-oriented Electrical Steels (to be submitted).

2. M. Mehdi, Y. He, E. J. Hilinski, L. A. Kestens, A. Edrisy, The Origins of the Goss Orientation in a 2.8 wt% Si Non-oriented Electrical Steel, Journal of steel research international (submitted).

3. M. Mehdi, Y. He, E. J. Hilinski, A. Edrisy, Texture Evolution of a 2.8% Si Non-oriented Electrical Steel and the Elimination of the <111>//ND Texture, Journal of Metallurgical and Materials Transactions A (submitted).

4. Mehdi, Mehdi, Youliang He, Erik J. Hilinski, and Afsaneh Edrisy. "Effect of skin pass rolling reduction rate on the texture evolution of a non-oriented electrical steel after inclined cold rolling." Journal of Magnetism and Magnetic Materials 429 (2017): 148-160. (published)

5. Mehdi, Mehdi, Youliang He, Erik J. Hilinski, and Afsaneh Edrisy, Non-oriented Electrical Steel with Core Losses Comparable to Grain-oriented Electrical Steel, Journal of Magnetism and Magnetic Materials (submitted).

6. He, Y., Mehdi, M., Hilinski, E. J., & Edrisy, A. (2018). Through-process characterization of local anisotropy of Non-oriented electrical steel using magnetic Barkhausen noise. Journal of Magnetism and Magnetic Materials, 453, 149-162.

7. He, Y., Mehdi, M., Hilinski, E. J., Edrisy, A., Mukundan, S., Mollaeian, A., & Kar, N. C. (2018). Evaluation of Local Anisotropy of Magnetic Response From Non-Oriented Electrical Steel by Magnetic Barkhausen Noise. IEEE Transactions on Magnetics, (99), 1-5.

8. He, Y. L., Mehdi, M., Hilinski, E. J., & Edrisy, A. (2018). Magnetic Barkhausen Noise Characterization of the Recrystallization of a Non-Oriented Electrical Steel after Cold Rolling at Different Angles to the Hot Rolling Direction. In Materials Science Forum (Vol. 941, pp. 274-279). Trans Tech Publications.

9. Sanjari, M., Mehdi, M., He, Y., Hilinski, E. J., Yue, S., Kestens, L. A., & Edrisy, A. (2017). Tracking the Evolution of Annealing Textures from Individual Deformed Grains in a Cross-Rolled Non-oriented Electrical Steel. Metallurgical and Materials Transactions A, 48(12), 6013-6026.

10. Mehdi, M., Farokhzadeh, K., & Edrisy, A. (2016). Dry sliding wear behavior of superelastic Ti–10V–2Fe–3Al β-titanium alloy. Wear, 350, 10-20.

11. Mehdi, M., He, Y., Hilinski, E. J., & Edrisy, A. (2018, June). Texture Evolution of a 2.8 wt% Si Non-Oriented Electrical Steel during Hot Band Annealing. In IOP Conference Series: Materials Science and Engineering (Vol. 375, No. 1, p. 012014). IOP Publishing.

12. Mehdi, M., He, Y., Hilinski, E. J., & Edrisy, A. (2017). Effect of Annealing Time on the Texture of a 2.8% Si Non-Oriented Electrical Steel After Inclined and Skew Rolling. In TMS 2017 146th Annual Meeting & Exhibition Supplemental Proceedings (pp. 683-691). Springer, Cham.

APPENDIX A: COPYRIGHT RELEASES FROM PUBLICATIONS

VITA AUCTORIS

NAME:	Mehdi Mehdi
PLACE OF BIRTH:	Media, Algeria
YEAR OF BIRTH:	1989
EDUCATION:	University of Windsor, Windsor, Ontario 2007-2011 B. Sc.
	University of Windsor, Windsor, Ontario 2011-2013 M. Sc.
	University of Windsor, Windsor, Ontario 2013-2019 Ph.D.